FAKULTÄT FÜR MASCHINENWESEN

LEHRSTUHL FÜR AERODYNAMIK UND STRÖMUNGSMECHANIK

Numerical methods for computational fluid dynamics - a new ENO paradigm and a new domain decomposition method

Lin Fu

Vollständiger Abdruck der von der Fakultät für Maschinenwesen der Technischen Universität München zur Erlangung des akademischen Grades eines

Doktor-Ingenieurs

genehmigten Dissertation.

Vorsitzender:		Prof. Dr.-Ing. Hans-Jakob Kaltenbach
Prüfer der Dissertation:	1.	Priv.-Doz. Dr.-Ing. habil. Xiangyu Hu
	2.	Prof. Takayuki Aoki
	3.	Prof. Dr.-Ing. Nikolaus A. Adams

Die Dissertation wurde am 02.08.2017 bei der Technischen Universität München eingereicht und durch die Fakultät für Maschinenwesen am 02.10.2017 angenommen.

Declaration

I hereby declare that except where specific reference is made to the work of others, the content of this dissertation is original and has not been submitted in whole or in part for consideration for any other degree or qualification in this, or any other university. This dissertation is my own work and contains nothing which is the outcome of work done in collaboration with others, except as specified in the text and Acknowledgements.

Lin Fu

02.10.2017

Abstract

In this cumulative thesis, several novel numerical methods, including the high-order shock-capturing targeted Essentially Non-oscillatory (TENO) schemes, smoothed-particle hydrodynamics (SPH) based partitioning method and Centroidal Voronoi Particle (CVP) domain decomposition method, are proposed and validated.

As the first part of the work, a family of high-order TENO schemes for compressible fluid simulations is proposed. Although classical Weighted Essentially Non-oscillatory (WENO) schemes have been popular over the last decades, there are some shortcomings, e.g. they are unnecessarily dissipative for resolving small-scale structures, and the very-high-order version may lack numerical robustness. The TENO schemes address these drawbacks by three novel ideas. (i) The high-order reconstruction is achieved by assembling a set of candidate stencils of incremental width. For very-high-order reconstructions, the TENO scheme can gradually degenerate from high-order to low-order according to the measurement of local flow scales. Since the smallest three stencils are identical to that of classical fifth-order WENO scheme, good numerical robustness can be recovered when there exist multiple discontinuities close to each other. Moreover, arbitrarily high-order schemes, i.e. both odd and even order, can be constructed in this unified framework. (ii) A novel Essentially Non-oscillatory (ENO)-like stencil selection procedure, which either applies one candidate stencil with the corresponding optimal weight or removes its contribution completely when crossed by discontinuities, is proposed as well as a strong scale-separation formula. While the scale-separation procedure efficiently isolates the discontinuities from smooth regions, the tailored ENO-like stencil selection enforces the ENO property near discontinuities while preserving the low-dissipation property for smooth regions. The spectral property of TENO schemes can be preserved exactly to that of the counterpart linear scheme for low to intermediate wavenumbers. (iii) The spectral properties of TENO

schemes can be optimized to satisfy a certain dispersion-relation by accuracy reduction of order one. Extensive numerical simulations demonstrate that the TENO family schemes are superior to WENO schemes in terms of both performance and robustness.

As the second part of the work, a novel smoothed-particle hydrodynamics based partitioning method for large-scale parallel load-balancing problem is proposed. For typical static load-balancing problems, the optimization objectives involve, e.g. the subdomains are approximately equal-sized, the communication between subdomains is minimized and the partitioning subdomains are continuous. In terms of dynamic load-balancing, the locality and incremental property of the partitioning subdomains serve as additional constraints. Based on the observation that the partitioning outcome has high similarity to a multi-phase system, a set of model equations is developed to characterize the background mesh topology and solved by multi-phase smoothed-particle hydrodynamics. Unlike traditional partitioning methods, i.e. the geometry-based and graph-based methods, all the objectives are optimized implicitly in a unified framework. A physics-motivated surface tension model is introduced to optimize the communication volume between subdomains and maintain the sharp, convex and compact shapes. In order to stabilize the particle evolution, viscous and skin friction models coupling with a tailored time integral algorithm are proposed. Moreover, a multi-resolution based cell linked list technique is proposed for particle neighbor searching and a dynamic ghost particle method is developed to enforce symmetry boundary condition. Numerical experiments show that the present method features several pronounced properties and is promising for large-scale load-balancing parallel simulations and other partitioning applications demanding high performance.

At last, a novel domain decomposition method by combing Centroidal Voronoi Tessellation (CVT) and Voronoi Particle (VP) dynamics is proposed. The CVT is introduced to achieve a high-level compactness of the partitioning subdomains by the Lloyd's algorithm which monotonically decreases the CVT energy. Voronoi Particle dynamics employing physical analogy with a tailored equations-of-state is developed, which relaxes the particle system towards the target partition with good load balance. Unlike CVT, CVP is able to achieve multiple optimization objectives simultaneously, i.e. the arbitrary target mass distribution and compactness. It is achieved regardless of the smoothness properties of the density function, the number of generators and the boundary complexity. The traditional CVT method, even with sufficiently smooth density function and infinite number of generators

based on Gersho's conjecture, cannot achieve arbitrary target mass distribution, e.g. nonequal-sized partitioning. For non-smooth density functions and small generator number, which is typical for practical partitioning problems of scientific computing, the CVT method is inferior to CVP. Extensive numerical experiments demonstrate that the CVP method generates high-quality partitioning and thus is promising for widespread scientific computing applications.

Acknowledgements

First of all, I would like to express my sincere gratitude to Prof. Nikolaus A. Adams and PD Dr. Xiangyu Hu for their kindness, patience and encouragement. Thanks for the inspiring suggestions from Prof. Adams in the weekly group meeting and the very detailed revising for my papers, which promote me a lot. I am very grateful to Xiangyu, who has been advising this work. I do appreciate the useful discussions.

I would like to thank China Scholarship Council for providing the CSC scholarship, which supported my four-year Ph.D study in TUM, Germany. This opportunity definitely changes my whole life.

Acknowledgment is also given to Prof. Takayuki Aoki, who kindly agrees to be committee member of my thesis defense.

Thanks for the stimulating discussions about bubble dynamics with Xiuxiu Lyu. I appreciate the collaborations with my colleague and friend Zhe Ji. We had a nice time together over the last two years and I really enjoyed the fruitful discussions about philosophy and research. I want to say thanks to Dr. Sergey Litvinov. He was always available for help. I acknowledge the accompany with Chi Zhang and many other colleagues.

This thesis is also dedicated to my high-school teacher, Hongzhi Li who just passed away last week. I appreciate his three-year earnestly instruct.

At last, I would like to express my gratitude to my father Shuocheng Fu, my mother Suxia Bian, my young brother Bin Fu and my wife Mengmeng Yan for their unconditional love, trust and long-term encouragement. From the beginning to the end, my parents support me in every aspect of my education and research. In order to take care of me, Mengmeng Yan gave up her job in China and accompanied me in Munich to overcome the hard time. I am indebted to you and I love you.

Table of contents

Abstract **v**

Acknowledgement **ix**

Nomenclature **xiii**

1 Introduction **1**

1.1 Compressible fluid dynamics 1

1.2 High-performance computational fluid dynamics 1

1.2.1 High-resolution simulation 3

1.2.2 Large-scale parallel computing 3

1.3 Outline 6

2 Numerical methods **9**

2.1 Hyperbolic Conservation Laws 9

2.1.1 Navier-Stokes equations 9

2.1.2 Weighted Essentially Non-oscillatory scheme 11

2.1.3 Runge-Kutta method 16

2.2 Smoothed Particle Hydrodynamics 17

2.2.1 Governing equations 17

2.2.2 Equation of state and kernel function 17

2.2.3 Discretization scheme 19

2.2.4 Time integration method 21

2.3 Domain Decomposition method 21

2.3.1 Voronoi Tessellation method 21
2.3.2 Centroidal Voronoi Tessellation method 22
2.3.3 Lloyd's algorithm 23

3 Achievements **25**

3.1 A family of high-order targeted ENO schemes for compressible-fluid simulations . . 25
3.1.1 State of the art 25
3.1.2 Summary of the proposed method 26
3.2 A novel partitioning method for block-structured adaptive meshes 28
3.2.1 State of the art 28
3.2.2 Summary of the proposed method 29
3.3 A physics-motivated Centroidal Voronoi Particle domain decomposition method . . . 31
3.3.1 State of the art 31
3.3.2 Summary of the proposed method 32

4 Conclusions and outlooks **35**

References **39**

Appendix A: **46**

Article I: A family of high-order targeted ENO schemes for compressible-fluid simulations 47

Appendix B: **80**

Article II: A novel partitioning method for block-structured adaptive meshes 81

Appendix C: **114**

Article III: A physics-motivated Centroidal Voronoi Particle domain decomposition method 115

Nomenclature

Notation

CFD	Computational Fluid Dynamics
PDE	Partial Differential Equation
ODE	Ordinary Differential Equation
NS	Navier–Stokes
RANS	Reynolds-averaged Navier–Stokes
LLF	Local Lax-Friedrichs
DNS	Direct Numerical Simulation
LES	Large-eddy Simulation
ILES	Implicit Large-eddy Simulation
CFL	Courant-Friedrich-Lewy
RK	Runge-Kutta
SSP	Strong Stability-Preserving
TVD	Total Variation Diminishing
ENO	Essentially Non-oscillatory
WENO	Weighted Essentially Non-oscillatory

TENO Targeted Essentially Non-oscillatory

ADR Approximate Dispersion Relation

SPH Smoothed-particle Hydrodynamics

CVT Centroidal Voronoi Tessellation

VP Voronoi Particle

CVP Centroidal Voronoi Particle

AMR Adaptive Mesh Refinement

HPC High-performance Computing

EOS Equations-of-State

RCB Recursive Coordinate Geometric Bisection

SFC Space-Filling Curve

RSB Recursive Spectral Bisection

Chapter 1

Introduction

1.1 Compressible fluid dynamics

For our daily life, water or other stiff fluids are regarded as "incompressible" or "weakly compressible" since the flow velocity is quite small in comparison with the sound speed of such fluid. For air-like gas dynamics, more often, when the flow speed approaches the fluid sound speed, the compressibility effect cannot be ignored and may even dominate the flow phenomena. For instance, the speed of modern commercial jets and space vehicles can be larger or even several-times larger than sound speed. Consequently, the aerodynamic compression is so strong that complex shockwave patterns can form and significantly increase the drag. Despite the shockwave dynamics, turbulence is a ubiquitous phenomena, which profoundly affects the physical processes in engineering applications, e.g. flow control, drag reduction, heat transfer and mixing. Until nowadays, turbulence is still regarded as one of the most important unresolved problems of classical physics [22]. Moreover, the interaction between shocks and turbulence can make the fluid system even more complicated, e.g. see Fig. 1.1. In a word, to study and understand the physics of compressible fluid dynamics is essentially important.

1.2 High-performance computational fluid dynamics

In addition to the theoretical analysis, there are two basic ways to study the physics of fluids, i.e. experiments and numerical simulations with the assistance of computers. Compared with experiments,

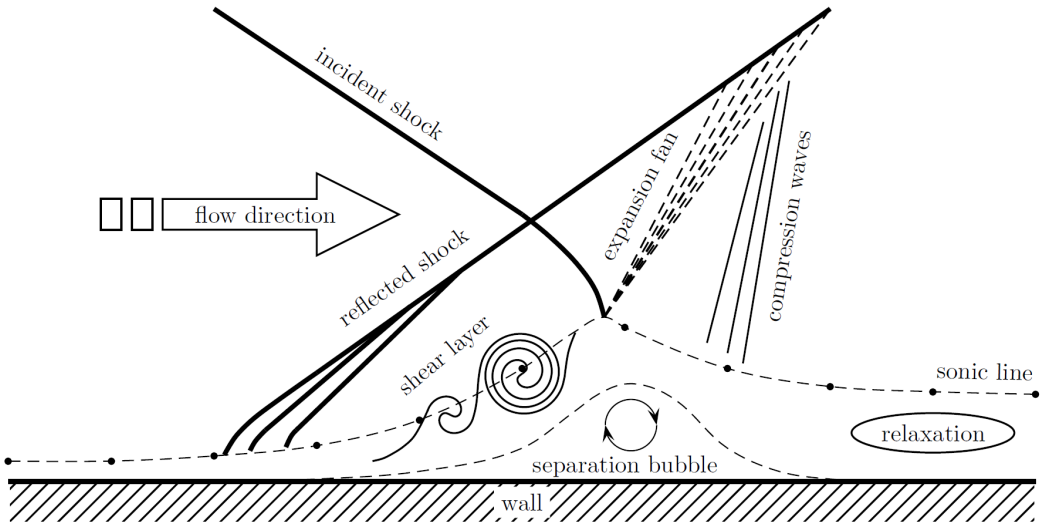

Fig. 1.1 Sketch of the oblique shock / boundary-layer interaction [104].

computational fluid dynamics (CFD) provides an inexpensive alternative by solving the governing equations, i.e. Navier-Stokes (NS) or Euler equations. Over the past decades, along with the inspiring progress of applied mathematics in solving convection dominated hyperbolic conservation laws, CFD has become an indispensable tool and is widely used in the engineering community [50][82][113][108]. There are three established methods to approximate the numerical solutions of NS equations, e.g. the direct numerical simulation (DNS), the large-eddy simulation (LES) [96] and Reynolds-averaged Navier-Stokes (RANS) [87] simulation. While the DNS method, which resolves all relevant scales, is not achievable in practice due to the large resolution required, the LES method models the viscous dissipation of small scales instead and can resolve much more dynamics than the RANS method. The LES method however strongly depends on the performance of high-resolution numerical schemes and the large-scale parallel computing [50][82]. Although the built-in dissipation of numerical schemes can stabilize the simulations, the range of well-resolved physical scales can be significantly reduced and the computational costs are increased correspondingly.

1.2.1 High-resolution simulation

In order to resolve the vast range of spatial and temporal length-scales in complex fluid, high-order and high-resolution schemes gain more and more attentions [95]. To achieve the same accuracy, high-order schemes allow for consuming much less computational costs compared with low-order schemes. For compressible flows with shocks and turbulence, it is much more challenging due to the contradictory requests that low numerical dissipation is expected to resolve the small-scale structures while adequate numerical dissipation is necessary for capturing shocks [82]. Traditional low-order schemes are able to capture the discontinuities monotonically, e.g. the first-order Godunov scheme [26]; however, the smooth parts of the solutions, e.g. vortical structures and acoustic waves, are also smeared by the large numerical dissipation. Many high-order numerical methods have been developed based on structured meshes, e.g. [31][60][61] and unstructured meshes, e.g. [10][45][62]. Among these, the concept to resolve shocks in an essentially non-oscillatory [31] manner gains widespread popularity and leads to the development of WENO schemes, which are widely used in applications nowadays. Recently, there have been many efforts in developing implicit large-eddy simulation (ILES) method, for which the truncation errors of high-order shock-capturing schemes are optimized to function as a physically-consistent subgrid-scale model to resolve turbulence [36][11][58]. Fig. 1.2 shows the high resolution simulation of Rayleigh-Taylor instability based on compact schemes and rich small-scale structures are resolved.

1.2.2 Large-scale parallel computing

Despite the high-resolution simulations and with the rapid development of computational capabilities in recent years, large-scale parallel computing in combination with adaptive mesh refinement (AMR) technique is widely used for flow simulations involving complex geometries or a wide spectrum of length-scales [59]. Concerning the AMR technique, dominant mesh elements are distributed close to flow fields of interest or discontinuous regions which strongly demand high resolution [29][7][48]. This type of nonuniform mesh topology, e.g. adaptive unstructured or block-structured meshes, corresponds to a compromise between computational accuracy and efficiency. As shown in Fig. 1.3, most of the computational domain is resolved with relatively coarse mesh whereas the

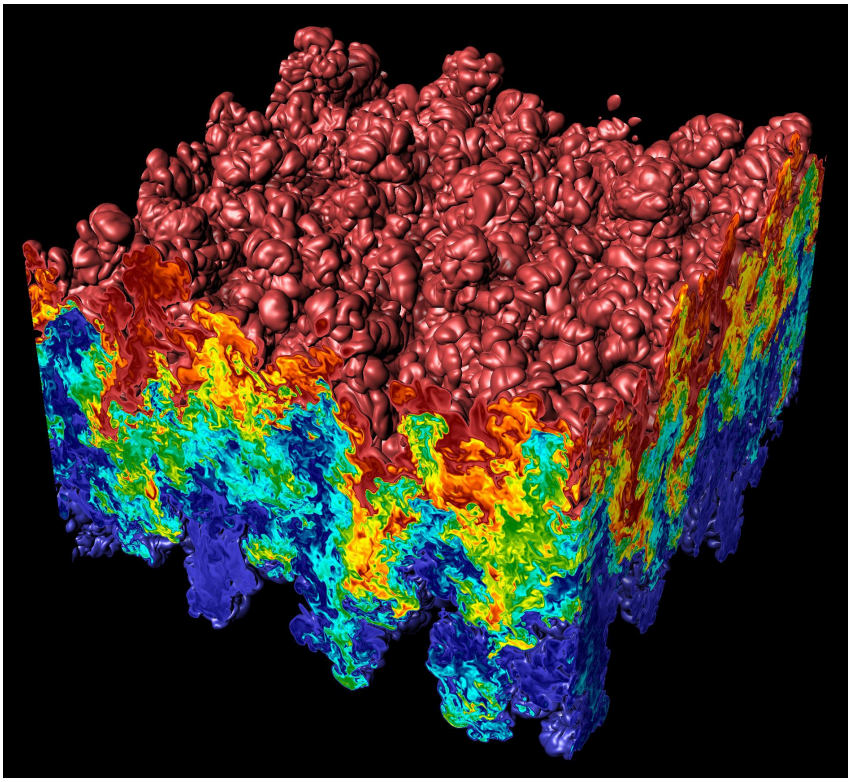

Fig. 1.2 High resolution simulation of Rayleigh-Taylor instability [12].

vortex flows are captured with refined resolution. Consequently, load-balancing problems arise along with the utilization of the aforementioned mesh topology and the large number of processors in high performance computing (HPC). Extensive practical applications reveal that the partitioning strategy for optimizing load-balance and inter-processor communication becomes the critical bottleneck, which bounds the performance of HPC [93]. Several open-source codes, e.g. Metis [51], ParMetis [54], PT-Scotch [81] and etc., have been developed to address above problems. Fig. 1.4 shows a mapping of adaptive mesh using a Space-Filling Curve (SFC) method [48]. A partitioning is obtained by cutting the one-dimensional sequence into desired pieces. Although it is highly efficient and simple, partitioning with the SFC method typically lacks locality and incremental property, which are particularly important for dynamic load-balancing problems.

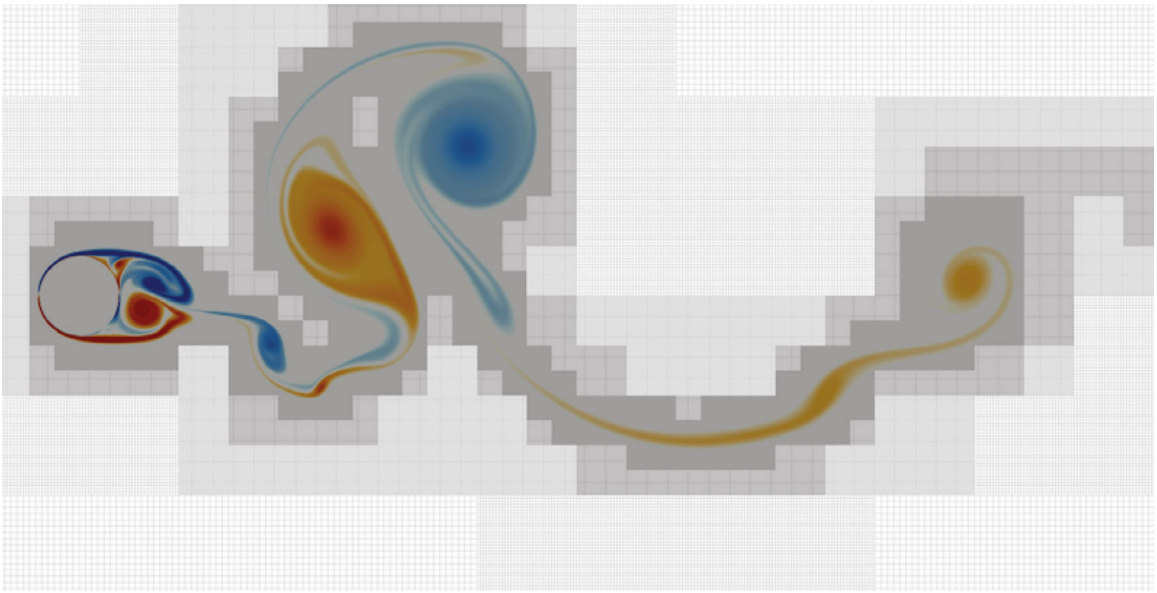

Fig. 1.3 Multi-resolution simulation of the flow past an impulsively-started cylinder [89].

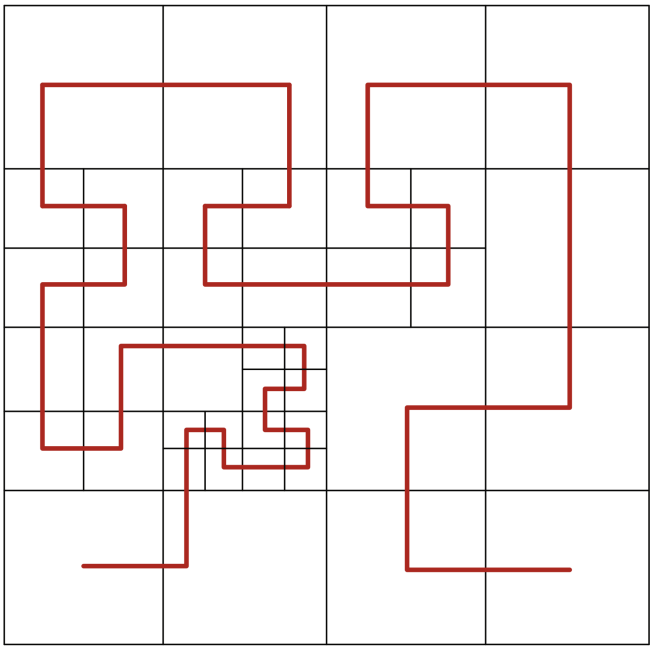

Fig. 1.4 Mapping of an adaptive mesh using a Space-Filling Curve method [48].

1.3 Outline

In this work, several novel numerical methods are developed to address the issues relevant to high-resolution simulation and large-scale parallel computing for compressible fluid dynamics.

- In Paper I, a family of high-order targeted ENO schemes is proposed for hyperbolic conservation laws. A novel weighting strategy is proposed such that low numerical dissipation is maintained for low and intermediate wavenumbers while the monotonicity is preserved near discontinuities. A set of benchmarks involving both discontinuities and wide range of length-scales is simulated. Numerical experiments demonstrate that the proposed TENO schemes are superior over classical WENO schemes in terms of wave-resolution capability and numerical robustness.

- In Paper II, a novel smoothed-particle hydrodynamics based partitioning method is proposed for large-scale parallel computing in continuum mechanics. Based on the observation that the optimal partitioning outcome is highly analogous to the relaxation state of a multiphase particle system, a set of model equations is developed and solved by the SPH method. Several physical mechanisms, e.g. the surface tension effect, are developed such that all objective functions are optimized implicitly during the relaxation of particle system. Extensive experiments suggest that the proposed partitioning method features several remarkable properties, rendering it promising for large-scale high-performance computing.

- In Paper III, a physics-motivated Centroidal Voronoi Particle method is proposed for domain decomposition. By combining the concept of Centroidal Voronoi Tessellation and Voronoi Particle dynamics, the CVP method can satisfy both objectives, i.e. the arbitrary target mass distribution and compactness, regardless of the smoothness of the background density field, the number of generators and the complexity of boundaries. The application of CVP to load-balancing problems reveals that the CVP method can generate high-quality partitioning.

The thesis is organized as follows. In **Chapter 2**, the classical numerical methods for hyperbolic conservation laws and domain decomposition, e.g. the WENO scheme, the SPH method and the CVT method, are reviewed. In **Chapter 3**, state-of-the-arts of the relevant numerical methods are reviewed

and achievements of the proposed methods are summarized. Conclusion and outlook are given in **Chapter 4**.

Chapter 2

Numerical methods

In this chapter, the concepts of numerical methods relevant to hyperbolic conservation laws, smoothed particle hydrodynamics and domain decomposition are reviewed.

2.1 Hyperbolic Conservation Laws

In this section, the classical finite-difference WENO scheme and Runge-Kutta method for solving hyperbolic conservation laws, i.e. Navier-Stokes equations, are introduced.

2.1.1 Navier-Stokes equations

For compressible fluid dynamics, the governing equations, i.e. Navier-Stokes equations, can be written in the conservative forms as

$$\frac{\partial \rho}{\partial t} + \nabla \cdot (\rho \mathbf{u}) = 0, \tag{2.1}$$

$$\frac{\partial (\rho \mathbf{u})}{\partial t} + \nabla \cdot (\rho \mathbf{u}\mathbf{u} + p\delta) = \nabla \cdot \tau, \tag{2.2}$$

$$\frac{\partial E}{\partial t} + \nabla \cdot (\mathbf{u}(E+p)) = \nabla \cdot (\mathbf{u} \cdot \tau - \dot{q}), \tag{2.3}$$

where ρ and $\mathbf{u}$ denote the density and the velocity vector, $E = \rho e + \frac{\rho \mathbf{u} \cdot \mathbf{u}}{2}$ is the total energy. To close the system of equations, the ideal-gas equations-of-state (EOS) $p = (\gamma - 1)\rho e$ with γ as the ratio of specific heats is employed. The heat flux is computed by $\dot{q} = -k\nabla T$ following Fourier's law.

According to Stokes' hypothesis for a Newtonian fluid, the viscous stress tensor τ is defined as

$$\tau = 2\mu\mathbf{S} - \frac{2}{3}\mu(\nabla\cdot\mathbf{u})\delta, \tag{2.4}$$

where μ denotes the dynamic viscosity and the strain rate sensor is defined as $\mathbf{S} = \frac{1}{2}(\nabla\mathbf{u} + (\nabla\mathbf{u})^T)$. Without considering the heat transfer and viscous effect, the NS equations reduce to the Euler equations, which will be our major concern in this work.

The Euler equations can be further written as a system of hyperbolic conservation laws

$$\frac{\partial\mathbf{Q}}{\partial t} + \nabla\cdot\mathbf{F}(\mathbf{Q}) = \mathbf{0}, \tag{2.5}$$

where $\mathbf{Q} = [\rho, \rho\mathbf{u}, E]^T$ denotes the conservative variables and $\mathbf{F} = [\rho\mathbf{u}, \rho\mathbf{u}\mathbf{u} + p\delta, \mathbf{u}(E+p)]^T$ denotes the flux tensor. The key point for modern numerical methods is to reconstruct the flux $\mathbf{F}$ at the cell interface $i+1/2$ such that high-order accuracy is restored in smooth regions while monotonicity is preserved near discontinuities.

Following the conservative finite-difference framework, the discretizations of the convective terms in Eq. (2.5) are typically applied in the characteristic space to avoid numerical oscillations induced by the interaction between different characteristic waves [49]. Firstly, the conservative variables and fluxes are projected into the characteristic space following

$$\mathbf{q}_m = \mathbf{R}^{-1}_{i+1/2}\mathbf{Q}_m,\ \mathbf{f}_m = \mathbf{R}^{-1}_{i+1/2}\mathbf{F}_m,\ m = \overbrace{\dots, i-1, i, \dots}^{K}, \tag{2.6}$$

where the left eigenvector matrix $\mathbf{R}^{-1}_{i+1/2}$ can be computed by the Roe average [88] at the cell interface.

Secondly, the projected fluxes are split by flux splitting methods as

$$f^{(l)\pm} = \frac{1}{2}(f^{(l)} \pm \lambda^{(l)}_{\max} q^{(l)}), \tag{2.7}$$

where $f^{(l)}$ and $q^{(l)}$ denote the l^{th} element of the vector $\mathbf{f}$ and $\mathbf{q}$, the sign "$+$" and "$-$" denote the positive and negative flux parts, such that $\frac{df^{(l)+}}{dq} \geq 0$ and $\frac{df^{(l)-}}{dq} \leq 0$. Considering the Rusanov scheme

[90], the eigenvalue of $\lambda_{\max}^{(l)}$ is defined over the entire computational flowfield by

$$\lambda_{\max}^{(l)} = \max \left| \lambda_m^{(l)} \right|, \; m = 1, \ldots, n, \tag{2.8}$$

where $\lambda_i^{(l)}$ denotes the l^{th} eigenvalue of $\partial \mathbf{F} / \partial \mathbf{Q}$ at cell i. Considering the local Lax-Friedrichs (LLF) scheme, the $\lambda_{\max}^{(l)}$ is defined as

$$\lambda_{\max}^{(l)} = \max |\lambda_m|, \;\; m = \overbrace{\ldots, i-1, i, \ldots}^{K} \tag{2.9}$$

where $|\lambda_m| = |u| + c$ and c denotes the sound speed. These two flux-splitting schemes will be mostly employed for the numerical experiments in this work.

Subsequently, the procedure designed for scalar model equation is applied to reconstruct the numerical flux at the cell interface $i + 1/2$ for each characteristic field,

$$\hat{f}_{i+1/2} = \hat{f}^{+}_{i+1/2} + \hat{f}^{-}_{i+1/2}. \tag{2.10}$$

At last, the invicid flux in the physical space can be obtained by a reverse projection

$$\hat{\mathbf{F}}_{i+1/2} = \mathbf{R}_{i+1/2} \hat{\mathbf{f}}_{i+1/2}. \tag{2.11}$$

2.1.2 Weighted Essentially Non-oscillatory scheme

In this section, the one-dimensional hyperbolic conservation law

$$\frac{\partial q}{\partial t} + \frac{\partial}{\partial x} f(q) = 0 \tag{2.12}$$

is considered as a prototype. The characteristic velocity is assumed to be positive $\frac{\partial f(q)}{\partial q} > 0$ without loss of generality.

After the discretization of Eq. (2.12) on a uniform mesh, e.g. x_i, a system of ordinary differential equations

$$\frac{dq_i}{dt} = -\frac{\partial f}{\partial x} |_{x=x_i}, \qquad i = 0, \cdots, n \tag{2.13}$$

is formed. Eq. (2.13) can be further discretized by a conservative finite difference formula in a semi-discrete form as

$$\frac{dq_i}{dt} = -\frac{1}{\Delta x}(h_{i+1/2} - h_{i-1/2}), \tag{2.14}$$

where the primitive function $h(x)$ is implicitly defined by

$$f(x) = \frac{1}{\Delta x}\int_{x-\Delta x/2}^{x+\Delta x/2} h(\xi)d\xi. \tag{2.15}$$

By introducing $\hat{f}_{i\pm1/2}$, reconstructed from the cell average value f_i, Eq. (2.14) is further approximated as

$$\frac{dq_i}{dt} \approx -\frac{1}{\Delta x}(\widehat{f}_{i+1/2} - \widehat{f}_{i-1/2}), \tag{2.16}$$

where $\hat{f}_{i\pm1/2}$ is assembled by a convex combination of r candidate stencil fluxes

$$\widehat{f}_{i+1/2} = \sum_{k=0}^{r-1} w_k \widehat{f}_{k,i+1/2}. \tag{2.17}$$

To obtain $(2r-1)$th-order approximation for $\widehat{f}_{i+1/2}$, $(r-1)$-degree polynomial distribution is supposed on each candidate stencil as

$$h(x) \approx \hat{f}_k(x) = \sum_{l=0}^{r-1} a_{l,k}x^l. \tag{2.18}$$

After substituting Eq. (2.18) into Eq. (2.15) and evaluating the integral functions at the stencil nodes, the coefficients a_l are determined by solving the resulting system of linear algebraic equations. Formulas for the negative splitting flux can be obtained by symmetry at cell interface $x_{i+1/2}$. Note that the above reconstruction procedure can be applied to multi-dimensional problems in a dimension-by-dimension manner without loss of formal accuracy [49].

For the five-point WENO schemes, expressions for the three candidate fluxes are

$$\begin{aligned}
\hat{f}_{0,i+1/2} &= \tfrac{1}{6}(2f_{i-2} - 7f_{i-1} + 11f_i),\\
\hat{f}_{1,i+1/2} &= \tfrac{1}{6}(-f_{i-1} + 5f_i + 2f_{i+1}),\\
\hat{f}_{2,i+1/2} &= \tfrac{1}{6}(2f_i + 5f_{i+1} - f_{i+2}).
\end{aligned} \tag{2.19}$$

The sketch of three candidate stencils is shown in Fig. 2.1.

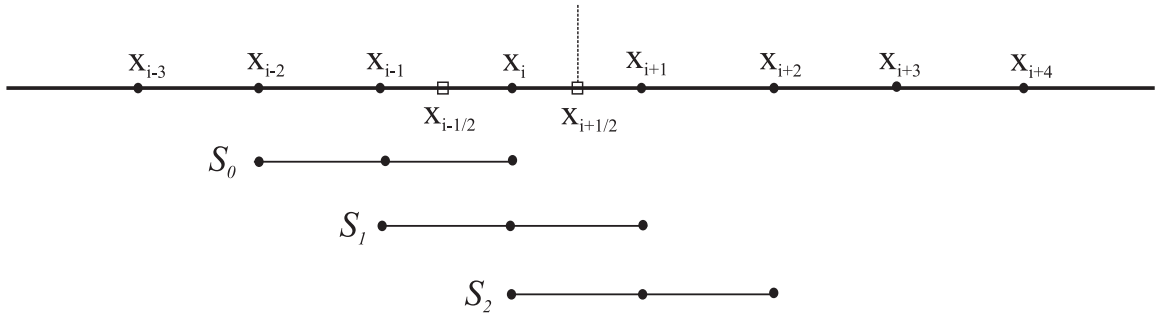

Fig. 2.1 Sketch of the candidate stencils for the five-point reconstruction WENO scheme.

The linear definition of the weight w_k typically leads to Gibbs oscillations [35] in the presence of discontinuities. In order to enforce the ENO property near discontinuities and restore the high-order accuracy in smooth region, the weights are defined to be nonlinearly adaptive and normalized by α_k as

$$w_k = \frac{\alpha_k}{\sum_{k=0}^{r-1} \alpha_k}, \ \alpha_k = \frac{d_k}{(\beta_k + \varepsilon)^2}, \tag{2.20}$$

where d_k denotes the optimal weight and is optimized to generate $(2r-1)$-th order upwind scheme with $(2r-1)$-point full stencil. For the five-point WENO schemes, the overall fifth-order accuracy is achieved with $d_0 = 0.1, d_1 = 0.6, d_2 = 0.3$. ε is a small value to prevent denominator to be 0, whereas further research demonstrates that it acts as a cut-off of smoothness measurement [8]. The indicator β_k, which measures the smoothness of candidate stencil, is defined as

$$\beta_k = \sum_{j=1}^{r-1} \Delta x^{2j-1} \int_{x_{i-1/2}}^{x_{i+1/2}} \left(\frac{d^j}{dx^j} \widehat{f}_k(x)\right)^2 dx \tag{2.21}$$

following Jiang and Shu [49].

In smooth regions, the discrepancies between the smoothness indicators are $\mathscr{O}(\Delta x^4)$. The convex combination of r stencils produces $(2r-1)$-th order approximate numerical flux evaluated at the cell face. If one certain stencil contains discontinuity, β_k is $\mathscr{O}(1)$ while others $\mathscr{O}(\Delta x^2)$. The weight of the corresponding stencil deteriorates to be nearly zero and the scheme degenerates to r-th order reconstruction. For the five-point WENO schemes, explicit expressions for the smoothness indicators

are

$$\begin{aligned}
\beta_0 &= \tfrac{1}{4}(f_{i-2} - 4f_{i-1} + 3f_i)^2 + \tfrac{13}{12}(f_{i-2} - 2f_{i-1} + f_i)^2, \\
\beta_1 &= \tfrac{1}{4}(f_{i-1} - f_{i+1})^2 + \tfrac{13}{12}(f_{i-1} - 2f_i + f_{i+1})^2, \\
\beta_2 &= \tfrac{1}{4}(3f_i - 4f_{i+1} + f_{i+2})^2 + \tfrac{13}{12}(f_i - 2f_{i+1} + f_{i+2})^2.
\end{aligned} \tag{2.22}$$

The thorough study of Henrick et al. [34] suggests that to guarantee the overall scheme restoring the formal fifth order, a strict condition of $w_k - d_k = \mathscr{O}(\Delta x^3)$ should be satisfied for the five-point WENO scheme. In order to improve the performance of classical WENO-JS scheme, Borges et al. [5] proposed a new weighting strategy as

$$\alpha_k = d_k(1 + \frac{\tau_K}{\beta_k + \varepsilon}), \tag{2.23}$$

by introducing a high-order undivided difference measured on the full $(2r-1)$ stencil points. For the fifth-order scheme, the global smoothness measurement τ_5 is devised as the absolute difference between β_0 and β_2, i.e. $\tau_5 = |\beta_0 - \beta_2|$, and

$$\frac{\tau_5}{\beta_k + \varepsilon} = \mathscr{O}(\Delta x^3),\ k = 0, 1, 2. \tag{2.24}$$

Consequently, the condition of fifth-order accuracy, i.e. $w_k - d_k = \mathscr{O}(\Delta x^3)$ [5], is fulfilled in cases where there are no critical points.

Further numerical experiments show that the fifth-order WENO schemes are too dissipative for resolving the small-scale structures, a sixth-order WENO scheme, which adapts between central and upwind schemes smoothly by a modified weighting strategy, is proposed in [43]. The basic idea is to introduce the contribution of the downwind stencil as

$$\hat{f}_{3,i+1/2} = \frac{1}{6}(11f_{i+1} - 7f_{i+2} + 2f_{i+3}). \tag{2.25}$$

The sketch of four candidate stencils is shown in Fig. 2.2.

In order to obtain a less dissipative scheme, and following Borges et al. [5], the nonlinear weights are computed by

$$w_k = \frac{\alpha_k}{\sum_{k=0}^{3} \alpha_k},\ \alpha_k = d_k \left(C + \frac{\tau_6}{\beta_k + \varepsilon} \right)^q,\ k = 0, 1, 2, 3, \tag{2.26}$$

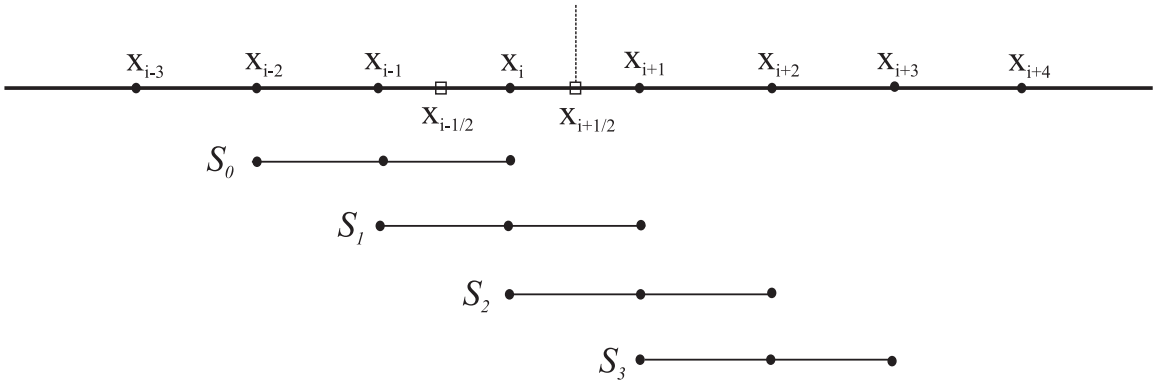

Fig. 2.2 Sketch of the candidate stencils for the six-point reconstruction WENO scheme.

where the constant $q = 1$ and $C = 20$. The large value of C can reduce the nonlinear adaptation in smooth regions and consequently the numerical dissipation is decreased. Here, the optimal weights are $d_0 = \frac{1}{20}, d_1 = \frac{9}{20}, d_2 = \frac{9}{20}, d_3 = \frac{1}{20}$ such that the combined scheme recovers to the standard sixth-order central scheme in smooth regions.

To avoid a pure downwind reconstruction, which is numerically unstable, the smoothness indicator β_3 is derived from the full six-point stencil as

$$\begin{aligned}
\beta_3 = \beta_6 &= \frac{1}{120960}\left[271779 f_{i-2}^2 + f_{i-2}(-2380800 f_{i-1} + 4086352 f_i - 3462252 f_{i+1}\right. \\
&+ 1458762 f_{i+2} - 245620 f_{i+3}) + f_{i-1}(5653317 f_{i-1} - 20427884 f_i \\
&+ 17905032 f_{i+1} - 7727988 f_{i+2} + 1325006 f_{i+3}) \\
&+ f_i(19510972 f_i - 35817664 f_{i+1} + 15929912 f_{i+2} - 2792660 f_{i+3}) \\
&+ f_{i+1}(17195652 f_{i+1} - 15880404 f_{i+2} + 2863984 f_{i+3}) \\
&+ \left. f_{i+2}(3824847 f_{i+2} - 1429976 f_{i+3}) + 139633 f_{i+3}^2\right]. \qquad (2.27)
\end{aligned}$$

The new global reference smoothness indicator τ_6 is defined as

$$\tau_6 = |\beta_6 - \frac{1}{6}(\beta_0 + \beta_2 + 4\beta_1)|. \qquad (2.28)$$

By Taylor expansion analysis,

$$\tau_6 = \mathscr{O}(\Delta x^6),\ \frac{\tau_6}{\beta_k + \varepsilon} = \mathscr{O}(\Delta x^4),\ k = 0,1,2,3, \qquad (2.29)$$

such that the condition, i.e. $w_k - d_k = \mathcal{O}(\Delta x^4)$, to restore the overall sixth-order accuracy in smooth regions, is satisfied.

Later, it has been found that the WENO-CU6 scheme [43] fails to reproduce the Kolmogorov scaling of $E(k) \propto k^{-5/3}$ within the inertial subrange of turbulent flows. With a physics-motivated scale-separation approach, the WENO-CU6-M scheme [42] is proposed for ILES of turbulent flows by revisiting the weighting strategy. The parameters are adapted as $C = 1000$ and $q = 4$.

With further loss of shock-capturing property, several new variants are proposed [92] by systematic adaptations of the weighting parameters such that incompressible turbulence can be well predicted.

2.1.3 Runge-Kutta method

After discretizing the spatial derivatives of hyperbolic conservation laws Eq. (2.5) following a method-of-lines approximation, a set of Ordinary Differential Equations (ODEs) is formed as

$$\frac{d\mathbf{Q}}{dt} = L(\mathbf{Q}). \tag{2.30}$$

To advance the conservative variables in time, a temporal discretization is necessary. While implicit methods allow for large timestep, explicit methods, e.g. the Runge-Kutta (RK) method [94][28], are popular for resolving the transient flows. Moreover, arbitrary high-order schemes are much easier to construct for explicit methods.

However, it is numerically proved that, even when the total variation diminishing (TVD) scheme is employed for spatial discretization, numerical oscillations may occur if the time discretization method lacks the strong stability property [27]. Gottlieb et al. [28] proposed a class of strong stability-preserving (SSP) high-order time discretizations for semi-discrete method-of-lines approximations of partial differential equations (PDEs). An optimal third-order SSP Runge-kutta method [28] is given as

$$\begin{aligned}
\mathbf{Q}^{(1)} &= \mathbf{Q}^n + \Delta t L(\mathbf{Q}^n) \\
\mathbf{Q}^{(2)} &= \tfrac{3}{4}\mathbf{Q}^n + \tfrac{1}{4}\mathbf{Q}^{(1)} + \tfrac{1}{4}\Delta t L(\mathbf{Q}^{(1)}) \quad , \\
\mathbf{Q}^{n+1} &= \tfrac{1}{3}\mathbf{Q}^n + \tfrac{2}{3}\mathbf{Q}^{(2)} + \tfrac{2}{3}\Delta t L(\mathbf{Q}^{(2)})
\end{aligned} \tag{2.31}$$

for a sufficiently small timestep constrained by a Courant-Friedrich-Lewy (CFL) condition [13].

2.2 Smoothed Particle Hydrodynamics

In this section, the concept of Smoothed Particle Hydrodynamics and the relevant numerical discretization schemes are briefly introduced.

2.2.1 Governing equations

For isothermal Newtonian flows, the Lagrangian form of continuity equation and momentum equations is

$$\frac{d\rho}{dt} = -\rho \nabla \cdot \mathbf{v}, \tag{2.32}$$

$$\frac{d\mathbf{v}}{dt} = -\mathbf{F_p} + \mathbf{F_v}, \tag{2.33}$$

where ρ is the fluid density, $\mathbf{v}$ is the velocity vector, and $\mathbf{F_p}$, $\mathbf{F_v}$ stand for the accelerations due to repulsive pressure force and viscous shear force, respectively. This set of equations can be solved by the particle based SPH method, which first has been proposed by Lucy [65] and Gingold and Monaghan [25]. The core idea is to compute a function field and the corresponding spatial derivatives with a smoothing kernel on arbitrarily distributed particles.

Due to the meshless nature and the exact convection property, the SPH method first has been applied to simulate astrophysical problems [65][25]. Later, it has been extended to a variety of applications, e.g. free-surface flows, compressible gas dynamics and weakly compressible flow simulations [72]. Compared with the Eulerian methods, the advantages include, e.g. the implicit tracking of complex interface evolutions, straightforward coupling of multi-physics problems, and exact conservation of mass and momentum.

2.2.2 Equation of state and kernel function

In order to close the system of governing equations, the pressure must be defined by an equation of state. For weakly compressible SPH methods, the pressure can be defined as a function of density by

$$p = p_0 \left[\left(\frac{\rho}{\rho_0} \right)^{\gamma} - 1 \right] + b, \tag{2.34}$$

where p_0, ρ_0 and b denote the reference pressure, the reference density and the background pressure. In order to enforce a quasi-incompressible condition during the entire simulation, the reference pressure is

$$p_0 = \frac{\rho_0 c^2}{\gamma}, \tag{2.35}$$

where $\gamma = 7$ and the artificial speed of sound c is chosen to be a least one order of magnitude larger than the maximum flow velocity [73].

The kernel function is one key point in SPH methodology and has been investigated in the literature [102][100]. In the limit of a vanishing smoothing length h, the radially symmetric smoothing kernel function should reduce to a delta function as

$$\lim_{h\to 0} W(\mathbf{r}-\mathbf{r}',h) = \delta(\mathbf{r}-\mathbf{r}'), \tag{2.36}$$

which gives an exact integral interpolation. And the normalization condition

$$\int W(\mathbf{r}-\mathbf{r}',h)d\mathbf{r}' = 1, \tag{2.37}$$

where $d\mathbf{r}'$ denotes the volume differential, is necessary for zero-order consistency.

The ideal option of a Gaussian kernel is generally abandoned because of the lack of compact support. Instead, well known B-spline functions with different order, e.g. cubic spline, quartic spline and etc., are widely accepted [85]. This type of kernel functions have a Gaussian-like kernel profile and compact support.

However, these kernel functions perform poorly in gradient evaluation. The first-order gradient of these kernels normally features a bell shape, generating a maximum negative value at $\frac{r}{h} \approx \frac{2}{3}$. If the ratio of smoothing length to average particle spacing is large, many particles will be distributed within this hump. These particles may exhibit the paring-instability problem [85][100] and gradually merge in pairs because the mutual repulsive force calculated from the kernel is too small. Recent research reveals that the Wendland function [14] can avoid the paring instability for all possible number of neighbors, e.g.

$$W(r_{ij},h) = \alpha(1-s)^8(1+8s+25s^2+32s^3), \tag{2.38}$$

in which $\mathbf{r}_{ij} = \mathbf{r}_i - \mathbf{r}_j, r_{ij} = \left|\mathbf{r}_{ij}\right|$, $s = \frac{r_{ij}}{h}$, and the normalization constant α is

$$\alpha = \begin{cases} \frac{78}{7\pi h^2}, & 2D, \\ \\ \frac{1365}{64\pi h^3}, & 3D. \end{cases} \tag{2.39}$$

Thomas and Couchman [102] propose to remove the hump region from cubic spline by forcing the kernel gradient to be constant within $\frac{r}{h} \leq \frac{2}{3}$. The modified kernel however leads to large errors in the density evaluation since it is not well normalized under this circumstance. Yang et al. [110] propose to use a hyperbolic-shaped kernel function with non-negative second-order derivative within the whole support domain as

$$W(r_{ij},h) = \alpha \begin{cases} s^3 - 6s + 6, & 0 \leq s < 1, \\ (2-s)^3, & 1 \leq s < 2, \\ 0, & 2 \leq s, \end{cases} \tag{2.40}$$

where

$$\alpha = \begin{cases} \frac{1}{3\pi h^2}, & 2D, \\ \\ \frac{15}{62\pi h^3}, & 3D. \end{cases} \tag{2.41}$$

This kernel successfully avoids the tensile instability and the paring instability, while satisfying the conventional requirements of a kernel function. The performance has been numerically studied for multi-phase SPH simulations [110].

2.2.3 Discretization scheme

Generally, the particle density can be calculated from the summation over all neighboring particles algebraically other than solving the continuity equation Eq. (2.32). Following the definition of

$$d_i = \sum_j W_{ij}, \tag{2.42}$$

which is approximately the inverse of specific particle volume [40][41], the particle average density is $m_i d_i$ and can be evaluated as

$$\rho_i = m_i \sum_j W(r_{ij}, h). \tag{2.43}$$

This formula is preferred for multi-phase simulation with density or mass jump because the neighboring particles only contribute the volume.

For specific particle i, the discretization of acceleration due to the conservative repulsive pressure force can be given as

$$\mathbf{F_p} = \sum_j m_j \left(\frac{p_i}{\rho_i^2} + \frac{p_j}{\rho_j^2} \right) \frac{\partial W(r_{ij}, h)}{\partial r_{ij}} \mathbf{e}_{ij}, \tag{2.44}$$

where $\mathbf{e}_{ij} = \frac{\mathbf{r}_{ij}}{r_{ij}}$ is the normalized vector from particle i to j. The arithmetic average of smoothing-lengths for particle pairs is used to ensure force anti-symmetry as

$$h = \frac{1}{2}(h_i + h_j). \tag{2.45}$$

In terms of the viscous effect, the acceleration of particle i induced by shear forces can be discretized as

$$\mathbf{F_v} = \sum_j \frac{2\eta_i \eta_j}{\eta_i + \eta_j} m_j \left(\frac{1}{\rho_i^2} + \frac{1}{\rho_j^2} \right) \frac{\partial W(r_{ij}, h)}{\partial r_{ij}} \frac{(\mathbf{v}_{ij} + \mathbf{e}_{ij}.\mathbf{v}_{ij}\mathbf{e}_{ij})}{r_{ij}}, \tag{2.46}$$

where the dynamic viscosity $\eta = \rho \nu$, and $\mathbf{v}_{ij} = \mathbf{v}_i - \mathbf{v}_j$ is the relative velocity vector from particle i to particle j [40]. For incompressible flows, Eq. (2.46) can be simplified as

$$\mathbf{F_v} = \sum_j \frac{2\eta_i \eta_j}{\eta_i + \eta_j} m_j \left(\frac{1}{\rho_i^2} + \frac{1}{\rho_j^2} \right) \frac{\partial W(r_{ij}, h)}{\partial r_{ij}} \frac{\mathbf{v}_{ij}}{r_{ij}}. \tag{2.47}$$

Note that the angular momentum conservation is not satisfied exactly by Eq. (2.46) and Eq. (2.47). Further discussions about the angular momentum conservation can be found in [40][39].

2.2.4 Time integration method

The governing equation system can be integrated in time with a velocity-Verlet scheme [106]. For particle i,

$$\begin{aligned}
\mathbf{v}_i^{n+\frac{1}{2}} &= \mathbf{v}_i^n + \tfrac{\Delta t}{2}\left(\tfrac{d\mathbf{v}_i}{dt}\right)^n, \\
\mathbf{r}_i^{n+\frac{1}{2}} &= \mathbf{r}_i^n + \tfrac{\Delta t}{2}\mathbf{v}_i^{n+\frac{1}{2}}, \\
\rho^{n+1} &= \rho^n + \Delta t \tfrac{d\rho^{n+\frac{1}{2}}}{dt}, \\
\mathbf{r}_i^{n+1} &= \mathbf{r}_i^{n+\frac{1}{2}} + \tfrac{\Delta t}{2}\mathbf{v}_i^{n+\frac{1}{2}}, \\
\mathbf{v}_i^{n+1} &= \mathbf{v}_i^{n+\frac{1}{2}} + \tfrac{\Delta t}{2}\left(\tfrac{d\mathbf{v}_i}{dt}\right)^{n+1}.
\end{aligned} \tag{2.48}$$

For stability, the timestep is constrained by a CFL condition

$$\Delta t \leq 0.25 \frac{h}{c_{\max} + |\mathbf{v}_{\max}|}, \tag{2.49}$$

and the viscous condition

$$\Delta t \leq 0.125 \frac{h^2}{\nu}. \tag{2.50}$$

2.3 Domain Decomposition method

In this section, the popular CVT [21] based domain decomposition method and the Lloyd's algorithm [64] for CVT generation are reviewed.

2.3.1 Voronoi Tessellation method

Given a set of points (generators) $\{\mathbf{x}_i\}_{i=0}^{k-1}$, in an open, simply-connected and convex domain $\Omega \subset \mathbb{R}^d$ without curved boundaries, the Voronoi region Ω_i corresponding to the generator x_i is defined as [17][78]

$$\Omega_i = \left\{\mathbf{x} \in \Omega \middle| \, \|\mathbf{x} - \mathbf{x}_i\| \leqslant \left\|\mathbf{x} - \mathbf{x}_j\right\|, \forall j \neq i\right\}, \tag{2.51}$$

where $\|\cdot\|$ denotes the Euclidean distance in $\mathbb{R}^d$. For $i \neq j$, $\Omega_i \cap \Omega_j = \emptyset$ and $\cup_{i=0}^{k-1}\Omega_i = \Omega$. Such a set of polyhedra $\{\Omega_i\}_{i=0}^{k-1}$ is called the Voronoi tessellation (Voronoi diagram) of Ω.

2.3.2 Centroidal Voronoi Tessellation method

Considering that we assign a density function $\rho(\mathbf{x}) > 0$ to Ω, the mass centroid of a Voronoi element Ω_i is defined by

$$\mathbf{z}_i = \frac{\int_{\Omega_i} \rho(\mathbf{x}) \mathbf{x} d\sigma}{\int_{\Omega_i} \rho(\mathbf{x}) d\sigma}, \tag{2.52}$$

where $d\sigma$ denotes the volume differential.

A Voronoi tessellation $\{\Omega_i\}_{i=0}^{k-1}$, for which the generators $\{\mathbf{x}_i\}_{i=0}^{k-1}$ coincide exactly with the mass centroids, i.e.

$$\mathbf{x}_i = \mathbf{z}_i, \tag{2.53}$$

is called Centroidal Voronoi Tessellation.

Based on Gersho's conjecture [21], when the generator number tends to infinity and the density function is smooth enough, the following relation applies to any two Voronoi cells i and j,

$$\begin{aligned} \rho_i h_i^{d+2} &\approx \rho_j h_j^{d+2}, \\ \rho_i |\Omega_i|^{2/d+1} &\approx \rho_j \left|\Omega_j\right|^{2/d+1}, \end{aligned} \tag{2.54}$$

where h, d and $|\Omega|$ denote the local length-scale of a Voronoi cell, spatial dimension and Voronoi cell volume. In the limit of large generator number, a uniform mass distribution is achieved for $\rho = \rho_t^2$ in two dimensions, i.e.

$$\rho_{t,i} |\Omega_i| \approx \rho_{t,j} \left|\Omega_j\right|, \; m_i \approx m_j, \tag{2.55}$$

where ρ_t denotes the target density function and $m_i = \rho_{t,i} |\Omega_i|$ denotes the mass.

Based on this conjecture, the CVT domain decomposition method is widely used for unstructured mesh generation [21]. However, the application of this conjecture may be limited where the two conditions are not valid, e.g. the density field may not be smooth and the generator number may be rather limited for load-balancing problems in parallel scientific computing.

2.3.3 Lloyd's algorithm

From the variational point of view [17], an energy functional can be defined as

$$F(\mathbf{x}) = \sum_{i=0}^{k-1} F_i(\mathbf{x}) = \sum_{i=0}^{k-1} \int_{\Omega_i} \rho(\mathbf{x}) \left\|\mathbf{x} - \mathbf{x}_i\right\|^2 d\sigma, \tag{2.56}$$

where $F_i(\mathbf{x})$ describes the compactness or inertia momentum [63] of Voronoi element Ω_i. The gradient of $F(\mathbf{x})$ [46][17] is

$$\frac{\partial F}{\partial \mathbf{x}_i} = 2m_i(\mathbf{x}_i - \mathbf{z}_i), \tag{2.57}$$

with

$$m_i = \int_{\mathbf{x}\in\Omega_i} \rho(\mathbf{x}) d\sigma. \tag{2.58}$$

For continuous density functions, numerical integration over polyhedral domains is employed [24][75][97].

For CVT, we have, for all i,

$$\mathbf{x}_i = \mathbf{z}_i = \frac{\int_{\Omega_i} \rho(\mathbf{x})\mathbf{x} d\sigma}{\int_{\Omega_i} \rho(\mathbf{x}) d\sigma}, \tag{2.59}$$

thus $\frac{\partial F}{\partial \mathbf{x}_i}$ is zero and the CVT configuration is a critical point of the energy functional. The energy functional Eq. (2.56) can be minimized by a CVT. Not every CVT configuration satisfying $\frac{\partial F}{\partial \mathbf{x}_i} = 0$ minimizes the energy functional due to the saddle point problem [17][19].

Since each Voronoi element depends on all generators $\{\mathbf{x}_i\}_{i=0}^{k-1}$, Eq. (2.59) constitutes a system of nonlinear equations. Through iteratively moving the generators to the mass centroids of Voronoi cells, a CVT configuration can be computed by Lloyd's method [64], as shown in Algorithm 1.

Algorithm 1 Lloyd's method

1: Given an initial set of points $\{\mathbf{x}_i\}_{i=0}^{k-1}$ in the computational domain Ω.

2: Construct Voronoi tessellation $\{\Omega_i\}_{i=0}^{k-1}$ corresponding to the generators $\{\mathbf{x}_i\}_{i=0}^{k-1}$.

3: Compute the mass centroids $\{\mathbf{z}_i\}_{i=0}^{k-1}$ of Voronoi elements; move each generator to the corresponding mass centroid, i.e. $\mathbf{x}_i = \mathbf{z}_i$.

4: Check whether the new generators satisfy a convergence criterion, e.g. the maximum generator displacement is less than a threshold value; if true, terminate; otherwise, return to step 2.

Chapter 3

Achievements

In this chapter, the state-of-the-art of relevant numerical methods and the major achievements of this thesis are briefly reviewed.

3.1 A family of high-order targeted ENO schemes for compressible-fluid simulations

For compressible fluid dynamics governed by the hyperbolic conservation laws, a high-resolution stable numerical scheme, which can capture discontinuities sharply while restoring high-order accuracy in smooth regions, is essential [82]. This section briefly reviews the established numerical methods and summarizes the proposed TENO schemes.

3.1.1 State of the art

Since the development of ENO [31] scheme, it has achieved celebrated success due to its superior performance over classical artificial viscosity schemes [107][47][84] and TVD schemes [30][57]. Rather than utilizing a fixed stencil, ENO schemes capture discontinuities by selecting the smoothest stencil from a set of candidate stencils. Later, Liu et al. [61] proposed the WENO scheme, which constructs the high-order approximation by a weighted combination of low-order candidate polynomials instead of selecting the smoothest stencil. Jiang and Shu [49] improved the WENO scheme by developing

a new smoothness indicator such that the formal fifth-order accuracy can be restored in the smooth region.

Further analyses revealed that the smoothness indicator by Jiang and Shu [49] may fail to guarantee the formal accuracy order near critical regions [34], where the first-order or second-order derivative vanishes. Henrick et al. [34] proposed the WENO-M scheme, which improves this problem by remapping the weights calculated from WENO-JS to satisfy the sufficient criteria of fifth-order accuracy. Borges et al. [5] proposed the WENO-Z scheme by introducing a global high-order undivided difference into the smoothness indicators.

However, applications of the aforementioned classical upwind WENO schemes for the turbulent flow simulations involving wide range of spatial and temporal scales are unsatisfactory due to the excessive built-in numerical dissipation [112][68]. Improvements involve different strategies, e.g. freezing the nonlinear adaptation [38] when the ratio between the maximum and minimum calculated smoothness indicator is less than a problem-dependent threshold and optimize the counterpart linear scheme with less dissipation and dispersion errors [109][98]. Hu and Adams [43] proposed an adaptive central-upwind sixth-order WENO-CU6 scheme by introducing the contribution of a downwind stencil, and later it has been developed into an ILES model through incorporating a physically-motivated scale-separation formula [42]. By optimizing the optimal stencil weights minimizing the weighted integral error in the wavenumber range of interest, the third-order WENO scheme with low numerical dissipation and dispersion errors is proposed in [109][69].

In order to enhance the numerical robustness of very-high-order WENO schemes, Suresh and Huynh [99] proposed to bound the solution near discontinuities by a monotonicity-preserving method. Other numerical approaches to overcome this problem include, e.g. the order-reduction method [103], which tends to recursively choose the lower-order stencils adaptively, and the positivity-preserving method [111].

3.1.2 Summary of the proposed method

The classical WENO schemes suffer from several shortcomings, i.e. the accuracy order may degenerate, they are unnecessarily dissipative for small-scale resolution, and they lack numerical robustness

for very-high-order versions. In order to address these drawbacks, Paper I proposes a family of high-order targeted ENO schemes for compressible fluid dynamics.

Unlike the classical WENO scheme, the high-order reconstruction is achieved by assembling a set of candidate stencils of incremental width. While only odd order scheme is available for classical WENO schemes, the arbitrarily odd and even order schemes can be constructed consistently within this framework. Moreover, the resulting TENO schemes can degenerate gradually from high-order to low-order reconstruction according to the smoothness of local scales. Since the first three stencils are identical to that of classical WENO-JS scheme, the numerical robustness of WENO-JS can be recovered even when there are multiple discontinuities close to each other.

A strong scale-separation formulation is proposed to isolate the discontinuities from smooth regions. For classical WENO schemes, a large value of C improves the performance in smooth regions but degrades the shock-capturing capability whereas the tendency is reversed in terms of the integer q. While it is difficult for WENO to achieve sufficient scale separation, with TENO schemes, it is accomplished by setting $C = 1$ (a relatively small value) and $q = 6$ (a relatively large value).

An ENO-like stencil selection procedure is proposed to maintain low numerical dissipation in smooth regions while enforcing the ENO property near discontinuities. The idea is that a stencil is either applied with the corresponding optimal weight or abandoned for the final reconstruction when crossed by discontinuities. The choice of C_T is determined upon the compromise between well spectral property and good numerical robustness for discontinuity detecting, through quasi-linear spectral analyses and numerical experiments respectively. By the approximate dispersion relation (ADR) analysis, it is observed that the spectral properties of TENO schemes can be preserved exactly the same as that of counterpart linear scheme for low and intermediate wavenumbers. Practical implementation shows that C_T can be optimized to be case-independent due to the non-dimensional nature and the accompanied strong scale-separation benefits. This key parameter also provides an effective way to control the nonlinear properties of underlying scheme for specific problem, e.g. the incompressible turbulence simulation embedded with shocklets, demanding extremely low dissipation and slight nonlinear behaviour.

By adjusting the combination of two $(K-1)$-th order component stencils, the spectral properties of a K-th order scheme can be optimized to satisfy a certain dissipation-dispersion relation. Consequently,

the high-wavenumber fluctuations can be better resolved while the accuracy is slightly reduced by order one.

My contribution to this work was the development of the method and the corresponding computer code for its implementation. I performed simulations and analyzed the results, and wrote the manuscript for the publication.

3.2 A novel partitioning method for block-structured adaptive meshes

With the utilization of AMR method and the large-scale parallel computing technique, the load-balancing problem becomes the potential bottleneck for further improving the efficiency [7][48][55][93]. In Paper II, a physics-motivated SPH based partitioning method is proposed for block-structured adaptive meshes. This section reviews established partitioning methods and summarizes the proposed method.

3.2.1 State of the art

Classical partitioning methods can be classified as geometry-based and graph-based approaches [4][55]. As the basic target of a partitioning method, approximately equal-sized domain decomposition with minimum neighboring communication volume is important for reducing processor idle time and inter-processor communication time. Moreover, the partitioning subdomains are expected to be physically localized and implicitly incremental since it is beneficial for data management and communication reduction [4].

Geometry-based partitioning approaches based on the physical coordinates of the background mesh typically are highly efficient [93]. Berger and Bokhari [2] proposed the Recursive Coordinate Geometric Bisection (RCB) method, with which the computational domain is recursively divided into equal-sized subdomains by the cutting planes orthogonal to coordinate axis. By first constructing a linear sequence of mesh elements through mapping the high-dimensional mesh into one dimension, the Space-Filling Curve [6][91][66] partitioning method generates the partitioning by simply cutting the sequence into desired pieces. Peano curve [79], Hilbert curve [37] and Morton order curve [74]

are the most popular mapping methods. By sacrificing certain degree of load balance, Nivarti et al. [77] proposed an inexpensive algorithm to improve the spatial locality of SFC partitioning.

Concerning the graph-based partitioning approaches, the load-balance optimization and edge-cut minimization are achieved via the Recursive Spectral Bisection (RSB) [83] or multilevel graph partitioning strategy [52][53][1][101]. RSB generates subgraphs by exploiting the eigenvalues of the Laplacian matrix associated with the target graph. It is highly effective but rather expensive due to the eigenvalue calculation [83]. The classical graph-based approaches suffer from issues related to optimizing the inadequate objective function. The partition objective of minimizing the total communication message is not directly equivalent to minimizing the edge-cuts since the edge-cuts are normally not proportional to the real communication volume [33][32]. In order to improve this problem, the hypergraph-based partitioning method, which encodes the communication volume better with additional complexity, is introduced [9][23]. It is also demonstrated that the boundary shape properties of partitioning subdomain, e.g. the aspect ratio [15], connectedness and the smoothness [80], are also crucial in communication reduction [86]. For dynamic partitioning problems, graph-based diffusive partitioners are generally adopted as they produce partitionings, which are much more implicitly incremental than that from classical multilevel partitioning strategies [44][70][71].

3.2.2 Summary of the proposed method

Although the geometry-based partitioning approaches are highly efficient, the partitioning quality is not guaranteed, i.e. the partitioning subdomains may be disconnected, and the communication volume is typically not optimized. The graph-based approaches can generate partitionings of better quality than that from geometry-based approaches but with significantly more complexity. The partitioning subdomain shapes, the locality and incremental property are also not well optimized in general. To address these drawbacks, Paper II proposes a physics-motivated SPH based partitioning method for block-structured adaptive meshes.

With the observation that the optimal partitioning outcome is highly similar to the relaxation state of a multiphase particle system, a Lagrangian particle based multi-phase problem can be defined accordingly. Then a set of model equations is proposed to characterize the multi-phase problem such that all the objectives are optimized implicitly during the relaxation of particle system.

An equations-of-state incorporating the target density is developed so that a SPH density summation procedure is eliminated. The particle pressure force depends on the pressure gradient, i.e. the misalignment between the target density and physical particle density. A stable equilibrium state of the particle system can be obtained, i.e. the pressure force vanishes, when the particle distribution conforms to the background target mesh.

Surface tension originates from the cohesion of like molecules and thus promotes the coherence of distinct flow phases. With the effects of surface tension force, the interface surface area tends to become minimum. With this observation, a surface tension model is introduced to regularize the multiphase particle evolution. Consequently, the partitioning subdomains possess convex boundary shapes, small aspect ratios and strict connectedness. The communication volume between partitioning subdomains is thus optimized implicitly.

In order to stabilize the particle evolution, friction model and viscous model coupling with a predictor-corrector time integration technique are developed. Since the solution of model equations continuously depends on the initial and boundary condition, the partitioning topology experiences minor update along with small mesh topology changes. The proposed partitioning method is implicitly incremental and physically localized.

The discontinuous distributions of density and pressure as well as the particle interaction cut-off radius make it a challenging problem for numerical algorithm. Several techniques are developed to improve the robustness as follows. The initial condition of particle distribution is set up by firstly dividing the domain with close packing method and then randomly assigning colored particles into the circles or spheres. This type of initial distribution is beneficial for particles to form energy-stable sharp interface. A multi-resolution based cell linked list for fast neighbor searching and Verlet's list construction is proposed. A symmetry boundary condition is enforced through a dynamic ghost particle method, in which a ghost particle list for certain boundary particle is reconstructed temporally. For the purpose of adaptation to the mesh topology changes, adaptive refinement and coarsening of particle number are developed so that certain ratio of total particle number to mesh element number is maintained throughout the SPH simulation.

My contribution to this work was the development of the method and the corresponding computer code for its implementation. I performed simulations and analyzed the results, and wrote the manuscript for the publication.

3.3 A physics-motivated Centroidal Voronoi Particle domain decomposition method

Domain decomposition methods, which allow to solve the global problem by a sequence of local problems following a divide and conquer principle, are widely used in many scientific applications [56][76]. In Paper III, a novel Centroidal Voronoi Particle based domain decomposition method is proposed and validated by typical partitioning problems. This section reviews popular Centroidal Voronoi Tessellation domain decomposition methods and summarizes the proposed CVP method.

3.3.1 State of the art

Centroidal Voronoi Tessellation is a classical geometry-based domain decomposition method and is widely used in data processing, mesh generation, and shape optimization [78] [17][105][20]. Du et al. [18] explored the CVT concept for unstructured isotropic mesh generation by utilizing the dual relation between Delaunay triangulation and Voronoi diagram. It has been further extended to anisotropic meshing and geometric surface meshing [105][20].

Given a set of sites $\{p_1, \cdots, p_n\}$, i.e. Voronoi generators, a Voronoi tessellation is a subdivision of a domain into n cells, with the property that a point q_x lies in the cell corresponding to a site p_i if $d(p_i, q_x) < d(p_j, q_x)$ for j distinct from i [78]. Provided that a domain is characterized by a given density function, a CVT decomposition is a specific Voronoi tessellation, for which the Voronoi generator coincides with the mass centroid of each Voronoi cell.

A CVT configuration can be computed by the probabilistic MacQueen's random algorithm [67] and the deterministic Lloyd's iteration [64]. While MacQueen's random algorithm is not widely used owing to its weak convergence property, the Lloyd's method is popular for its numerical robustness and simplicity [64]. The CVT energy function, which describes the compactness of partitioning subdomains, can be decreased monotonically by the Lloyd's iteration without step-size constraint,

and linear convergence can be obtained [16]. In order to improve the convergence rate, Liu et al. [63] proposed a quasi-Newton method to compute CVT.

For CVT configuration, Gersho's conjecture [21] states that "asymptotically speaking, all cells of the optimal CVT, while forming a tessellation, are congruent to a basic cell which depends on the dimension." Based on Gersho's conjecture, when the generator number tends to infinity and the density function is smooth enough, the equal distribution property of mass can be asymptotically achieved [3]. However, the condition cannot be satisfied with practical applications, where the density may be discontinuous and the generator number may be rather limited, e.g. the partitioning problems of parallel computing.

3.3.2 Summary of the proposed method

In order to overcome the limitations and drawbacks of CVT based domain decomposition method, Paper III proposes a Centroidal Voronoi Particle based domain decomposition method.

First of all, a physics-motivated Voronoi Particle method is developed. The particles, i.e. the generators, are evolved following the momentum equations for a fluid in Lagrangian form. The pressure is defined by a tailored EOS, which incorporates the target mass. If the target mass distribution has not been reached, the particle pressure is not uniform in the computational domain, and consequently the particle system will be driven to relax by the pressure force. In other words, the particle relaxation converges when and only when $\forall i$, $m_i = m_{tg,i}$.

Afterwards, the Centroidal Voronoi Particle based domain decomposition method is proposed by combing the CVT concept and the VP dynamics. Considering that Lloyd's method converges without step-size constraint while the VP method is limited by a timestep criterion, a straightforward combination leads to poor convergence. A global step-size condition for Lloyd's method is developed such that one particle moves less than certain threshold in one explicit time integration step, which is consistent with the timestep condition of VP method. In order to obtain good convergence, an explicit two-step strategy for particle evolution is proposed.

Different from the CVT method, both the two concerned objectives, i.e. the arbitrary target mass distribution and compactness, can be optimized regardless of the smoothness of density function, the number of the generators and the boundary complexity. Applications of CVP method to the

load-balancing problems are analyzed. All objectives, i.e. the equal-sized partitioning with minimum communication volume, the convex subdomain shapes, and the locality and incremental property, are optimized implicitly.

My contribution to this work was the development of the method and the corresponding computer code for its implementation. I performed simulations and analyzed the results, and wrote the manuscript for the publication.

Chapter 4

Conclusions and outlooks

In this work, several new numerical methods have been developed for high-performance computational fluid dynamics. A family of high-order TENO schemes is proposed for the hyperbolic conservation laws. A multiphase SPH based partitioning method is proposed for solving the load-balancing problems of high-performance computing. A CVP based domain decomposition method is proposed for the general partitioning problems in scientific computing.

In order to address the shortcomings of classical WENO schemes, the high-order TENO family schemes are proposed. Within a unified framework, the arbitrarily high-order reconstruction is achieved by combing a set of candidate stencils of incremental width. TENO scheme can gradually degenerate to low-order reconstruction according to the smoothness of local flow scales. Since the three smallest stencils are identical to that of classical WENO-JS scheme, the numerical robustness is thus improved even for very-high-order versions. A strong scale-separation formula is developed to isolate discontinuities from smooth regions. An ENO-like stencil selection procedure, which either applies the candidate stencil with optimal weight or removes its contribution completely when crossed by discontinuities, is proposed to generate low numerical dissipation for smooth regions while maintaining the monotonicity near discontinuities. By ADR analysis, the spectral properties of the nonlinear TENO scheme are preserved exactly to that of its counterpart linear scheme for low to intermediate wavenumbers. Reducing the formal order of accuracy by one, a spectral optimization method is proposed such that a certain dissipation-dispersion relation is enforced. Extensive numerical experiments demonstrate that the high-order TENO schemes are superior to the classical WENO

schemes. In detail, the TENO schemes can resolve much more small-scale structures with less numerical dissipation while capturing the discontinuities sharply and robustly. The theoretical accuracy order can be restored up to intermediate wavenumbers. The computational complexity is similar to that of WENO since the most time-consuming part for calculating the smoothness indicators is the same. Moreover, the proposed TENO schemes are applicable for discretizing general PDEs.

Based on the present work, the performances of very-high-order (higher than sixth-order) TENO schemes, in particular the numerical robustness, can be explored in the future. More general approaches to optimize the spectral properties of TENO schemes should be developed. The choice of the case-independent cut-off parameter C_T can be further studied. The resolution properties of TENO schemes for incompressible and compressible turbulence are also attractive and should be investigated quantitatively.

While classical geometry-based and graph-based methods fail to optimize the multiple objective functions of a partitioning problem simultaneously, a novel physics-motivated SPH based partitioning method is proposed with the observation that the optimal partitioning outcome has high similarity to the relaxation state of a multi-phase system. A set of model equations is developed to characterize the background mesh topology. With this method, all the objectives are optimized implicitly and consistently. With a tailored EOS, the load-imbalance error is reduced during the particle relaxation and can be controlled with a convergence criterion. Unlike graph-based methods which optimize the communication volume by minimizing the edge-cuts, the proposed method dedicates to optimizing the mesh element number near subdomain boundaries by a surface tension model. With an SPH method solving the model equations, the solution continuously depends on the initial and boundary condition and consequently the partitioning is physically localized and implicitly incremental. With sufficient surface tension between distinct particle phases, the partitioned subdomains are guaranteed to be connected. Extensive experiments demonstrate that the proposed method produces high-quality partitioning for block-structured adaptive mesh.

Although the present method is efficient for dynamic partitioning, the static partitioning can be slow due to the fact that the initial particle distribution typically is far from the convergent configuration. One choice to remedy this problem is to develop the large-scale parallel algorithms for present method. The numerical robustness should be investigated in practical load-balancing

simulations. Moreover, this method can be further extended as a general domain decomposition method for smooth density filed, e.g. as the isotropic and anisotropic unstructured mesh generator. With proper boundary conditions and level-set based geometry descriptions, high-quality adaptive unstructured meshes can be generated for complex geometries.

Considering that the partitioning generator number may be rather limited and the background density function may be discontinuous for practical scientific applications, it is difficult for classical CVT methods to guarantee a target partitioning. In order to handle such problems, a CVP based domain decomposition is proposed by combining the CVT and VP concept. By generating the CVT configuration, Lloyd's method optimizes the energy function monotonically, which enhances the compactness of the convex partitioning subdomains. With a tailored EOS, an equal-sized or nonequal-sized partitioning can be obtained by solving the physics-motivated particle evolution model with VP method. The proposed method is highly efficient and applicable for both smooth and discontinuous background density field. The two objectives, i.e. arbitrary target mass distribution and compactness, can be achieved regardless of the number of generators and the boundary complexity. When applied to typical load-balancing problems for parallel computing, all the concerned objectives, i.e. the equal-sized partitioning with minimum communication volume, the convex subdomain shapes, and the locality and incremental property, are optimized implicitly. Numerical experiments demonstrate that the CVP method performs superior than CVT in the typical partitioning applications of particle configuration, adaptive structured and unstructured mesh.

While the present investigation is limited to the static partitioning of discontinuous density fields, the performances of CVP method for dynamic partitioning problems and for continuous smooth density fields should be studied in the future. The convergence of CVP method for large generator number will be investigated. More efficient approaches to construct the CVT configuration are also attractive. For large generator numbers, the CVT construction may be the efficiency bottleneck of CVP method. On the other hand, parallel algorithms of CVP method in distributed-memory computing environment should be developed.

References

[1] Barnard, S. T. and Simon, H. D. (1994). Fast multilevel implementation of recursive spectral bisection for partitioning unstructured problems. *Concurrency: Practice and Experience*, 6(2):101–117.

[2] Berger, M. and Bokhari, S. (1987). A partitioning strategy for nonuniform problems on multiprocessors. *IEEE Trans. Computers*, 36:570–580.

[3] Bo, W. and Shashkov, M. (2015). Adaptive reconnection-based arbitrary lagrangian eulerian method. *Journal of Computational Physics*, 299:902–939.

[4] Boman, E., Devine, K., Heaphy, R., Hendrickson, R., Leung, V., and Vaughan, L. A. C. (2007). Zoltan: parallel partitioning, load balancing and data management services. pages 1–173.

[5] Borges, R., Carmona, M., Costa, B., and Don, W. S. (2008). An improved weighted essentially non-oscillatory scheme for hyperbolic conservation laws. *J. Comput. Phys.*, 227:3191–3211.

[6] Butz, A. R. (1968). Space filling curves and mathematical programming. *Information and Control*, 12:314–330.

[7] Carroll-Nellenback, J. J., Shroyer, B., Frank, A., and Ding, C. (2013). Efficient parallelization for amr mhd multiphysics calculations; implementation in astrobear. *J. Comput. Phys.*, 236:461–476.

[8] Castro, M., Costa, B., and Don, W. S. (2011). High order weighted essentially non-oscillatory weno-z schemes for hyperbolic conservation laws. *J. Comput. Phys.*, 230:1766–1792.

[9] Catalyurek, U. and Aykanat, C. (1999). Hypergraph-partitioning-based decomposition for parallel sparse-matrix vector multiplication. *Parallel and Distributed Systems, IEEE Transactions on*, 10(7):673–693.

[10] Cockburn, B. and Shu, C.-W. (1989). Tvb runge-kutta local projection discontinuous galerkin finite element method for conservation laws. ii. general framework. *Mathematics of computation*, 52(186):411–435.

[11] Cook, A. W. (2007). Artificial fluid properties for large-eddy simulation of compressible turbulent mixing. *Physics of Fluids (1994-present)*, 19(5):055103.

[12] Cook, A. W. and Youngs, D. (2009). Rayleigh-taylor instability and mixing. *Scholarpedia*, 4(2):6092.

[13] Courant, R., Friedrichs, K., and Lewy, H. (1967). On the partial difference equations of mathematical physics. *IBM journal*, 11(2):215–234.

[14] Dehnen, W. and Aly, H. (2012). Improving convergence in smoothed particle hydrodynamics simulations without pairing instability. *Monthly Notices of the Royal Astronomical Society*, 425:1068–1082.

[15] Diekmann, R., Preis, R., Schlimbach, F., and Walshaw, C. (2000). Shape-optimized mesh partitioning and load balancing for parallel adaptive fem. *Parallel Computing*, 26(12):1555–1581.

[16] Du, Q., Emelianenko, M., and Ju, L. (2006). Convergence of the lloyd algorithm for computing centroidal voronoi tessellations. *SIAM journal on numerical analysis*, 44(1):102–119.

[17] Du, Q., Faber, V., and Gunzburger, M. (1999). Centroidal voronoi tessellations: applications and algorithms. *SIAM review*, 41(4):637–676.

[18] Du, Q. and Gunzburger, M. (2002). Grid generation and optimization based on centroidal voronoi tessellations. *Applied Mathematics and Computation*, 133(2):591–607.

[19] Du, Q., Gunzburger, M., and Ju, L. (2010). Advances in studies and applications of centroidal voronoi tessellations. *Numerical Mathematics: Theory, Methods and Applications*, 3(2):119–142.

[20] Du, Q. and Wang, D. (2005a). Anisotropic centroidal voronoi tessellations and their applications. *SIAM Journal on Scientific Computing*, 26(3):737–761.

[21] Du, Q. and Wang, D. (2005b). The optimal centroidal voronoi tessellations and the gersho's conjecture in the three-dimensional space. *Computers & Mathematics with Applications*, 49(9):1355–1373.

[22] Eames, I. and Flor, J. (2011). New developments in understanding interfacial processes in turbulent flows.

[23] Fortmeier, O., Bücker, H. M., Fagginger Auer, B., and Bisseling, R. H. (2013). A new metric enabling an exact hypergraph model for the communication volume in distributed-memory parallel applications. *Parallel Computing*, 39:319–335.

[24] Genz, A. and Cools, R. (2003). An adaptive numerical cubature algorithm for simplices. *ACM Transactions on Mathematical Software (TOMS)*, 29(3):297–308.

[25] Gingold, R. A. and Monaghan, J. J. (1977). Smoothed particle hydrodynamics: theory and application to non-spherical stars. *Monthly notices of the royal astronomical society*, 181(3):375–389.

[26] Godunov, S. K. (1959). A difference method for numerical calculation of discontinuous solutions of the equations of hydrodynamics. *Matematicheskii Sbornik*, 89(3):271–306.

[27] Gottlieb, S. and Shu, C.-W. (1998). Total variation diminishing runge-kutta schemes. *Mathematics of computation of the American Mathematical Society*, 67(221):73–85.

[28] Gottlieb, S., Shu, C.-W., and Tadmor, E. (2001). Strong stability-preserving high-order time discretization methods. *SIAM review*, 43(1):89–112.

[29] Han, L. H., Hu, X. Y., and Adams, N. A. (2014). Adaptive multi-resolution method for compressible multi-phase flows with sharp interface model and pyramid data structure. *J. Comput. Phys.*, 262:131–152.

[30] Harten, A. (1983). A high resolution scheme for the computation of weak solutions of hyperbolic conservation laws. *J. Comput. Phys.*, 49:357–393.

[31] Harten, A., Engquist, B., Osher, S., and Chakravarthy, S. R. (1987). Uniformly high order accurate essentially non-oscillatory schemes, iii. *J. Comput. Phys.*, 71:231–303.

[32] Hendrickson, B. (1998). Graph partitioning and parallel solvers: Has the emperor no clothes? In *Solving Irregularly Structured Problems in Parallel*, pages 218–225. Springer.

[33] Hendrickson, B. and Kolda, T. G. (2000). Graph partitioning models for parallel computing. *Parallel Computing*, 26(12):1519–1534.

[34] Henrick, A. K., Aslam, T., and Powers, J. M. (2005). Mapped weighted essentially non-oscillatory schemes: achieving optimal order near critical points. *J. Comput. Phys.*, 207:542–567.

[35] Hewitt, E. and Hewitt, R. E. (1979). The gibbs-wilbraham phenomenon: An episode in fourier analysis. *Archive for History of Exact Sciences*, 21:129–160.

[36] Hickel, S., Adams, N. A., and Domaradzki, J. A. (2006). An adaptive local deconvolution method for implicit les. *J. Comput. Phys.*, 213(1):413–436.

[37] Hilbert, D. (1891). ueber die stetige abbildung einer linie auf ein flaechenstueck. *Mathematische Annalen*, 38(3):459–460.

[38] Hill, D. and Pullin, D. (2004). Hybrid tuned center-difference-weno method for large eddy simulations in the presence of strong shocks. *J. Comput. Phys.*, 194:435–450.

[39] Hu, X. Y. and Adams, N. A. (2006a). Angular-momentum conservative smoothed particle dynamics for incompressible viscous flows. *Physics of Fluids*, 18(10):101702.

[40] Hu, X. Y. and Adams, N. A. (2006b). A multi-phase sph method for macroscopic and mesoscopic flows. *Journal of Computational Physics*, 213(2):844–861.

[41] Hu, X. Y. and Adams, N. A. (2007). An incompressible multi-phase sph method. *J. Comput. Phys.*, 227:264–278.

[42] Hu, X. Y. and Adams, N. A. (2011). Scale separation for implicit large eddy simulation. *J. Comput. Phys.*, 230:7240–7249.

[43] Hu, X. Y., Wang, Q., and Adams, N. A. (2010). An adaptive central-upwind weighted essentially non-oscillatory scheme. *J. Comput. Phys.*, 229:8952–8965.

[44] Hu, Y. and Blake, R. (1999). An improved diffusion algorithm for dynamic load balancing. *Parallel Computing*, 25(4):417–444.

[45] Huynh, H. T. (2007). A flux reconstruction approach to high-order schemes including discontinuous galerkin methods. In *18th AIAA Computational Fluid Dynamics Conference*, page 4079.

[46] Iri, M., Murota, K., and Ohya, T. (1984). A fast voronoi-diagram algorithm with applications to geographical optimization problems. In *System Modelling and Optimization*, pages 273–288. Springer.

[47] Jameson, A. (1994). Analysis and design of numerical schemes for gas dynamics, 1: artificial diffusion, upwind biasing, limiters and their effect on accuracy and multigrid convergence. *Int J Comput Fluid Dynam*, 4:171–218.

[48] Ji, H., Lien, F.-S., and Yee, E. (2010). A new adaptive mesh refinement data structure with an application to detonation. *Journal of Computational Physics*, 229(23):8981–8993.

[49] Jiang, G. S. and Shu, C.-W. (1996). Efficient implementation of weighted eno schemes. *J. Comput. Phys.*, 126(1):202–228.

[50] Johnsen, E., Larsson, J., Bhagatwala, A. V., Cabot, W. H., Moin, P., Olson, B. J., Rawat, P. S., Shankar, S. K., Sjögreen, B., Yee, H., et al. (2010). Assessment of high-resolution methods for numerical simulations of compressible turbulence with shock waves. *Journal of Computational Physics*, 229(4):1213–1237.

[51] Karypis, G. and Kumar, V. (1998). A software package for partitioning unstructured graphs, partitioning meshes, and computing fill-reducing orderings of sparse matrices. *University of Minnesota, Department of Computer Science and Engineering, Army HPC Research Center, Minneapolis, MN*.

[52] Karypis, G. and Kumar, V. (1999a). A fast and high quality multilevel scheme for partitioning irregular graphs. *SIAM Journal on Scientific Computing*, 20:359–392.

[53] Karypis, G. and Kumar, V. (1999b). Parallel multilevel series k-way partitioning scheme for irregular graphs. *SIAM Review*, 41(2):278–300.

[54] Karypis, G., Schloegel, K., and V, K. (2003). Parmetis parallel graph partitioning and sparse matrix ordering library. version 3.1. *http://glaros.dtc.umn.edu/gkhome/metis/parmetis/overview*, pages 1–29.

[55] Kavouklis, C. and Kallinderis, Y. (2010). Parallel adaptation of general three-dimensional hybrid meshes. *Journal of Computational Physics*, 229(9):3454 – 3473.

[56] Keyes, D. E. et al. (1992). *Fifth International Symposium on Domain Decomposition Methods for Partial Differential Equations*. Number 55. Siam.

[57] Kim, K. H. and Kim, C. (2005). Accurate, efficient and monotonic numerical methods for multi-dimensional compressible flows part ii: Multi-dimensional limiting process. *J. Comput. Phys.*, 208:570–615.

[58] Kotov, D., Yee, H., Wray, A., Sjögreen, B., and Kritsuk, A. (2016). Numerical dissipation control in high order shock-capturing schemes for les of low speed flows. *Journal of Computational Physics*, 307:189–202.

[59] Lee, A., Yau, C., Giles, M. B., Doucet, A., and Holmes, C. C. (2010). On the utility of graphics cards to perform massively parallel simulation of advanced monte carlo methods. *J. Comput. Phys.*, 19:769–789.

[60] Lele, S. K. (1992). Compact finite difference schemes with spectral-like resolution. *J. Comput. Phys.*, 103:16–42.

[61] Liu, X. D., Osher, S., and Chan, T. (1994). Weighted essentially non-oscillatory schemes. *J. Comput. Phys.*, 115:200–212.

[62] Liu, Y., Vinokur, M., and Wang, Z. (2006). Discontinuous spectral difference method for conservation laws on unstructured grids. In *Computational Fluid Dynamics 2004*, pages 449–454. Springer.

[63] Liu, Y., Wang, W., Lévy, B., Sun, F., Yan, D.-M., Lu, L., and Yang, C. (2009). On centroidal voronoi tessellation-energy smoothness and fast computation. *ACM Transactions on Graphics (ToG)*, 28(4):101.

[64] Lloyd, S. P. (1982). Least squares quantization in pcm. *Information Theory, IEEE Transactions on*, 28(2):129–137.

[65] Lucy, L. B. (1977). A numerical approach to the testing of the fission hypothesis. *The astronomical journal*, 82:1013–1024.

[66] Ma, Z. H., Wang, H., and Pu, S. H. (2014). Gpu computing of compressible flow problems by a meshless method with space-filling curves. *J. Comput. Phys.*, 263:113–135.

[67] MacQueen, J. et al. (1967). Some methods for classification and analysis of multivariate observations. In *Proceedings of the fifth Berkeley symposium on mathematical statistics and probability*, volume 1, pages 281–297. Oakland, CA, USA.

[68] Martin, M. P. (2000). Shock-capturing in les of high-speed flows. *Center for Turbulence Research Annual Research Briefs 2000*.

[69] Martín, M. P., Taylor, E. M., Wu, M., and Weirs, V. G. (2006). A bandwidth-optimized weno scheme for the effective direct numerical simulation of compressible turbulence. *Journal of Computational Physics*, 220(1):270–289.

[70] Meyerhenke, H., Monien, B., and Sauerwald, T. (2008). A new diffusion-based multilevel algorithm for computing graph partitions of very high quality. In *Parallel and Distributed Processing, 2008. IPDPS 2008. IEEE International Symposium on*, pages 1–13.

[71] Meyerhenke, H., Monien, B., and Schamberger, S. (2009). Graph partitioning and disturbed diffusion. *Parallel Computing*, 35(10 - 11):544 – 569.

[72] Monaghan, J. J. (2005). Smoothed particle hydrodynamics. *Rep. Prog. Phys.*, 68:1703–1759.

[73] Morris, J. P., Fox, P. J., and Zhu, Y. (1997). Modeling low reynolds number incompressible flows using sph. *Journal of computational physics*, 136(1):214–226.

[74] Morton, G. (1966). *A Computer Oriented Geodetic Data Base and a New Technique in File Sequencing*. International Business Machines Company.

[75] Mousavi, S. and Sukumar, N. (2011). Numerical integration of polynomials and discontinuous functions on irregular convex polygons and polyhedrons. *Computational Mechanics*, 47(5):535–554.

[76] Nepomnyaschikh, S. (2007). Domain decomposition methods. *Radon Series Comp. Appl. Math*, 1:89–160.

[77] Nivarti, G. V., Salehi, M. M., and Bushe, W. K. (2015). A mesh partitioning algorithm for preserving spatial locality in arbitrary geometries. *J. Comput. Phys.*, 281:352–364.

[78] Okabe, A., Boots, B., Sugihara, K., and Chiu, S. N. (2009). *Spatial tessellations: concepts and applications of Voronoi diagrams*, volume 501. John Wiley & Sons.

[79] Peano, G. (1890). Sur une courbe, qui remplit toute une aire plane. *Mathematische Annalen*, 36(1):157–160.

[80] Pellegrini, F. (2007). A parallelisable multi-level banded diffusion scheme for computing balanced partitions with smooth boundaries. In *Euro-Par 2007 Parallel Processing*, volume 4641 of *Lecture Notes in Computer Science*, pages 195–204.

[81] Pellegrini, F. (2008). Scotch and libscotch 5.1. user's guide. *http://www.labri.fr/perso/pelegrin/scotch/*, pages 1–127.

[82] Pirozzoli, S. (2011). Numerical methods for high-speed flows. *Annual Review of Fluid Mechanics*, 43:163–194.

[83] Pothen, A., Simon, H., and Liou, K. (1990). Partitioning sparse matrices with eigenvectors of graphs. *SIAM Journal on Matrix Analysis and Applications*, 11(3):430–452.

[84] Premasuthan, S., Liang, C., and Jameson, A. (2014). Computation of flows with shocks using the spectral difference method with artificial viscosity, i: Basic formulation and application. *J. Comput. Phys.*, 98:111–121.

[85] Price, D. J. (2012). Smoothed particle hydrodynamics and magnetohydrodynamics. *J. Comput. Phys.*, 231:759–794.

[86] Rama Mohan Rao, A. (2009). Parallel mesh-partitioning algorithms for generating shape optimised partitions using evolutionary computing. *Advances in Engineering Software*, 40(2):141–157.

[87] Reynolds, O. (1894). On the dynamical theory of incompressible viscous fluids and the determination of the criterion. *Proceedings of the Royal Society of London*, 56(336-339):40–45.

[88] Roe, P. L. (1981). Approximate riemann solvers, parameter vectors, and difference schemes. *Journal of computational physics*, 43(2):357–372.

[89] Rossinelli, D., Hejazialhosseini, B., van Rees, W., Gazzola, M., Bergdorf, M., and Koumoutsakos, P. (2015). Mrag-i2d: Multi-resolution adapted grids for remeshed vortex methods on multicore architectures. *Journal of Computational Physics*, 288:1–18.

[90] Rusanov, V. V. (1961). Calculation of interaction of non-steady shock waves with obstacles. *USSR J. Comp. Math. Phys.*, pages 267 – 279.

[91] Sagan, H. (1994). Space-filling curves. *Springer*.

[92] Schranner, F. S., Hu, X. Y., and Adams, N. A. (2013). A physically consistent weakly compressible high-resolution approach to underresolved simulations of incompressible flows. *Computers & Fluids*, 86:109–124.

[93] Shang, Z. (2014). Impact of mesh partitioning methods in cfd for large scale parallel computing. *Comput. Fluids*, 103:1–5.

[94] Shu, C.-W. (1988). Total-variation-diminishing time discretizations. *SIAM Journal on Scientific and Statistical Computing*, 9(6):1073–1084.

[95] Shu, C.-W. (2009). High order weighted essentially nonoscillatory schemes for convection dominated problems. *SIAM review*, 51(1):82–126.

[96] Smagorinsky, J. (1963). General circulation experiments with the primitive equations: I. the basic experiment. *Monthly weather review*, 91(3):99–164.

[97] Sudhakar, Y. and Wall, W. A. (2013). Quadrature schemes for arbitrary convex/concave volumes and integration of weak form in enriched partition of unity methods. *Computer Methods in Applied Mechanics and Engineering*, 258:39–54.

[98] Sun, Z.-S., Luo, L., Ren, Y.-X., and Zhang, S.-Y. (2014). A sixth order hybrid finite difference scheme based on the minimized dispersion and controllable dissipation technique. *J. Comput. Phys.*, 270:238–254.

[99] Suresh, A. and Huynhb, H. (1997). Accurate monotonicity-preserving schemes with runge-kutta time stepping. *J. Comput. Phys.*, 136:83–99.

[100] Swegle, J. W., Hicks, D. L., and Attaway, S. W. (1995). Smoothed particle hydrodynamics stability analysis. *Monthly Notices of the Royal Astronomical Society*, 116:123–134.

[101] Teresco, J., Devine, K., and Flaherty, J. (2006). Partitioning and dynamic load balancing for the numerical solution of partial differential equations. In *Numerical Solution of Partial Differential Equations on Parallel Computers*, volume 51, pages 55–88. Springer Berlin Heidelberg.

[102] Thomas, P. A. and Couchman, H. M. P. (1992). Simulating the formation of a cluster of galaxies. *MNRAS*, 257:11?1.

[103] Titarev, V. and Toro, E. (2004). Finite-volume weno schemes for three-dimensional conservation laws. *J. Comput. Phys.*, 201(1):238–260.

[104] Touber, E. and Sandham, N. (2008). Oblique shock impinging on a turbulent boundary layer: Low-frequency mechanisms. In *38th Fluid Dynamics Conference and Exhibit*, page 4170.

[105] Valette, S., Chassery, J.-M., and Prost, R. (2008). Generic remeshing of 3d triangular meshes with metric-dependent discrete voronoi diagrams. *Visualization and Computer Graphics, IEEE Transactions on*, 14(2):369–381.

[106] Verlet, L. (1967). Computer" experiments" on classical fluids. i. thermodynamical properties of lennard-jones molecules. *Physical review*, 159(1):98.

[107] von, N. J. and Richtmyer, R. (1950). A method for the numerical calculation of hydrodynamic shocks. *J. Appl. Phys.*, 21:232.

[108] Wang, Z. J., Fidkowski, K., Abgrall, R., Bassi, F., Caraeni, D., Cary, A., Deconinck, H., Hartmann, R., Hillewaert, K., Huynh, H. T., et al. (2013). High-order cfd methods: current status and perspective. *International Journal for Numerical Methods in Fluids*, 72(8):811–845.

[109] Weirs, V. and Candler, G. (1997). Optimization of weighted eno schemes for dns of compressible turbulence. *AIAA Paper*, pages 97–1940.

[110] Yang, X. F., Liu, M. B., and Peng, S. L. (2014). Smoothed particle hydrodynamics modeling of viscous liquid drop without tensile instability. *Comput. Fluids*, 92:199–208.

[111] Zhang, X. and Shu, C.-W. (2012). Positivity-preserving high order finite difference weno schemes for compressible euler equations. *Journal of Computational Physics*, 231(5):2245–2258.

[112] Zhao, S., Lardjane, N., and Fedioun, I. (2014). Comparison of improved finite-difference weno schemes for the implicit large eddy simulation of turbulent non-reacting and reacting high-speed shear flows. *Comput. Fluids*, 95:74–87.

[113] Zhong, X. and Wang, X. (2012). Direct numerical simulation on the receptivity, instability, and transition of hypersonic boundary layers. *Annual Review of Fluid Mechanics*, 44:527–561.

Appendix A:

I

Article I

A family of high-order targeted ENO schemes for compressible-fluid simulations

In *Journal of Computational Physics*, Volume 305, 15 January 2016, pp. 333-359, DOI http://dx.doi.org/10.1016/j.jcp.2015.10.037.

Contribution: My contribution to this work was the development of the method and the corresponding computer code for its implementation. I performed simulations and analyzed the results, and wrote the manuscript for the publication.

ELSEVIER LICENSE TERMS AND CONDITIONS

Jul 06, 2017

This Agreement between Institute of Aerodynamics and Fluid Mechanics, Technical University of Munich -- Lin Fu ("You") and Elsevier ("Elsevier") consists of your license details and the terms and conditions provided by Elsevier and Copyright Clearance Center.

The publisher has provided special terms related to this request that can be found at the end of the Publisher's Terms and Conditions.

License Number	4143000376553
License date	Jul 06, 2017
Licensed Content Publisher	Elsevier
Licensed Content Publication	Journal of Computational Physics
Licensed Content Title	A family of high-order targeted ENO schemes for compressible-fluid simulations
Licensed Content Author	Lin Fu,Xiangyu Y. Hu,Nikolaus A. Adams
Licensed Content Date	Jan 15, 2016
Licensed Content Volume	305
Licensed Content Issue	n/a
Licensed Content Pages	27
Start Page	333
End Page	359
Type of Use	reuse in a thesis/dissertation
Intended publisher of new work	other
Portion	full article
Format	both print and electronic
Are you the author of this Elsevier article?	Yes
Will you be translating?	No
Order reference number	
Title of your thesis/dissertation	Numerical methods for computational fluid dynamics
Expected completion date	Aug 2017
Estimated size (number of pages)	126
Elsevier VAT number	GB 494 6272 12
Requestor Location	Institute of Aerodynamics and Fluid Mechanics, Technical University of Munich 85748 Garching Germany Munich, 85748 Germany Attn: Institute of Aerodynamics and Fluid Mechanics, Technical University of Munich
Publisher Tax ID	GB 494 6272 12
Billing Type	Invoice
Billing Address	Institute of Aerodynamics and Fluid Mechanics, Technical University of Munich 85748 Garching Germany Munich, Germany 85748 Attn: Institute of Aerodynamics and Fluid Mechanics, Technical University of Munich

Total **0.00 EUR**

Terms and Conditions

INTRODUCTION

1. The publisher for this copyrighted material is Elsevier. By clicking "accept" in connection with completing this licensing transaction, you agree that the following terms and conditions apply to this transaction (along with the Billing and Payment terms and conditions established by Copyright Clearance Center, Inc. ("CCC"), at the time that you opened your Rightslink account and that are available at any time at http://myaccount.copyright.com).

GENERAL TERMS

2. Elsevier hereby grants you permission to reproduce the aforementioned material subject to the terms and conditions indicated.
3. Acknowledgement: If any part of the material to be used (for example, figures) has appeared in our publication with credit or acknowledgement to another source, permission must also be sought from that source. If such permission is not obtained then that material may not be included in your publication/copies. Suitable acknowledgement to the source must be made, either as a footnote or in a reference list at the end of your publication, as follows:
"Reprinted from Publication title, Vol /edition number, Author(s), Title of article / title of chapter, Pages No., Copyright (Year), with permission from Elsevier [OR APPLICABLE SOCIETY COPYRIGHT OWNER]." Also Lancet special credit - "Reprinted from The Lancet, Vol. number, Author(s), Title of article, Pages No., Copyright (Year), with permission from Elsevier."
4. Reproduction of this material is confined to the purpose and/or media for which permission is hereby given.
5. Altering/Modifying Material: Not Permitted. However figures and illustrations may be altered/adapted minimally to serve your work. Any other abbreviations, additions, deletions and/or any other alterations shall be made only with prior written authorization of Elsevier Ltd. (Please contact Elsevier at permissions@elsevier.com). No modifications can be made to any Lancet figures/tables and they must be reproduced in full.
6. If the permission fee for the requested use of our material is waived in this instance, please be advised that your future requests for Elsevier materials may attract a fee.
7. Reservation of Rights: Publisher reserves all rights not specifically granted in the combination of (i) the license details provided by you and accepted in the course of this licensing transaction, (ii) these terms and conditions and (iii) CCC's Billing and Payment terms and conditions.
8. License Contingent Upon Payment: While you may exercise the rights licensed immediately upon issuance of the license at the end of the licensing process for the transaction, provided that you have disclosed complete and accurate details of your proposed use, no license is finally effective unless and until full payment is received from you (either by publisher or by CCC) as provided in CCC's Billing and Payment terms and conditions. If full payment is not received on a timely basis, then any license preliminarily granted shall be deemed automatically revoked and shall be void as if never granted. Further, in the event that you breach any of these terms and conditions or any of CCC's Billing and Payment terms and conditions, the license is automatically revoked and shall be void as if never granted. Use of materials as described in a revoked license, as well as any use of the materials beyond the scope of an unrevoked license, may constitute copyright infringement and publisher reserves the right to take any and all action to protect its copyright in the materials.
9. Warranties: Publisher makes no representations or warranties with respect to the licensed material.
10. Indemnity: You hereby indemnify and agree to hold harmless publisher and CCC, and their respective officers, directors, employees and agents, from and against any and all claims arising out of your use of the licensed material other than as specifically authorized pursuant to this license.
11. No Transfer of License: This license is personal to you and may not be sublicensed, assigned, or transferred by you to any other person without publisher's written permission.
12. No Amendment Except in Writing: This license may not be amended except in a writing signed by both parties (or, in the case of publisher, by CCC on publisher's behalf).
13. Objection to Contrary Terms: Publisher hereby objects to any terms contained in any purchase order, acknowledgment, check endorsement or other writing prepared by you, which terms are inconsistent with these terms and conditions or CCC's Billing and Payment terms and conditions. These terms and conditions, together with CCC's Billing and Payment terms and conditions (which are incorporated herein), comprise the entire agreement between you and publisher (and CCC) concerning this licensing transaction. In the event of any conflict between your obligations established by these terms and conditions and those established by CCC's Billing and Payment terms and conditions, these terms and conditions shall control.
14. Revocation: Elsevier or Copyright Clearance Center may deny the permissions described in this License at their sole discretion, for any reason or no reason, with a full refund payable to you. Notice of such denial will be made using the contact information provided by you. Failure to receive such notice will not alter or invalidate the denial. In no event will Elsevier or Copyright Clearance Center be responsible or liable for any costs, expenses or damage incurred by you as a result of a denial of your permission request, other than a refund of the amount(s) paid by you to Elsevier and/or Copyright Clearance Center for denied permissions.

LIMITED LICENSE

The following terms and conditions apply only to specific license types:
15. **Translation**: This permission is granted for non-exclusive world **English** rights only unless your license was granted for translation rights. If you licensed translation rights you may only translate this content into the languages you requested. A professional translator must perform all translations and reproduce the content word for word preserving the integrity of the article.
16. **Posting licensed content on any Website**: The following terms and conditions apply as follows: Licensing material from an Elsevier journal: All content posted to the web site must maintain the copyright information line on the bottom of each image; A hyper-text must be included to the Homepage of the journal from which you are licensing at http://www.sciencedirect.com/science/journal/xxxxx or the Elsevier homepage for books at http://www.elsevier.com; Central

Storage: This license does not include permission for a scanned version of the material to be stored in a central repository such as that provided by Heron/XanEdu.
Licensing material from an Elsevier book: A hyper-text link must be included to the Elsevier homepage at http://www.elsevier.com . All content posted to the web site must maintain the copyright information line on the bottom of each image.

Posting licensed content on Electronic reserve: In addition to the above the following clauses are applicable: The web site must be password-protected and made available only to bona fide students registered on a relevant course. This permission is granted for 1 year only. You may obtain a new license for future website posting.
17. **For journal authors:** the following clauses are applicable in addition to the above:
Preprints:
A preprint is an author's own write-up of research results and analysis, it has not been peer-reviewed, nor has it had any other value added to it by a publisher (such as formatting, copyright, technical enhancement etc.).
Authors can share their preprints anywhere at any time. Preprints should not be added to or enhanced in any way in order to appear more like, or to substitute for, the final versions of articles however authors can update their preprints on arXiv or RePEc with their Accepted Author Manuscript (see below).
If accepted for publication, we encourage authors to link from the preprint to their formal publication via its DOI. Millions of researchers have access to the formal publications on ScienceDirect, and so links will help users to find, access, cite and use the best available version. Please note that Cell Press, The Lancet and some society-owned have different preprint policies. Information on these policies is available on the journal homepage.
Accepted Author Manuscripts: An accepted author manuscript is the manuscript of an article that has been accepted for publication and which typically includes author-incorporated changes suggested during submission, peer review and editor-author communications.
Authors can share their accepted author manuscript:

- immediately
  - via their non-commercial person homepage or blog
  - by updating a preprint in arXiv or RePEc with the accepted manuscript
  - via their research institute or institutional repository for internal institutional uses or as part of an invitation-only research collaboration work-group
  - directly by providing copies to their students or to research collaborators for their personal use
  - for private scholarly sharing as part of an invitation-only work group on commercial sites with which Elsevier has an agreement
- After the embargo period
  - via non-commercial hosting platforms such as their institutional repository
  - via commercial sites with which Elsevier has an agreement

In all cases accepted manuscripts should:

- link to the formal publication via its DOI
- bear a CC-BY-NC-ND license - this is easy to do
- if aggregated with other manuscripts, for example in a repository or other site, be shared in alignment with our hosting policy not be added to or enhanced in any way to appear more like, or to substitute for, the published journal article.

Published journal article (JPA): A published journal article (PJA) is the definitive final record of published research that appears or will appear in the journal and embodies all value-adding publishing activities including peer review co-ordination, copy-editing, formatting, (if relevant) pagination and online enrichment.
Policies for sharing publishing journal articles differ for subscription and gold open access articles:
Subscription Articles: If you are an author, please share a link to your article rather than the full-text. Millions of researchers have access to the formal publications on ScienceDirect, and so links will help your users to find, access, cite, and use the best available version.
Theses and dissertations which contain embedded PJAs as part of the formal submission can be posted publicly by the awarding institution with DOI links back to the formal publications on ScienceDirect.
If you are affiliated with a library that subscribes to ScienceDirect you have additional private sharing rights for others' research accessed under that agreement. This includes use for classroom teaching and internal training at the institution (including use in course packs and courseware programs), and inclusion of the article for grant funding purposes.
Gold Open Access Articles: May be shared according to the author-selected end-user license and should contain a CrossMark logo, the end user license, and a DOI link to the formal publication on ScienceDirect.
Please refer to Elsevier's posting policy for further information.
18. **For book authors** the following clauses are applicable in addition to the above: Authors are permitted to place a brief summary of their work online only. You are not allowed to download and post the published electronic version of your chapter, nor may you scan the printed edition to create an electronic version. **Posting to a repository:** Authors are permitted to post a summary of their chapter only in their institution's repository.
19. **Thesis/Dissertation**: If your license is for use in a thesis/dissertation your thesis may be submitted to your institution in either print or electronic form. Should your thesis be published commercially, please reapply for permission. These requirements include permission for the Library and Archives of Canada to supply single copies, on demand, of the complete thesis and

include permission for Proquest/UMI to supply single copies, on demand, of the complete thesis. Should your thesis be published commercially, please reapply for permission. Theses and dissertations which contain embedded PJAs as part of the formal submission can be posted publicly by the awarding institution with DOI links back to the formal publications on ScienceDirect.

Elsevier Open Access Terms and Conditions

You can publish open access with Elsevier in hundreds of open access journals or in nearly 2000 established subscription journals that support open access publishing. Permitted third party re-use of these open access articles is defined by the author's choice of Creative Commons user license. See our open access license policy for more information.

Terms & Conditions applicable to all Open Access articles published with Elsevier:

Any reuse of the article must not represent the author as endorsing the adaptation of the article nor should the article be modified in such a way as to damage the author's honour or reputation. If any changes have been made, such changes must be clearly indicated.

The author(s) must be appropriately credited and we ask that you include the end user license and a DOI link to the formal publication on ScienceDirect.

If any part of the material to be used (for example, figures) has appeared in our publication with credit or acknowledgement to another source it is the responsibility of the user to ensure their reuse complies with the terms and conditions determined by the rights holder.

Additional Terms & Conditions applicable to each Creative Commons user license:

CC BY: The CC-BY license allows users to copy, to create extracts, abstracts and new works from the Article, to alter and revise the Article and to make commercial use of the Article (including reuse and/or resale of the Article by commercial entities), provided the user gives appropriate credit (with a link to the formal publication through the relevant DOI), provides a link to the license, indicates if changes were made and the licensor is not represented as endorsing the use made of the work. The full details of the license are available at http://creativecommons.org/licenses/by/4.0.

CC BY NC SA: The CC BY-NC-SA license allows users to copy, to create extracts, abstracts and new works from the Article, to alter and revise the Article, provided this is not done for commercial purposes, and that the user gives appropriate credit (with a link to the formal publication through the relevant DOI), provides a link to the license, indicates if changes were made and the licensor is not represented as endorsing the use made of the work. Further, any new works must be made available on the same conditions. The full details of the license are available at http://creativecommons.org/licenses/by-nc-sa/4.0.

CC BY NC ND: The CC BY-NC-ND license allows users to copy and distribute the Article, provided this is not done for commercial purposes and further does not permit distribution of the Article if it is changed or edited in any way, and provided the user gives appropriate credit (with a link to the formal publication through the relevant DOI), provides a link to the license, and that the licensor is not represented as endorsing the use made of the work. The full details of the license are available at http://creativecommons.org/licenses/by-nc-nd/4.0. Any commercial reuse of Open Access articles published with a CC BY NC SA or CC BY NC ND license requires permission from Elsevier and will be subject to a fee.

Commercial reuse includes:

- Associating advertising with the full text of the Article
- Charging fees for document delivery or access
- Article aggregation
- Systematic distribution via e-mail lists or share buttons

Posting or linking by commercial companies for use by customers of those companies.

20. **Other Conditions**: Permission is granted to submit your article in electronic format. This license permits you to post this Elsevier article online on your Institution's website if the content is embedded within your thesis.

v1.9

Questions? customercare@copyright.com or +1-855-239-3415 (toll free in the US) or +1-978-646-2777.

Journal of Computational Physics 305 (2016) 333–359

Contents lists available at ScienceDirect

Journal of Computational Physics

www.elsevier.com/locate/jcp

A family of high-order targeted ENO schemes for compressible-fluid simulations

Lin Fu, Xiangyu Y. Hu *, Nikolaus A. Adams

Institute of Aerodynamics and Fluid Mechanics, Technische Universität München, 85748 Garching, Germany

ARTICLE INFO

Article history:
Received 16 April 2015
Received in revised form 18 August 2015
Accepted 24 October 2015
Available online 2 November 2015

Keywords:
WENO-JS
WENO-Z
WENO-CU6
Optimal scheme
High-order scheme
Shock–turbulence interaction

ABSTRACT

Although classical WENO schemes have achieved great success and are widely accepted, they exhibit several shortcomings. They are too dissipative for direct simulations of turbulence and lack robustness when very-high-order versions are applied to complex flows. In this paper, we propose a family of high-order targeted ENO schemes which are applicable for compressible-fluid simulations involving a wide range of flow scales. In order to increase the numerical robustness as compared to very-high-order classical WENO schemes, the reconstruction dynamically assembles a set of low-order candidate stencils with incrementally increasing width. While discontinuities and small-scale fluctuations are efficiently separated, the numerical dissipation is significantly diminished by an ENO-like stencil selection, which either applies a candidate stencil with its original linear weight, or removes its contribution when it is crossed by a discontinuity. The background linear scheme is optimized under the constraint of preserving an approximate dispersion–dissipation relation. By means of quasi-linear analyses and practical numerical experiments, a set of case-independent parameters is determined. The general formulation of arbitrarily high-order schemes is presented in a straightforward way. A variety of benchmark-test problems, including broadband waves, strong shock and contact discontinuities are studied. Compared to well-established classical WENO schemes, the present schemes exhibit significantly improved robustness, low numerical dissipation and sharp discontinuity capturing. They are particularly suitable for DNS and LES of shock–turbulence interactions.

1. Introduction

The development of advanced numerical schemes, that are simultaneously capable of resolving small-scale flow structures and of capturing discontinuities, is a long-standing subject of computational fluid dynamics research. The apparent contradicting requirements of low-dissipation for resolving small-scale flow features and sufficient numerical dissipation for stable capturing of discontinuities pose the key problem [1]. Several approaches, such as total variation diminishing (TVD) schemes [2], essentially non-oscillatory (ENO) [3] and weighted essentially non-oscillatory (WENO) schemes [4], have been presented in the paper to overcome this problem. While TVD schemes are able to provide sufficient numerical dissipation to capture discontinuities, and to restore formal high-order accuracy in smooth regions without critical points [5–7], they degenerate to first-order and produce excessive numerical dissipation near critical points. ENO schemes choose the smoothest

* Corresponding author.
E-mail addresses: lin.fu@tum.de (L. Fu), xiangyu.hu@tum.de (X.Y. Hu), nikolaus.adams@tum.de (N.A. Adams).

http://dx.doi.org/10.1016/j.jcp.2015.10.037
0021-9991/

stencil to capture discontinuities from a set of candidate approximation stencils and reduce numerical dissipation compared to TVD schemes [3,8]. WENO schemes exploit a weighted average of approximations from all candidate stencils. Based on the smoothness indicators, the weights are designed to recover the ENO property for capturing discontinuities and to restore the background linear schemes in smooth regions of the solution [4,9]. WENO schemes are widely used in gas dynamics research [10–13]. However, for turbulent flow simulations classical WENO schemes exhibit excessive dissipation, which damps the small-scale flow structures significantly [14,15]. As shown by the approximated dispersion relation (ADR) analysis [16], the spectral property of WENO schemes is inferior to that of low-dissipation linear schemes. Furthermore, although the classical fifth-order WENO scheme is sufficiently robust for many applications, even higher-order schemes may fail when there exist multiple discontinuities close to each other [17,18].

Noticing that classical WENO schemes fail to recover the formal fifth-order accuracy near critical points, where low-order derivatives vanish, Henrick et al. [19] propose WENO-M to deal with this problem by remapping the WENO-JS weights [9] so that the sufficient criteria for fifth-order are satisfied. Borges et al. [20] find that the improved results of WENO-M for shock capturing problems are due to the non-linear adaptation, i.e. larger weights assigned to the non-smooth stencils, rather than due to the high-order accuracy in smooth regions. In order to decrease the dissipation induced by the nonlinear adaption, Hill and Pullin [21] propose a switch function to freeze the adaption when the ratio between the largest and the smallest calculated smoothness indicator does not exceed a certain threshold. However, the threshold value for this shifting is likely to be problem dependent, i.e. large thresholds may cause numerical problems whereas small values degenerate the effectiveness [22]. In order to achieve both high order and less nonlinear adaption, Hu et al. [23] propose an adaptive central-upwind 6th-order WENO-CU6 scheme by introducing the contribution from a downwind stencil. WENO-CU6 has been further developed into an Implicit Large Eddy Simulation (ILES) approach by incorporating a physically-motivated scale-separation formulation [24]. The drawback of WENO-CU6 schemes is that spurious waves may appear at marginally-resolved wave numbers as the background central scheme cannot suppress disturbances from accumulated dispersion errors [25].

The built-in dissipation from the background linear scheme is another main dissipation source [22,26,27]. One choice is to optimize directly the spectral property of the background linear scheme. Weirs and Candler [28] construct a six-point scheme with low dissipation and third-order accuracy by introducing a downwind stencil. Another approach [22] is to optimize stencil weights by minimizing the dispersion and dissipation errors simultaneously and consequentially delaying the dissipative bandwidth to a certain wave number. However, the resulting optimal background schemes typically exhibit some anti-dissipation for a certain wave-number range [22]. Hu et al. [25] propose a general dispersion–dissipation relation, which can serve as a guideline for optimizing the dispersion and dissipation of both linear and nonlinear schemes. The minimum dissipation is determined such that it is sufficient to damp spurious high wave-number oscillations. Numerical experiments show that the optimized schemes perform well for turbulence simulations [29,25].

Several methods have been developed to improve the numerical robustness of very high-order WENO schemes. Suresh and Huynh [30] propose to bound the solution near discontinuities by a monotonicity-preserving method. The problem of this technique is that it fails to maintain the formal order of the original WENO scheme [17]. Another approach is the order-reduction method [17,18], which recursively resorts to lower-order stencils. However, feasibility of the high-order approximation is checked by an empirical reconstruction-failure detector based on density and pressure, which makes it problematic for complex applications. Recently, an *a posteriori* approach, which first detects the critical numerical fluxes that may lead to negative pressure or density and then imposes a positivity-preserving flux limiter to correct the fluxes, has been proposed by Hu et al. [31]. This approach is simple and effective for general high-order conservative schemes.

In this paper, we propose a family of high-order targeted ENO (TENO) schemes preserving low dissipation for the low to intermediate wave-number range, sharp shock-capturing capacity and good robustness. Several new ideas are introduced to resolve the aforementioned issues:

1. Different from the classical WENO scheme assembling candidate stencils of same width, we create a high-order reconstruction by assembling a set of low-order (higher than third) upwind-biased candidate stencils with incremental width. The new scheme can gradually degenerate to third order, according to local flow features, thus avoiding the problem of multiple discontinuities and recovering the robustness of the classical fifth-order WENO-JS scheme.
2. Inspired by the work of Hu and Adams [24], an even stronger scale-separation formulation is designed to isolate discontinuities from high wave-number physical fluctuations.
3. Unlike WENO which assigns smooth weights to candidate stencils, a candidate stencil either is applied with optimal weight, or eliminated entirely when it contains a genuine discontinuity with certain strength, following an ENO-like stencil selection. This approach suppresses numerical dissipation to the limit of the background linear scheme for the wave-number region of interest while it preserves robust shock-capturing capability.
4. Since the background linear scheme is one main source of numerical dissipation, the optimization algorithm proposed by Hu and Adams [25] is adopted. Such optimization results in an order degeneration of one, but provides favorable spectral properties satisfying the dispersion–dissipation relation.

It is straightforward and fairly simple to construct arbitrarily high-order TENO schemes. As canonical example, we focus on fifth-order and sixth-order TENO schemes and discuss their performances for a wide range of test problems. The remainder of this paper is organized as follows. In Section 2, a brief summary of WENO schemes is given as general introduction. In Section 3, generalized formulations of the new TENO schemes are proposed, and the construction of fifth-order and

sixth-order TENO schemes is discussed in detail. In Section 4, an optimization algorithm is introduced for fifth-order and sixth-order TENO schemes in combination with the ADR analysis. In Section 5, a set of benchmark cases involving strong discontinuities and broadband fluctuations is simulated. The performance of the proposed schemes for compressible flow simulations is discussed and compared with that of established WENO schemes. In the last section, the overall properties of the proposed schemes are discussed.

2. Brief review of WENO schemes

In this section, we first review basic concepts of classical WENO schemes. Then the construction of typical five-point and six-point stencil schemes is given.

2.1. Fundamental concepts of WENO schemes

For simplicity, we consider the one-dimensional hyperbolic conservation law

$$\frac{\partial u}{\partial t}+\frac{\partial}{\partial x}f(u)=0, \tag{1}$$

where the characteristic velocity is further assumed to be positive $\frac{\partial f(u)}{\partial u}>0$ without loss of generality. After the discretization of Eq. (1) on a uniform mesh, e.g. x_i, a system of ordinary differential equations

$$\frac{du_i}{dt}=-\frac{\partial f}{\partial x}\Big|_{x=x_i},\ i=0,\cdots,n, \tag{2}$$

is formed and marched in time by an explicit strongly-stable Runge–Kutta method. Eq. (1) can be approximated by a conservative finite difference scheme in semi-discrete form as

$$\frac{du_i}{dt}=-\frac{1}{\Delta x}(h_{i+1/2}-h_{i-1/2}), \tag{3}$$

where the primitive function $h(x)$ is implicitly defined by

$$f(x)=\frac{1}{\Delta x}\int_{x-\Delta x/2}^{x+\Delta x/2}h(\xi)d\xi. \tag{4}$$

Eq. (3) is further approximated as

$$\frac{du_i}{dt}\approx-\frac{1}{\Delta x}(\widehat{f}_{i+1/2}-\widehat{f}_{i-1/2}), \tag{5}$$

where the numerical fluxes $\hat{f}_{i\pm1/2}$ is computed from a convex combination of r candidate-stencil fluxes

$$\widehat{f}_{i+1/2}=\sum_{k=0}^{r-1}w_k\widehat{f}_{k,i+1/2}. \tag{6}$$

To obtain a $(2r-1)$-order approximation for $\widehat{f}_{i+1/2}$, an $(r-1)$-degree interpolation on each candidate stencil leads to

$$h(x)\approx\hat{f}_k(x)=\sum_{l=0}^{r-1}a_{l,k}x^l. \tag{7}$$

After substituting Eq. (7) into Eq. (4) and evaluating the integral functions at the stencil nodes, the coefficients a_l are determined by solving the resulting system of linear algebraic equations. The negative split flux can be obtained by symmetry at the cell interface $x_{i+1/2}$.

2.2. Fifth-order WENO-JS and WENO-Z schemes

For the classical fifth-order WENO scheme with $r=3$, a 2-degree polynomial approximation results in

$$h(x)\approx\widehat{f}_k(x)=a_{0,k}+a_{1,k}x+a_{2,k}x^2. \tag{8}$$

For each stencil, a 3rd-order approximation of the numerical flux evaluated at the cell face $i+\frac{1}{2}$ gives

$$\hat{f}_{0,i+1/2} = \tfrac{1}{6}(2f_{i-2} - 7f_{i-1} + 11f_i),$$
$$\hat{f}_{1,i+1/2} = \tfrac{1}{6}(-f_{i-1} + 5f_i + 2f_{i+1}),$$
$$\hat{f}_{2,i+1/2} = \tfrac{1}{6}(2f_i + 5f_{i+1} - f_{i+2}). \tag{9}$$

With Taylor expansion analysis, we obtain

$$\hat{f}_{k,i+1/2} = h_{k,i+1/2} + A_k \Delta x^3 + \mathcal{O}(\Delta x^4),\ k = 0, 1, 2, \tag{10}$$

where A_k is a constant independent of Δx and may be different for different candidate stencils. For suppressing Gibbs oscillations [32] in the presence of discontinuities, the weights in Eq. (6) are defined as

$$w_k = \frac{\alpha_k}{\sum_{k=0}^{2} \alpha_k},\ \alpha_k = \frac{d_k}{(\beta_k + \varepsilon)^q}, \tag{11}$$

where d_k are optimal weights that generate a $(2r-1)$-th order scheme on a $(2r-1)$-point full stencil. Here, $d_0 = 0.1$, $d_1 = 0.6$, $d_2 = 0.3$. ε is a small value to prevent division by zero, whereas further research has shown that it indeed acts as a cutoff of the smoothness measure [33]. $q \geq 1$, generally defined as $q = 2$, is devised to accelerate the nonlinear adaptation towards the essentially non-oscillatory property. The local smoothness indicator β_k, determining to what extent certain candidate stencil should contribute to the final reconstruction, is defined as

$$\beta_k = \sum_{j=1}^{2} \Delta x^{2j-1} \int_{x_{i-1/2}}^{x_{i+1/2}} \left(\frac{d^j}{dx^j} \widehat{f}_k(x) \right)^2 dx \tag{12}$$

according to Jiang and Shu [9]. Explicit expression in terms of cell-averaged quantities f_i gives

$$\beta_0 = \tfrac{1}{4}(f_{i-2} - 4f_{i-1} + 3f_i)^2 + \tfrac{13}{12}(f_{i-2} - 2f_{i-1} + f_i)^2,$$
$$\beta_1 = \tfrac{1}{4}(f_{i-1} - f_{i+1})^2 + \tfrac{13}{12}(f_{i-1} - 2f_i + f_{i+1})^2,$$
$$\beta_2 = \tfrac{1}{4}(3f_i - 4f_{i+1} + f_{i+2})^2 + \tfrac{13}{12}(f_i - 2f_{i+1} + f_{i+2})^2. \tag{13}$$

In smooth regions, the local variation of the smoothness indicators is $\mathcal{O}(\Delta x^4)$, leading to w_k with approximately optimal weight. The convex combination of r stencils produces a $(2r-1)$-th order numerical flux approximation at the cell face. If a certain stencil k contains a discontinuity, β_k is $\mathcal{O}(1)$ while the others are $\mathcal{O}(\Delta x^2)$. The corresponding weight w_k becomes very small, thus the discontinuity is avoided, but the scheme degenerates to r-th order. Henrick et al. [19] investigate the effective order of classical WENO schemes and conclude that an overall $(2r-1)$-th order accuracy requires the condition $w_k - d_k = \mathcal{O}(\Delta x^3)$ to be satisfied in smooth regions. WENO-JS [9] degenerates to third-order near critical points, where the first-order derivative vanishes. Only second-order overall accuracy can be achieved when the second-order derivative vanishes as well. Motivated by the work of Henrick et al. [19], Borges et al. [20] propose a new weighting strategy as

$$\alpha_k = d_k \left(1 + \left(\frac{\tau_5}{\beta_k + \varepsilon} \right)^q \right),\ \tau_5 = |\beta_0 - \beta_2|, \tag{14}$$

by introducing a high-order reference value calculated from the full $(2r-1)$ stencil. The global smoothness measure τ_5, devised as the absolute difference between β_0 and β_2, is $\mathcal{O}(\Delta x^5)$ and

$$\frac{\tau_5}{\beta_k + \varepsilon} = \mathcal{O}(\Delta x^3),\ k = 0, 1, 2. \tag{15}$$

The condition $w_k - d_k = \mathcal{O}(\Delta x^3)$ is satisfied provided there are no critical points. Despite the limited success in enhancing accuracy near critical points, it was demonstrated that the new weight converges much faster to the optimal weight than classical WENO-JS in smooth regions, and that the new WENO-Z scheme performs better than WENO-JS and WENO-M. Furthermore, it was suggested to set $q = 1$ in Eq. (14) as a larger value of q results in a too dissipative scheme in non-smooth regions [20].

2.3. Sixth-order WENO-CU6 and WENO-CU6-M schemes

In order to ameliorate the built-in dissipation from the background linear scheme, Hu and Adams [23] propose to admit the contribution from the downwind stencil, constructing a sixth-order WENO-CU6 scheme which adapts between central and upwind schemes smoothly by a new weighting strategy. Following the previous discussion, the approximate numerical flux at the cell face using the downwind candidate stencil gives

$$\hat{f}_{3,i+1/2} = \frac{1}{6}(11f_{i+1} - 7f_{i+2} + 2f_{i+3}). \tag{16}$$

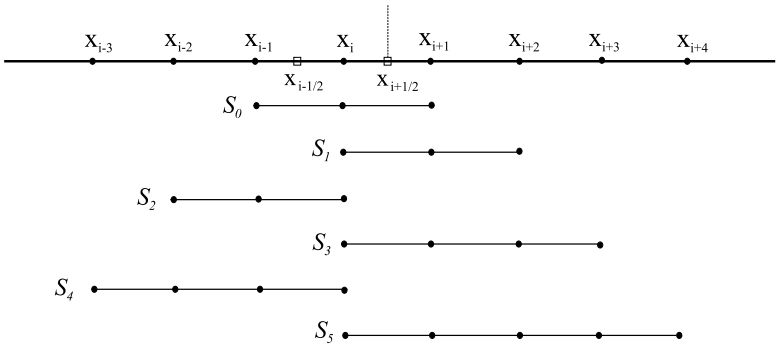

Fig. 1. Candidate stencils with incremental width towards high-order reconstruction.

Inspired by Borges et al. [20], the nonlinear weights are computed by

$$w_k = \frac{\alpha_k}{\sum_{k=0}^{3}\alpha_k},\ \alpha_k = d_k\left(C + \frac{\tau_6}{\beta_k + \varepsilon}\right)^q,\ k = 0, 1, 2, 3, \tag{17}$$

where $C = 20$ and $q = 1$ are parameters, and the optimal weights $d_0 = \frac{1}{20}$, $d_1 = \frac{9}{20}$, $d_2 = \frac{9}{20}$, $d_3 = \frac{1}{20}$ guarantee that the combined scheme recovers to the standard sixth-order central scheme with 6-point stencil. The smoothness indicator β_3 is evaluated from the full 6-point stencil as

$$\begin{aligned}\beta_3 = \beta_6 = \frac{1}{120960}\Big[&271779 f_{i-2}^2 + f_{i-2}(-2380800 f_{i-1} + 4086352 f_i - 3462252 f_{i+1}\\ &+ 1458762 f_{i+2} - 245620 f_{i+3}) + f_{i-1}(5653317 f_{i-1} - 20427884 f_i\\ &+ 17905032 f_{i+1} - 7727988 f_{i+2} + 1325006 f_{i+3})\\ &+ f_i(19510972 f_i - 35817664 f_{i+1} + 15929912 f_{i+2} - 2792660 f_{i+3})\\ &+ f_{i+1}(17195652 f_{i+1} - 15880404 f_{i+2} + 2863984 f_{i+3})\\ &+ f_{i+2}(3824847 f_{i+2} - 1429976 f_{i+3}) + 139633 f_{i+3}^2\Big]\end{aligned} \tag{18}$$

rather than from the generic formula (12) with 3-point stencil. The basic idea is that the contribution of the downwind stencil should vanish as long as the full 6-point stencil contains a discontinuity. The new global reference smoothness indicator τ_6 is defined as

$$\tau_6 = \beta_6 - \frac{1}{6}(\beta_0 + \beta_2 + 4\beta_1), \tag{19}$$

where

$$\tau_6 = \mathcal{O}(\Delta x^6),\ \frac{\tau_6}{\beta_k + \varepsilon} = \mathcal{O}(\Delta x^4),\ k = 0, 1, 2, 3. \tag{20}$$

As $w_k - d_k = \mathcal{O}(\Delta x^4)$, the requirement for maintaining overall sixth-order accuracy is satisfied. Hu and Adams [24] further propose another modified version WENO-CU6-M with $C = 1000$ and $q = 4$ by incorporating a physically-motivated scale-separation mechanism. This larger integer power of the smoothness-measure serves to separate the marginally-resolved and non-resolved flow scales. Numerical results imply that the new scheme functions as a physically-consistent implicit SGS model while retaining the shock-capturing capability.

3. Construction of targeted ENO scheme

In this section, we introduce a family of targeted ENO schemes. The general procedure to construct arbitrarily high-order schemes is discussed first; we then design five-point and six-point stencil targeted ENO schemes in detail.

3.1. Systematic formulation of targeted ENO schemes

3.1.1. Candidate stencils with incremental width

In analogy with the classical WENO scheme, a set of candidate stencils has to be derived for the high-order reconstruction. A new approach, by which the high-order full stencil is constructed from low-order stencils with incrementally increasing width, is proposed as shown in Fig. 1. In addition to the first three-point stencil S_0, each candidate stencil with

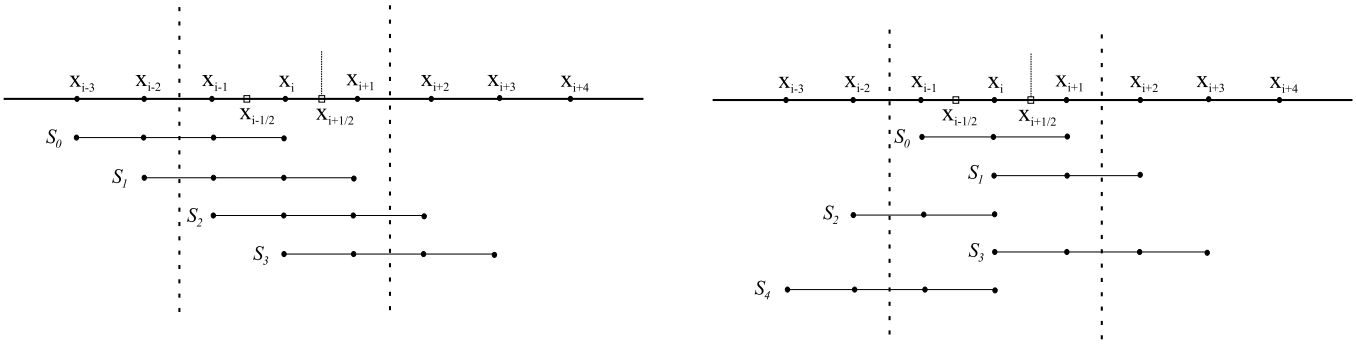

Fig. 2. Sketch of reconstruction schemes with closely located shock waves: the dashed lines represent two shock discontinuities. Classical 7th-order WENO scheme (left) and 7th-order TENO scheme (right).

Table 1
Numerical flux $\widehat{f}_{k,i+1/2} = \sum_m c_m f_m$ evaluated from the candidate stencil S_k.

$\widehat{f}_{k,i+1/2}$	c_{i-3}	c_{i-2}	c_{i-1}	c_i	c_{i+1}	c_{i+2}	c_{i+3}	c_{i+4}
$k=0$			$-\frac{1}{6}$	$\frac{5}{6}$	$\frac{2}{6}$			
$k=1$				$\frac{2}{6}$	$\frac{5}{6}$	$-\frac{1}{6}$		
$k=2$		$\frac{2}{6}$	$-\frac{7}{6}$	$\frac{11}{6}$				
$k=3$				$\frac{3}{12}$	$\frac{13}{12}$	$-\frac{5}{12}$	$\frac{1}{12}$	
$k=4$	$-\frac{3}{12}$	$\frac{13}{12}$	$-\frac{23}{12}$	$\frac{25}{12}$				
$k=5$				$\frac{12}{60}$	$\frac{77}{60}$	$-\frac{43}{60}$	$\frac{17}{60}$	$-\frac{3}{60}$

one end node at x_i contains at least one-point upwind, thus decreasing the strong anti-dissipation induced by a pure downwind stencil. In Fig. 2, we compare sketches for the reconstruction of 7th-order schemes for the classical WENO scheme and the proposed TENO scheme in the case of closely located two shock waves. For the classical WENO scheme all candidate stencils are crossed by the two discontinuities. The weighting strategy of the classical WENO schemes fails to guarantee the ENO property. However, for the TENO scheme the three-point candidate stencil S_0 avoids the crossing of discontinuities and thus can be singled out as smooth candidate stencil to contribute to the final reconstruction. Since practical numerical experiments reveal that fifth-order WENO scheme is robust for such configurations, the TENO schemes also can recover the robustness of fifth-order WENO scheme even for very-high-order reconstructions.

We redefine the symbol r as the width of a specific candidate stencil. Conservative numerical fluxes $\widehat{f}_{k,i+1/2}$ on different candidate stencils are evaluated with Eq. (7) in the same way as for WENO. The respective coefficients are presented in Table 1 up to $k=5$.

The sequence of stencil widths r of low-order candidate stencils k for maximum order $K \geq 3$ on the full stencil is given as

$$\{r_k\} = \begin{cases} \{\underbrace{3,3,3,4,\cdots,\frac{K+2}{2}}_{k=0,\cdots,K-3}\}, & \text{if } \mod(K,2)=0, \\ \{\underbrace{3,3,3,4,\cdots,\frac{K+1}{2}}_{k=0,\cdots,K-3}\}, & \text{if } \mod(K,2)=1. \end{cases} \tag{21}$$

In the context of a K-point full stencil, an order K reconstruction can be achieved by the stencil combination $\bigcup_{k=0}^{K-3} S_k$. A $(K+1)$-order scheme is reconstructed from the stencil combination $\bigcup_{k=0}^{K-3} S_k$ with one additional upwind or downwind-biased stencil S_{K-2}. Arbitrarily high-order odd (upwind) or even (central) schemes can be devised by this recursion. Optimal weights for maximum order up to $K=8$ on the full-point stencil are given in Table 2.

3.1.2. Scale separation

Motivated by Hu et al. [24] and Borges et al. [20], the smoothness measure is defined as

$$\gamma_k = \left(C + \frac{\tau_K}{\beta_{k,r} + \varepsilon}\right)^q, \; k = 0, \cdots, K-3, \tag{22}$$

where τ_K is the global reference smoothness indicator. We set $C=1$ and the integer power q is defined as a large value, typically $q=6$. With both WENO-Z and WENO-CU6, $q>1$ is avoided as the resulting strong adaptation introduces excessive nonlinear dissipation at intermediate and high wave numbers. WENO-CU6-M sets $q=4$ to incorporate

Table 2
Optimal weights for the upwind or central scheme for maximum order K.

Order	d_0	d_1	d_2	d_3	d_4	d_5
$K=3$	1					
$K=4$	$\frac{3}{6}$	$\frac{3}{6}$				
$K=5$	$\frac{6}{10}$	$\frac{3}{10}$	$\frac{1}{10}$			
$K=6$	$\frac{9}{20}$	$\frac{6}{20}$	$\frac{1}{20}$	$\frac{4}{20}$		
$K=7$	$\frac{18}{35}$	$\frac{9}{35}$	$\frac{3}{35}$	$\frac{4}{35}$	$\frac{1}{35}$	
$K=8$	$\frac{30}{70}$	$\frac{18}{70}$	$\frac{4}{70}$	$\frac{12}{70}$	$\frac{1}{70}$	$\frac{5}{70}$

The d_k represents the optimal weight for candidate stencil S_k to assemble a K-th order scheme.

a physically-motivated scale-separation mechanism while setting $C = 1000$ for compensation. Such a choice reduces the effectiveness of discontinuity detection, which in turn compromises the robustness in simulations with strong shock waves. On the contrary, larger integer power exponent q and smaller C are preferable for an even stronger separation between resolved and non-resolved scales in the present study. The discontinuity-detection capability is significantly enhanced rather than sacrificed. Low dissipation for smooth regions is maintained by a tailored ENO-like stencil selection in the next section.

$\beta_{k,r}$ can be evaluated following Jiang and Shu [9] as

$$\beta_{k,r} = \sum_{j=1}^{r-1} \Delta x^{2j-1} \int_{x_{i-1/2}}^{x_{i+1/2}} \left(\frac{d^j}{dx^j} \hat{f}_k(x) \right)^2 dx. \tag{23}$$

Taylor expansion of $\beta_{k,r}$ gives [17]

$$\beta_{k,r} = \sum_{\ell=1}^{\left\lfloor \frac{r+1}{2} \right\rfloor} Q_{\beta_{2\ell}}(x_i) \Delta x^{2\ell} + B_{\beta_{k,r}} \left(\frac{df}{dx} \frac{d^r f}{dx^r} \right) \Big|_{x=x_i} \Delta x^{r+1} + \mathcal{O}(\Delta x^{r+2}),\ r = 3, \cdots, \tag{24}$$

where the first term on the right hand side represents the common part for all stencils and $\lfloor\rfloor$ is the Gauss bracket. Provided that the flow is sufficiently smooth, the leading term of $\beta_{k,r}$ is $\mathcal{O}(\Delta x^2)$ for candidate stencils with different widths. In non-smooth regions, candidate stencils with larger width r are more likely to be crossed by discontinuities with $\beta_{k,r}$ of $\mathcal{O}(1)$. In this case the scheme is driven towards low-order reconstruction with smaller stencil-width. Since the first three stencils are the same as that of the classical fifth-order WENO-JS, the desirable robustness of WENO-JS is recovered in this case.

3.1.3. ENO-like stencil selection

The smoothness measure is normalized first as

$$\chi_k = \frac{\gamma_k}{\sum_{k=0}^{K-3} \gamma_k}, \tag{25}$$

and then subjected to a sharp cutoff function

$$\delta_k = \begin{cases} 0, & \text{if } \chi_k < C_T, \\ 1, & \text{otherwise.} \end{cases} \tag{26}$$

The cutoff ensures that a candidate stencil is fully suppressed for the final reconstruction if the measured smoothness is below a certain threshold, otherwise it is adopted with its original weight. The choice of the threshold C_T can be determined from a compromise between good spectral properties and numerical robustness for discontinuity detection through quasi-linear spectral analyses and numerical experiments respectively, and will be discussed in the subsequent sections.

Note that parameter C_T also provides an effective and direct means to control the spectral properties of the underlying scheme for specific problems, e.g. compressible turbulence simulation with embedded shocklets, demanding for extremely low dissipation and slight nonlinear adaption.

3.1.4. Assembled high-order reconstruction scheme

The optimal weights d_k subjected to the cut-off δ_k are re-normalized as

$$w_k = \frac{d_k \delta_k}{\sum_{k=0}^{K-3} d_k \delta_k}, \tag{27}$$

so that the contributions from stencils containing discontinuities vanish. The final K-th order reconstructed numerical flux evaluated at cell face $i + \frac{1}{2}$ is assembled as

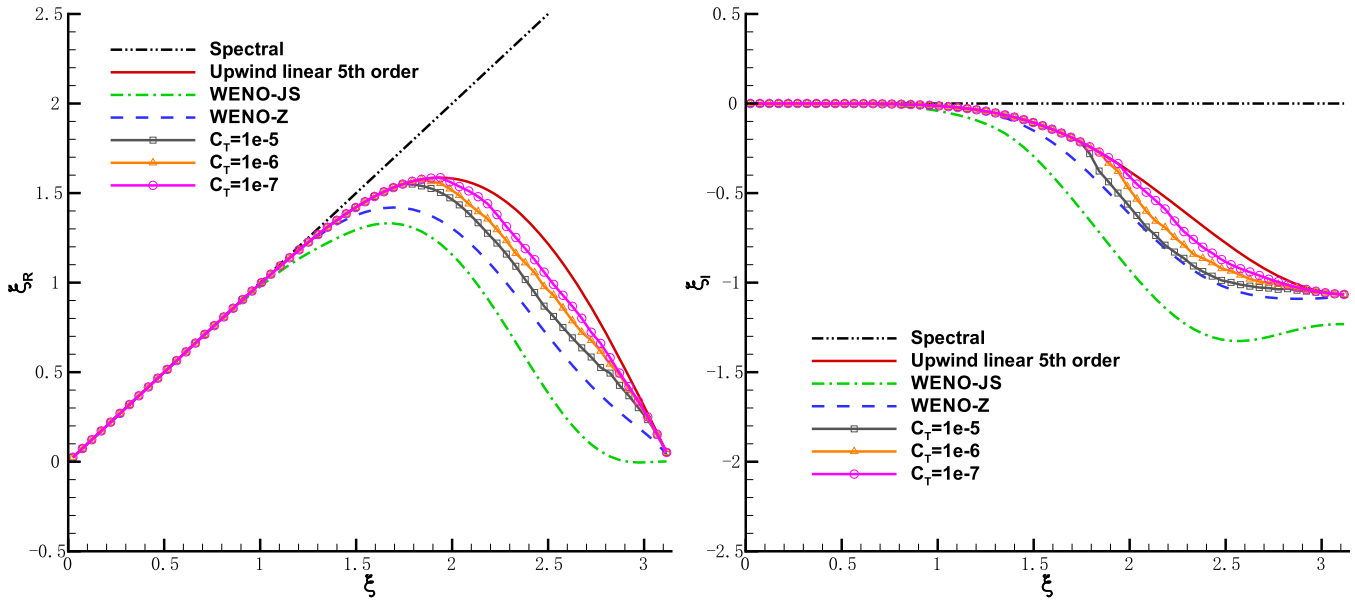

Fig. 3. Approximate dispersion and dissipation properties for five-point stencil schemes: dispersion (left) and dissipation (right).

$$\hat{f}^{K}_{i+1/2} = \sum_{k=0}^{K-3} w_k \hat{f}_{k,i+1/2}. \tag{28}$$

Since the δ_k function switches between 0 and 1, a smooth-transition from high-order to low-order through the weighting strategy is prevented. Nevertheless, the resulting scheme can achieve arbitrarily high-order accuracy while satisfying the ENO property. For this reason, we call the new scheme "targeted ENO" (TENO) scheme.

3.1.5. Formal order of accuracy in smooth regions

Due to the ENO-like stencil selection, a sufficient condition for the overall scheme to restore its formal order of accuracy in smooth regions is $\chi_k \geq C_T$, which can be satisfied by the condition that all γ_k converges to C of Eq. (22) when Δx approaches zero. It is equivalent to the condition

$$\frac{\tau_K}{\beta_{k,r} + \varepsilon} = O(\Delta x^s), \quad s > 0. \tag{29}$$

This is a much weaker condition than those required for previous WENO schemes [19,20,24]. Note that such condition leads to relative flexible choice of the global reference smoothness indicator τ_K, as given in the following subsections and Appendix A, which ameliorates the order-degeneration problem suffered by classical WENO schemes.

3.2. Fifth-order TENO scheme

For a five-point TENO scheme, the involved candidate stencils $\{S_0, S_1, S_2\}$ are the same as for the classical fifth-order WENO-JS scheme. $\{\beta_{0,3}, \beta_{1,3}, \beta_{2,3}\}$ are calculated from Eq. (13), and the fifth-order undivided difference τ_5 is taken from Eq. (14) in WENO-Z. It is easy to find that τ_5 satisfies the condition (29) for the formal order of accuracy in smooth regions even near critical points.

The spectral properties of various five-point stencil schemes are shown in Fig. 3, following the ADR analysis [16]. The fifth-order TENO schemes with different thresholds constant C_T have much better spectral resolution than the WENO-JS and the WENO-Z schemes for almost the entire wave-number range. The dispersion and dissipation property of the fifth-order linear scheme is recovered up to wave numbers 1.75, 1.85 and 1.95, with $C_T = 10^{-5}$, 10^{-6} and 10^{-7} respectively. The wave-resolution capability of the TENO scheme follows that of the background linear scheme for low to intermediate wave numbers, while nonlinear dissipation is restricted to the high wave-number region.

3.3. Sixth-order TENO scheme

Considering the six-point stencil TENO scheme, the candidate stencils $\{S_0, S_1, S_2, S_3\}$ with the stencil width r distribution $\{3, 3, 3, 4\}$ are quite different from that of the WENO-CU6 scheme with $\{3, 3, 3, 3\}$. Note that, unlike the smoothness indicator β_3 of the downwind stencil in WENO-CU6, $\{\beta_{0,3}, \beta_{1,3}, \beta_{2,3}, \beta_{3,4}\}$ is evaluated from Eq. (22) without exception. This simplification benefits from the new reconstruction approach, where candidate stencils with incremental width have at least one-point upwind. In this paper, Eq. (19) from WENO-CU6 is employed as sixth-order undivided difference τ_6. It is easy to find that τ_6 satisfies the condition (29) for the formal order of accuracy in smooth regions even near critical points.

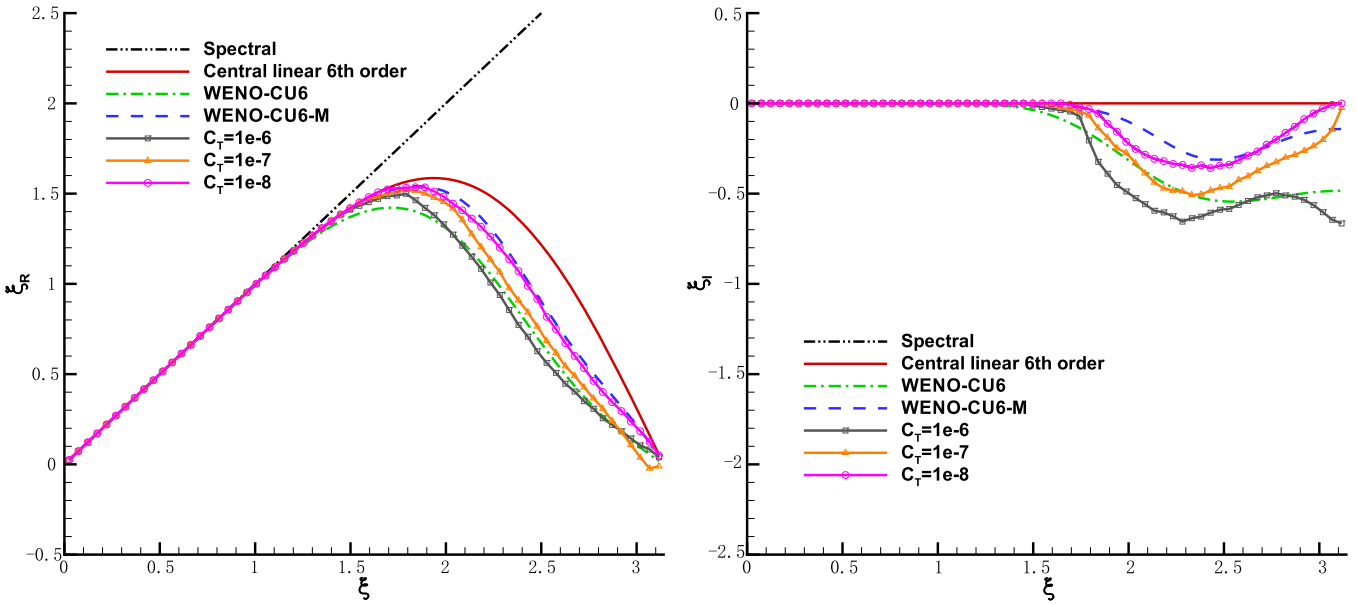

Fig. 4. Approximate dispersion and dissipation properties for six-point stencil schemes: dispersion (left) and dissipation (right).

Fig. 4 describes the spectral properties of various six-point stencil schemes. In comparison with the WENO-CU6 scheme, which departs from the linear scheme in both dispersion and dissipation at wave-number 1.2, the sixth-order TENO schemes delay the transition wave-number significantly. The TENO6 scheme with cutoff threshold C_T of 10^{-6} has the largest dissipation in high wave-number region, followed by WENO-CU6. WENO-CU6-M exhibits the lowest dispersion and dissipation among all the underlying six-point schemes.

4. Optimization of the TENO schemes

In this section, a generally effective optimization procedure of wave-resolution properties for both linear and nonlinear schemes is discussed. It is applied to the five- and six-point TENO schemes proposed in the previous section.

4.1. Guideline for optimizing linear and nonlinear schemes

Dissipation of the background linear scheme is a main dissipation source for the nonlinear shock-capturing scheme, so that low-dissipation and low-dispersion schemes always are preferable [26]. With an effective optimization strategy the generally-used traditional finite difference schemes can be optimized with respect to their dispersion and dissipation properties. Weirs and Candler [28] construct a six-point scheme with low dissipation and third-order accuracy by introducing the downwind stencil (WENO-SYMBO). Arshed and Hoffmann [22] propose the WENO-BO scheme by optimizing the weighted integral error for dispersion and dissipation within the intermediate wave-number region. However, both schemes produce anti-dissipation in the low to intermediate wave-number range, see Fig. 1 of [22].

Following Pirozzoli's ADR analysis [16], Hu et al. [25] propose a dispersion–dissipation relation for a general finite difference scheme to estimate the numerical dissipation necessary to damp spurious high wave-number errors from

$$\zeta = \frac{\left|\frac{d\xi_R}{d\xi} - 1\right|}{-\xi_I} \approx \mathcal{O}(10) \tag{30}$$

where ξ_R and ξ_I are the real and imaginary parts of the modified wave number for the non-resolved wave-number range. Although this relation is obtained from a linear analysis, application to nonlinear schemes is fairly straightforward. Thus it becomes a guideline for optimizing linear and nonlinear schemes to possess appropriate dissipation.

The dispersion–dissipation relation of various nonlinear schemes is shown in Fig. 5. Due to the excessive dissipation of the fifth-order upwind linear scheme, $\zeta \leqslant 5.5$ for all the nonlinear five-point schemes, indicating that they are free from spurious waves. High wave-number Fourier modes supported by the utilized mesh resolution are rapidly damped, especially for the classical fifth-order WENO-JS, as ζ decreases rapidly in the high wave-number region. WENO-Z and TENO5 produce relatively smaller dissipation but still are too dissipative, e.g., for turbulence simulations. For the purpose of implicit large eddy simulations, as clarified by Zhao et al. [14], no notable advantages of the improved WENO-Z could be found compared with WENO-JS.

For the six-point stencil schemes, $\zeta \approx \mathcal{O}(100)$ between wave-number 1.1 and 1.8, as the background sixth-order central scheme is non-dissipative. For preventing the proliferation of numerical errors owing to nonlinear transport, it is crucial

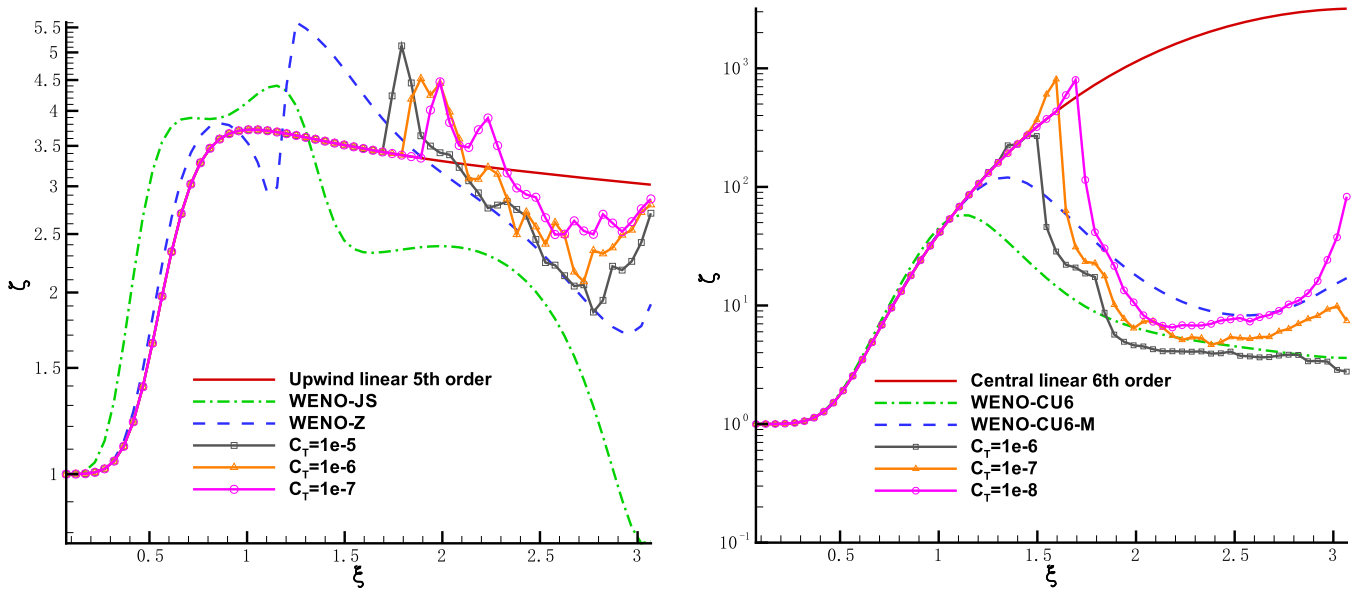

Fig. 5. Approximate dispersion–dissipation relation for various nonlinear schemes: five-point stencil schemes (left) and six-point stencil schemes (right). y axis is in log form and $\zeta = \frac{\left|\frac{d\tilde{\xi}_R}{d\xi} - 1\right| + 10^{-3}}{-\xi_I + 10^{-3}}$ approximately.

Table 3
Optimal weights based on the dispersion–dissipation condition for five-point-stencil schemes.

η	d_0	d_1	d_2
0.35	0.5875	0.325	0.0875
0.30	0.5750	0.350	0.0750
0.25	0.5625	0.375	0.0625
0.20	0.5500	0.400	0.0500

to properly balance the dissipation and dispersion by a reasonable choice of ζ, so that physically-consistent schemes could be obtained. An interesting observation is that the ζ distributions of both WENO-SYMBO and WENO-BO apparently fail to satisfy the dispersion–dissipation relation [29].

Here, we present a simple way to optimize the background scheme following an appropriate dispersion–dissipation relation. Instead of minimizing the dispersion errors, an order K scheme can be optimized by assembling two sub-schemes of order $(K-1)$ as

$$f^{opt}_{i+\frac{1}{2}} = \eta g^{K-1}_{i+\frac{1}{2}}(1) + (1-\eta) g^{K-1}_{i+\frac{1}{2}}(2). \tag{31}$$

For even K, the sub-schemes are upwind biased and downwind biased featuring the same dispersion errors. Since the two sub-schemes have the same dispersion error, the optimization procedure adjusts dissipation only to achieve the optimization objective. On the other hand, for odd K, the dispersion error also is affected as the sub-schemes possess different dispersion properties. The combination of these two schemes leads to lower dissipation than the order K standard scheme while introducing extra dispersion errors. Since ζ is the optimization objective function, such slightly increased dispersion errors are tolerated and do not pollute the solution according to [25].

4.2. Optimization of the fifth-order TENO scheme

Based on the five-point stencil, the two fourth-order sub-schemes are given as

$$\begin{aligned} g^4_{i+\frac{1}{2}}(1) &= \tfrac{1}{12}(f_{i-2} - 5f_{i-1} + 13f_i + 3f_{i+1}), \\ g^4_{i+\frac{1}{2}}(2) &= \tfrac{1}{12}(-f_{i-1} + 7f_i + 7f_{i+1} - f_{i+2}), \end{aligned} \tag{32}$$

where $g^4_{i+\frac{1}{2}}(1)$ is an upwind scheme and $g^4_{i+\frac{1}{2}}(2)$ is a central non-dissipative scheme. The combined overall scheme recovers the classical upwind fifth-order scheme when $\eta = 0.4$. Gradually decreasing η drives the overall scheme biased towards a central scheme as shown in Table 3, which gives the corresponding optimal weights for incremental-width stencils. The spectral property of these optimized schemes is shown in Fig. 6. As η decreases from 0.35 to 0.2, the dissipation property is greatly improved, and the extremum of ζ increases from approximately 5.5 to 16.5, maintaining order $\mathcal{O}(10)$.

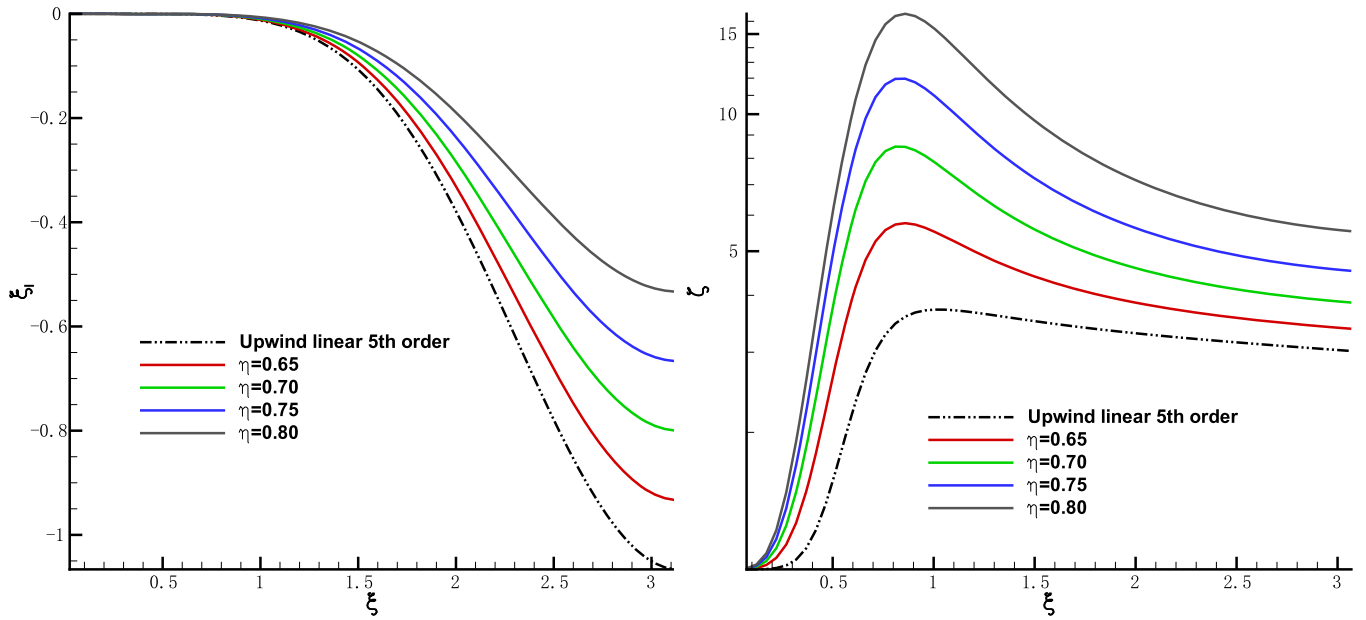

Fig. 6. Spectral properties of the optimized linear five-point stencil schemes: dissipation (left) and dispersion–dissipation relation (right).

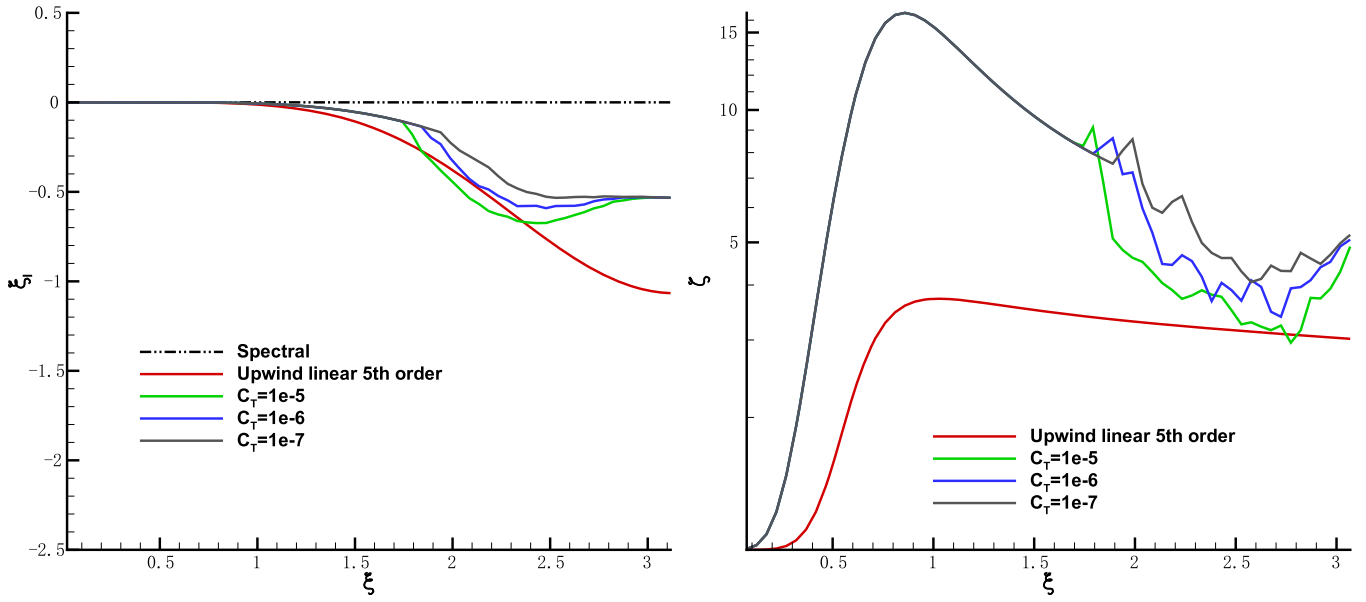

Fig. 7. Spectral property of optimized nonlinear five-point stencil schemes: dissipation property (left) and dispersion–dissipation relationship (right).

A straightforward implementation of optimal weights with $\eta = 0.2$ to the nonlinear TENO scheme proposed in previous section results in a nonlinear five-point optimized TENO scheme. As illustrated in Fig. 7, the nonlinear procedure induces extra dissipation only at high wave numbers and further decreases ζ in this region. The overall nonlinear TENO5 scheme is less dissipative than a classical fifth-order linear scheme especially for intermediate wave numbers, thus it is expected to resolve significantly more flow scales.

4.3. Optimization of the sixth-order TENO scheme

The two fifth-order sub-schemes for a six-point stencil are given as

$$g^5_{i+\frac{1}{2}}(1) = \frac{1}{60}(2f_{i-2} - 13f_{i-1} + 47f_i + 27f_{i+1} - 3f_{i+2}),$$
$$g^5_{i+\frac{1}{2}}(2) = \frac{1}{60}(-3f_{i-1} + 27f_i + 47f_{i+1} - 13f_{i+2} + 2f_{i+3}). \tag{33}$$

As $g^5_{i+\frac{1}{2}}(1)$ and $g^5_{i+\frac{1}{2}}(2)$ possess the same dispersion property as the standard sixth-order central scheme the combined overall scheme maintains the dispersion errors. Compared to $\eta = 0.5$ which leads to a non-dissipative central scheme, the

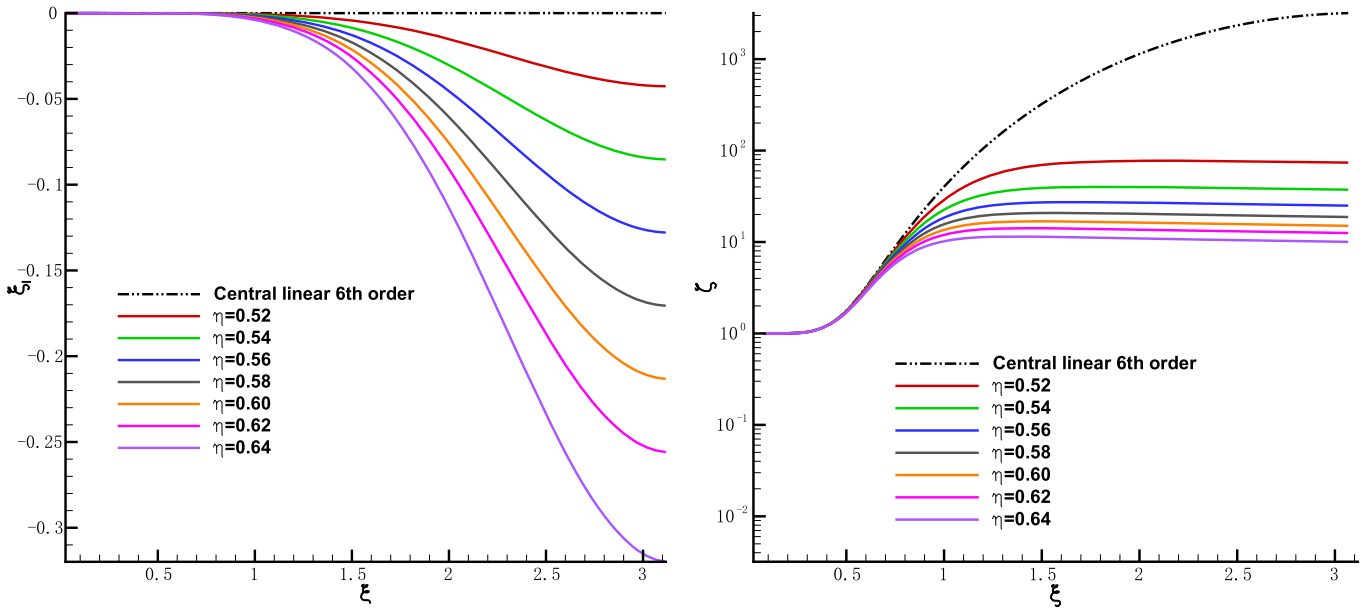

Fig. 8. Spectral properties of optimized linear six-point stencil schemes: dissipation property (left) and dispersion–dissipation relation (right).

Table 4
Optimal weights based on the dispersion–dissipation condition for six-point-stencil schemes.

η	d_0	d_1	d_2	d_3
0.52	0.456	0.3	0.052	0.192
0.54	0.462	0.3	0.054	0.184
0.56	0.468	0.3	0.056	0.176
0.58	0.474	0.3	0.058	0.168
0.60	0.480	0.3	0.060	0.160
0.62	0.486	0.3	0.062	0.152
0.64	0.492	0.3	0.064	0.144

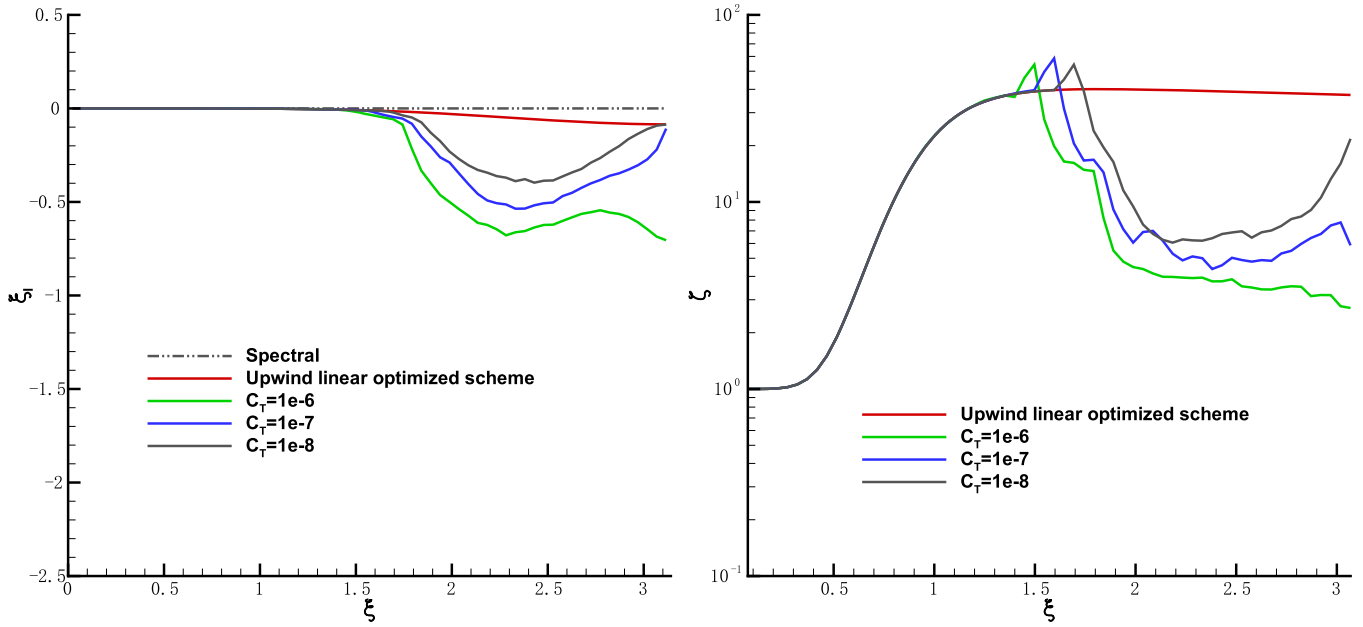

Fig. 9. Spectral properties of the optimized nonlinear six-point stencil schemes: dissipation (left) and dispersion–dissipation relation (right).

overall scheme exhibits correspondingly increasing dissipation with increasing η. Table 4 addresses the optimal weights for increasing stencil widths with specific η. Fig. 8 shows the optimized spectral properties. Note that ζ exhibits a nonlinear growth tendency with decreasing η.

Table 5
Parameters of TENO-family schemes for numerical validation.

Scheme	d_0	d_1	d_2	d_3	C	q	C_T
TENO5	0.600	0.300	0.100	/	1.0	6	10^{-5}
TENO5-opt	0.550	0.400	0.050	/	1.0	6	10^{-5}
TENO6	0.450	0.300	0.050	0.200	1.0	6	10^{-7}
TENO6-opt	0.462	0.300	0.054	0.184	1.0	6	10^{-7}

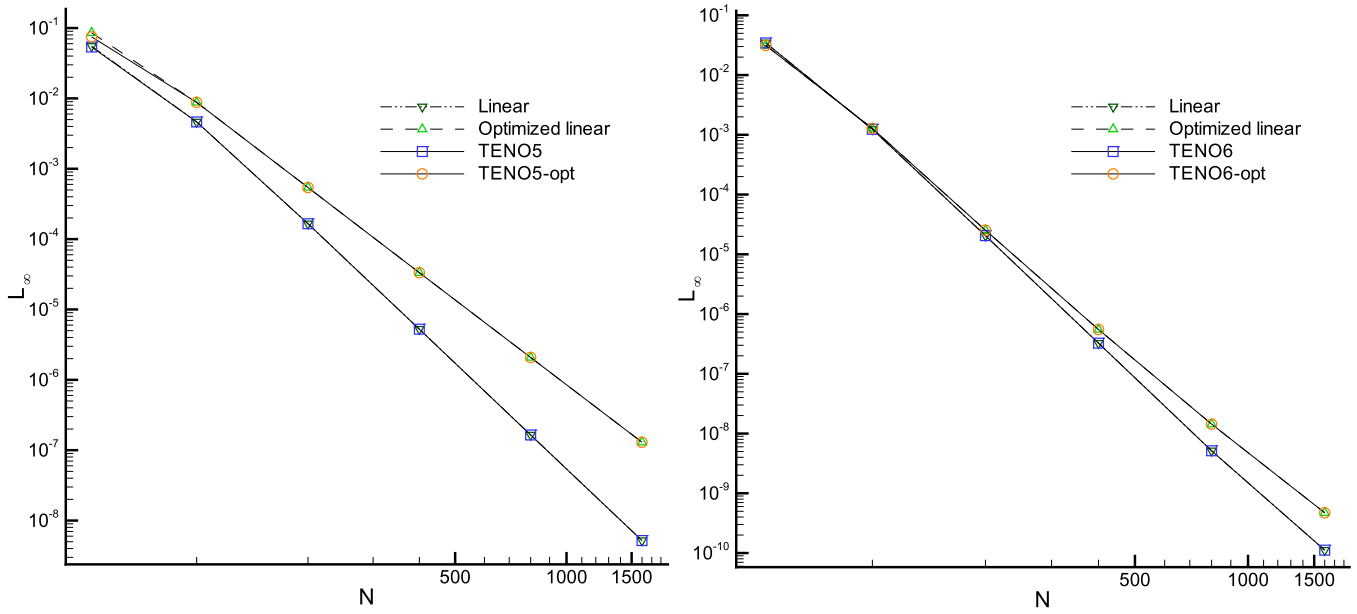

Fig. 10. Convergence of the L_∞-error: five-point stencil schemes (left) and six-point stencil schemes (right). The linear scheme represents the maximum-order background scheme of TENO and the optimized linear scheme represents the spectrally optimized background scheme of optimized TENO.

Rather than as shown in [25] the optimized fifth-order linear scheme is obtained by enforcing the constraint $\zeta = 10$ at $\xi = 1.302$ according to Eq. (30). Full-stencil scheme is constructed with $\eta = 0.54$ implying less dissipation. The spectral properties of the optimized nonlinear six-point TENO schemes is shown in Fig. 9. Throughout the entire wave-number range $\zeta \leq 35$, and decreases to less than 10 at high wave numbers.

5. Numerical validation

A variety of benchmark problems is considered to assess the proposed schemes. Compressible Navier–Stokes equations and Euler equations are applied as physical models for viscous and inviscid flow simulations. The ideal-gas equation of state $p = (\gamma - 1)\rho e$ with $\gamma = 1.4$ is adopted to close the conservation laws. As a default setting, the Roe average is exploited for characteristic decomposition at the cell face, and the Global Lax–Friedrichs (GLF) is utilized for flux splitting. For one-dimensional cases uniformly distributed grid points are used and the 3rd-order strongly stable Runge–Kutta [34] scheme is chosen for time integration. For two-dimensional cases the wavelet-based multi-resolution method [35] is applied with the 2nd-order strongly stable Runge–Kutta scheme [34]. The fifth-order and sixth-order TENO schemes are compared with the well-validated WENO-JS, WEMO-Z, WENO-CU6 and WENO-CU6-M comprehensively. In all computations, a single set of parameters as given in Table 5 and a CFL number of 0.6 are applied.

5.1. Linear advection problem

We first consider the one-dimensional Gaussian pulse advection problem [36] to validate the numerical order of proposed schemes. The linear advection equation

$$\frac{\partial u}{\partial t} + \frac{\partial u}{\partial x} = 0, \tag{34}$$

with initial condition

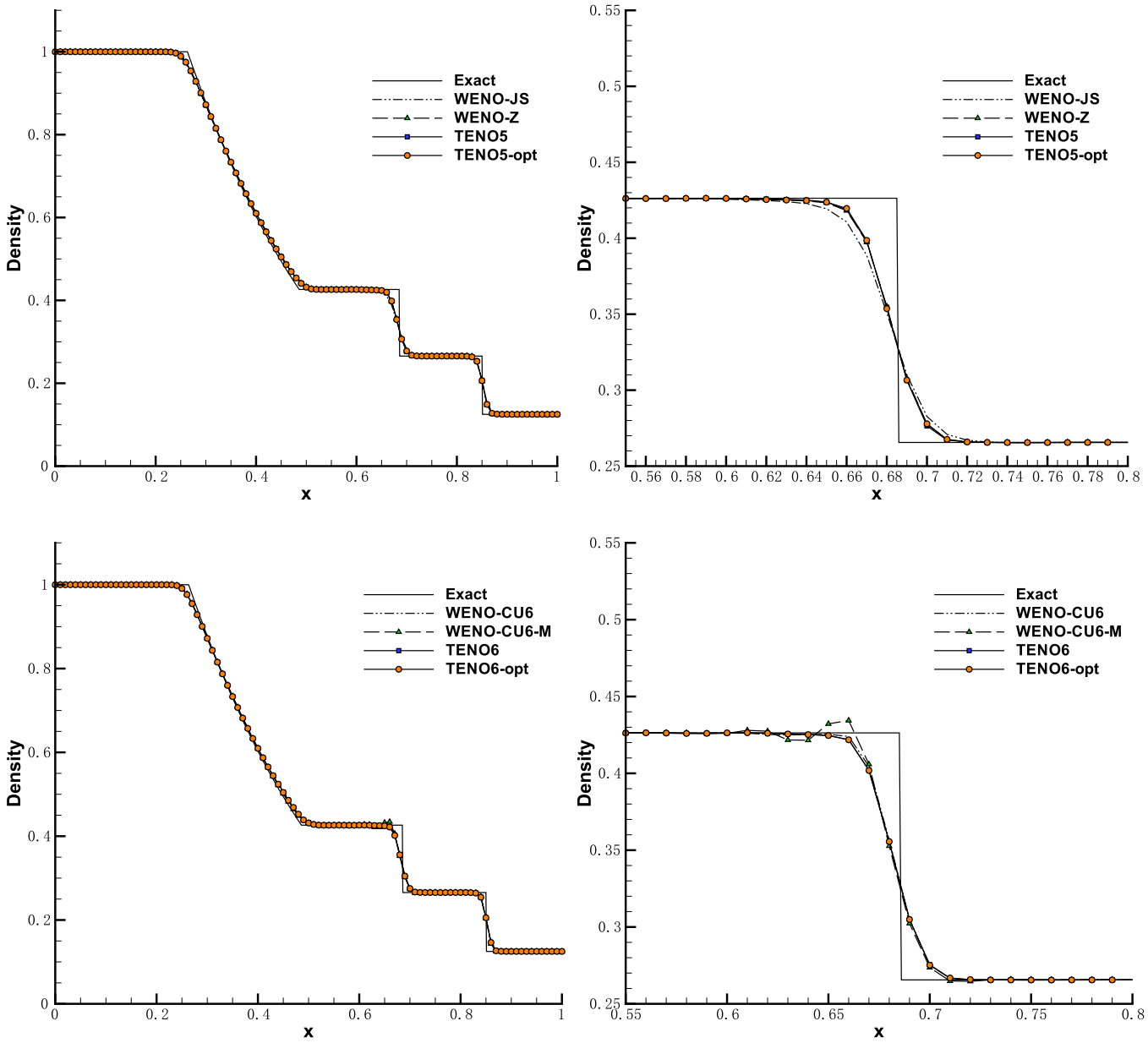

Fig. 11. Sod shock-tube problem: density distribution (left) and a zoom of the region near contact discontinuity (right). Top: five-point stencil schemes. Bottom: six-point stencil schemes. Discretization on 100 uniformly distributed grid points. "Exact" represents the theoretical solution of the Riemann problem.

$$u_0(x) = e^{-300(x-x_c)^2},\ x_c = 0.5, \tag{35}$$

is solved on a computational domain $0 \le x \le 1$.

Periodic boundary conditions are imposed at $x = 0$ and $x = 1$. The solution is advanced to $t = 1$ corresponding to one period in time, and a sequence of globally refined uniform grids is employed to investigate the L_∞-error convergence. The timestep is decreased so that the time-integration error can be neglected. As shown in Fig. 10, the L_∞-error convergence histories of all proposed TENO schemes coincide with their corresponding background linear schemes and therefore the desirable order of accuracy is achieved. Order-degeneration and instability of the classical WENO schemes, as shown in [36], are overcome. As expected, both the optimized linear and nonlinear schemes are by one order less accurate than the maximum-order accuracy standard schemes.

5.2. Shock-tube problem

Two typical shock-tube test problems, i.e. the Sod problem taken from [37] and the Lax problem from [38], are simulated to validate the shock-capturing capability of proposed schemes.

The initial condition for the Sod problem is

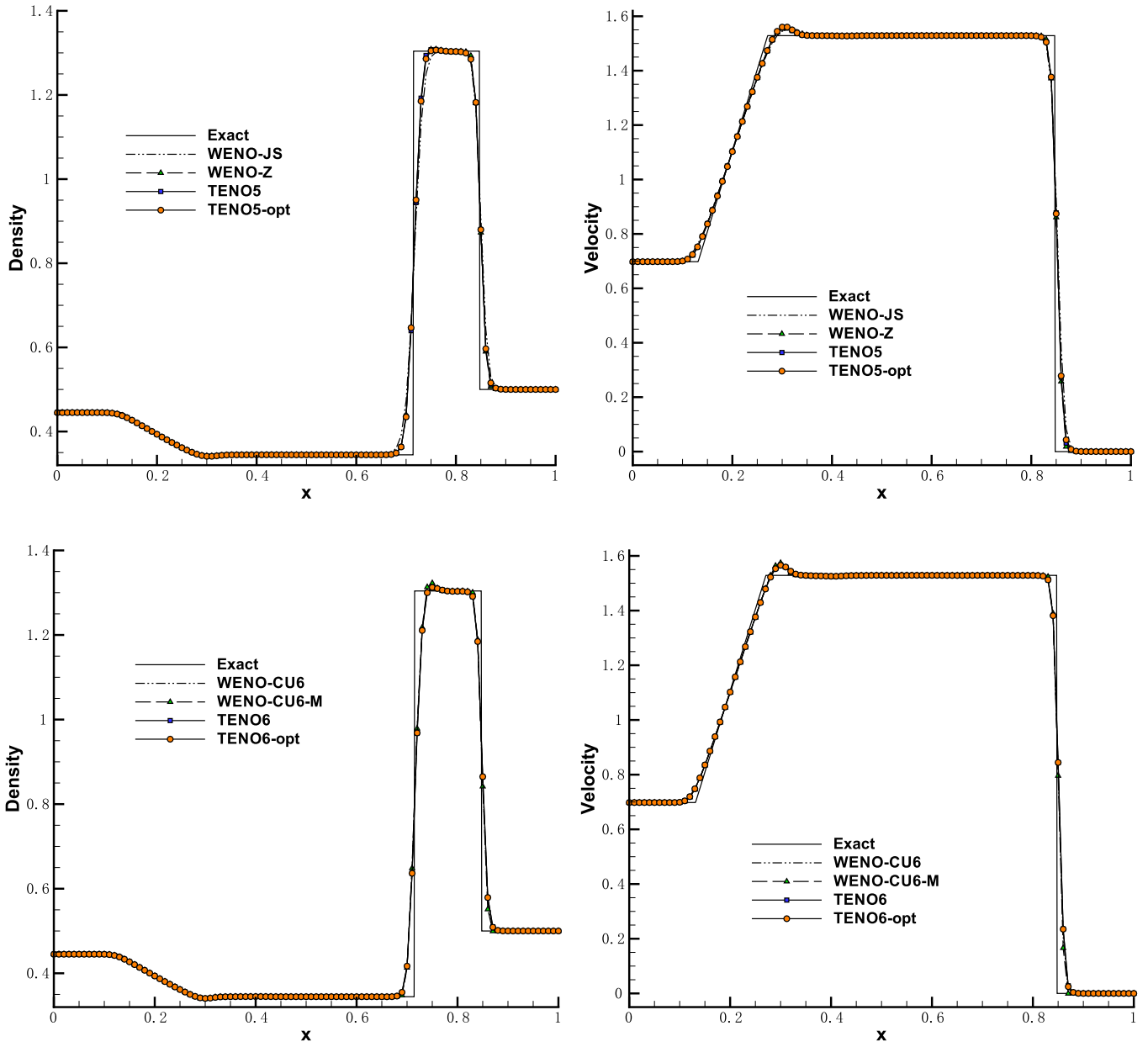

Fig. 12. Lax shock-tube problem: density distribution (left) and velocity distribution (right). Top: five-point stencil schemes. Bottom: six-point stencil schemes. Discretization on 100 uniformly distributed grid points. "Exact" represents the theoretical solution of the Riemann problem.

$$(\rho, u, p) = \begin{cases} (1, 0, 1), & \text{if } 0 \le x < 0.5, \\ (0.125, 0, 0.1), & \text{if } 0.5 \le x \le 1, \end{cases} \tag{36}$$

and the final simulation time is $t = 0.2$.

Fig. 11 shows the computed density distribution from five-point and six-point stencil schemes. The solutions from WENO-Z, TENO5 and TENO5-opt are obviously better than that of WENO-JS in resolving the contact discontinuity. The shock wave is captured stably and no overshoots or oscillations can be observed. Considering the six-point stencil schemes, slight oscillations appear near the contact discontinuity for WENO-CU6-M. TENO6 and TENO6-opt perform as well as WENO-CU6.

The initial condition for the Lax problem is

$$(\rho, u, p) = \begin{cases} (0.445, 0.689, 3.528), & \text{if } 0 \le x < 0.5, \\ (0.5, 0, 0.5710), & \text{if } 0.5 \le x \le 1, \end{cases} \tag{37}$$

and the final simulation time is $t = 0.14$.

Fig. 12 gives a comparison of the computed density and velocity distribution. WENO-JS exhibits marginally larger dissipation than the others while WENO-CU6-M produces slight overshoots for the density profile near the contact discontinuity. All schemes preserve monotonicity near the shock wave.

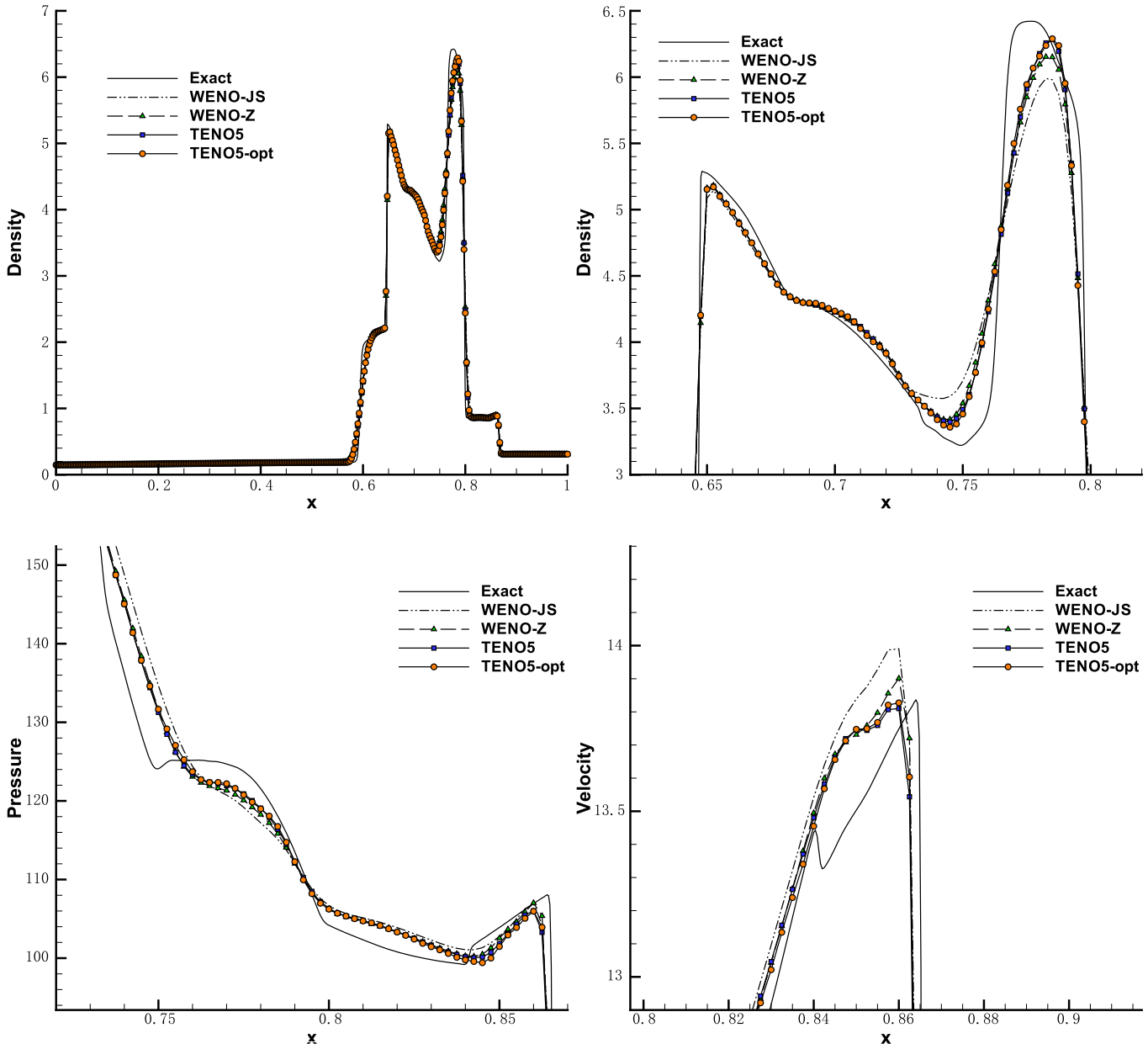

Fig. 13. Interacting blast waves problem: solution from five-point stencil schemes. Top: density distribution (left) and a zoom of the density profile (right). Bottom: zoom of the pressure profile (left) and zoom of the velocity profile (right). Discretization on 400 uniform grid points.

5.3. Interacting blast waves

The two-blast-wave interaction taken from Woodward and Colella [39] is considered. The initial condition is

$$(\rho, u, p) = \begin{cases} (1, 0, 1000), & \text{if } 0 \le x < 0.1, \\ (1, 0, 0.01), & \text{if } 0.1 \le x < 0.9, \\ (1, 0, 100), & \text{if } 0.9 \le x \le 1. \end{cases} \tag{38}$$

A reflective boundary condition is imposed at $x = 0$ and $x = 1$. The simulation is performed on a uniform mesh with $N = 400$ until final time $t = 0.038$. The reference "exact" solution is produced by the fifth-order WENO-JS scheme on a uniform mesh with $N = 2500$. A Roe scheme with entropy-fix is applied for evaluating the numerical flux.

In terms of five-point stencil schemes, TENO5 and TENO5-opt resolve the density profile much better than WENO-JS, especially near the valley $x = 0.75$ and the right peak $x = 0.78$ in Fig. 13. Furthermore, TENO5 and TENO5-opt exhibit less dissipation than WENO-Z, which can be seen at $x = 0.78$. For the pressure profile, TENO5 and TENO5-opt again provide much better results. With respect to the velocity profile, WENO-JS and WENO-Z produce strong overshoots near $x = 0.86$ while TENO5 and TENO5-opt perform well. Fig. 14 depicts the calculated results from six-point stencil schemes. Except that WENO-CU6-M fails to pass this case, the other three schemes provide an overall better result than that of five-point

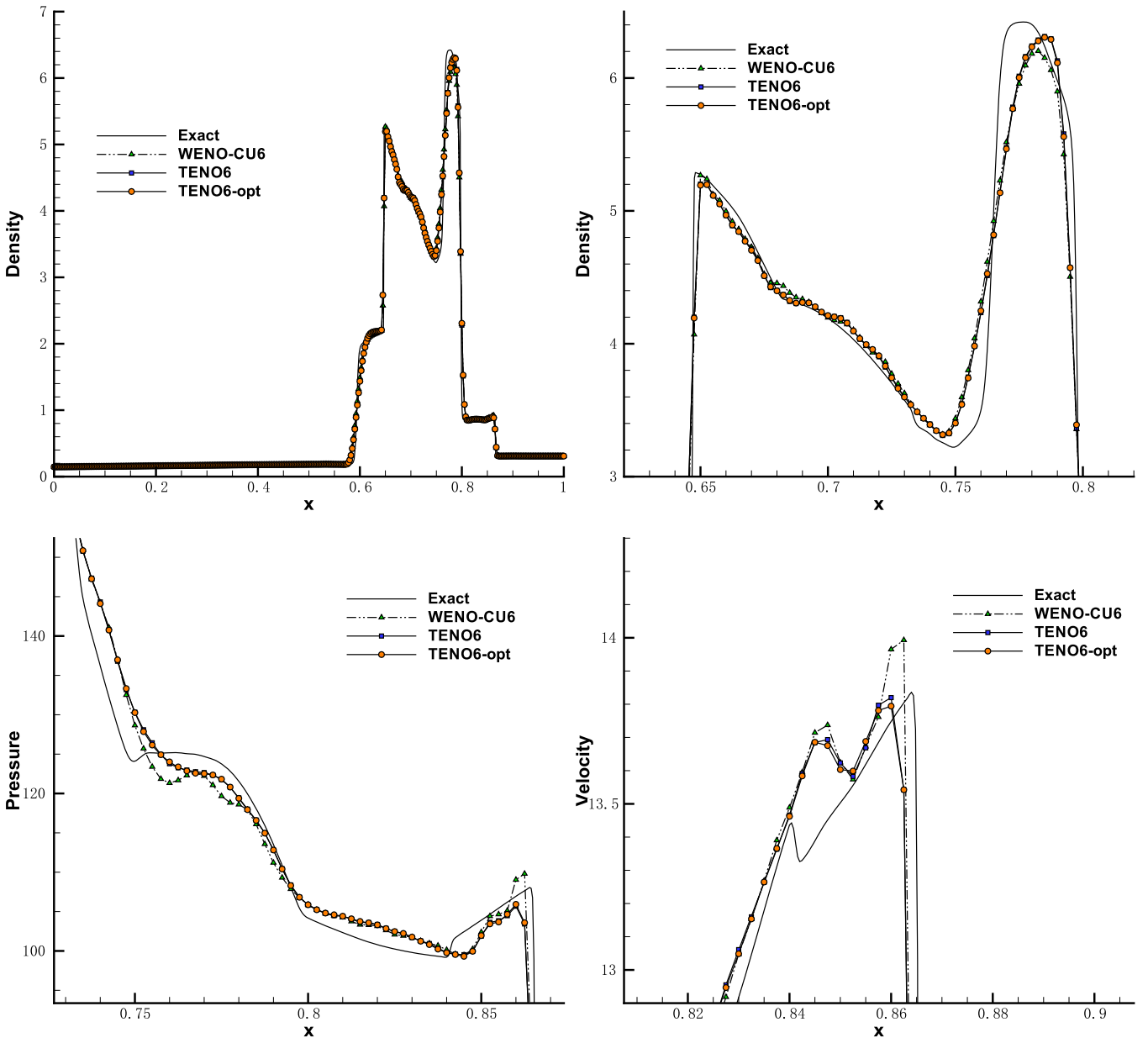

Fig. 14. Interacting blast waves problem: solution from six-point stencil schemes. Top: density distribution (left) and a zoom of the density distribution (right). Bottom: zoom of the pressure profile (left) and zoom of the velocity profile (right). Discretization on 400 uniform grid points. WENO-CU6-M fails to pass this case.

stencil schemes. WENO-CU6 produces spurious waves near $x = 0.75$ and $x = 0.86$ in the pressure profile, and overshoots at $x = 0.86$ in the velocity distribution. TENO6 and TENO6-opt however do not exhibit such spurious oscillations and resolve the density profile better at $x = 0.78$.

5.4. Shock–density wave interaction

This case is proposed by Shu and Osher [40]. A one-dimensional Mach 3 shock wave interacts with a perturbed density field generating both small-scale structures and discontinuities, hence it is selected to validate shock-capturing and wave-resolution capability. The initial condition is given as

$$(\rho, u, p) = \begin{cases} (3.857, 2.629, 10.333), & \text{if } 0 \le x < 1, \\ (1 + 0.2\sin(5x), 0, 1), & \text{if } 1 \le x \le 10. \end{cases} \tag{39}$$

The computational domain is $[0, 10]$ with $N = 200$ uniformly distributed mesh cells and the final evolution time is $t = 1.8$. The reference "exact" solution is obtained by the fifth-order WENO-JS scheme with $N = 2000$.

As shown in Fig. 15, all schemes are capable of capturing the acoustic waves with shocklets successfully. Concerning the entropy waves, significant improvements can be observed from the new proposed schemes. Specifically, TENO5-opt shows

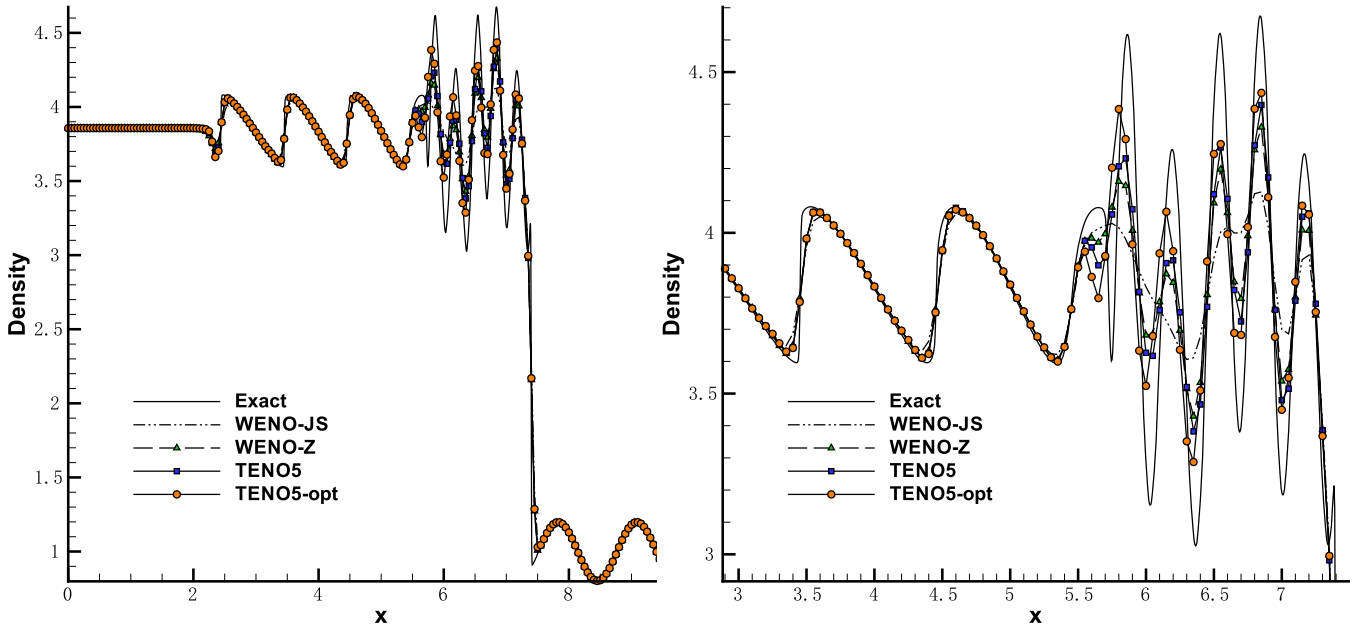

Fig. 15. Shock–density wave interaction problem: solutions from five-point stencil schemes. Density distribution (left) and a zoom of the density distribution (right). Discretization on 200 uniformly distributed grid points.

the best resolution in maintaining the amplitudes of density waves, followed by TENO5, and then WENO-Z. The WENO-JS scheme smears the flow features substantially exhibiting the largest dissipation. For capturing the shock waves, TENO5 and TENO5-opt produce slightly better results than WENO-JS scheme as well. This implies that TENO5 and TENO5-opt feature much better wave-resolution properties and shock-capturing capability than the WENO-JS scheme. For six-point stencil schemes, numerical results further improve as indicated in Fig. 16. It can be noticed that TENO6, TENO6-opt and WENO-CU6-M are less dissipative than WENO-CU6. TENO6 obtains qualitatively almost the same result as WENO-CU6-M, retaining the entropy wave amplitude up to 4.52 which is higher than that of TENO5-opt at about 4.4. In terms of the shock region, WENO-CU6 and WENO-CU6-M suffer from slight numerical oscillations for both density and velocity profiles. TENO6 and TENO6-opt are free from such spurious waves while sharply capturing the shock waves.

5.5. Double Mach reflection of a strong shock

This two-dimensional case is taken from Woodward and Colella [39]. The initial condition is

$$(\rho, u, v, p) = \begin{cases} (1.4, 0, 0, 1), & \text{if } y < 1.732(x - 0.1667), \\ (8, 7.145, -4.125, 116.8333), & \text{otherwise.} \end{cases} \tag{40}$$

The computational domain is $[0, 4] \times [0, 1]$ and the final simulation time is $t = 0.2$. Initially, a right-moving Mach 10 shock wave is placed at $x = 0.1667$ with an incidence angle of 60° to the x-axis. The post-shock condition is imposed from $x = 0$ to $x = 0.1667$ whereas a reflecting wall condition is enforced from $x = 0.1667$ to $x = 4$ at the bottom. For the top boundary condition, the fluid variables are defined as to exactly follow the evolution of the Mach 10 shock wave. Generic inflow and outflow conditions are imposed for the left and right side of the computational domain. An adaptive multi-resolution mesh [35] is applied with the effective resolution of 1024×256, i.e. grid space $\Delta x = \Delta y = 1/256$.

As described in Fig. 17 and Fig. 18, only the domain region $[2, 3] \times [0, 0.9]$ is presented for the facilitation of comparison. Except that WENO-CU6-M fails the simulation, other schemes reproduce the solutions having significant differences in the region around the double Mach stems. Among all the five-point stencil schemes, TENO5-opt resolves the finest small-scale structures and the strongest wall jet, which are comparable to that from the fifth-order WENO-JS scheme at resolution $\Delta x = \Delta y = 1/960$, see Fig. 1 in [41], followed by TENO5. When considering the results from TENO6, TENO6-opt and WENO-CU6, remarkable improvements in resolving small-scale structures can be observed in Fig. 18. Specifically, TENO6 produces the richest small-scale structures, comparable to that from the ninth-order WENO-JS scheme at resolution $\Delta x = \Delta y = 1/960$, see Fig. 1 in [41]. TENO6-opt resolves slightly less structures than TENO6 due to the dissipation added in the optimization procedure. Nevertheless, the result is still much better than that of WENO-CU6.

5.6. Rayleigh–Taylor instability

As another canonical problem, which contains both discontinuities and complex flow structures, the inviscid Rayleigh–Taylor instability case proposed by Xu and Shu [42] is considered. The initial condition is

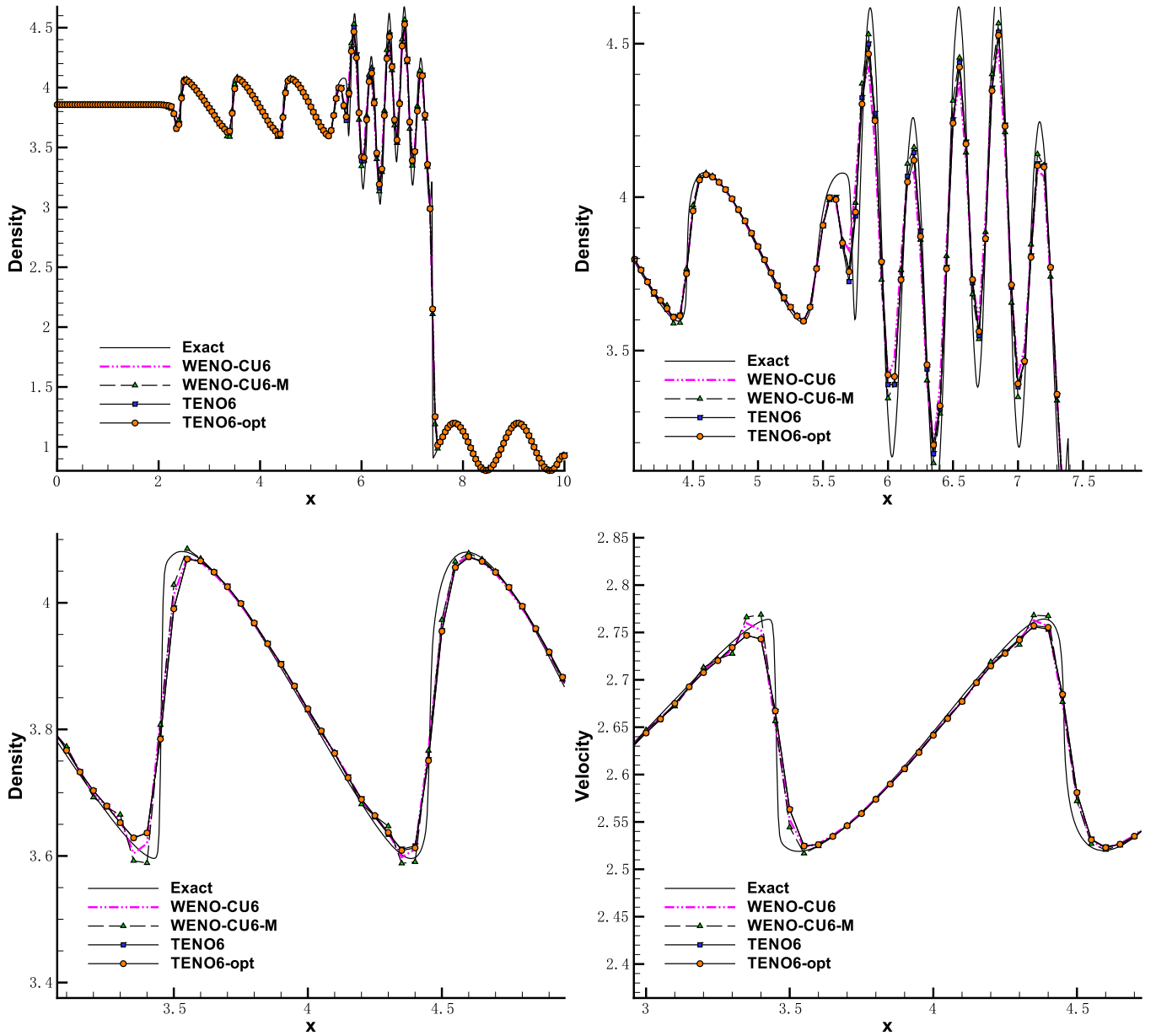

Fig. 16. Shock–density wave interaction problem: solutions from six-point stencil schemes. Top: density distribution (left) and a zoom of the density distribution (right). Bottom: zoom of the density profile (left) and zoom of the velocity profile (right). Discretization on 200 uniformly distributed grid points.

$$(\rho, u, v, p) = \begin{cases} (2, 0, -0.025c\cos(8\pi x), 1 + 2y), & \text{if } 0 \le y < 1/2, \\ (1, 0, -0.025c\cos(8\pi x), y + 3/2), & \text{if } 1/2 \le y \le 1, \end{cases} \tag{41}$$

where the sound speed is $c = \sqrt{\gamma \frac{p}{\rho}}$ with $\gamma = \frac{5}{3}$. The computational domain is $[0, 0.25] \times [0, 1]$. Reflective boundary conditions are imposed at the left and right side of the domain. Constant primitive variables $(\rho, u, v, p) = (2, 0, 0, 1)$ and $(\rho, u, v, p) = (1, 0, 0, 2.5)$ are set for the bottom and top boundaries, respectively. Initially, the interface located at $y = 0.5$ separates the heavy and light fluid, forming a contact discontinuity. For inviscid simulation solving Euler equations, the smaller magnitude of numerical dissipation from high-order shock-capturing scheme results in richer fine structures.

Fig. 19 shows the solutions from all 8 schemes at a resolution 128×512, i.e. grid space $\Delta x = \Delta y = 1/512$. TENO5-opt and TENO5 have resolved much richer vortical structures than WENO-JS and WENO-Z. Furthermore, the low-dissipation property of TENO5-opt and TENO5 induce symmetry breaking of flow field. A more dissipative scheme is more likely to preserve this symmetry even when increasing the resolution significantly, see Fig. 2 in [41]. For six-point stencil schemes, further improved results are obtained especially with TENO6, TENO6-opt and WENO-CU6-M. When the mesh resolution is doubled in both coordinate directions, the solution from WENO-CU6 also loses symmetry in Fig. 20. Another noticeable outcome is that small structures resolved from TENO5-opt and TENO5 with resolution of 128×512 are comparable to that from WENO-JS and WENO-Z with resolution of 256×1024.

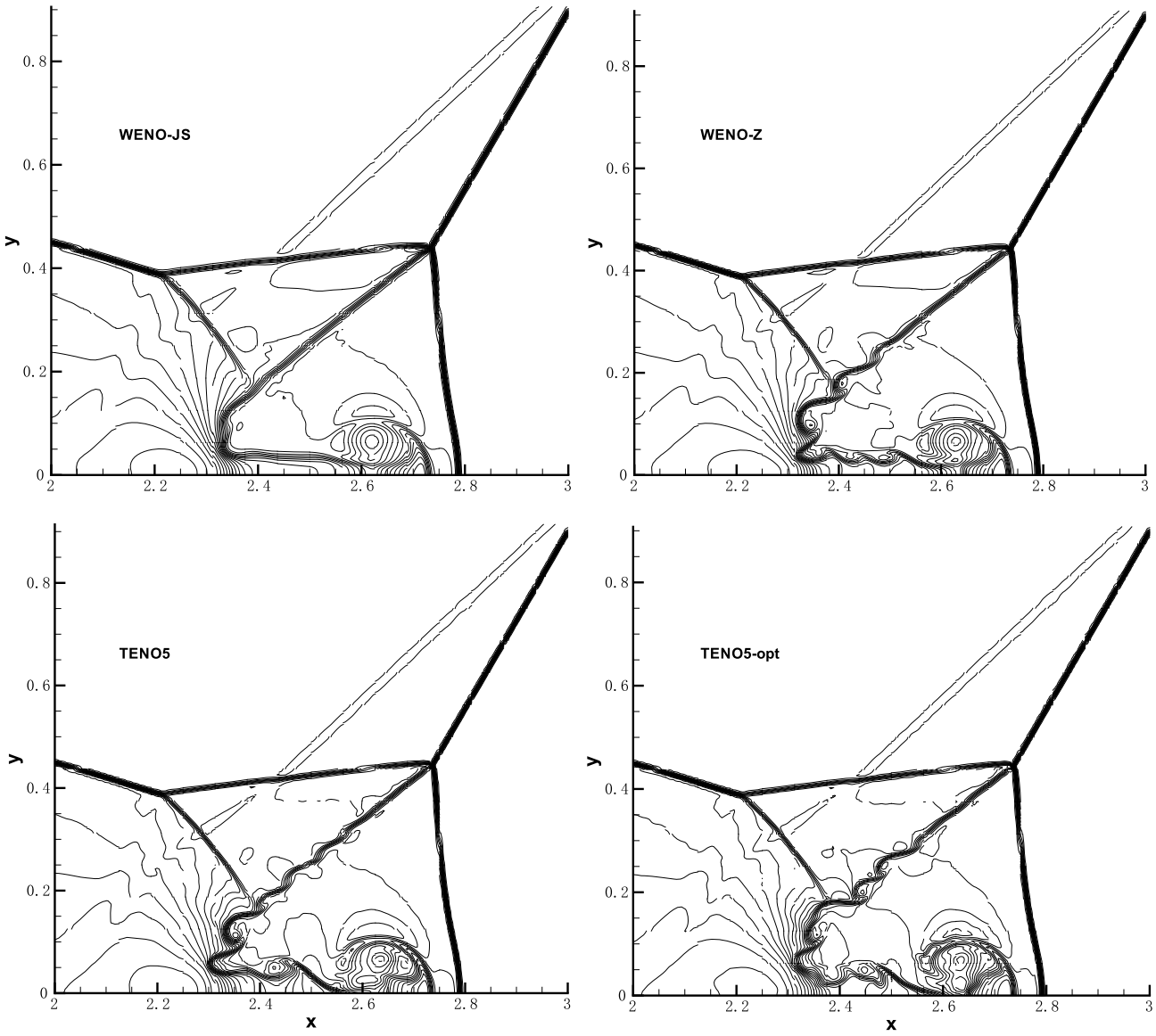

Fig. 17. Double Mach reflection of a strong shock: density contours from five-point stencil schemes. Resolution 1024×256. This figure is drawn with 43 density contours between 1.887 and 20.9.

5.7. Two-dimensional viscous shock-tube problem

This case is general for the study of shock/boundary-layer interactions, and has been investigated in [43,44] with different numerical methods. The initial condition is

$$(\rho, u, v, p) = \begin{cases} (120, 0, 0, 120/\gamma), & \text{if } 0 \le x < 1/2, \\ (1.2, 0, 0, 1.2/\gamma), & \text{if } 1/2 \le x \le 1. \end{cases} \tag{42}$$

The computational domain is $[0, 0.5] \times [0, 1]$. The viscosity is assumed to be constant and the Prandtl number is 0.73. A symmetry condition and an adiabatic viscous wall condition ($\frac{\partial T}{\partial n} = 0$) are imposed for the upper side of the domain and the other boundaries, respectively. The viscous stresses and heat-fluxes are calculated by a generic 4th-order central scheme. Initially, a Mach number 2.37 shock wave, located at $x = 1/2$, separates two different states of the stationary gas. The incident shock wave and contact discontinuity propagate from left to right, producing a thin boundary layer near the horizontal no-slip wall. After the shock wave reflects at the right wall at time $t = 0.2$, strong shock/boundary-layer interactions develop generating complex flow structures and shock reflections [43]. We simulate this problem at Reynolds number 1000, and the density field at the non-dimensional time $t = 1$ will be discussed. A reference solution is computed utilizing the fifth-order WENO-JS scheme at resolution 5120×2560 as shown in Fig. 21. In order to compare different schemes, we employ a coarse mesh with effective resolution of 1280×640.

As shown in Fig. 22, the results of distinct schemes show remarkable differences, which should be attributed primarily to the different resolution capabilities of the boundary layer and the separation bubbles. Specifically, the large-vortex shapes

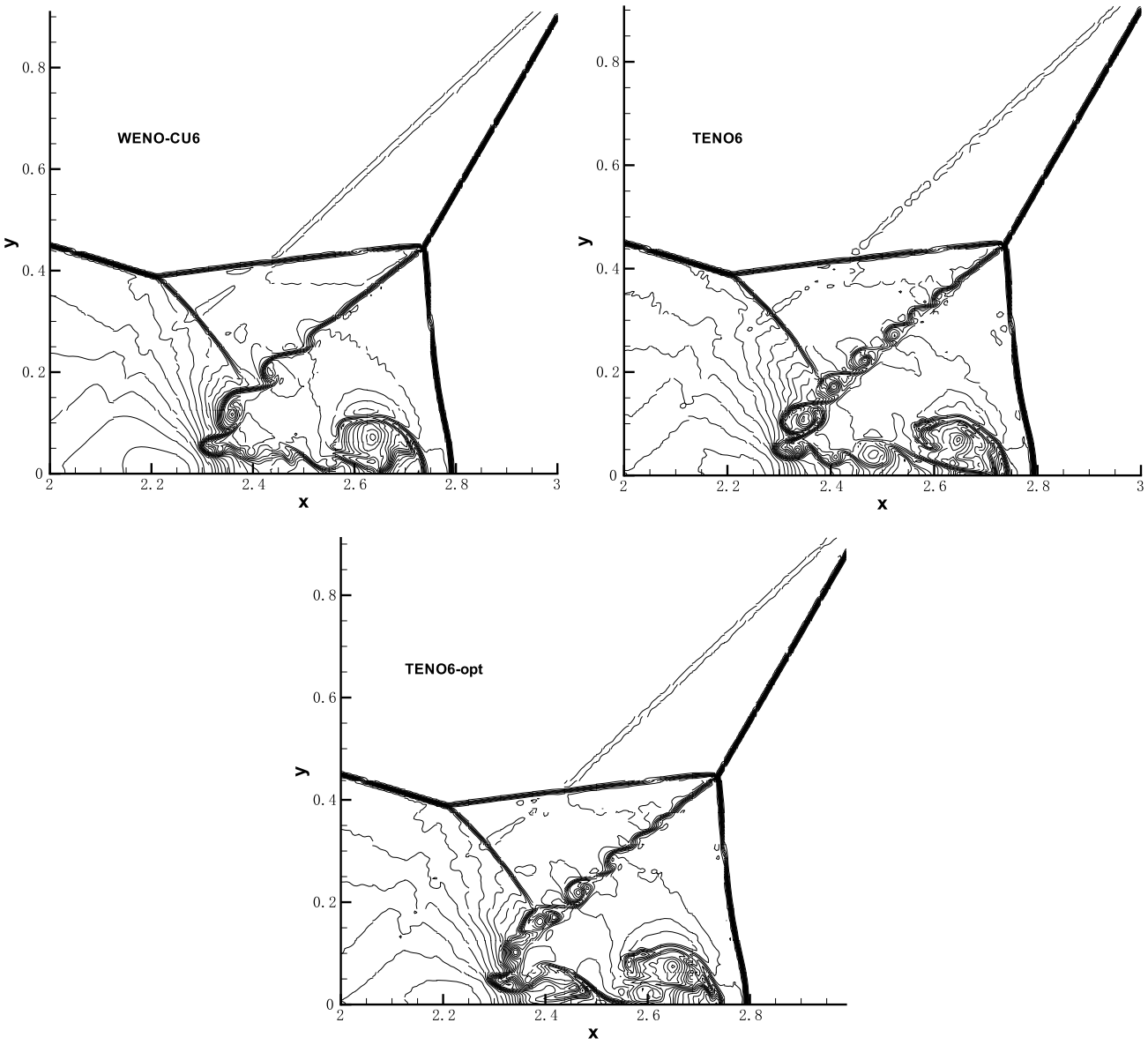

Fig. 18. Double Mach reflection of a strong shock: density contours from six-point stencil schemes. Resolution 1024×256. This figure is drawn with 43 density contours between 1.887 and 20.9. WENO-CU6-M fails to pass this case.

and shock-wave patterns produced by WENO-JS and WENO-Z are significantly different from the reference solution and the "converged" result in [44]. TENO5 and TENO5-opt, however, predict such structures quite well. And TENO5 and TENO5-opt have captured the incident shock wave much more sharply than WENO-JS. Furthermore, Fig. 23 reveals that TENO6 and TENO6-opt produce typically much better results than the other schemes. Especially, the dominant vortex structure of TENO6-opt fits the reference quite well whereas that from WENO-CU6-M is slightly distorted due to the lack of dissipation in high wave-number range.

6. Conclusions

In this paper, we have proposed a new concept to construct a family of high-order targeted ENO schemes. Fifth-order and sixth-order TENO schemes are designed and discussed in detail. Extensive one-, two- and three-dimensional benchmark tests, involving strong discontinuities and broadband fluctuations, have been performed. Concluding comments about the performances of underlying schemes are as follows:

- Robustness: except for WENO-CU6-M, which fails in the test problem "Interacting blast waves" and "Double Mach reflection of a strong shock", the investigated schemes perform well. In particular, for all cases, the new TENO schemes produce mostly better results than previous solutions with a unique fit of parameters. Note that the positivity-preserving method proposed by Hu and Adams [31] can also be applied to the TENO schemes to further improve robustness.

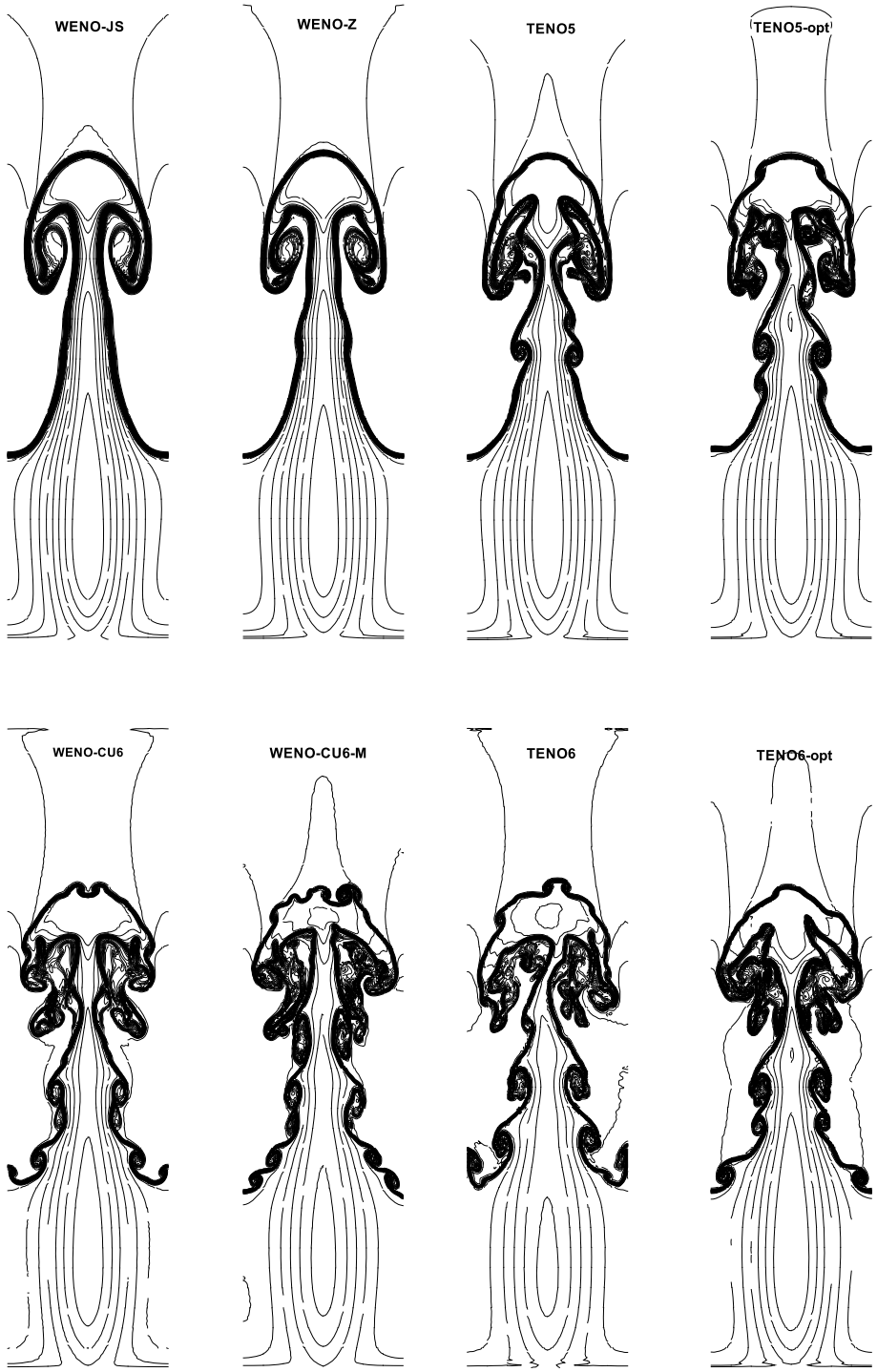

Fig. 19. Rayleigh–Taylor instability: density contours. Resolution 128×512.

- Discontinuity capturing: WENO-CU6 and WENO-CU6-M exhibit minor numerical oscillations and overshoots for strong contact discontinuities and shock waves. The new TENO schemes capture such discontinuities slightly sharper than classical WENO-JS in most cases while preserving strict monotonicity.
- Wave-resolution capability: the new TENO schemes clearly resolve intermediate and high wave-number fluctuations better than the other schemes.
- Efficiency: although not specially studied, the arithmetic operations of TENO schemes are similar to that of the classical WENO schemes. The most time-consuming part calculating the smoothness measurements as almost the same.

Classical WENO schemes exhibit robustness problems when there exist multiple shock waves close to each other as all stencils may contain discontinuities. The TENO schemes address this issue based on a combination of low-order ap-

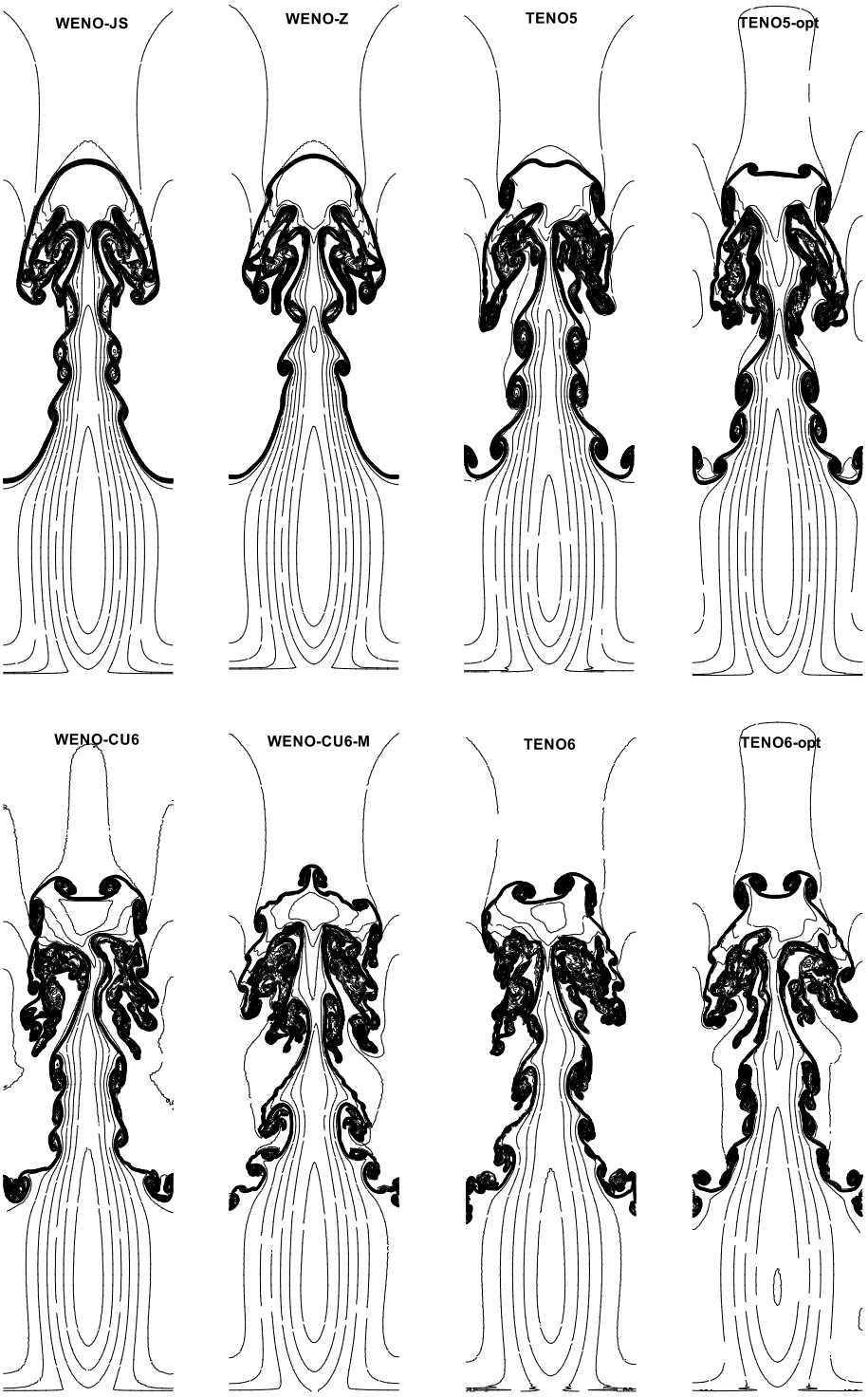

Fig. 20. Rayleigh–Taylor instability: density contours. Resolution 256×1024.

proximation polynomials with incremental stencil width. The combined low-order stencils with narrow width improve the robustness and allow for convenient construction of arbitrarily high-order (both odd- or even-order) schemes.

In order to capture shock waves while resolving broadband fluctuations, strong separation of these entities effectively is necessary. For general WENO schemes, a large value of C improves the performance in smooth regions but degrades the shock capturing capability, thus it is difficult to achieve a sufficient scale separation. With the TENO schemes, this is accomplished by increasing q up to 6 and decreasing C to 1 compared with WENO-CU6-M.

For the TENO schemes, it is fairly simple to control the dissipation in both smooth and non-smooth regions while still remaining sensitive to shock waves by an ENO-like stencil selection. Unlike the classical WENO schemes which favor the selection of the smoother stencils by a convex combination, the stencil is fully suppressed when it is detected as non-smooth

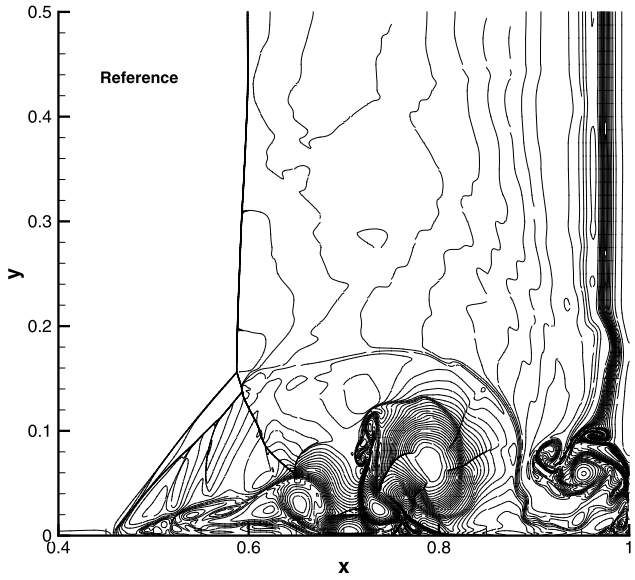

Fig. 21. Two-dimensional viscous shock-tube problem: reference density result from WENO-JS scheme. Resolution 5120×2560.

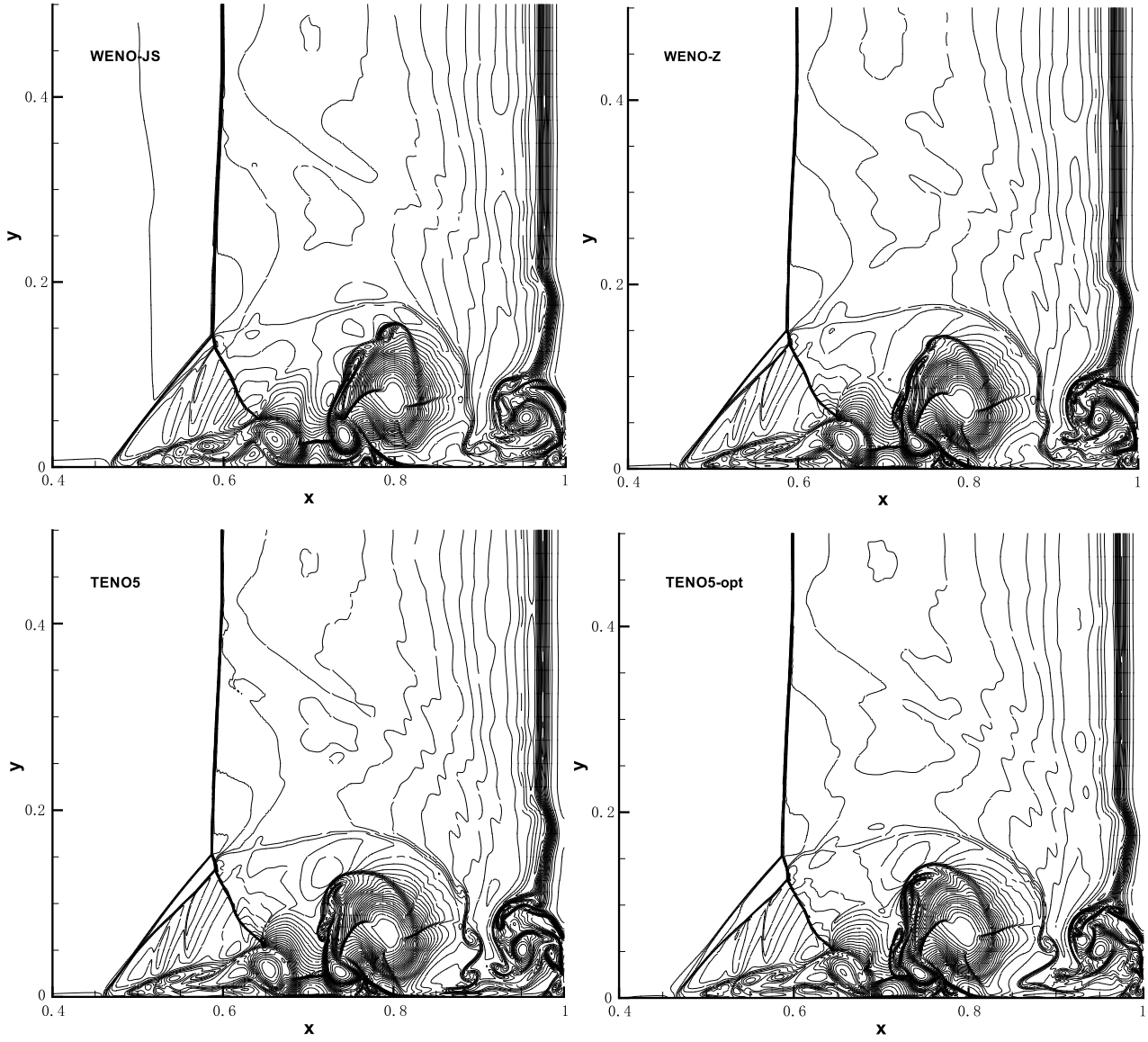

Fig. 22. Two-dimensional viscous shock-tube problem: density solutions from five-point stencil schemes. Resolution 1280×640.

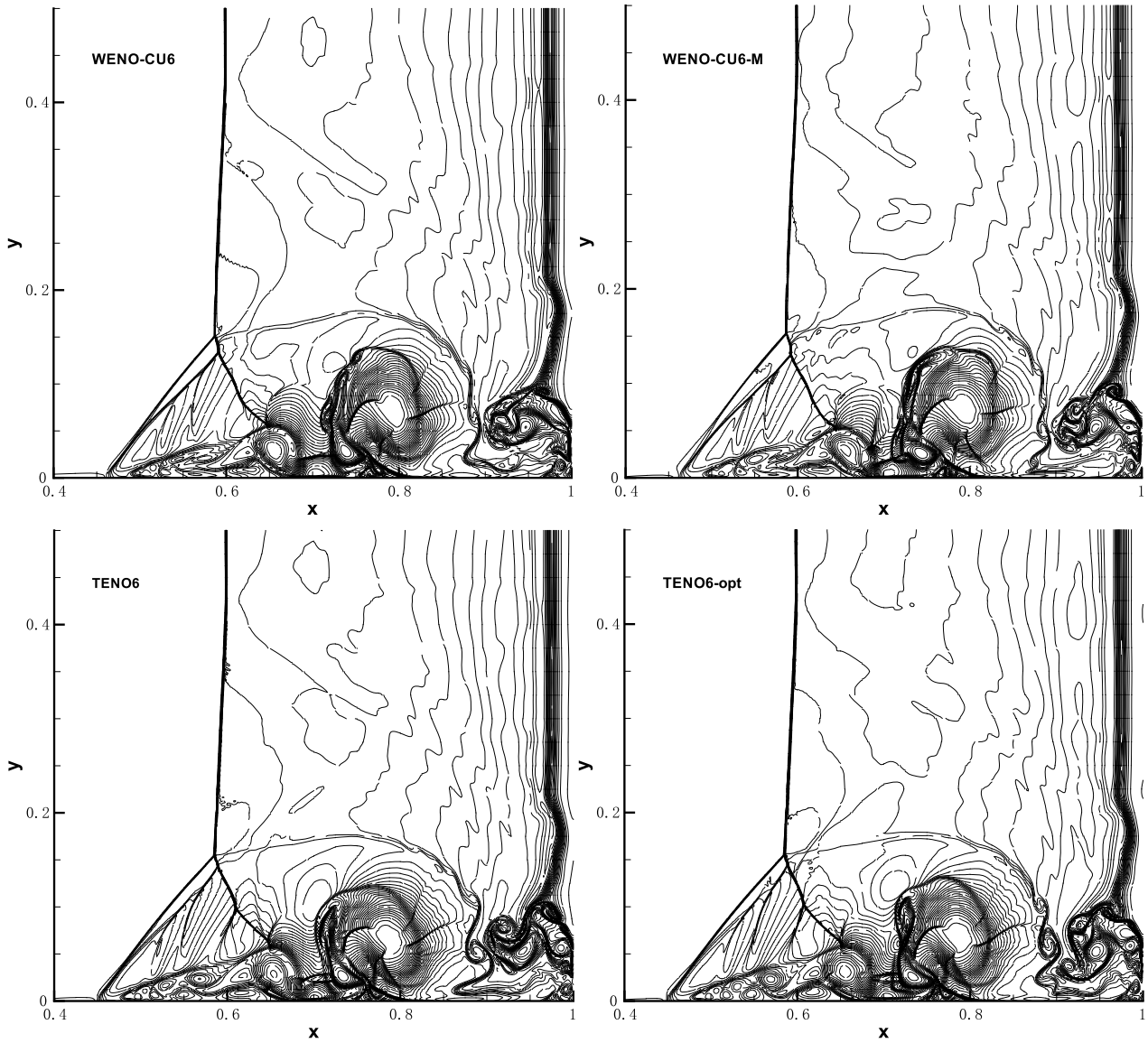

Fig. 23. Two-dimensional viscous shock-tube problem: density solutions from six-point stencil schemes. Resolution 1280×640.

according to a threshold. Otherwise it always contributes to the final reconstruction with its standard weight. The threshold is determined by spectral analysis and is problem independent with efficient scale-separation as the priority.

For high-resolution schemes, high-order accuracy is not the most important issue, e.g. high odd-order upwind scheme may still be unnecessarily dissipative. We optimize the TENO schemes by enforcing certain relation between dissipation and dispersion. For order K TENO scheme, this is achieved through adjusting the combination of two order $(K-1)$ component stencils.

Since the presented TENO5 and TENO6 schemes exhibit good spectral properties and shock-capturing capabilities, it can be expected that eighth- or even higher-order TENO schemes may provide further improved performances.

Acknowledgements

The first author is partially supported by the China Scholarship Council (No. 201206290022). The first author wishes to acknowledge Dr. Sergej Litvinov for helpful discussions on using the open source software Maxima, which produced some figures in this context.

Appendix A. Construction of the global reference smoothness indicator τ_K

Besides τ_5 and τ_6 given in the main text, a general τ_K can be constructed on K-point full stencil as

$$\tau_K = \sum_{j=K'}^{K-1} \Delta x^{2j-1} \int_{x_{i-1/2}}^{x_{i+1/2}} \left(\frac{d^j}{dx^j} \hat{f}_K(x) \right)^2 dx, \tag{A.1}$$

where

$$K' = \begin{cases} \frac{K+1}{2}, & \text{if } \mod(K,2) = 1, \\ \frac{K}{2}, & \text{if } \mod(K,2) = 0. \end{cases} \tag{A.2}$$

This leads to

$$\tau_K = \Delta x^{2K'} (f^{(K')}(x_i))^2 + O(\Delta x^{2K'+2}) \approx O(\Delta x^K). \tag{A.3}$$

It is easy to find that τ_K satisfies the condition (29) for the formal order of accuracy in smooth regions even near critical points.

References

[1] S. Pirozzoli, Numerical methods for high-speed flows, Annu. Rev. Fluid Mech. 43 (2011) 163–194.
[2] A. Harten, A high resolution scheme for the computation of weak solutions of hyperbolic conservation laws, J. Comput. Phys. 49 (1983) 357–393.
[3] A. Harten, B. Engquist, S. Osher, S.R. Chakravarthy, Uniformly high order accurate essentially non-oscillatory schemes, III, J. Comput. Phys. 71 (1987) 231–303.
[4] X.D. Liu, S. Osher, T. Chan, Weighted essentially non-oscillatory schemes, J. Comput. Phys. 115 (1994) 200–212.
[5] V. Daru, C. Tenaud, Evaluation of TVD high resolution schemes for unsteady viscous shocked flows, Comput. Fluids 30 (2001) 89–113.
[6] O. San, K. Kara, Numerical assessments of high-order accurate shock capturing schemes: Kelvin–Helmholtz type vortical structures in high-resolutions, Comput. Fluids 89 (2014) 254–276.
[7] S. Bidadi, S.L. Rani, Quantification of numerical diffusivity due to TVD schemes in the advection equation, J. Comput. Phys. 261 (2014) 65–82.
[8] C.-W. Shu, S. Osher, Efficient implementation of essentially non-oscillatory shock-capturing schemes, J. Comput. Phys. 77 (1988) 439–471.
[9] G.S. Jiang, C.-W. Shu, Efficient implementation of weighted ENO schemes, J. Comput. Phys. 126 (1) (1996) 202–228.
[10] Y. Xing, C.-W. Shu, High order finite difference WENO schemes with the exact conservation property for the shallow water equations, J. Comput. Phys. 208 (1) (2005) 206–227.
[11] K.H. Kim, C. Kim, Accurate, efficient and monotonic numerical methods for multi-dimensional compressible flows, part II: multi-dimensional limiting process, J. Comput. Phys. 208 (2005) 570–615.
[12] P. Zhang, S. Wong, C.-W. Shu, A weighted essentially non-oscillatory numerical scheme for a multi-class traffic flow model on an inhomogeneous highway, J. Comput. Phys. 212 (2) (2006) 739–756.
[13] J.A. Carrillo, I.M. Gamba, A. Majorana, C.-W. Shu, 2d semiconductor device simulations by WENO–Boltzmann schemes: efficiency, boundary conditions and comparison to Monte Carlo methods, J. Comput. Phys. 214 (1) (2006) 55–80.
[14] S. Zhao, N. Lardjane, I. Fedioun, Comparison of improved finite-difference WENO schemes for the implicit large eddy simulation of turbulent non-reacting and reacting high-speed shear flows, Comput. Fluids 95 (2014) 74–87.
[15] M.P. Martin, Shock-Capturing in LES of High-Speed Flows, Center for Turbulence Research Annual Research Briefs, 2000.
[16] S. Pirozzoli, On the spectral properties of shock-capturing schemes, J. Comput. Phys. 219 (2006) 489–497.
[17] G. Gerolymos, D. Sénéchal, I. Vallet, Very-high-order WENO schemes, J. Comput. Phys. 228 (2009) 8481–8524.
[18] V. Titarev, E. Toro, Finite-volume WENO schemes for three-dimensional conservation laws, J. Comput. Phys. 201 (1) (2004) 238–260.
[19] A.K. Henrick, T. Aslam, J.M. Powers, Mapped weighted essentially non-oscillatory schemes: achieving optimal order near critical points, J. Comput. Phys. 207 (2005) 542–567.
[20] R. Borges, M. Carmona, B. Costa, W.S. Don, An improved weighted essentially non-oscillatory scheme for hyperbolic conservation laws, J. Comput. Phys. 227 (2008) 3191–3211.
[21] D. Hill, D. Pullin, Hybrid tuned center-difference-WENO method for large eddy simulations in the presence of strong shocks, J. Comput. Phys. 194 (2004) 435–450.
[22] G.M. Arshed, K.A. Hoffmann, Minimizing errors from linear and nonlinear weights of WENO scheme for broadband applications with shock waves, J. Comput. Phys. 246 (2013) 58–77.
[23] X.Y. Hu, Q. Wang, N.A. Adams, An adaptive central-upwind weighted essentially non-oscillatory scheme, J. Comput. Phys. 229 (2010) 8952–8965.
[24] X.Y. Hu, N.A. Adams, Scale separation for implicit large eddy simulation, J. Comput. Phys. 230 (2011) 7240–7249.
[25] X.Y. Hu, V.K. Tritschler, S. Pirozzoli, N.A. Adams, Dispersion–dissipation condition for finite difference schemes, arXiv:1204.5088 [physics.flu-dyn].
[26] S.K. Lele, Compact finite difference schemes with spectral-like resolution, J. Comput. Phys. 103 (1992) 16–42.
[27] D. Fauconnier, C.D. Langhe, E. Dick, A family of dynamic finite difference schemes for large-eddy simulation, J. Comput. Phys. 228 (2009) 1830–1861.
[28] V. Weirs, G. Candler, Optimization of weighted ENO schemes for DNS of compressible turbulence, AIAA paper 97-1940, 1997.
[29] Z.-S. Sun, L. Luo, Y.-X. Ren, S.-Y. Zhang, A sixth order hybrid finite difference scheme based on the minimized dispersion and controllable dissipation technique, J. Comput. Phys. 270 (2014) 238–254.
[30] A. Suresh, H. Huynhb, Accurate monotonicity-preserving schemes with Runge–Kutta time stepping, J. Comput. Phys. 136 (1997) 83–99.
[31] X.Y. Hu, N.A. Adams, C.-W. Shu, Positivity-preserving method for high-order conservative schemes solving compressible Euler equations, J. Comput. Phys. 242 (1) (2013) 169–180.
[32] E. Hewitt, R.E. Hewitt, The Gibbs–Wilbraham phenomenon: an episode in Fourier analysis, Arch. Hist. Exact Sci. 21 (1979) 129–160.
[33] M. Castro, B. Costa, W.S. Don, High order weighted essentially non-oscillatory WENO-Z schemes for hyperbolic conservation laws, J. Comput. Phys. 230 (2011) 1766–1792.
[34] M.O. Domingues, S.M. Gomes, O. Roussel, K. Schneider, An adaptive multiresolution scheme with local time stepping for evolutionary PDEs, J. Comput. Phys. 227 (2008) 3758–3780.
[35] L.H. Han, X.Y. Hu, N.A. Adams, Adaptive multi-resolution method for compressible multi-phase flows with sharp interface model and pyramid data structure, J. Comput. Phys. 262 (2014) 131–152.
[36] N.K. Yamaleev, M.H. Carpenter, A systematic methodology for constructing high-order energy stable WENO schemes, J. Comput. Phys. 228 (11) (2009) 4248–4272.
[37] G.A. Sod, A survey of several finite difference methods for systems of nonlinear hyperbolic conservation laws, J. Comput. Phys. 27 (1978) 1–31.

[38] P.D. Lax, Weak solutions of nonlinear hyperbolic equations and their numerical computation, Commun. Pure Appl. Math. 7 (1954) 159–193.
[39] P. Woodward, The numerical simulation of two-dimensional fluid flow with strong shocks, J. Comput. Phys. 54 (1984) 115–173.
[40] C.W. Shu, S. Osher, Efficient implementation of essentially non-oscillatory shock-capturing schemes, II, J. Comput. Phys. 83 (1989) 32–78.
[41] J. Shi, Y.T. Zhang, C.W. Shu, Resolution of high order WENO schemes for complicated flow structures, J. Comput. Phys. 186 (2003) 690–696.
[42] Z. Xu, C.W. Shu, Anti-diffusive flux corrections for high order finite difference WENO schemes, J. Comput. Phys. 205 (2005) 458–485.
[43] V. Daru, C. Tenaud, Evaluation of TVD high resolution schemes for unsteady viscous shocked flows, Comput. Fluids 30 (2000) 89–113.
[44] B. Sjoegreen, H.C. Yee, Grid convergence of high order methods for multiscale complex unsteady viscous compressible flow, J. Comput. Phys. 185 (2003) 1–26.

Appendix B:

Article II

A novel partitioning method for block-structured adaptive meshes

In *Journal of Computational Physics*,Volume 341, 15 July 2017, pp. 447-473, DOI http://dx.doi.org/10.1016/j.jcp.2016.11.016.

II

Contribution: My contribution to this work was the development of the method and the corresponding computer code for its implementation. I performed simulations and analyzed the results, and wrote the manuscript for the publication.

ELSEVIER LICENSE TERMS AND CONDITIONS

Jul 06, 2017

This Agreement between Institute of Aerodynamics and Fluid Mechanics, Technical University of Munich -- Lin Fu ("You") and Elsevier ("Elsevier") consists of your license details and the terms and conditions provided by Elsevier and Copyright Clearance Center.

The publisher has provided special terms related to this request that can be found at the end of the Publisher's Terms and Conditions.

License Number	4143000253011
License date	Jul 06, 2017
Licensed Content Publisher	Elsevier
Licensed Content Publication	Journal of Computational Physics
Licensed Content Title	A novel partitioning method for block-structured adaptive meshes
Licensed Content Author	Lin Fu,Sergej Litvinov,Xiangyu Y. Hu,Nikolaus A. Adams
Licensed Content Date	Jul 15, 2017
Licensed Content Volume	341
Licensed Content Issue	n/a
Licensed Content Pages	27
Start Page	447
End Page	473
Type of Use	reuse in a thesis/dissertation
Intended publisher of new work	other
Portion	full article
Format	both print and electronic
Are you the author of this Elsevier article?	Yes
Will you be translating?	No
Order reference number	
Title of your thesis/dissertation	Numerical methods for computational fluid dynamics
Expected completion date	Aug 2017
Estimated size (number of pages)	126
Elsevier VAT number	GB 494 6272 12
Requestor Location	Institute of Aerodynamics and Fluid Mechanics, Technical University of Munich 85748 Garching Germany Munich, 85748 Germany Attn: Institute of Aerodynamics and Fluid Mechanics, Technical University of Munich
Publisher Tax ID	GB 494 6272 12
Billing Type	Invoice
Billing Address	Institute of Aerodynamics and Fluid Mechanics, Technical University of Munich 85748 Garching Germany Munich, Germany 85748 Attn: Institute of Aerodynamics and Fluid Mechanics, Technical University of Munich

Total **0.00 EUR**

Terms and Conditions

INTRODUCTION

1. The publisher for this copyrighted material is Elsevier. By clicking "accept" in connection with completing this licensing transaction, you agree that the following terms and conditions apply to this transaction (along with the Billing and Payment terms and conditions established by Copyright Clearance Center, Inc. ("CCC"), at the time that you opened your Rightslink account and that are available at any time at http://myaccount.copyright.com).

GENERAL TERMS

2. Elsevier hereby grants you permission to reproduce the aforementioned material subject to the terms and conditions indicated.
3. Acknowledgement: If any part of the material to be used (for example, figures) has appeared in our publication with credit or acknowledgement to another source, permission must also be sought from that source. If such permission is not obtained then that material may not be included in your publication/copies. Suitable acknowledgement to the source must be made, either as a footnote or in a reference list at the end of your publication, as follows:
"Reprinted from Publication title, Vol /edition number, Author(s), Title of article / title of chapter, Pages No., Copyright (Year), with permission from Elsevier [OR APPLICABLE SOCIETY COPYRIGHT OWNER]." Also Lancet special credit - "Reprinted from The Lancet, Vol. number, Author(s), Title of article, Pages No., Copyright (Year), with permission from Elsevier."
4. Reproduction of this material is confined to the purpose and/or media for which permission is hereby given.
5. Altering/Modifying Material: Not Permitted. However figures and illustrations may be altered/adapted minimally to serve your work. Any other abbreviations, additions, deletions and/or any other alterations shall be made only with prior written authorization of Elsevier Ltd. (Please contact Elsevier at permissions@elsevier.com). No modifications can be made to any Lancet figures/tables and they must be reproduced in full.
6. If the permission fee for the requested use of our material is waived in this instance, please be advised that your future requests for Elsevier materials may attract a fee.
7. Reservation of Rights: Publisher reserves all rights not specifically granted in the combination of (i) the license details provided by you and accepted in the course of this licensing transaction, (ii) these terms and conditions and (iii) CCC's Billing and Payment terms and conditions.
8. License Contingent Upon Payment: While you may exercise the rights licensed immediately upon issuance of the license at the end of the licensing process for the transaction, provided that you have disclosed complete and accurate details of your proposed use, no license is finally effective unless and until full payment is received from you (either by publisher or by CCC) as provided in CCC's Billing and Payment terms and conditions. If full payment is not received on a timely basis, then any license preliminarily granted shall be deemed automatically revoked and shall be void as if never granted. Further, in the event that you breach any of these terms and conditions or any of CCC's Billing and Payment terms and conditions, the license is automatically revoked and shall be void as if never granted. Use of materials as described in a revoked license, as well as any use of the materials beyond the scope of an unrevoked license, may constitute copyright infringement and publisher reserves the right to take any and all action to protect its copyright in the materials.
9. Warranties: Publisher makes no representations or warranties with respect to the licensed material.
10. Indemnity: You hereby indemnify and agree to hold harmless publisher and CCC, and their respective officers, directors, employees and agents, from and against any and all claims arising out of your use of the licensed material other than as specifically authorized pursuant to this license.
11. No Transfer of License: This license is personal to you and may not be sublicensed, assigned, or transferred by you to any other person without publisher's written permission.
12. No Amendment Except in Writing: This license may not be amended except in a writing signed by both parties (or, in the case of publisher, by CCC on publisher's behalf).
13. Objection to Contrary Terms: Publisher hereby objects to any terms contained in any purchase order, acknowledgment, check endorsement or other writing prepared by you, which terms are inconsistent with these terms and conditions or CCC's Billing and Payment terms and conditions. These terms and conditions, together with CCC's Billing and Payment terms and conditions (which are incorporated herein), comprise the entire agreement between you and publisher (and CCC) concerning this licensing transaction. In the event of any conflict between your obligations established by these terms and conditions and those established by CCC's Billing and Payment terms and conditions, these terms and conditions shall control.
14. Revocation: Elsevier or Copyright Clearance Center may deny the permissions described in this License at their sole discretion, for any reason or no reason, with a full refund payable to you. Notice of such denial will be made using the contact information provided by you. Failure to receive such notice will not alter or invalidate the denial. In no event will Elsevier or Copyright Clearance Center be responsible or liable for any costs, expenses or damage incurred by you as a result of a denial of your permission request, other than a refund of the amount(s) paid by you to Elsevier and/or Copyright Clearance Center for denied permissions.

LIMITED LICENSE

The following terms and conditions apply only to specific license types:
15. **Translation**: This permission is granted for non-exclusive world **English** rights only unless your license was granted for translation rights. If you licensed translation rights you may only translate this content into the languages you requested. A professional translator must perform all translations and reproduce the content word for word preserving the integrity of the article.
16. **Posting licensed content on any Website**: The following terms and conditions apply as follows: Licensing material from an Elsevier journal: All content posted to the web site must maintain the copyright information line on the bottom of each image; A hyper-text must be included to the Homepage of the journal from which you are licensing at http://www.sciencedirect.com/science/journal/xxxxx or the Elsevier homepage for books at http://www.elsevier.com; Central

Storage: This license does not include permission for a scanned version of the material to be stored in a central repository such as that provided by Heron/XanEdu.
Licensing material from an Elsevier book: A hyper-text link must be included to the Elsevier homepage at http://www.elsevier.com . All content posted to the web site must maintain the copyright information line on the bottom of each image.

Posting licensed content on Electronic reserve: In addition to the above the following clauses are applicable: The web site must be password-protected and made available only to bona fide students registered on a relevant course. This permission is granted for 1 year only. You may obtain a new license for future website posting.
17. **For journal authors:** the following clauses are applicable in addition to the above:
Preprints:
A preprint is an author's own write-up of research results and analysis, it has not been peer-reviewed, nor has it had any other value added to it by a publisher (such as formatting, copyright, technical enhancement etc.).
Authors can share their preprints anywhere at any time. Preprints should not be added to or enhanced in any way in order to appear more like, or to substitute for, the final versions of articles however authors can update their preprints on arXiv or RePEc with their Accepted Author Manuscript (see below).
If accepted for publication, we encourage authors to link from the preprint to their formal publication via its DOI. Millions of researchers have access to the formal publications on ScienceDirect, and so links will help users to find, access, cite and use the best available version. Please note that Cell Press, The Lancet and some society-owned have different preprint policies. Information on these policies is available on the journal homepage.
Accepted Author Manuscripts: An accepted author manuscript is the manuscript of an article that has been accepted for publication and which typically includes author-incorporated changes suggested during submission, peer review and editor-author communications.
Authors can share their accepted author manuscript:

- immediately
  - via their non-commercial person homepage or blog
  - by updating a preprint in arXiv or RePEc with the accepted manuscript
  - via their research institute or institutional repository for internal institutional uses or as part of an invitation-only research collaboration work-group
  - directly by providing copies to their students or to research collaborators for their personal use
  - for private scholarly sharing as part of an invitation-only work group on commercial sites with which Elsevier has an agreement
- After the embargo period
  - via non-commercial hosting platforms such as their institutional repository
  - via commercial sites with which Elsevier has an agreement

In all cases accepted manuscripts should:

- link to the formal publication via its DOI
- bear a CC-BY-NC-ND license - this is easy to do
- if aggregated with other manuscripts, for example in a repository or other site, be shared in alignment with our hosting policy not be added to or enhanced in any way to appear more like, or to substitute for, the published journal article.

Published journal article (JPA): A published journal article (PJA) is the definitive final record of published research that appears or will appear in the journal and embodies all value-adding publishing activities including peer review co-ordination, copy-editing, formatting, (if relevant) pagination and online enrichment.
Policies for sharing publishing journal articles differ for subscription and gold open access articles:
Subscription Articles: If you are an author, please share a link to your article rather than the full-text. Millions of researchers have access to the formal publications on ScienceDirect, and so links will help your users to find, access, cite, and use the best available version.
Theses and dissertations which contain embedded PJAs as part of the formal submission can be posted publicly by the awarding institution with DOI links back to the formal publications on ScienceDirect.
If you are affiliated with a library that subscribes to ScienceDirect you have additional private sharing rights for others' research accessed under that agreement. This includes use for classroom teaching and internal training at the institution (including use in course packs and courseware programs), and inclusion of the article for grant funding purposes.
Gold Open Access Articles: May be shared according to the author-selected end-user license and should contain a CrossMark logo, the end user license, and a DOI link to the formal publication on ScienceDirect.
Please refer to Elsevier's posting policy for further information.
18. **For book authors** the following clauses are applicable in addition to the above: Authors are permitted to place a brief summary of their work online only. You are not allowed to download and post the published electronic version of your chapter, nor may you scan the printed edition to create an electronic version. **Posting to a repository:** Authors are permitted to post a summary of their chapter only in their institution's repository.
19. **Thesis/Dissertation**: If your license is for use in a thesis/dissertation your thesis may be submitted to your institution in either print or electronic form. Should your thesis be published commercially, please reapply for permission. These requirements include permission for the Library and Archives of Canada to supply single copies, on demand, of the complete thesis and

include permission for Proquest/UMI to supply single copies, on demand, of the complete thesis. Should your thesis be published commercially, please reapply for permission. Theses and dissertations which contain embedded PJAs as part of the formal submission can be posted publicly by the awarding institution with DOI links back to the formal publications on ScienceDirect.

Elsevier Open Access Terms and Conditions

You can publish open access with Elsevier in hundreds of open access journals or in nearly 2000 established subscription journals that support open access publishing. Permitted third party re-use of these open access articles is defined by the author's choice of Creative Commons user license. See our open access license policy for more information.

Terms & Conditions applicable to all Open Access articles published with Elsevier:

Any reuse of the article must not represent the author as endorsing the adaptation of the article nor should the article be modified in such a way as to damage the author's honour or reputation. If any changes have been made, such changes must be clearly indicated.

The author(s) must be appropriately credited and we ask that you include the end user license and a DOI link to the formal publication on ScienceDirect.

If any part of the material to be used (for example, figures) has appeared in our publication with credit or acknowledgement to another source it is the responsibility of the user to ensure their reuse complies with the terms and conditions determined by the rights holder.

Additional Terms & Conditions applicable to each Creative Commons user license:

CC BY: The CC-BY license allows users to copy, to create extracts, abstracts and new works from the Article, to alter and revise the Article and to make commercial use of the Article (including reuse and/or resale of the Article by commercial entities), provided the user gives appropriate credit (with a link to the formal publication through the relevant DOI), provides a link to the license, indicates if changes were made and the licensor is not represented as endorsing the use made of the work. The full details of the license are available at http://creativecommons.org/licenses/by/4.0.

CC BY NC SA: The CC BY-NC-SA license allows users to copy, to create extracts, abstracts and new works from the Article, to alter and revise the Article, provided this is not done for commercial purposes, and that the user gives appropriate credit (with a link to the formal publication through the relevant DOI), provides a link to the license, indicates if changes were made and the licensor is not represented as endorsing the use made of the work. Further, any new works must be made available on the same conditions. The full details of the license are available at http://creativecommons.org/licenses/by-nc-sa/4.0.

CC BY NC ND: The CC BY-NC-ND license allows users to copy and distribute the Article, provided this is not done for commercial purposes and further does not permit distribution of the Article if it is changed or edited in any way, and provided the user gives appropriate credit (with a link to the formal publication through the relevant DOI), provides a link to the license, and that the licensor is not represented as endorsing the use made of the work. The full details of the license are available at http://creativecommons.org/licenses/by-nc-nd/4.0. Any commercial reuse of Open Access articles published with a CC BY NC SA or CC BY NC ND license requires permission from Elsevier and will be subject to a fee.

Commercial reuse includes:

- Associating advertising with the full text of the Article
- Charging fees for document delivery or access
- Article aggregation
- Systematic distribution via e-mail lists or share buttons

Posting or linking by commercial companies for use by customers of those companies.

20. **Other Conditions**: Permission is granted to submit your article in electronic format. This license permits you to post this Elsevier article online on your Institution's website if the content is embedded within your thesis.

v1.9

Questions? customercare@copyright.com or +1-855-239-3415 (toll free in the US) or +1-978-646-2777.

Journal of Computational Physics 341 (2017) 447–473

Contents lists available at ScienceDirect

Journal of Computational Physics

www.elsevier.com/locate/jcp

A novel partitioning method for block-structured adaptive meshes

Lin Fu, Sergej Litvinov [1], Xiangyu Y. Hu *, Nikolaus A. Adams

Institute of Aerodynamics and Fluid Mechanics, Technische Universität München, 85748 Garching, Germany

ARTICLE INFO

Article history:
Received 15 December 2015
Received in revised form 26 September 2016
Accepted 3 November 2016
Available online 18 November 2016

Keywords:
Lagrangian particle method
Smoothed-particle hydrodynamics
Multi-resolution cell-linked list
Dynamic ghost particle method
Adaptive mesh refinement
Grid partitioning

ABSTRACT

We propose a novel partitioning method for block-structured adaptive meshes utilizing the meshless Lagrangian particle concept. With the observation that an optimum partitioning has high analogy to the relaxation of a multi-phase fluid to steady state, physically motivated model equations are developed to characterize the background mesh topology and are solved by multi-phase smoothed-particle hydrodynamics. In contrast to well established partitioning approaches, all optimization objectives are implicitly incorporated and achieved during the particle relaxation to stationary state. Distinct partitioning sub-domains are represented by colored particles and separated by a sharp interface with a surface tension model. In order to obtain the particle relaxation, special viscous and skin friction models, coupled with a tailored time integration algorithm are proposed. Numerical experiments show that the present method has several important properties: generation of approximately equal-sized partitions without dependence on the mesh-element type, optimized interface communication between distinct partitioning sub-domains, continuous domain decomposition which is physically localized and implicitly incremental. Therefore it is particularly suitable for load-balancing of high-performance CFD simulations.

1. Introduction

Massively parallel computing is essential for Computational Fluid Dynamics (CFD) to cope with flow simulations involving complex geometries or a wide spectrum of length scales [1]. To reduce computational costs, unstructured or adaptive structured mesh topologies are frequently employed as state-of-the-art mesh discretization methods [2]. Refined mesh elements are distributed at flow regions of interest or regions containing discontinuities. Such nonuniform mesh topologies are the consequence of the compromise between computational accuracy and efficiency [3]. However, partitioning problems arise with the utilization of such locally refined mesh topologies when the number of processor cores increases in massively parallel computing environments. The optimization strategy for load-balancing and inter-processor communication becomes the critical bottleneck and limits the computational performance. A partitioning method should accomplish approximately equal-sized domain decomposition with minimum neighbor communication patterns as it reduces processor operation idle time and inter-processor communication time. Moreover, each individual sub-domain is expected to be physically localized and continuous since it facilitates data management and reduces communications [4]. Partitioning operations for parallel computing can be categorized into static partitioning and dynamic partitioning. For the latter, additional requirements are

* Corresponding author.
E-mail addresses: lin.fu@tum.de (L. Fu), sergej.litvinov@aer.mw.tum.de (S. Litvinov), xiangyu.hu@tum.de (X.Y. Hu), nikolaus.adams@tum.de (N.A. Adams).
[1] Current address: Computational Science and Engineering Laboratory, ETH Zürich, Clausiusstrasse 33, CH-8092, Switzerland.

http://dx.doi.org/10.1016/j.jcp.2016.11.016
0021-9991/

that small topology changes should only result in slight modification of the partitioning (implicitly incremental) and the repartitioning time cost is minimized [5].

Classical partitioning methods can be roughly classified as geometry-based and graph-based approaches [4,6]. Several open-source codes, such as Metis [7], have been developed to meet these principles. The former is based on the physical coordinates of the original background mesh and generally leads to very fast algorithms. The Recursive Coordinate Bisection (RCB) method recursively divides the computational domain into equal-sized sub-domains by cutting planes that are orthogonal to the coordinate axes and has been proposed by Berger and Bokhari [8] to partition meshes generated by Adaptive Mesh Refinement [9]. RCB is an efficient method to provide a basic partitioning for structured or unstructured meshes when the connectivity information between mesh elements is not at hand. However, the partitioning quality suffers from possible discontinuous sub-domains and inefficient communication requirements [4]. The key idea of Space-Filling Curve (SFC) [10,11] partitioning is to construct a linear sequence of mesh elements through mapping the higher-dimensional mesh onto one dimension. Partitioning is obtained by cutting the one-dimensional sequence into desired pieces. The advantages of this approach are that it is fast, robust and geometrically localized. It also provides an efficient data structure as all elements can be assigned a globally unique index, enabling direct access. Furthermore, physical adjacency more or less is preserved. However, similarly to RCB, communication needs cannot be controlled explicitly during the partitioning, and disconnected sub-domains may exist [4]. Nivarti et al. [12] develop an inexpensive algorithm to improve the spatial locality of SFC partitioning by sacrificing a certain degree of load balance. Despite the moderate partitioning quality, geometry-based partitioning approaches play important roles in applications without inherent connectivity information, such as for particle based simulations.

In terms of graph-based approaches, a graph, where vertices represent the mesh elements to be partitioned and edges stand for communications between elements, is generated to characterize the background mesh. Load-balancing optimization and edge-cut minimization are achieved via Recursive Spectral Bisection (RSB) [13] or a multilevel graph partitioning strategy [14,15] Thus, the detailed connectivity information of the partitioning mesh must be available. RSB generates subgraphs by exploiting the eigenvectors of the Laplacian matrix associated with the target graph. It is quite expensive due to the eigenvector calculation. The multilevel partitioning paradigm is much more efficient and mainly consists of three substages: (i) graph coarsening which generates a sequence of coarser graphs preserving the essential properties of the original graph; (ii) partitioning of the representative coarsest graph; and (iii) graph refinement (Kernighan–Lin [16] heuristics and its variant Fiduccia–Mattheyses algorithm [17] are widely employed) which improves the partition by interpolating the coarser partitioned graph back to the original one in combination with a fast local search algorithm [18]. These approaches have significant advantages over geometry-based approaches by generating high-quality domain decomposition with controllable interface communication, although they are more time consuming. However, classical graph-based approaches may suffer from the problem that the optimization objective function is not always adequate. The partition objective of minimizing the total communication message size is not directly equivalent to minimizing edge-cuts because edge-cuts are in general not proportional to the communication volume [19]. For many applications, the number of graph vertices located at the boundaries of partitioning sub-domains (boundary vertices) indeed characterizes the real communication cost much more accurately than the number of edge-cuts [20]. Boundary properties of partitioning sub-domain, e.g. aspect ratio [21], connectedness and smoothness [22], are also crucial in communication reduction [23]. This problem can be improved largely by introducing the Hypergraph partitioning concept, which encodes the communication volume better, with higher running time [24]. With respect to dynamic load-balancing which introduces additional optimization objectives, the problem arises in parallelizing the widely-used Kernighan–Lin [16] method on distributed-memory architecture and designing the multiple optimization metrics [25]. In such a scenario, graph-based diffusive partitioners [26,20] are generally applied as they produce partitions, that have more implicit incrementality and higher-quality than those from classical multilevel partitioning strategies. A drawback of these graph-based partitioners is that strictly-connected partitions cannot be guaranteed in principle [20]. Nevertheless, graph-based partitioning methods are widely accepted in well-established software [7].

We will explain below, that the partitioning result has high similarity to a stationary multi-phase fluid. Based on this observation, we propose a new partitioning method based on multi-phase particle simulation. Using the topology information from a background mesh, a set of physically motivated model equations is formulated and solved by a meshless multiphase Smoothed Particle Hydrodynamics method [27]. While most graph-based partitioning approaches explicitly optimize the communication by minimizing the edge-cuts, we seek to minimize the number of boundary vertices and optimize the partitioning-sub-domain shapes. All optimization objectives are implicitly incorporated and optimized during the particle evolution process. Our proposed partitioning method guarantees connected partitioning, optimized interface communication, good load-balancing and possesses the implicitly incremental property. Moreover, it does not depend on the specific mesh element type and can be straightforwardly extended to unstructured mesh partitioning.

2. Physically motivated models

2.1. Mathematical concepts

For parallel simulations, the load-balancing requirement can be formulated as a problem in graph theory. Considering an undirected graph $G = (V, E)$, where V denotes a set of vertices corresponding to the computation units and E denotes a

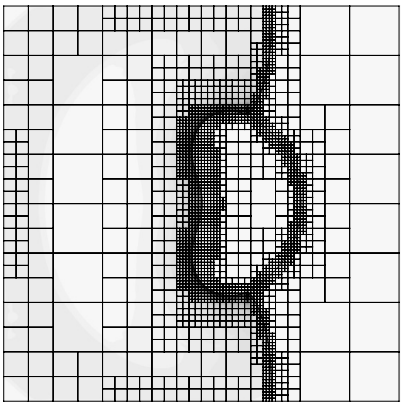

Fig. 1. Sketch of a block-structured mesh generated by multi-resolution analysis [2] with maximum tree level 6. Each mesh element represents a grid-block consisting typically of hundreds of cells in two-dimensions.

set of edges corresponding to the communications between computation units, the objective is to find subsets of vertices $V_1, V_2, \cdots, V_n$ which partitions graph G into n disjoint subgraphs and has the following properties [28,19]

(i) $V_1 \cup V_2 \cdots \cup V_n = V$ and $V_i \cap V_j = \emptyset$ with $i \neq j$;
(ii) $|V_i| \approx \lceil \frac{|V|}{n} \rceil,\ i = 1, \cdots, n$;
(iii) $\sum_{i<j} E_{ij}$ is minimized, where $E_{ij} = \{\{u, v\} \in E | u \in V_i \bigwedge v \in V_j\}$.

More generally, the graph vertices and edges can be assigned with attribute value w, resulting in a weighted graph, which we do not further consider below.

2.2. Basic idea

In the following context, we refer to the block-structured nonuniform mesh as in Fig. 1, in which a mesh element represents a computation unit within a partitioning sub-domain, or a graph vertex. An adjacency relationship between two mesh elements located separately in a sub-domain pair implies a communication element within a graph edge. Communication occurs at the subdomain boundaries, and the amount is proportional to the mesh element number in the neighborhood of subdomain boundaries.

With the observation that the load-balancing partitioning outcome has high analogy to the equilibrium of multi-phase fluid [2], a Lagrangian particle based multi-phase problem can be defined accordingly which relaxes to an equilibrium state with the following properties:

(i) The particle distribution exactly represents the mesh topology. Each mesh element contains the same number of particles which are uniformly distributed inside.
(ii) Each particle features a color function and particles of same color tend to concentrate. Furthermore, each phase, characterized by color, possesses the same number of particles.
(iii) The phase interface is sharp, convex, and the mesh element number close to the interface is optimized.
(iv) The particle evolution is localized and incremental.

If the equilibrium solution of the model equations satisfies these three properties, the remaining issue is to develop an algorithm to compute this equilibrium from a given initial configuration.

2.3. Governing equations

For isothermal compressible flows, the Lagrangian form of governing equations is

$$\frac{d\rho}{dt} = -\rho \nabla \cdot \mathbf{v}, \tag{1}$$

$$\frac{d\mathbf{v}}{dt} = -\mathbf{F_p} + \mathbf{F_v} + \mathbf{F_s} + \mathbf{F_f}, \tag{2}$$

where ρ is the fluid density, $\mathbf{v}$ is the velocity vector, t is the time and $\mathbf{F_p}$, $\mathbf{F_v}$, $\mathbf{F_s}$, $\mathbf{F_f}$ stand for the accelerations due to repulsive pressure force, viscous shear force, surface tension force and friction force respectively. This set of equations can be solved by the Smoothed Particle Hydrodynamics (SPH) method [27].

The same mass is assigned to all particles

$$m = 1. \tag{3}$$

Density can be calculated from summation over all neighboring particles rather than solving the continuity equation Eq. (1). Following the definition of $d_i = \sum_j W(r_{ij}, h)$ which is approximately the inverse of the specific particle volume [29], the particle average density is $m_i d_i$ and can be evaluated as

$$\rho_i = m_i \sum_j W(r_{ij}, h), \tag{4}$$

where $\mathbf{r}_{ij} = \mathbf{r}_i - \mathbf{r}_j$, $r_{ij} = |\mathbf{r}_{ij}|$, h denotes the particle smoothing-length [29] and $W(r_{ij}, h)$ denotes the kernel function [27].

The discretization of the conservative repulsive pressure force is given as

$$\mathbf{F_p} = \sum_j m_j \left(\frac{p_i}{\rho_i^2} + \frac{p_j}{\rho_j^2} \right) \frac{\partial W(r_{ij}, h)}{\partial r_{ij}} \mathbf{e}_{ij}, \tag{5}$$

where $\mathbf{e}_{ij} = \frac{\mathbf{r}_{ij}}{r_{ij}}$ is the normalized vector from particle i to j and p denotes the particle pressure. The arithmetic average of smoothing-lengths for particle pairs is used to ensure force anti-symmetry as

$$h = \frac{1}{2}(h_i + h_j). \tag{6}$$

In order to close the system of governing equations, the pressure must be defined by an Equation of State (EOS). For SPH methods, $p = \rho c^2$ or $p = p_0 \left[\left(\frac{\rho}{\rho_0} \right)^\gamma - 1 \right] + b$ are used [27]. Here, we define the pressure as

$$p = p_0 \frac{\rho^2}{\rho_t^2}, \tag{7}$$

which incorporates the target density ρ_t (the definition of ρ_t will be given later) and a constant reference pressure p_0. Substituting Eq. (7) into Eq. (5), we obtain

$$\mathbf{F_p} = \sum_j m_j \left(\frac{p_0}{\rho_{t,i}^2} + \frac{p_0}{\rho_{t,j}^2} \right) \frac{\partial W(r_{ij}, h)}{\partial r_{ij}} \mathbf{e}_{ij}. \tag{8}$$

In standard SPH, the accurate density summation depends on sufficient number of particle neighbors with respect to the kernel function support [27]. With the introduction of Eq. (7), direct density calculation becomes unnecessary.

2.4. Target information

The particle target information can be obtained straightforwardly from the background mesh. The target smoothing-length, representing the local mesh resolution, is approximated as

$$h_t = \vartheta \sqrt[3]{volume} \approx \vartheta \max(\Delta x, \Delta y, \Delta z), \tag{9}$$

where ϑ is defined such that the particle interaction cut-off radius for the chosen kernel function equals the local mesh resolution.

The target density can be calculated by

$$\rho_t = \frac{\sum_{i=1}^{n} m_i}{volume}, \tag{10}$$

provided that n particles are assumed to be distributed uniformly in each mesh element.

Each particle is mapped onto one certain background mesh element according to physical coordinate information. For a specific particle i,

$$\begin{cases} h_i \approx h_{t,i} = h_t(\mathbf{r_i}), \\ \rho_{t,i} = \rho_t(\mathbf{r_i}). \end{cases} \tag{11}$$

The repulsive force $\mathbf{F_p} = \frac{\nabla p}{\rho}$ depends on density and pressure gradient. If the particle distribution does not represent the mesh topology, i.e. $\rho \neq \rho_t$ and thus $p = p_0 \frac{\rho^2}{\rho_t^2}$ is not constant throughout the computational domain, particles will be

driven by the repulsive force produced by the pressure gradient. For $\rho = \rho_t$ everywhere, the pressure gradient vanishes and a relaxed equilibrium configuration is reached. In this way, the first partitioning design target is achieved.

The data required from the background mesh topology are volume and element location, both of which are basic mathematical properties of the specific type of elements and can be calculated in a fairly simple way. Consequently, our model equations are independent of mesh element types, such as structured mesh, adaptive unstructured mesh or hybrid mesh, and remain generic to a large extent.

2.5. Kernel function without paring instability

Considering smoothing kernels which denote the integral function based on discrete points, well known B-spline functions of different orders, e.g. cubic spline and quartic spline, are widely accepted [27]. However, gradient evaluation based on these kernel functions can produce numerical artifacts. The first-order gradients of these kernels exhibit a bell shape, generating a maximum negative value at $\frac{r}{h} \approx \frac{2}{3}$. When the ratio of smoothing-length to average particle spacing is large, particles tend to accumulate within the hump and develop the so-called paring instability [27].

Yang et al. [30] propose to use a hyperbolic-shaped kernel function with non-negative second-order derivative within the entire support as

$$W(r_{ij}, h) = \alpha \begin{cases} s^3 - 6s + 6, & 0 \le s < 1, \\ (2-s)^3, & 1 \le s < 2, \\ 0, & 2 \le s, \end{cases} \tag{12}$$

where $s = \frac{r_{ij}}{h}$ and α is a normalization

$$\alpha = \begin{cases} \frac{1}{3\pi h^2}, & 2D, \\ \frac{15}{62\pi h^3}, & 3D. \end{cases} \tag{13}$$

This kernel successfully avoids paring instability while satisfying the conventional requirements of a kernel function. In the following, we adopt this kernel for the force calculations.

2.6. Surface tension model

The classical metric, i.e. the number of edge-cuts between different partitioning sub-domains, is not a good measure for the real communication costs [19]. Partitioning sub-domains with convex boundary shapes, small aspect ratios and strict connectedness are preferred with respect to communication reduction [23,31]. Based on these observations, the objective is to optimize the area of partitioning-sub-domain boundaries which leads to convex shapes. This objective, i.e. the third design target, can be achieved physically by the introduction of a suitable surface tension model.

Surface tension originates from the cohesion of like molecules and thus promotes the coherence of distinct flow phases. With the effects of the surface tension force, the interface surface area tends to become minimum. This property naturally fulfills the optimization objective.

Although the interface curvature can be derived from the particle color function in SPH [29], we propose a simplified model which avoids a direct calculation of curvature by modifying the computation of the repulsive force.

The acceleration due to the inter-particle mutual repulsive pressure force can be redefined as

$$\mathbf{f_p} = \beta m_j \left(\frac{p_i}{\rho_i^2} + \frac{p_j}{\rho_j^2} \right) \frac{\partial W(r_{ij}, h)}{\partial r_{ij}} \mathbf{e}_{ij}, \tag{14}$$

where β is a constant representing the surface tension coefficient and is defined as

$$\beta = \begin{cases} 1, & C_i = C_j, \\ \sigma, & \text{otherwise}, \end{cases} \tag{15}$$

where C_k denotes the color function of particle k. σ determines the surface tension strength, and $\sigma = 4$ is adopted throughout all applications of our method. The total acceleration due to repulsive pressure force and surface tension effects for each particle is

$$\mathbf{F_p} = \sum_j \mathbf{f_p}. \tag{16}$$

Particles near an interface segment with large curvature are expected to have more neighboring particles of different color and thus subject to a larger repulsive force from distinct phases. In this way, the interface-curvature effect is implicitly incorporated.

2.7. Viscous and friction model

The particle acceleration induced by shear forces is approximated as

$$\mathbf{F_v} = \sum_j \frac{2\eta_i\eta_j}{\eta_i+\eta_j} m_j \left(\frac{1}{\rho_i^2}+\frac{1}{\rho_j^2}\right) \frac{\partial W(r_{ij},h)}{\partial r_{ij}} \frac{(\mathbf{v}_{ij}+\mathbf{e}_{ij}.\mathbf{v}_{ij}\mathbf{e}_{ij})}{r_{ij}}, \tag{17}$$

where the dynamic viscosity is $\eta = \rho\nu$, and $\mathbf{v}_{ij} = \mathbf{v}_i - \mathbf{v}_j$ is the relative velocity vector from particle i to particle j [29]. The particle density is approximated as

$$\rho \approx \rho_t \tag{18}$$

for simplicity. The kinematic viscosity coefficient is defined as

$$\nu \sim 0.1 r_c |\mathbf{v}|, \tag{19}$$

where r_c is the kernel cut-off radius, leading to a local Reynolds number $\mathcal{O}(10)$.

The evolution of the particle system is determined by the background potential force and the viscous force. The potential force relaxes the particles towards the target configuration whereas the viscous force damps the velocity fluctuations. Mostly, the viscous effect is insufficient to damp all particle kinetic energies, making it difficult for the whole particle system to relax fully to steady state. Therefore, we propose a further damping at each time step by resetting the particle velocity

$$\mathbf{v}_n = \mathbf{0}, \tag{20}$$

after updating the particle positions.

2.8. Time integration method

For SPH, the Velocity-Verlet algorithm is widely utilized as time integration method [32]. This scheme is second-order accurate and reversible in time without viscous calculation. However it is quite time consuming because the total force for all particles is accumulated twice. As we seek for a steady solution, second-order accuracy is not necessary. We exploit a simple time integration method as

$$\begin{aligned} \tilde{\mathbf{v}}_{n+\frac{1}{2}} &= \mathbf{v}_n + \tfrac{1}{2}\mathbf{a}_n \Delta t, \\ \mathbf{v}_{n+\frac{1}{2}} &= \tilde{\mathbf{v}}_{n+\frac{1}{2}} + \tfrac{1}{2}\tilde{\mathbf{a}}_{n+\frac{1}{2}} \Delta t, \\ \mathbf{r}_{n+1} &= \mathbf{r}_n + \mathbf{v}_{n+\frac{1}{2}} \Delta t, \end{aligned} \tag{21}$$

where the acceleration $\mathbf{a}_n$ is calculated from the repulsive force $\mathbf{F_p}$ and $\mathbf{F_s}$, and the predicted velocity $\tilde{\mathbf{v}}_{n+\frac{1}{2}}$ at the mid-point is updated in the first step. The viscous force $\mathbf{F_v}$ is computed utilizing the predicted velocity field and $\tilde{\mathbf{a}}_{n+\frac{1}{2}}$ is obtained from this viscous force only. After that, a modified velocity field is defined in the second step, and the new particle coordinates are updated according to the modified velocity field. If the viscosity coefficient is zero, the second step is skipped and $\mathbf{v}_{n+\frac{1}{2}} = \tilde{\mathbf{v}}_{n+\frac{1}{2}}$.

For numerical stability, the time step Δt is constrained by a body force criterion

$$\Delta t \le 0.25\sqrt{\frac{r_c}{|\mathbf{a}|}}, \tag{22}$$

a Courant–Friedrichs–Lewy (CFL) criterion [33] assuming that the sound speed $c \approx 40|\mathbf{v}|_{\max}$, and a viscous criterion

$$\Delta t \le \min\left(\frac{1}{40}\frac{r_c}{|\mathbf{v}|}, 0.125\frac{r_c^2}{\nu}\right). \tag{23}$$

With the CFL constraint, in each iteration, the particle position is updated by a small step, which is proportional to the local smoothing length. Therefore, the fourth objective, i.e. the locality and incremental property, is satisfied.

3. Numerical algorithms

3.1. Initial condition

There are several basic ways to distribute the particles for the initial condition, e.g. uniformly or randomly. For our case, particles with the same color must be continuously distributed and this requirement can be achieved by two steps.

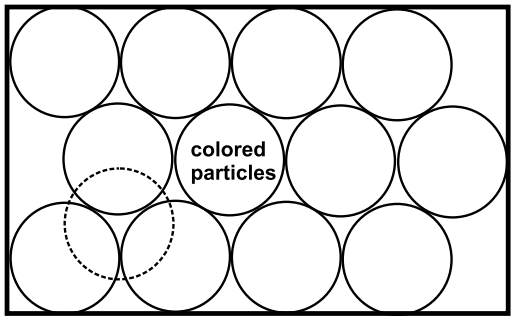

Fig. 2. Sketch for close packing methods. The circle with dotted line illustrates a projection of sphere in the third direction. Each circle is assigned with the same number of colored particles in the second step.

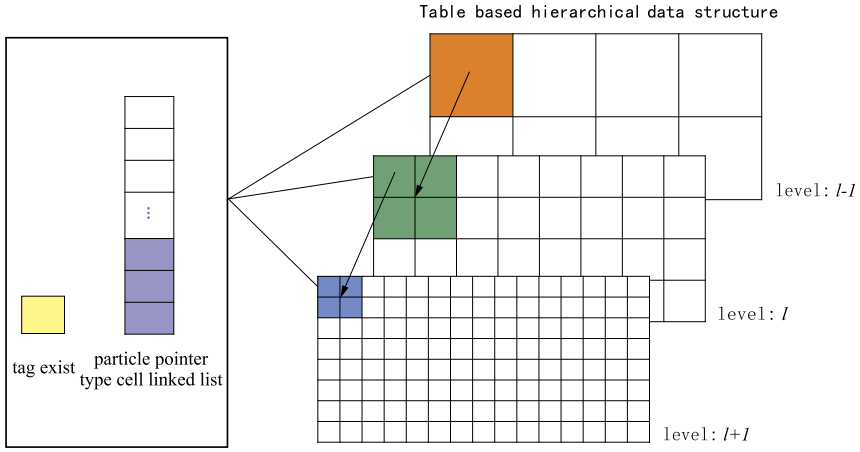

Fig. 3. Illustration of the multi-resolution cell-linked list for two dimensions. At each level, a table based data structure, which consists of an identifier *exist* and a cell-linked list, is initialized and dynamically updated throughout the simulation. The orange table element is the parent of the green ones while four blue table elements are the children of the green one. (For interpretation of the references to color in this figure legend, the reader is referred to the web version of this article.)

The first step is to roughly divide the physical domain into a desired number of partition sub-domains. We propose to exploit the geometry based close packing technique [34], which densely arranges an initial set of congruent circles (spheres in 3D) in a regular domain. There are two main types of lattice arrangements, i.e. face-centered cubic (fcc) for which every third layer is the same and hexagonal close-packed (hcp) for which every other layer is identical, to achieve the highest density packing. Here, the hexagonal close-packing method is adopted and the physical coordinates of the circle centers or the sphere centers can be generated by

$$\mathbf{r}_{center} = \begin{bmatrix} 2i + 1 + \mathrm{mod}(j,2) + \mathrm{mod}(k,2) \\ \sqrt{3}j + 1 + \frac{\sqrt{3}}{3}\mathrm{mod}(k,2) \\ \frac{2\sqrt{6}}{3}k + 1 \end{bmatrix} R, \tag{24}$$

where the index (i, j, k) starts with $(0, 0, 0)$, and R represents the radius of the circle or the sphere. For the second step, an equal number of particles with like color are randomly distributed within the corresponding circle or sphere as shown in Fig. 2. By this initial condition and the surface tension model, the second design target can be satisfied.

3.2. Fast neighbor search method

Cell-linked list [35] and Verlet list [32], which provide access to neighbor partners with $\mathcal{O}(1)$ operations, are two typical data structures to reduce the complexity for simulations with constant kernel cut-off radius. With the cell-linked list approach, the computational domain is divided into uniformly-distributed cells with edge length equal to the kernel cut-off radius. Each particle is mapped onto the corresponding cell-linked list by a pointer to the particle. By traversing the cell-linked list, where a certain particle is recorded, and the adjacent ones, all neighbor particles can be found rapidly. A Verlet list explicitly stores all the neighbor particles but strongly depends on an efficient construction method. A buffer is generally introduced to prevent frequent reconstruction of the Verlet list [32]. However, both of these methods are quite inefficient for resolution-adaptive particle simulations with variable kernel cut-off radii. Tree-based data structures have been proposed to address this problem [36].

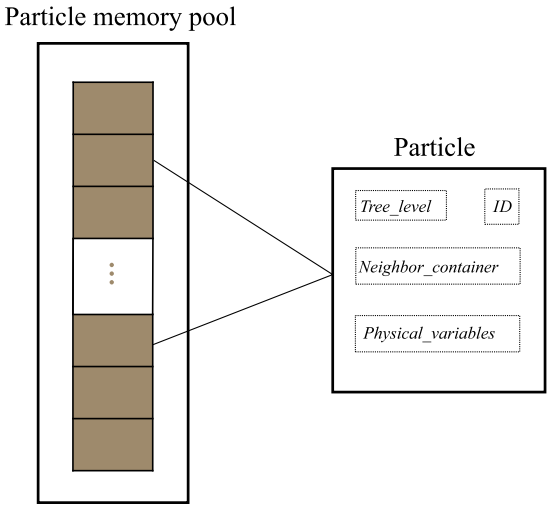

Fig. 4. Illustration of the particle data structure. *Physical_variables* denote the important particle properties, such as mass, density, pressure, smoothing-length. The particle data memories and the related operations, i.e. allocation and release, are managed by a "memory pool" [37].

We develop a multi-resolution neighbor search algorithm in combination with the Verlet list without margin to enable efficient neighbor access. Motivated by scatter-type sampling, the particle pairs are mutual neighbors when

$$r_{ij} \leq \max(r_{c,i}, r_{c,j}) \tag{25}$$

is satisfied. r_c is a function of physical space $r_c = r_c(\mathbf{r})$. The maximum multi-resolution level can be determined by

$$L_{max} = \log_2 \left(\frac{r_{c,\max}}{r_{c,\min}} \right) + 1. \tag{26}$$

The edge length of a cell on level l is

$$\Delta_l = \frac{r_{c,\max}}{2^l}, \quad l = 0, \cdots, L_{max} - 1\,. \tag{27}$$

At each level, a cell-linked list table, where the particle address pointers are recorded, is generated as shown in Fig. 3. The corresponding identifier *exist* is designed to record the status of a certain cell-linked list.

Fig. 4 shows the basic data structure for a particle, in which *Neighbor_container* is a pointer-type dynamic array to construct the Verlet list and ID is the globally unique particle identifier. The particle property *Tree_level* is defined as the level l at which

$$\frac{r_{c,\max}}{2^{l+1}} < r_c \leq \frac{r_{c,\max}}{2^l}. \tag{28}$$

Tree_level represents which level a certain particle belongs to and is unchanged within one time step. A specific particle is mapped onto the cell-linked list at level $l = Tree\_level$ with index (i, j)

$$(i, j) = \left(\text{int}(\frac{r_x}{\Delta_l}), \text{int}(\frac{r_y}{\Delta_l}) \right). \tag{29}$$

From the finest to the coarsest level, all members in the cell-linked list at level $l+1$ are additionally appended to the parent cell-linked list at level l. The parent cell-linked list index (i, j) can be derived from the children cell-linked list index (m, n) by

$$(i, j)_l = \left(\text{int}(\frac{m}{2}), \text{int}(\frac{n}{2}) \right)_{l+1}; \tag{30}$$

The children cell-linked list index can also be derived from its parent by

$$(m, n)_{l+1} = (2i + \delta_1, 2j + \delta_2)_l\,,\ \delta_1, \delta_2 = (0, 1). \tag{31}$$

Subsequently, the identifier *exist* is marked as 1 if the corresponding cell-linked list is occupied and 0 if it is empty. Each particle pointer is not only registered in the cell-linked list at *Tree_level* but also recorded at all coarser levels. Consequently, if a particle at *Tree_level* finds neighbors by searching the cell list where it is recorded and the adjacent ones, it can find particles at the same level and particles projected from the finer level. Particles can directly access others with equal or smaller kernel cut-off radius, but not those with larger kernel cut-off.

Algorithm 1 Fast neighbor search and Verlet list construction.

```
determine parameters and initialize multi-resolution based hierarchical data structure;
for all particles do
    define Tree_level through Eq. (28);
    map current particle to cell-linked list (i, j) on Tree_level through Eq. (29);
end for
for level from (L_max - 2) → 0 do
    for all cell-linked lists at current level do
        current cell-linked list ← current cell-linked list ∪ children cell lists at (level + 1);
    end for
end for
update the tag system exist;
for level from 0 → (L_max - 1) do
    for all cell-linked lists at current level ⋀ exist = 1 do
        for all particles in current cell-linked list do
            if Tree_level = current level then
                traverse all particles in current and adjacent lists, define as target particle;
                if Tree_level of target particle = current level then
                    Verlet list of current particle ⇐ target particle if satisfying Eq. (25);
                else
                    Verlet list of current particle ⇐ target particle if satisfying Eq. (25);
                    Verlet list of target particle ⇐ current particle if satisfying Eq. (25);
                end if
            end if
        end for
    end for
end for
```

As the final step, the multi-level cell-linked lists are traversed recursively from the coarsest to the finest level. For each particle registered in the cell list, if the tag $Tree\_level$ equals current loop level, then the particle neighbors can be detected in a similar way as that of cell-linked list technique with constant kernel cut-off radius, and the corresponding Verlet list is constructed at the same time. Note that particle pairs with the same $Tree\_level$ will access each other twice while only once with different values of $Tree\_level$. Details are given in Algorithm 1.

3.3. Boundary condition

For particles in the vicinity of a computational domain border, the support region of kernel function is incomplete and adequate boundary conditions, which are physically meaningful and numerically stable, must be imposed. The boundary force particle method [38], the ghost particle method [39], the semi-analytical method [40] are classical techniques to provide the full kernel support. The ghost particle method with mirror-particle technique is believed to be problem independent and suitable for simple geometries. Image particles are reconstructed by reflection of inner particles at the domain boundaries. Symmetry and wall boundary condition can be enforced by defining the velocity of the ghost particles appropriately. However, for variable kernel cut-off radii which may differ by orders of magnitude, a general implementation of the ghost particle method is quite storage consuming, as the size of particle reflection region must correspond to the largest kernel cut-off radius. As remedy, we develop a dynamic ghost particle method, which temporally reconstructs the ghost particles for inner boundary particles.

As sketched in Fig. 5, all particles first are checked and marked as boundary particle if the minimum distance d from the particle to the nearest boundary is less than the kernel cut-off r_c. For each boundary particle, all neighbors in the inner-domain have already been found and recorded in the Verlet list. If a particle is not recorded as neighbor in the Verlet list, its mirrored image particle will also not contribute to density or force evaluation. Based on this idea, a temporary list of ghost particles for each boundary particle can be generated by mirroring the neighboring particles in the Verlet list, and the force contribution from these ghost particles are accumulated. Since this reconstruction is local and temporary, the amount of ghost particles depends on the individual kernel cut-off radius of each boundary particle.

3.4. Refinement and coarsening of particle number

In order to represent the background mesh topology well and to provide an appropriate number of neighboring particles, the total particle number involved in the simulation should be maintained on a certain level. The scale ratio is defined as

$$S = \frac{N_p}{N_e}, \tag{32}$$

where N_p, N_e represent the total number of particles and mesh elements, respectively. We set

$$S_t = \begin{cases} 4, & 2D, \\ 8, & 3D. \end{cases} \tag{33}$$

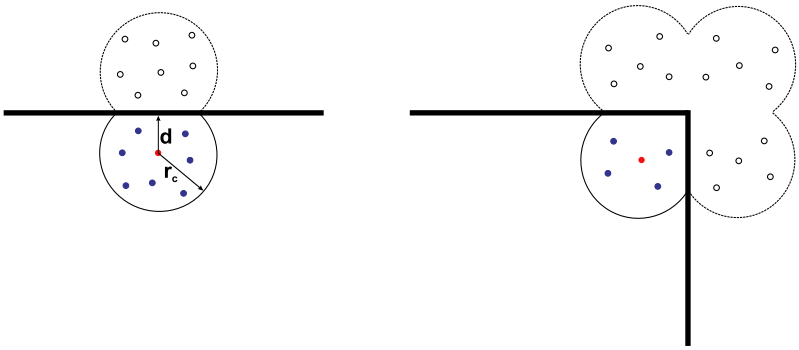

Fig. 5. Sketch for dynamic ghost particle method in two dimensions. The red particle denotes a specific boundary particle, and the blue ones are its neighbors inside the computational domain. The particles without colors are ghost particles constructed by current algorithm. The left panel indicates the boundary particle near a domain edge and the right panel near a domain corner. (For interpretation of the references to color in this figure legend, the reader is referred to the web version of this article.)

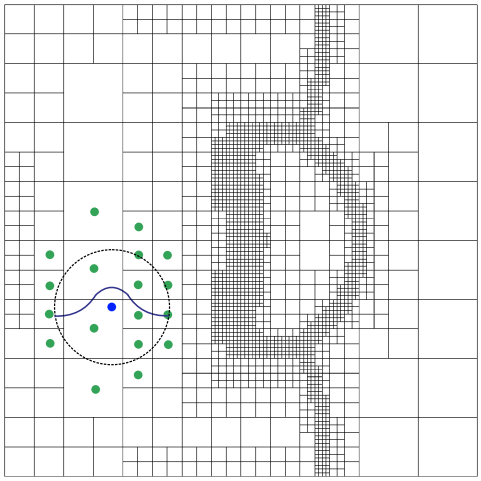

Fig. 6. Illustration for sampling procedure. The blue dot represents a simulation particle while green dots denote sampling particles. The blue curve indicates the kernel function shape on its support. The particle interaction cut-off radius is increased by a factor of 1.5 to take into account that some sampling particles fail to interact with any simulation particles. (For interpretation of the references to color in this figure legend, the reader is referred to the web version of this article.)

When the particle simulation starts, the user may not know exactly the number of mesh elements from background mesh topology. The input particle number then does not satisfy the target criterion in Eq. (33). This scenario frequently appears when the mesh topology undergoes big changes in dynamic load-balancing simulations. For adaptive adjustment of the total particle number satisfying the target criterion, we develop a refinement and coarsening strategy.

When the difference between S and S_t is larger than a threshold, a corresponding refinement or coarsening procedure is invoked. The number of particles to be added or deleted can be calculated by

$$N = \alpha \frac{\left| N_p - N_e S_t \right|}{N_c}, \tag{34}$$

where N_c represents the total number of particle colors and α is a relaxation factor. Concerning refinement, new particles should be generated away from interface and boundaries such that the interface is not disturbed. Otherwise, the new inserted particles close to an interface may lead to penetration into the other phase. Moreover, a certain number of new particles is distributed in the respective phase in a random way. Too many new generated particles gathering together tend to induce numerical instability.

3.5. Sampling procedure for post-processing

In order to assign all mesh elements to a certain partitioning sub-domain, an averaged sampling algorithm is designed as post-processing method. We construct a set of sampling particles at the coordinate centers of leaf mesh elements as shown in Fig. 6. Each simulation particle interacts with all sampling particles located in its kernel support.

For sampling particle i, the sampling function $C_{i,k}$ defined by

$$C_{i,k} = \sum_j \gamma_{jk} W(r_{ij}, h), \quad \begin{cases} i = 0, \cdots, N_e - 1, \\ j = 0, \cdots, N_p - 1, \\ k = 0, \cdots, N_c - 1, \end{cases} \tag{35}$$

where $\gamma_{jk} = \begin{cases} 1, & C_j = k, \\ 0, & \text{otherwise}, \end{cases}$ is calculated. The Wendland kernel [41]

$$W(r_{ij}, h) = \alpha(1-s)^8(1 + 8s + 25s^2 + 32s^3), \tag{36}$$

with

$$\alpha = \begin{cases} \frac{78}{7\pi h^2}, & 2D, \\ \frac{1365}{64\pi h^3}, & 3D, \end{cases} \tag{37}$$

is chosen as smoothing function.

During this procedure another traverse of the multi-resolution based hierarchical data structure is involved. A specific simulation particle is mapped onto every level of the multi-resolution cell-linked list, sampling particles within the support domain of its kernel are searched and the sampling function $C_{i,k}$ is calculated. The computational cost of this procedure is negligible, as the number of sampling particles is relatively small and it is conducted only when a detailed load-balance measurement is needed during the simulation. Finally, one mesh element represented by the sampling particle i is assigned to a partitioning sub-domain of color k_0 satisfying

$$C_{i,k_0} = \max(C_{i,0}, \cdots, C_{i,N_c-1}),\ k_0 = 0, \cdots, N_c - 1. \tag{38}$$

3.6. Convergence criteria

The imbalance error of a certain mesh topology partition can converge to zero when an appropriate number of particles is used and the relaxation is performed for sufficient time. However, the global zero-error target implies a prohibitive amount of computational cost in certain cases. A maximum imbalance error Er_{max} is defined as

$$Er_k = \frac{\left| N_{e,k} - \frac{N_e}{N_c} \right|}{\frac{N_e}{N_c}},\ k = 0, \cdots, N_c - 1, \tag{39}$$

$$Er_{max} = \max(Er_0, \cdots, Er_{N_c-1}), \tag{40}$$

where $N_{e,k}$ stands for the number of mesh elements belonging to partitioning sub-domain k. A predefined threshold of Er_{max}, e.g. 4%, is adopted as load-balance convergence criterion in our current implementation. Such a small level of load-imbalance is also accepted through user-tunable parameter in other partitioners [20]. Some particles may never come fully to rest as the solution of our model equations may not be unique. A second criterion is developed as follows: within a certain number of iterations, e.g. 50, the partitioning sub-domains do not change. The simulation terminates under the condition that both of these criteria are satisfied.

For dynamic load-balancing simulation, the above algorithms are repeated consecutively after the mesh topology changes. The major difference is that the SPH simulation result of the previous background mesh topology acts as the initial condition for a new mesh partition.

In practice, if we want to partition one mesh topology with few elements into too many parts, it may be quite difficult to decrease Er_{max} to less than the predefined threshold. Total iterations are generally limited to a certain number, e.g. $8000 \sim 10000$ for static partitioning and 40 for dynamic partitioning, if not mentioned otherwise.

4. Validation

In this section, we consider validation examples in two spatial dimensions. The restriction to two dimensions is to facilitate the presentation. We emphasize that the algorithm also applies to three dimensions with analogous results. Due to space limitations, we refer the presentation of three-dimensional results to the forthcoming 2nd part of this paper.

An adaptive multi-resolution code (MR-SIM) [2] is employed to perform the fluid simulations and to provide the background mesh topology for partitioning. We compute two types of partitionings, a static partitioning for the initial mesh topology generated by multi-resolution analysis before the actual flow simulation starts, and a dynamic partitioning for adaptive mesh topology following flow evolution. We point out that at this point, the dynamic partitioning algorithms have not yet been parallelized on distributed-memory architectures, i.e. all algorithms are implemented in a serial version. In order to measure and compare the computational efficiency, all simulations are carried out on the same desktop workstation equipped with 12 Intel(R) Xeon(R) CPU E5-2620 V2 cores (2.1 GHz and 32 GB memory) and Scientific Linux 6.7 system.

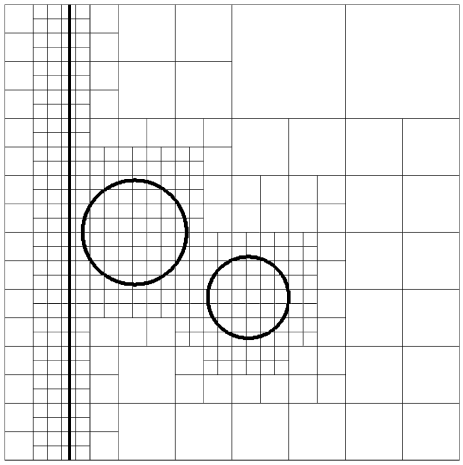

Fig. 7. Shock double water-columns interaction: target block-structured initial background mesh topology and schlieren-type images of density gradient $|\nabla\rho|$.

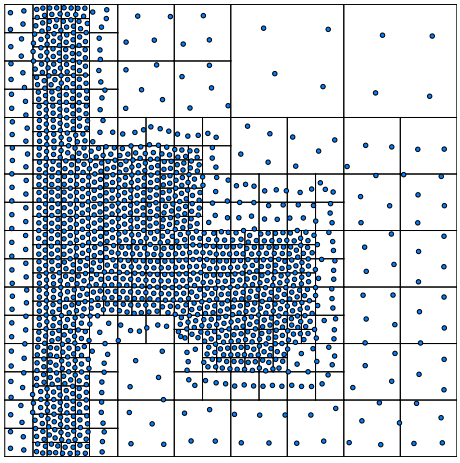

Fig. 8. Shock double water-columns interaction: particle representation of the target mesh topology. The blue circles represent simulated particles. (For interpretation of the references to color in this figure legend, the reader is referred to the web version of this article.)

4.1. Shock double water-columns interaction

The computational domain for this case is $[0, 2.8]\times[0, 2.8]$. The initial physical condition contains a shock wave and two water-columns close to each other. After multi-resolution analysis, the initial mesh topology is given in Fig. 7. The mesh resolution differs at most 8 times.

In order to check whether the target background mesh topology can be well represented, the surface tension model is turned off and all the simulated particles feature the same color. As shown in Fig. 8, the mesh resolution distribution is well characterized by the particle distribution. Each mesh element contains approximately 4 uniformly-distributed particles, which fully meets the design requirements.

We investigate the effect of the initial condition. In Fig. 9, the left panel shows uniformly distributed particles with colored function as straightforward choice of initial condition; on the right, particles are randomly assembled in circles arranged by a close packing method as newly proposed initial condition. The radius R is scaled slightly such that a gap between different particle phases is preset. This initial gap guarantees that there is enough time left to establish the sharp interface of multi-phase flow. It can be observed that particles near interface corners are always surrounded by four distinct phases for the former initial condition. Fig. 10 shows two time snapshots of SPH simulation results, the interface shape of the central phase gradually develops into quadrilateral with uniform initial condition. It becomes a hexagon or pentagon with our newly proposed initial condition. The latter ensures that all interface corners are shared by three phases and the interface angle is approximately 120°, which is a stable interface configuration.

Fig. 11 shows the particle distribution after 8000 iterations and the corresponding domain decomposition. The interface shape of particle phase with dark-orange color originating from a uniform initial condition forms a longer and thinner filaments than that from new initial condition. Particles in the filament may break away from their host phase and penetrate into other phases, as the inherent function of surface tension is unphysical. Furthermore, the sub-domain with purple color

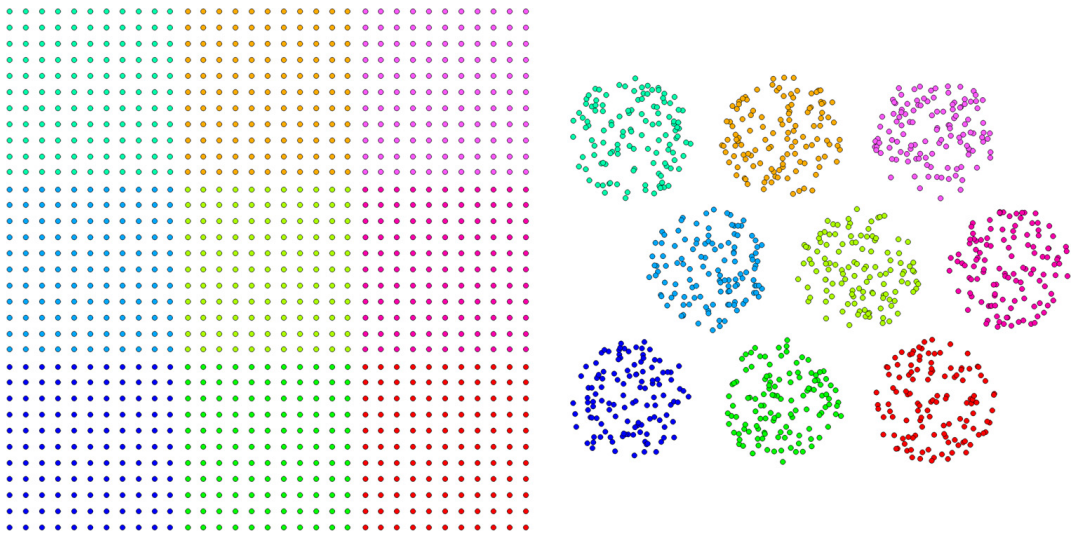

Fig. 9. Shock double water-columns interaction: initial particle distribution. Uniform distribution (left) and random distribution in combination with close packing method (right). The domain is partitioned into 9 sub-domains.

Table 1
Maximum imbalance error measurement and wall-clock time.

Number of total mesh elements	Number of partitioning sub-domains	Iteration number	Er_{max}	Wall-clock time (s)
385	4	3200	3%	38.4
385	6	3200	3%	38.7
385	9	8000	5% $\sim$ 10%	82.5

Shock double water-columns interaction. The wall-clock time is measured without multi-threaded parallelization. For block-structured mesh, 385 mesh elements mean typical 98560 cells with each block of resolution 16×16 [2].

generated by the uniform initial condition contains one mesh element with only a point connected to its host phase, while all mesh elements of the partition produced by the new initial condition connect to the other elements of the same phase or color with an edge. The new initial condition is beneficial for numerical robustness, interface communication reduction and the production of well connected sub-domains.

In Fig. 12, particles are mapped onto the background mesh topology. The left panel shows that the interfacial gap is less than the local mesh element size, and each mesh element contains approximate 4 particles except for those within an interface neighborhood. The right panel shows the coordinate relationship between the final partitioning sub-domains and the colored particle distributions. The proposed sampling procedure accurately classifies mesh elements into respective partitioning sub-domains.

Fig. 13 provides the distribution of the particle-neighbor number and the distribution of target density. Except for boundary particles, particles generally possess 10 neighbors, which is insufficient for standard SPH. The target density differs at most 64 times throughout the computational domain and jumps according to the mesh resolution change. With our proposed physically motivated models and specially designed EOS, the simulation is numerically stable and relaxes to the target result.

As shown in Table 1, for partition number less than 9, the simulations reach the imbalance error tolerance and converge within 3200 iterations. The error exhibits oscillations between 5% $\sim$ 10% and the simulation fails to achieve convergence until the iteration limit upon increasing the partition number to 9. Considering that the number of total mesh elements is too small at about 385 (representing 98560 mesh cells), when the computational domain is expected to be divided into 9 parts, the interfacial region dominates over partitioning sub-domains. Although the partitioning load-balance is sacrificed somewhat, a parallel simulation will still gain benefits as the interface communication is well optimized. For static partitioning, the proposed method is more time-consuming than the state-of-the-art methods. However, the present particle-based method is straightforward to be parallelized in a multi-threaded environment so that the wall-clock time can be reduced significantly. On the other hand, the dynamic partitioning can be quite efficient since only 40 iterations are necessary after the mesh topology changes. A preconditioning method may further improve the static partitioning efficiency. Another notable result is that the total computing-time only depends on the total mesh element number and the iteration number regardless of the partitioning number.

Table 2 gives the run-time analysis in detail. It is noted that the particle evolution algorithm accounts for the largest proportion of total wall-clock time.

Fig. 14 shows the dynamic partitioning results including particle distribution and partitioning sub-domains. It can be observed that the background mesh topology adjusts significantly during the simulation. Since our refinement and coarsening algorithms always adjust the total particle number correspondingly, the mesh topology is well represented with the

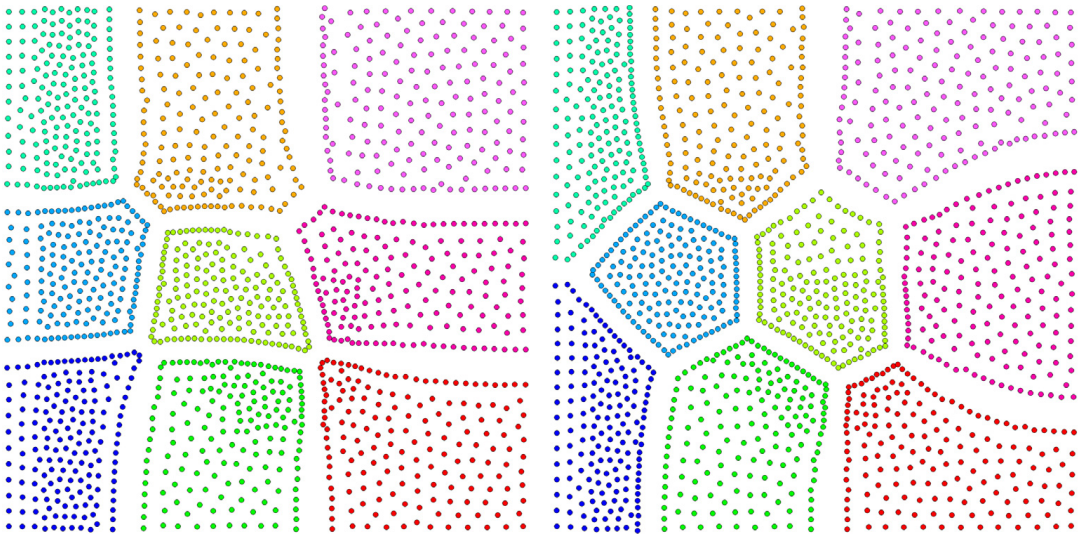

(a) Solution after 1000 iterations

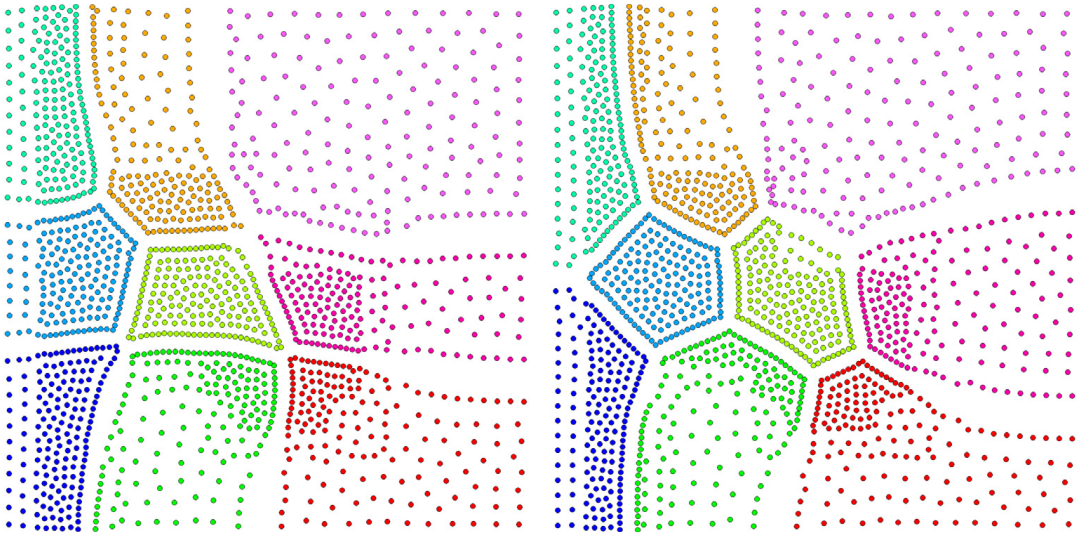

(b) Solution after 2000 iterations

Fig. 10. Shock double water-columns interaction: evolution of SPH simulation results. Uniform initial distribution (left) and random initial distribution in combination with close packing method (right).

Table 2
Wall-clock time measurement for component algorithms.

Total time (s)	Refinement and coarsening (s)	Boundary condition (s)	Fast neighbor search (s)	Particle evolution (s)
82.5	0.02 (0.02%)	6.3 (7.6%)	2.9 (3.5%)	73.28 (88.8%)

Shock double water-columns interaction with 385 mesh elements. The partitioning number is 9.

same accuracy throughout the simulation. The boundaries of different particle phases preserve convex and smooth shapes satisfying the design target. Although the mesh topology varies strongly, the partitioning topology however merely suffers from minor adaption, which implies that the produced partition is physically localized and implicitly incremental. For high performance computing, the data migration between processors is considerably reduced.

Fig. 15 gives the performance data of the load-balancing and the communication volume. During the simulation, the maximum imbalance error is approximately maintained to be 5% $\sim$ 10%. For the static partitioning, the communication volume is optimized by the surface tension model and converges roughly within 4000 iterations. For dynamic partitioning, the communication volume is optimized to decrease almost monotonically.

In order to demonstrate the potential of proposed method, static partitionings of 36 and 64 subdomains are computed for this case. The background mesh is generated at simulation time $t = 0.3$ of flow evolution. As shown in Fig. 16, the mesh element number is 10485, corresponding to a mesh cell size 2684160 in 2D. Fig. 17 gives the converged particle distribution.

(a) Solution after 8000 iterations

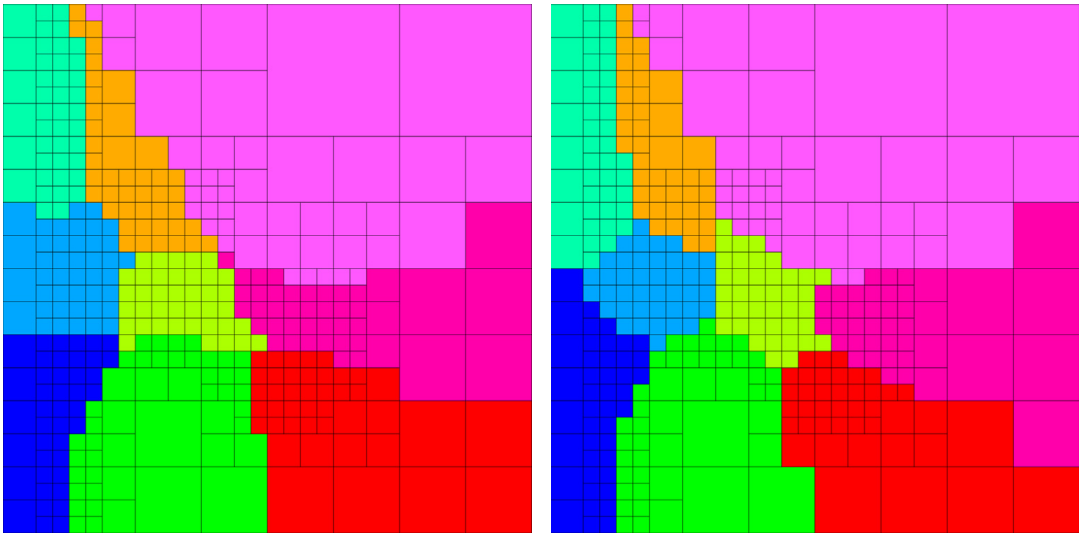

(b) Partitioning sub-domains after post-processing

Fig. 11. Shock double water-columns interaction: convergent solution of SPH simulation and domain decomposition. With initial uniform distribution (left) and random initial distribution in combination with close packing method (right). (For interpretation of the references to color in this figure, the reader is referred to the web version of this article.)

Table 3
Memory consumption.

Method	8^3 cells per mesh element			16^3 cells per mesh element		
	Number of elements	Memory consumption (GB)	Relative	Number of elements	Memory consumption (GB)	Relative
MR-SIM	7120	3.25	100%	5972	16.90	100%
partition	7120	0.56	17.23%	5972	0.55	3.25%

3D shock water-droplet interaction: the partitioning number is 8. The statistical data of MR-SIM represents the memory consumption of all fluid variables and the AMR data structure while that of partition denotes all the memory consumptions by our partitioning method.

The partitioning subdomains mostly are convex with sharp interfaces. As shown in Fig. 18, both the load-imbalance error and the communication volume are well optimized.

In order to test the memory consumption, we run a rather large realistic simulation of similar case. As shown in Table 3, when each mesh element represents 8^3 cells, the total memory usage increases by 17.23% with our partitioning method. If 16^3 cells are distributed in each mesh element following a typical setting [2], the memory consumption of our partitioning method only accounts for 3.25% of that taken by the fluid simulation. The increased memory consumption is small even without code optimization.

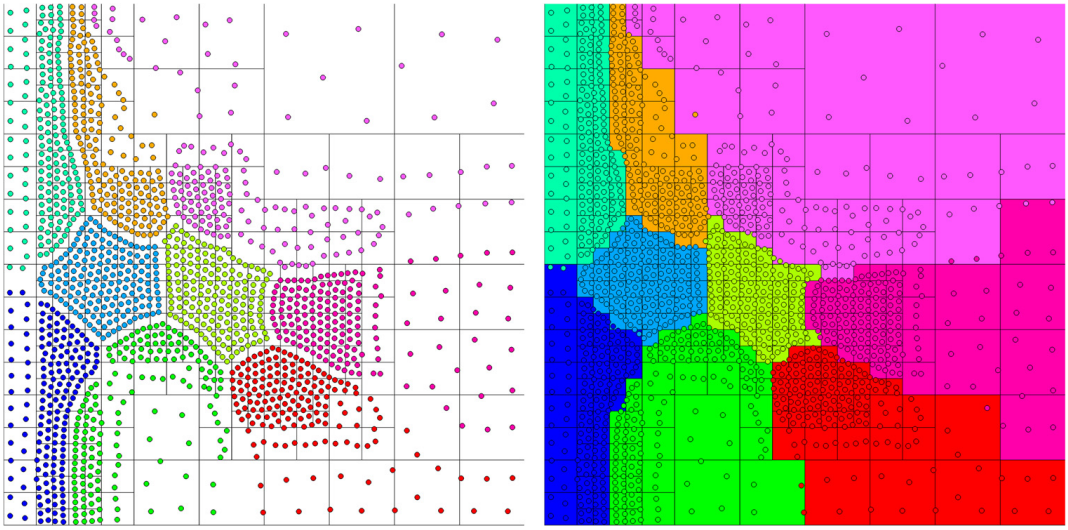

Fig. 12. Shock double water-columns interaction: post-processing procedure. Colored particles with background mesh (left) and partitioning sub-domains with particles after post processing (right).

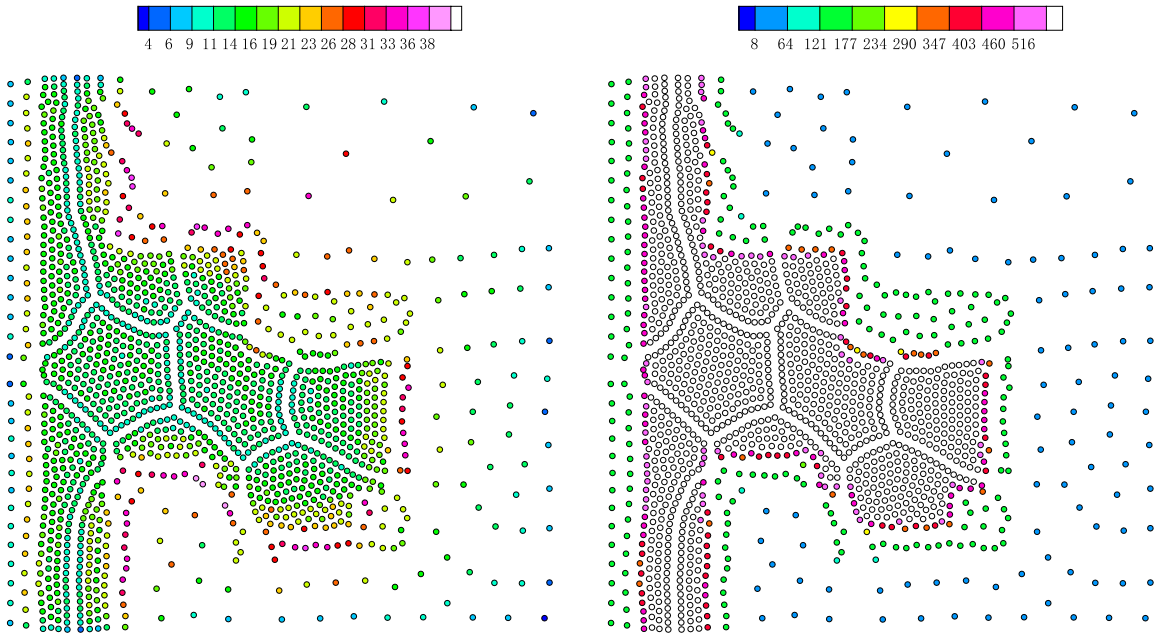

Fig. 13. Shock double water-columns interaction: distribution of the particle-neighbor number (left) and the target density (right) for a convergent solution. (For interpretation of the colors in this figure, the reader is referred to the web version of this article.)

4.2. Uniform mesh partitioning

We consider a static partition for uniform background mesh topology, which consists of 30×30 mesh elements (representing 230400 mesh cells). The SPH simulation involves 3600 particles and converges to target convergence criteria within 3200 iterations. Fig. 19 shows the SPH simulation result and the corresponding domain decomposition. Since all partitioning sub-domains preserve convex shapes as expected, the total interfacial area is well optimized. A considerably larger static partition, which involves 230400 particles and 57600 uniform mesh elements (representing 14745600 mesh cells), is shown in Fig. 20. The maximum imbalance error Er_{max} is approximate 4.17% with 50000 iterations. It can be observed that our partitioning result is similar to that from representative diffusion BUBBLE-FOS/C graph (Re)partitioning heuristic (see their Fig. 1 and Fig. 7 [20]) and is better than the solutions delivered by well-established softwares, e.g. Metis [7]. H. Meyerhenke et al. [20] point out that such convex sub-domain shapes, e.g. hexagon, are the regular shapes which cover a two-dimensional domain with smallest interface areas and thus the total interfacial energy is reduced to minimum.

As shown in Fig. 21, the load imbalance error and the communication volume are optimized to decrease monotonically.

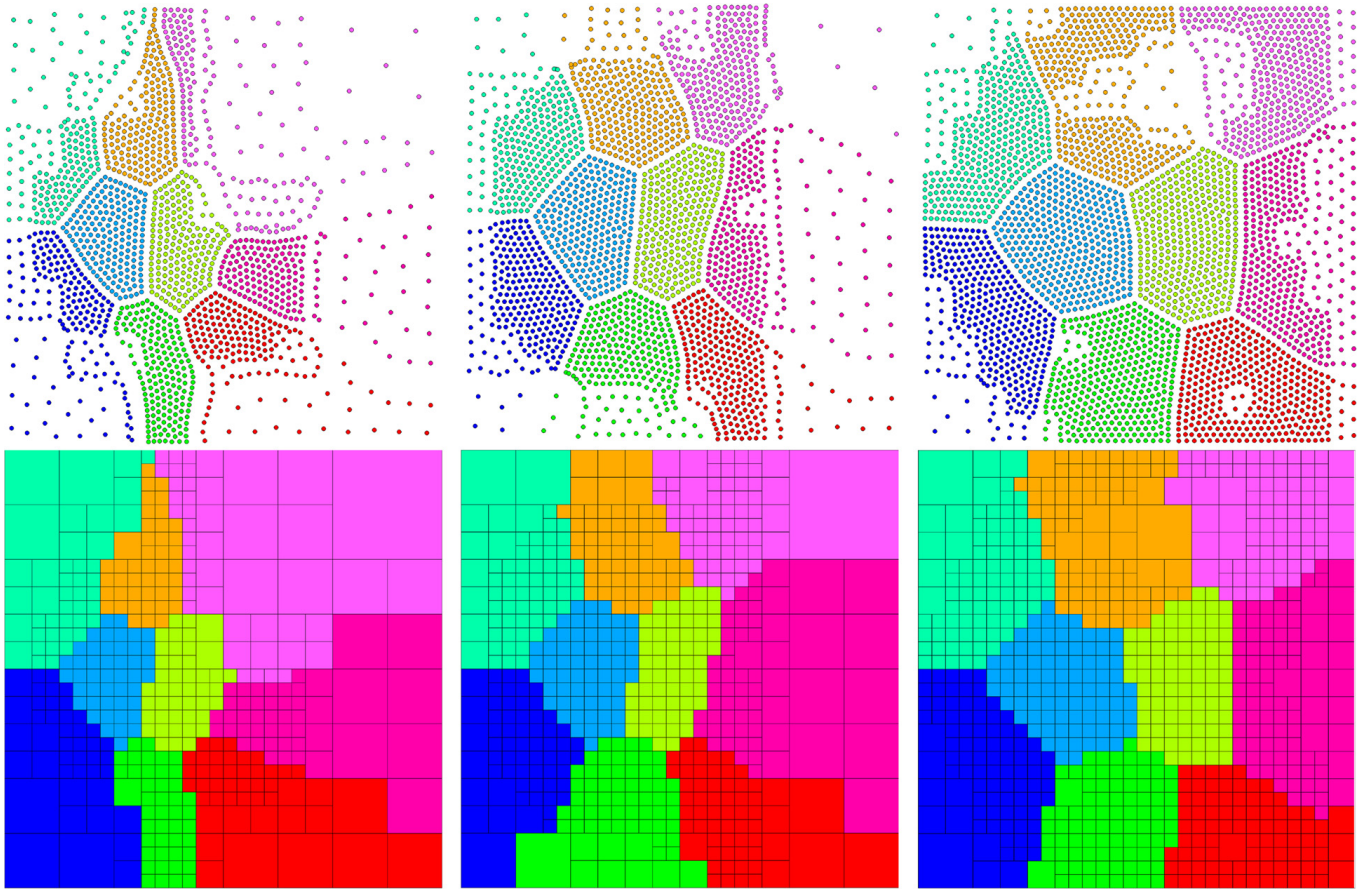

Fig. 14. Shock double water-columns interaction: dynamic load-balancing. SPH simulation solution (top) and domain decomposition with background mesh (bottom). From left to right: snapshots of simulation result at time 0.1, 0.2, 0.3.

4.3. Underwater explosion

This case is carried out in the computational domain $[0, 4]\times[0, 4]$. The ratio of the highest to the lowest resolution is 16 and most of mesh elements gather together in a narrow region as shown in Fig. 22. This inhomogeneity imposes a great deal of suffering on partitioning methods and is considerably challenging.

Fig. 23 gives the comparisons of SPH simulation result and domain decomposition with partition number of 4 and 9. The particle simulation converges within 3400 iterations when partitioning the domain into 4 parts while experiences 8000 iterations for partition number 9. The reason is similar to that discussed in case 1. All the particle phases maintain sharp and convex shapes well. The consumed wall-clock time is 61.0 s and 112.0 s, respectively without multi-threaded parallelization. Note that the 448 mesh elements typically represent 114688 mesh cells [2].

Fig. 24 shows the results of dynamic load-balancing simulation with partition number 4. It is obvious that the mesh topology experiences extremely large changes during the simulation. The mesh element distribution is continuously reconstructed via the coarsening and refinement procedures of multi-resolution analysis [2]. The total number of mesh elements involved grows rapidly from 448 (representing 114688 mesh cells) to 1822 (representing 466432 mesh cells). Nevertheless, the topology of partitioning sub-domains is highly analogous and the interface of the multi-phase flow only adjusts the position and shape slightly. In addition, all mesh elements connect to host partitioning sub-domain with edge, leading to strictly continuous partition. The surface tension builds up the sharp interface between distinct particle phases and keeps individual partitioning sub-domain closed. No particle penetration occurs throughout the entire simulation. When the partition number increases to 9, we once again obtain domain decompositions, which are physically localized and strictly connected with optimized interface area as sketched in Fig. 25.

The history of maximum imbalance error Er_{max} and scale ratio S involving both static and dynamic load-balancing simulations is shown in Fig. 26. For the partition number 4, SPH simulation always obtains a convergent result since the iteration number 3000. According to our numerical experiments, the error can be further reduced to nearly zero if more iterations are conducted when mesh topology changes. In terms of the partition number 9, Er_{max} fluctuates between 5% $\sim$ 10%, hence resulting in more total iterations accordingly. For both scenarios, the target scale ratio $S_t = 4$ is well maintained after 1000 iterations by the proposed refinement and coarsening algorithms.

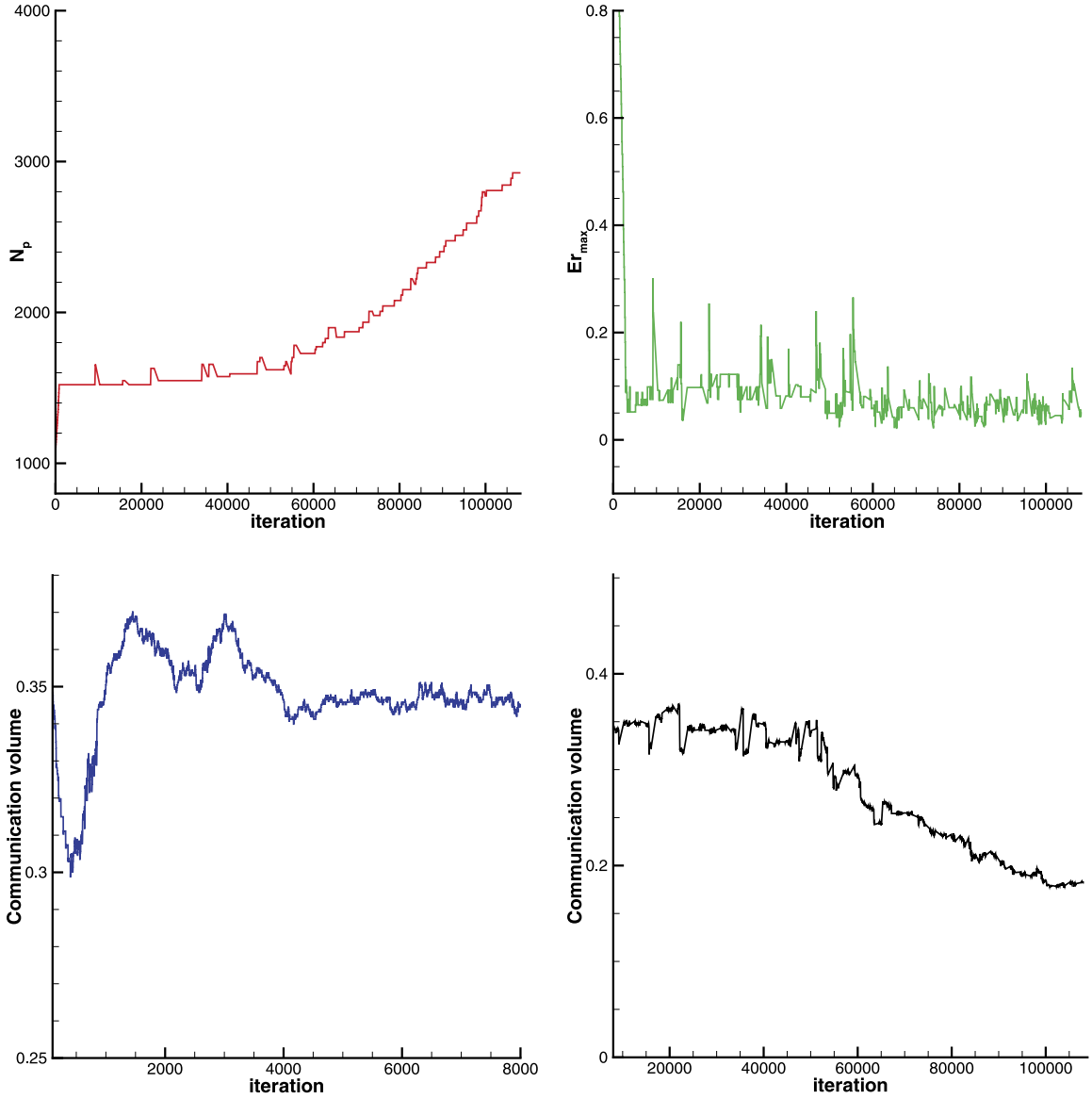

Fig. 15. Shock double water-columns interaction: history of total particle number N_p (top left panel), maximum imbalance error Er_{max} (top right panel), communication volume for static partitioning (bottom left panel) and dynamic partitioning (bottom right panel) versus iteration number. The partition number is 9. The communication volume is defined as the boundary particle number normalized by the total particle number while the boundary particle number is defined as the number of particles which feature neighboring particle of different color within its smoothing region.

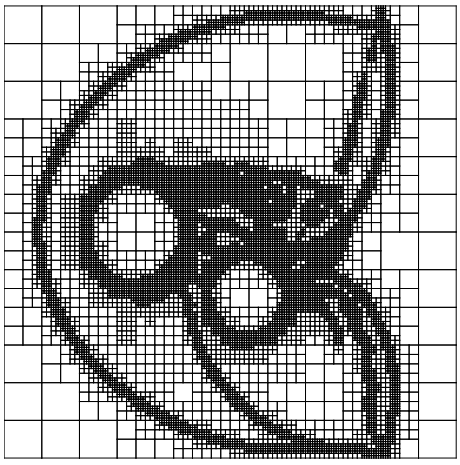

Fig. 16. Shock double water-columns interaction: target block-structured background mesh topology. The mesh element number is 10485, corresponding to a mesh cell size 2684160 in 2D.

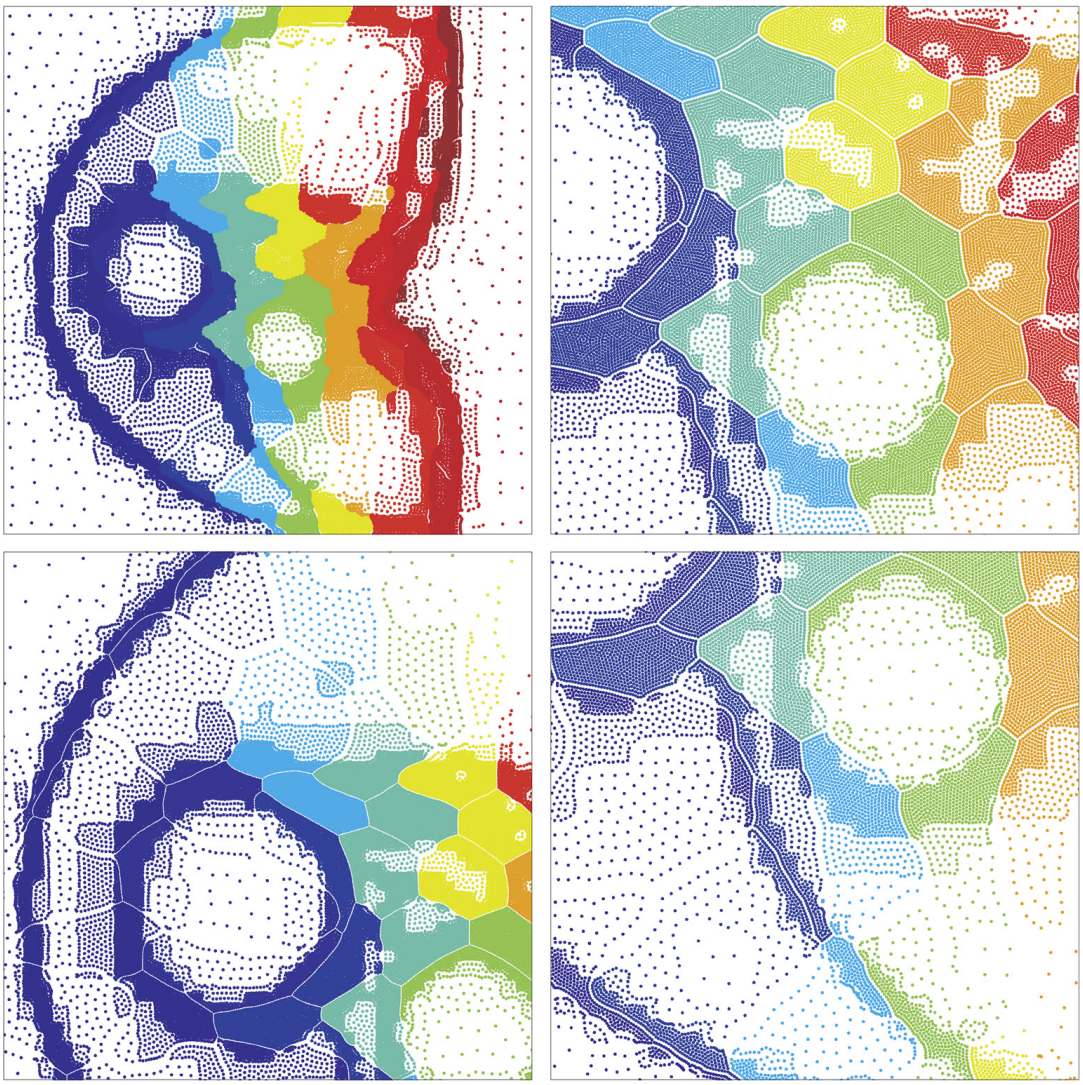

Fig. 17. Shock double water-columns interaction: the partitioning number is 64. The simulated particle number is 41728. The overall view (top left panel) and zoom-in views (others).

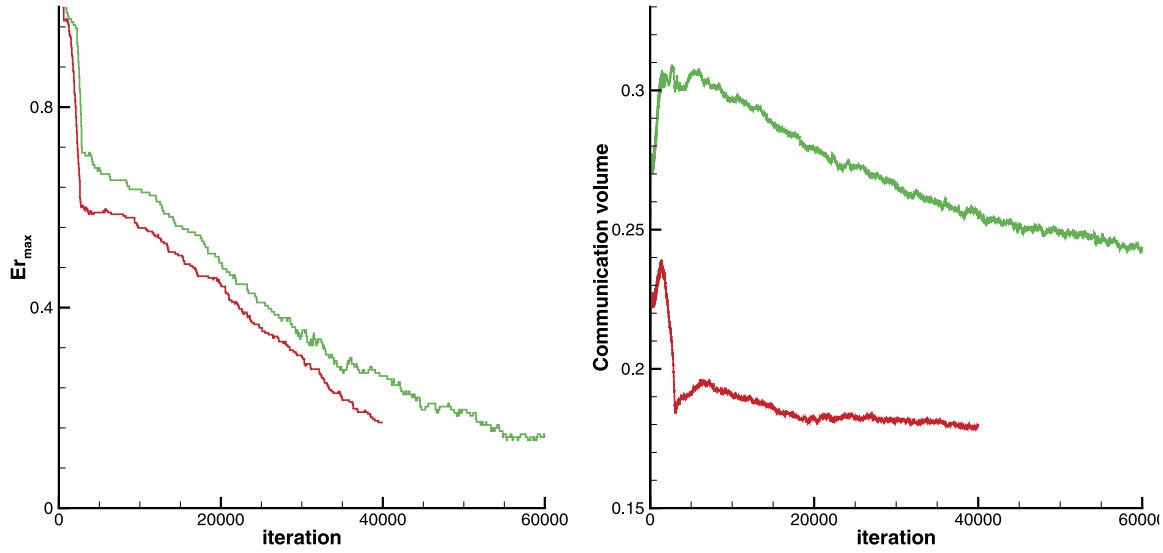

Fig. 18. Shock double water-columns interaction: history of load-imbalance error and communication volume versus iteration number (static partitioning). The red line represents the partition number 36 while the green line represents the partition number 64. (For interpretation of the references to color in this figure legend, the reader is referred to the web version of this article.)

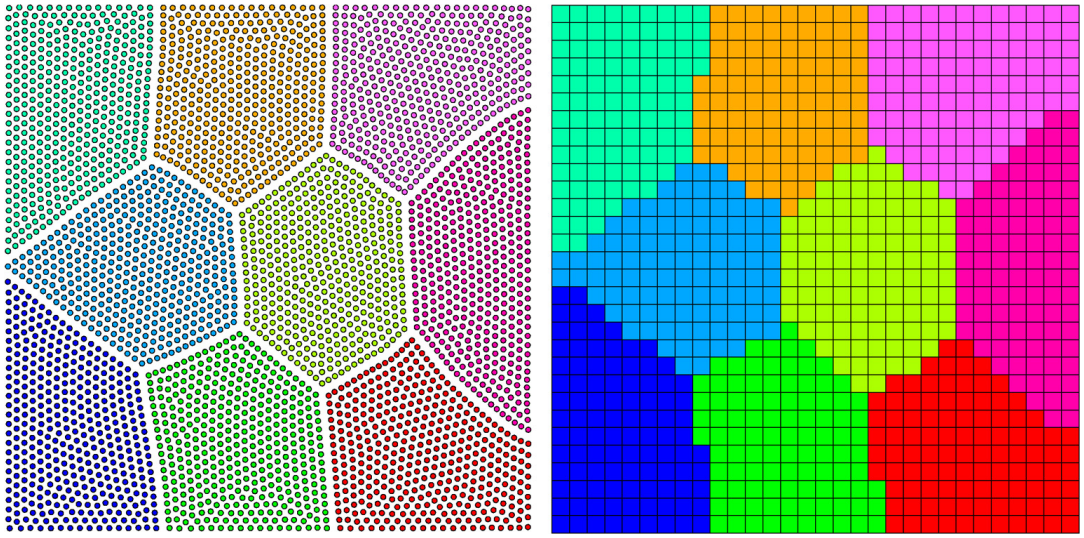

Fig. 19. Static partitioning for uniform mesh. SPH simulation solution (left panel) and domain decomposition with background mesh (right panel). The partition number is 9. The mesh element number is 900, corresponding to 230400 mesh cells.

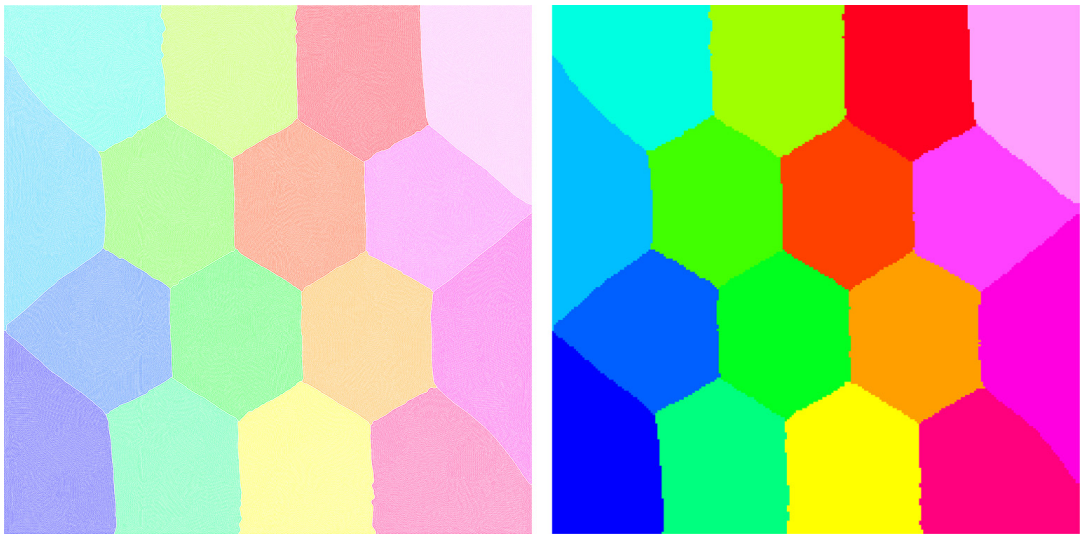

Fig. 20. Static partitioning for uniform mesh. SPH simulation solution (left panel) and domain decomposition (right panel). The partition number is 16. The mesh element number is 57600, corresponding to 14745600 mesh cells.

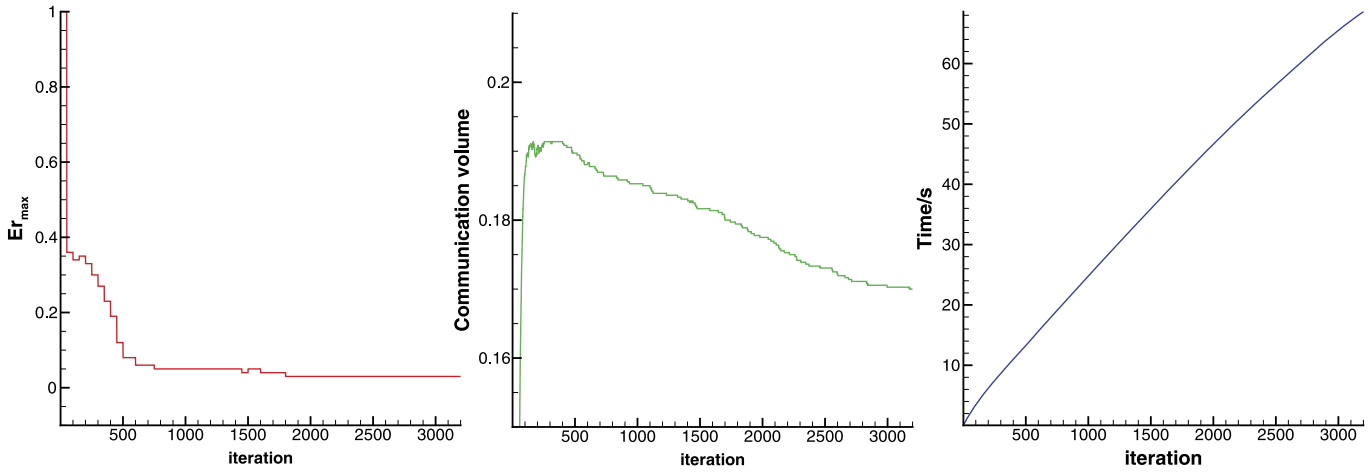

Fig. 21. Static partitioning for uniform mesh. History of maximum imbalance error Er_{max} (left), communication volume (middle) and wall-clock time (right) versus iteration number. The partition number is 9.

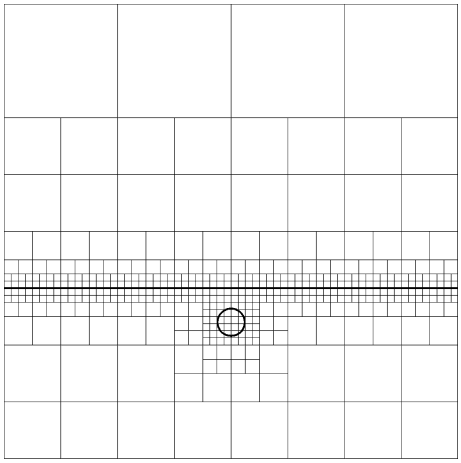

Fig. 22. Underwater explosion: target initial background mesh topology and schlieren-type images of density gradient $|\nabla\rho|$.

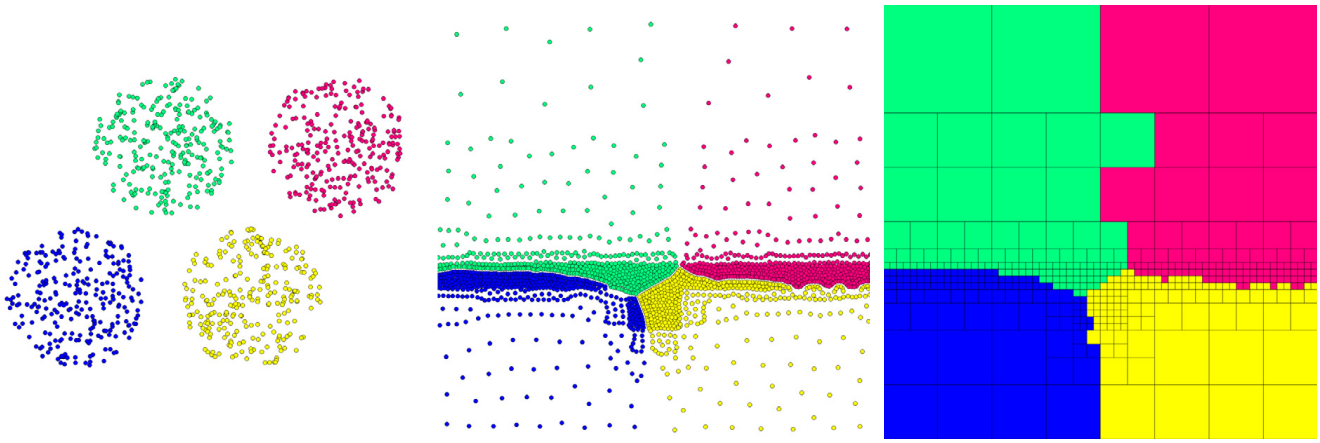

(a) From left to right: initial condition, solution at iteration number 3400, domain decomposition. The consumed wall-clock time is 61.0s.

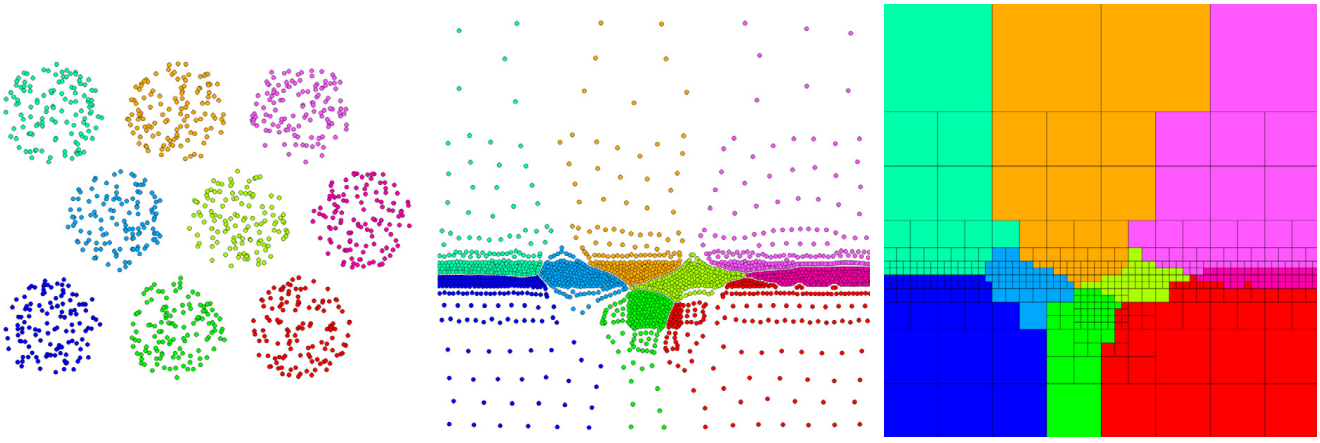

(b) From left to right: initial condition, solution at iteration number 8000, domain decomposition. The consumed wall-clock time is 112.0s.

Fig. 23. Underwater explosion: solution of SPH simulation and corresponding domain decomposition. The domain partition number is 4 (top) and 9 (bottom) respectively. The total mesh element number is 448 representing 114688 mesh cells.

As shown in Fig. 27, for the static partitioning, the communication volume converges well. For the dynamic partitioning, the communication volume is well optimized and decreases monotonically. The large partitioning number typically induces more communication and larger iteration numbers.

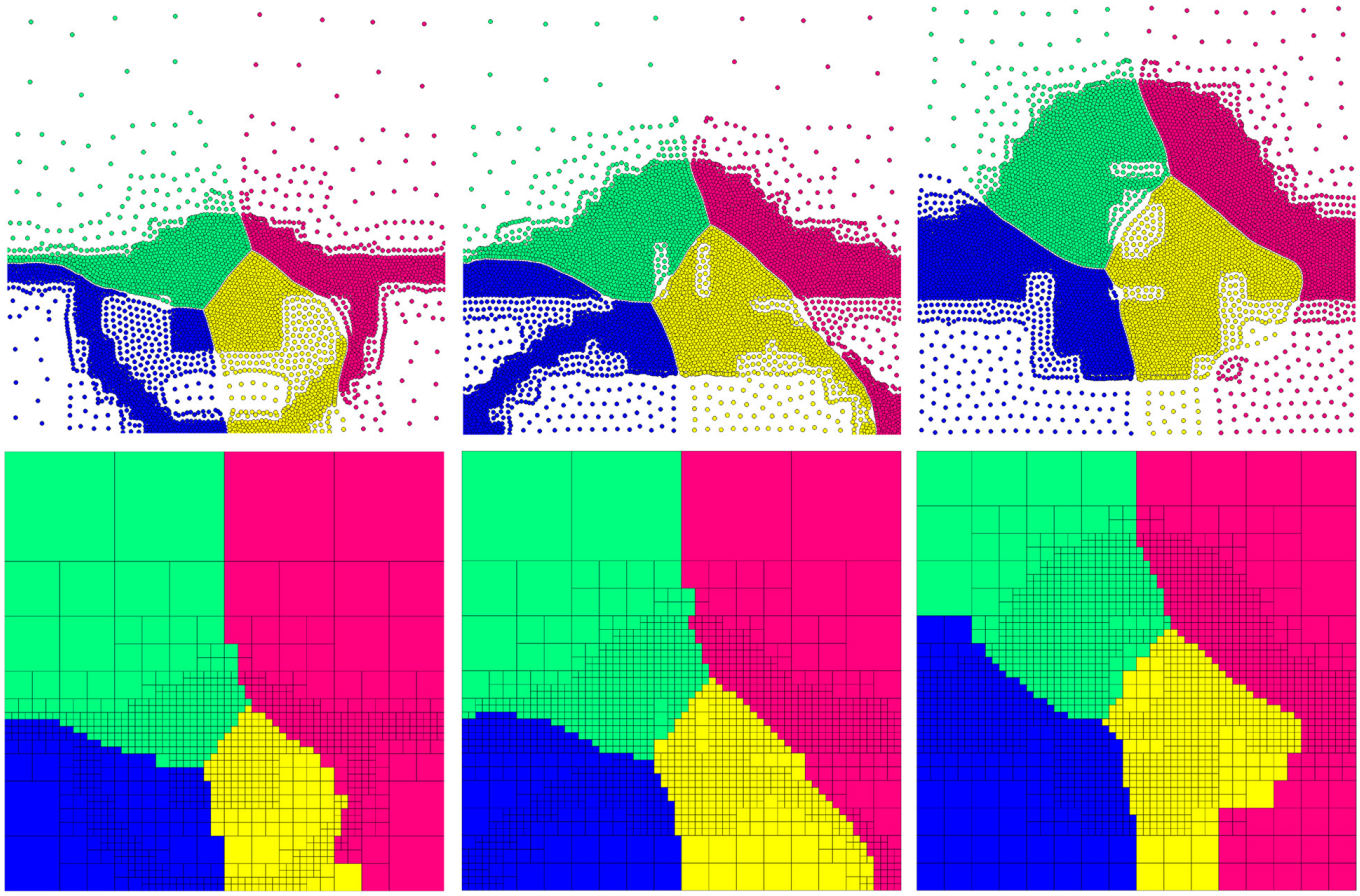

Fig. 24. Underwater explosion: solution of SPH simulation and corresponding domain decomposition. From left to right: SPH solution at fluid simulation time 0.06, 0.12, 0.20. Top: particle distribution, bottom: domain decomposition. The domain partition number is 4.

Table 4
Maximum imbalance error measurement and wall-clock time.

Number of total mesh elements	Number of partitioning subdomains	Iteration number	Er_{max}	Wall-clock time (s)
548	4	6850	4%	348.0
548	6	7200	3%	364.8
548	9	8000	10∼13%	381.4

Shock air-R22 bubble interaction. The wall-clock time is measured without multi-threaded parallelization. For block-structured mesh, 548 mesh elements mean typical 140288 cells with each block of resolution 16×16 [2].

4.4. Shock air-R22 bubble interaction

For this case, the mesh topology is canonical for the shock-bubble interaction simulation as Fig. 28. The computational domain is $[0, 0.445]\times[0, 0.089]$ with high aspect ratio. The mesh resolution differs by 16 times, leading to ratios of target density up to 256.

Fig. 29 and Fig. 30 provide the simulation results for static partition. Initially, particles are distributed in a small region and then expand to fill the full computational domain. After the simulations have converged, the characteristics of background mesh topology are well represented. As shown in Table 4, the SPH simulations converge within less than 8000 iterations for the partition number 4 and 6. In terms of larger partition number 9, it takes more iterations and produces larger imbalance error due to the relatively too small number of total mesh elements $N_e = 548$ (representing 140288 mesh cells).

Fig. 31 shows the dynamic partition results for the partition number 9. Although the mesh topology changes strongly, the SPH simulation robustly captures these target mutations and provides satisfactory domain decompositions, which are strictly continuous and localized. The relative-position relationship between distinct partitioning subdomains is preserved while minimizing the data movements among processors for parallel simulations.

Fig. 32 gives the convergence history of the communication volume. The communication volume converges well for the static partitioning and decreases monotonically during the dynamic partitioning.

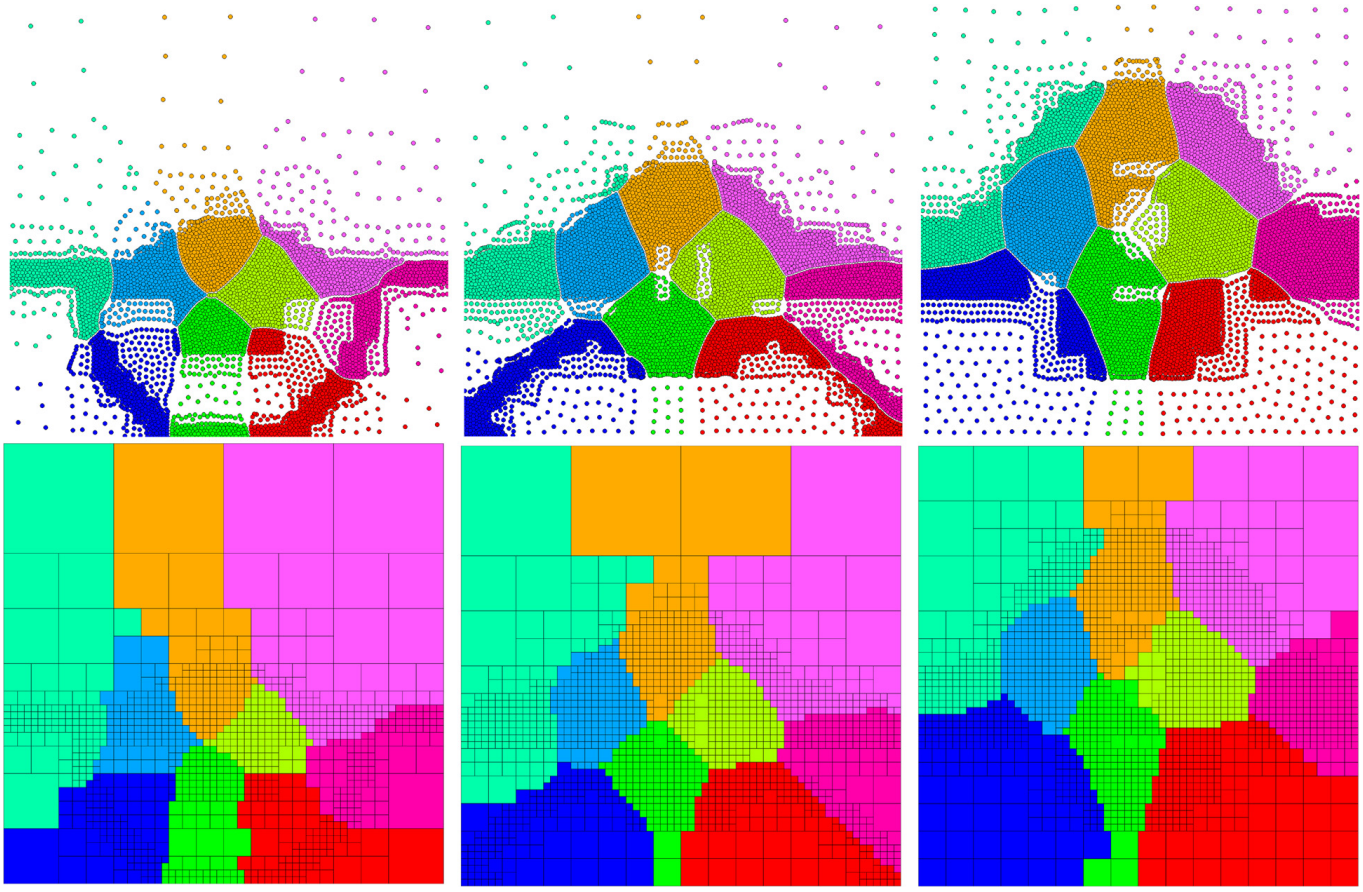

Fig. 25. Underwater explosion: solution of SPH simulation and corresponding domain decomposition. From left to right: SPH solution at fluid simulation time 0.06, 0.12, 0.20. Top: particle distribution, bottom: domain decomposition. The domain partition number is 9.

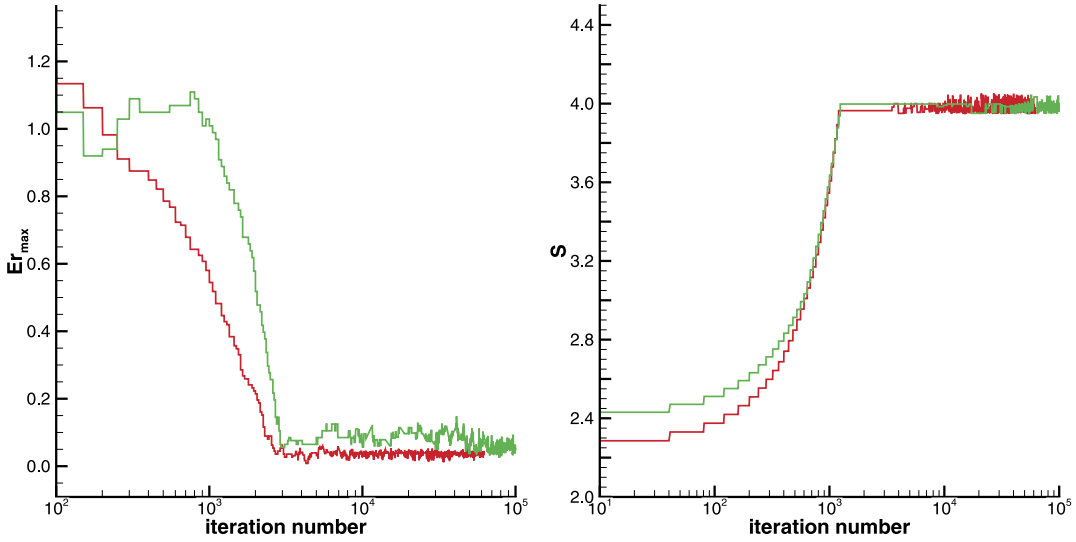

Fig. 26. Underwater explosion: history of maximum imbalance error Er_{max} (left panel) and scale ratio S (right panel) versus iteration number. The red line represents partition number 4 while the green line represents partition number 9. (For interpretation of the references to color in this figure legend, the reader is referred to the web version of this article.)

5. Conclusion

In this paper, we propose a novel approach to partition complex mesh topologies following a physically motivated approach. A set of model equations is developed and solved by a multi-phase SPH method based on physically meaningful variables extracted from the background mesh. The main properties of our proposed method are summarized as follows:

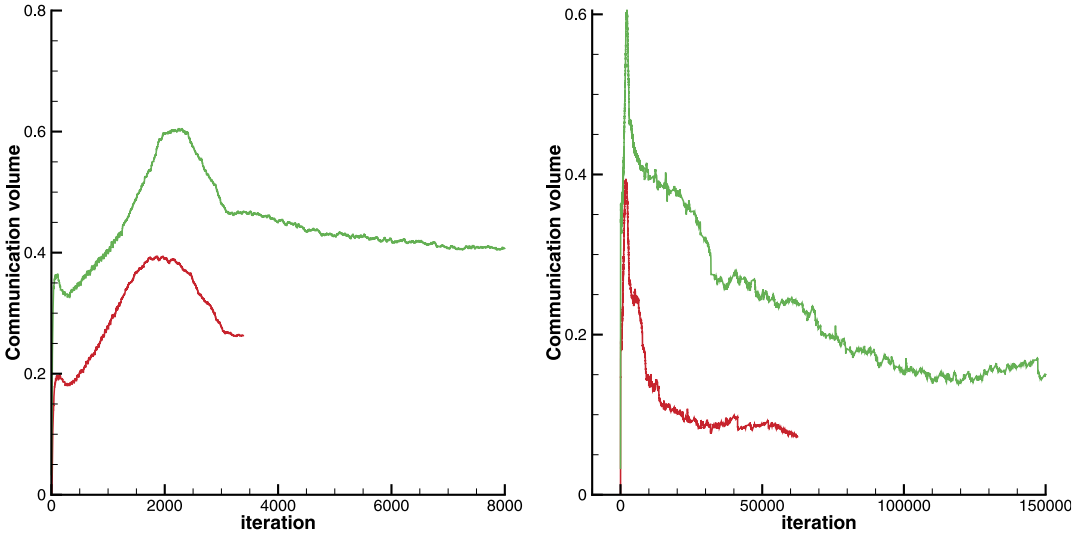

Fig. 27. Underwater explosion: history of communication volume versus iteration number. Left: for static partitioning; right: for dynamic partitioning. The red line represents partition number 4 while the green line represents partition number 9. (For interpretation of the references to color in this figure legend, the reader is referred to the web version of this article.)

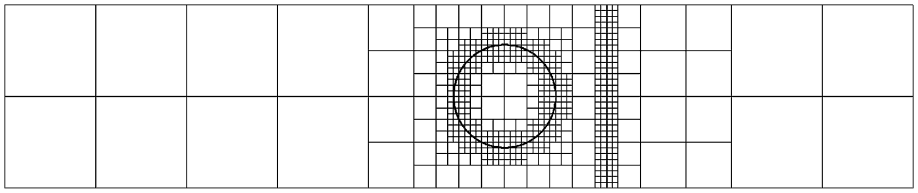

Fig. 28. Shock air-R22 bubble interaction: target background mesh topology and schlieren-type images of density gradient $|\nabla\rho|$.

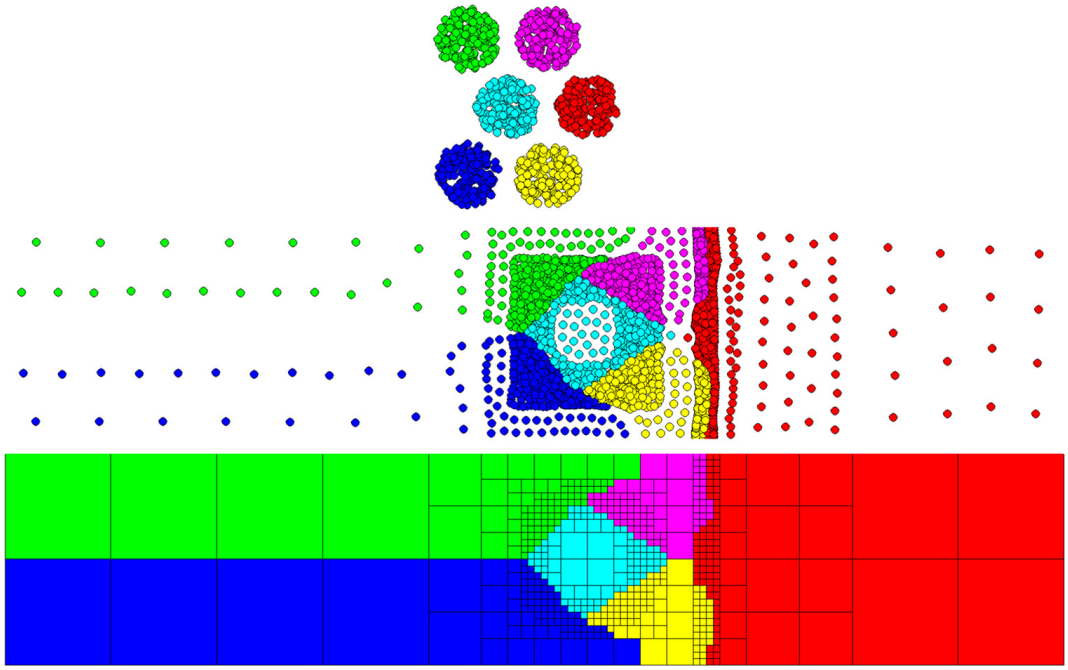

Fig. 29. Shock air-R22 bubble interaction: initial condition, solution at iteration 7200, convergent partition result. The domain partition number is 6. The total mesh element number is 548, corresponding to 140288 mesh cells.

(1) The imbalance error can be controlled with convergence criteria. In practice, it is sufficient to perform a certain number of iterations, as a compromise of computational efficiency and accuracy, instead of driving the imbalance error to zero.
(2) Different from graph-based partitioning approaches (except for the diffusion-based partitioning), which optimize the communications between distinct partitioning sub-domains by minimizing the number of edge-cuts explicitly, the proposed method optimizes mass near boundaries, i.e. element number, by a surface tension model implicitly.

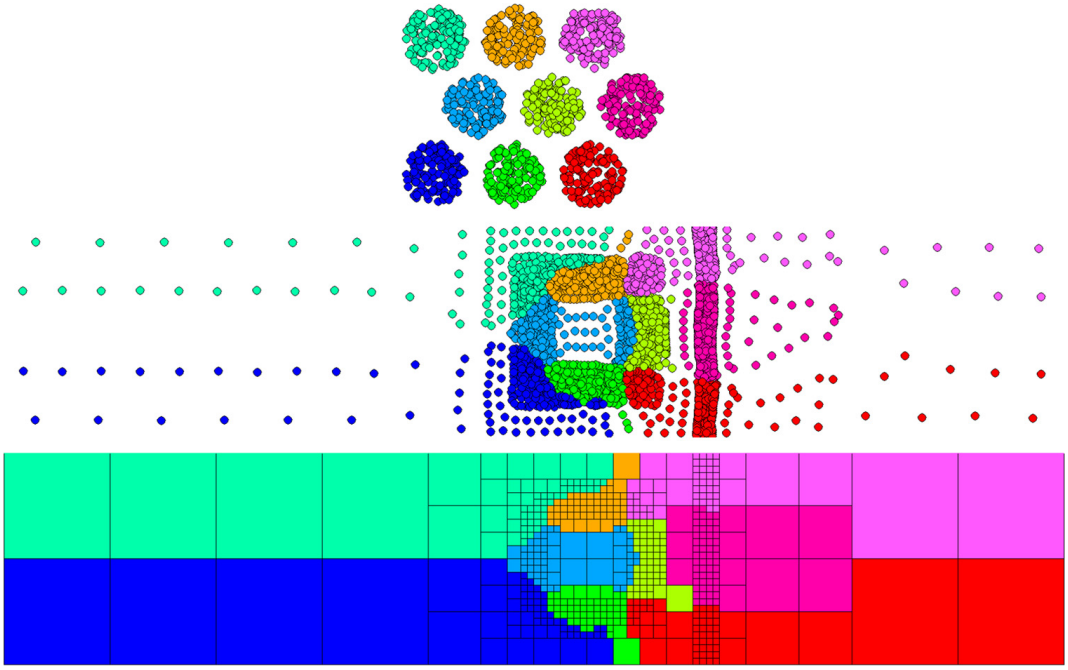

Fig. 30. Shock air-R22 bubble interaction: initial condition, solution at iteration 8000, convergent partition result. The domain partition number is 9. The total mesh element number is 548, corresponding to 140288 mesh cells.

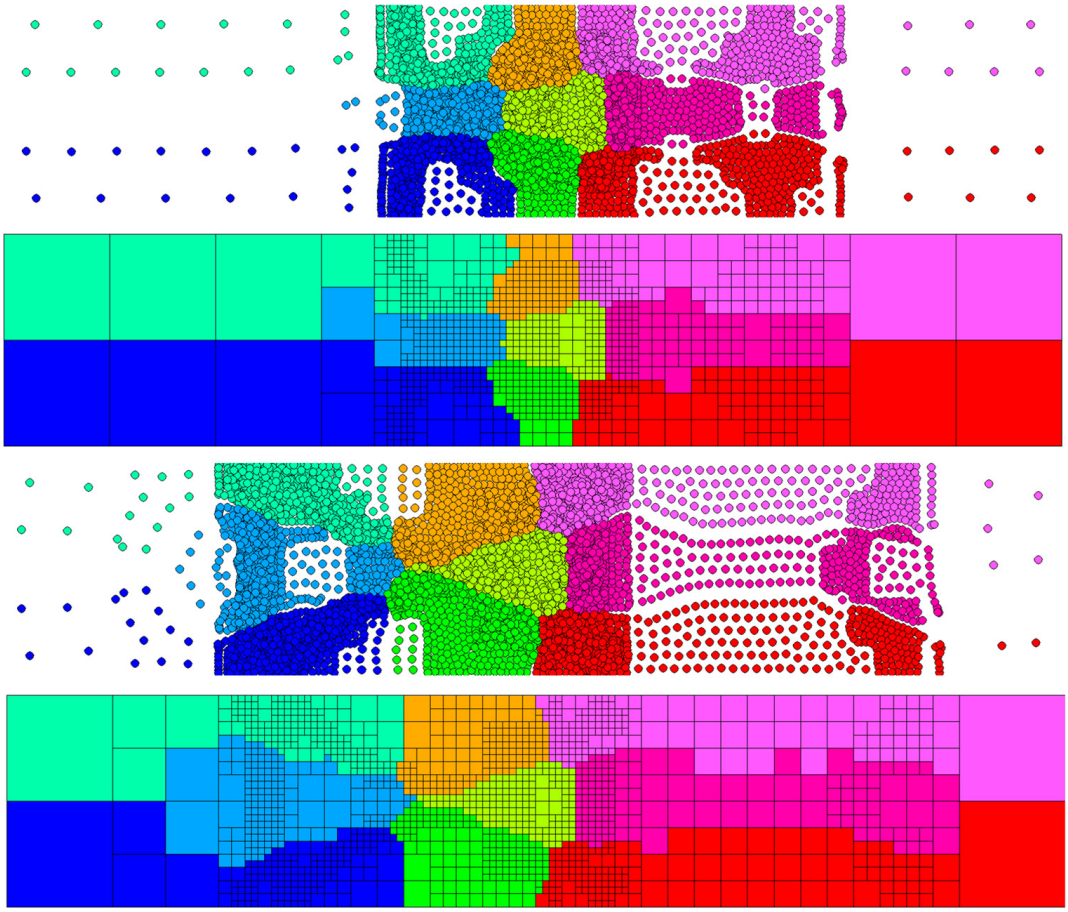

Fig. 31. Shock air-R22 bubble interaction: solution of SPH simulation and domain decomposition at fluid simulation time 0.0892 and 0.1386. Top: particle distribution; bottom: domain decomposition. The domain partition number is 9. The final mesh topology consists of 1244 mesh elements, corresponding to 318464 mesh cells.

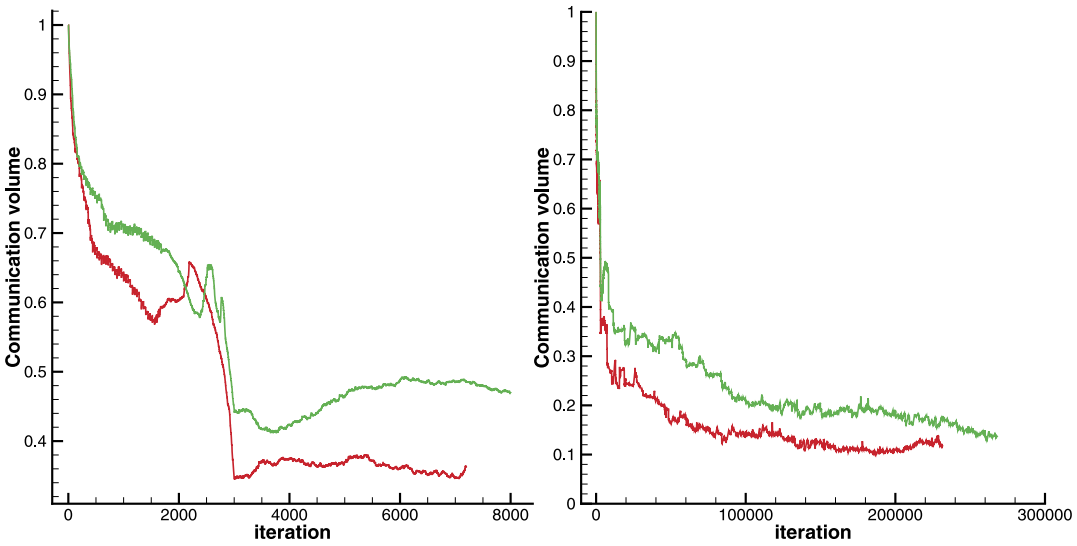

Fig. 32. Shock air-R22 bubble interaction: history of communication volume versus iteration number. Left: for static partitioning; right: for dynamic partitioning. The red line represents partition number 6 while the green line represents partition number 9. (For interpretation of the references to color in this figure legend, the reader is referred to the web version of this article.)

(3) Since the solution of the model equations continuously depends on the initial and boundary condition, the partition topology experiences minor changes when the mesh topology evolves. Thus, our proposed method is implicitly incremental and physically localized.
(4) The sufficient surface tension model guarantees the coherence of each particle phase, such that connected sub-domains are produced.

For static partitioning, the method may be slower than state-of-the-art graph-based partitioning methods because the initial particle distribution may be far from the equilibrium state and the SPH evolution is explicit in time. However, for dynamic load-balancing, the method becomes efficient as typically the number of necessary iterations becomes quite small due to its implicitly incremental and physical localization properties.

Acknowledgements

The first author is partially supported by China Scholarship Council (No. 201206290022). The second author acknowledges the support from his current institute.

References

[1] D. Butz, Y. Gao, A.M. Kempf, N. Chakraborty, Large eddy simulations of a turbulent premixed swirl flame using an algebraic scalar dissipation rate closure, Combust. Flame 162 (9) (2015) 3180–3196.
[2] L.H. Han, X.Y. Hu, N.A. Adams, Adaptive multi-resolution method for compressible multi-phase flows with sharp interface model and pyramid data structure, J. Comput. Phys. 262 (2014) 131–152.
[3] H. Ji, F.S. Lien, E. Yee, A new adaptive mesh refinement data structure with an application to detonation, J. Comput. Phys. 229 (2010) 8981–8993.
[4] E. Boman, K. Devine, R. Heaphy, R. Hendrickson, V. Leung, L.A.C. Vaughan, Zoltan: Parallel Partitioning, Load Balancing and Data Management Services, User's Guide Version 3.0 2007, pp. 1–173.
[5] B. Hendrickson, K. Devine, Dynamic load balancing in computational mechanics, Comput. Methods Appl. Mech. Eng. 184 (2C4) (2000) 485–500.
[6] C. Kavouklis, Y. Kallinderis, Parallel adaptation of general three-dimensional hybrid meshes, J. Comput. Phys. 229 (9) (2010) 3454–3473.
[7] G. Karypis, V. Kumar, Metis: A Software Package for Partitioning Unstructured Graphs, Partitioning Meshes, and Computing Fill-Reducing Orderings of Sparse Matrices, 1995.
[8] M. Berger, S. Bokhari, A partitioning strategy for nonuniform problems on multiprocessors, IEEE Trans. Comput. 36 (1987) 570–580.
[9] M.J. Berger, J. Oliger, Adaptive mesh refinement for hyperbolic partial differential equations, J. Comput. Phys. 53 (3) (1984) 484–512.
[10] A.R. Butz, Space filling curves and mathematical programming, Inf. Control 12 (1968) 314–330.
[11] H. Sagan, Space-Filling Curves, Springer, 1994.
[12] G.V. Nivarti, M.M. Salehi, W.K. Bushe, A mesh partitioning algorithm for preserving spatial locality in arbitrary geometries, J. Comput. Phys. 281 (2015) 352–364.
[13] A. Pothen, H. Simon, K. Liou, Partitioning sparse matrices with eigenvectors of graphs, SIAM J. Matrix Anal. Appl. 11 (3) (1990) 430–452.
[14] G. Karypis, V. Kumar, A fast and high quality multilevel scheme for partitioning irregular graphs, SIAM J. Sci. Comput. 20 (1999) 359–392.
[15] S.T. Barnard, H.D. Simon, Fast multilevel implementation of recursive spectral bisection for partitioning unstructured problems, Concurr., Pract. Exp. 6 (2) (1994) 101–117, http://dx.doi.org/10.1002/cpe.4330060203.
[16] B.W. Kernighan, S. Lin, An efficient heuristic procedure for partitioning graphs, Bell Syst. Tech. J. 49 (2) (1970) 291–307.
[17] C.M. Fiduccia, R.M. Mattheyses, A linear-time heuristic for improving network partitions, in: 19th Conference on Design Automation, IEEE, 1982, pp. 175–181.
[18] A. Buluç, H. Meyerhenke, I. Safro, P. Sanders, C. Schulz, Recent advances in graph partitioning, CoRR, arXiv:1311.3144, http://arxiv.org/abs/1311.3144.
[19] B. Hendrickson, T.G. Kolda, Graph partitioning models for parallel computing, Parallel Comput. 26 (12) (2000) 1519–1534.

[20] H. Meyerhenke, B. Monien, S. Schamberger, Graph partitioning and disturbed diffusion, Parallel Comput. 35 (10–11) (2009) 544–569.
[21] R. Diekmann, R. Preis, F. Schlimbach, C. Walshaw, Shape-optimized mesh partitioning and load balancing for parallel adaptive fem, Parallel Comput. 26 (12) (2000) 1555–1581.
[22] F. Pellegrini, A parallelisable multi-level banded diffusion scheme for computing balanced partitions with smooth boundaries, in: Euro-Par 2007 Parallel Processing, in: Lect. Notes Comput. Sci., vol. 4641, 2007, pp. 195–204.
[23] A. Rama Mohan Rao, Parallel mesh-partitioning algorithms for generating shape optimised partitions using evolutionary computing, Adv. Eng. Softw. 40 (2) (2009) 141–157.
[24] U. Catalyurek, C. Aykanat, Hypergraph-partitioning-based decomposition for parallel sparse-matrix vector multiplication, IEEE Trans. Parallel Distrib. Syst. 10 (7) (1999) 673–693.
[25] H. Meyerhenke, J. Gehweiler, On dynamic graph partitioning and graph clustering using diffusion, in: Dagstuhl Seminar Proceedings, 2010.
[26] H. Meyerhenke, B. Monien, T. Sauerwald, A new diffusion-based multilevel algorithm for computing graph partitions of very high quality, in: IEEE International Symposium on Parallel and Distributed Processing, IPDPS 2008, 2008, pp. 1–13.
[27] J.J. Monaghan, Smoothed particle hydrodynamics, Rep. Prog. Phys. 68 (2005) 1703–1759.
[28] K. Andreev, H. Raecke, Balanced graph partitioning, in: Proceedings of the Sixteenth Annual ACM Symposium on Parallelism in Algorithms and Architectures, 2004, pp. 120–124.
[29] X.Y. Hu, N.A. Adams, A multi-phase SPH method for macroscopic and mesoscopic flows, J. Comput. Phys. 213 (2006) 844–861.
[30] X.F. Yang, M.B. Liu, S.L. Peng, Smoothed particle hydrodynamics modeling of viscous liquid drop without tensile instability, Comput. Fluids 92 (2014) 199–208.
[31] B. Osting, C.D. White, É. Oudet, Minimal Dirichlet energy partitions for graphs, SIAM J. Sci. Comput. 36 (4) (2014) A1635–A1651.
[32] L. Verlet, Computer experiments on classical fluids. I. thermodynamical properties of Lennard–Jones molecules, Phys. Rev. 159 (1967) 98–103.
[33] R. Courant, K. Friedrichs, H. Lewy, Über die partiellen Differenzengleichungen der mathematischen Physik, Math. Ann. 100 (1) (1928) 32–74.
[34] S. Diehl, G. Rockefelle, C.L. Fryer, D. Riethmiller, T.S. Statler, Generating optimal initial conditions for smooth particle hydrodynamics simulations, arXiv:1211.0525.
[35] R.W. Hockney, J.W. Eastwood, Computer Simulation Using Particles, Institute of Physics Publishing, 1998.
[36] L. Arge, M.D. Berg, H.J. Haverkort, K. Yi, The priority r-tree: a practically efficient and worst-case optimal r-tree, in: Proc. SIGMOD, Intl. Conf. Management of Data.
[37] G. Contreras, M. Martonosi, Characterizing and improving the performance of Intel threading building blocks, in: 2008 IEEE International Symposium on Workload Characterization, IISWC2008, 2008, pp. 57–66.
[38] J.J. Monaghan, J.B. Kajtar, SPH particle boundary forces for arbitrary boundaries, Comput. Phys. Commun. 180 (2009) 1811–1820.
[39] A. Ferrari, M. Dumbser, E.F. Toro, A. Armanini, A new 3d parallel SPH scheme for free surface flows, Comput. Fluids 38 (2009) 1203–1217.
[40] A. Leroy, D. Violeau, M. Ferrand, C. Kassiotis, Unified semi-analytical wall boundary conditions applied to 2-D incompressible SPH, J. Comput. Phys. 261 (2014) 106–129.
[41] W. Dehnen, H. Aly, Improving convergence in smoothed particle hydrodynamics simulations without pairing instability, Mon. Not. R. Astron. Soc. 425 (2012) 1068–1082.

Appendix C:

Article III

A physics-motivated Centroidal Voronoi Particle domain decomposition method

In *Journal of Computational Physics*, Volume 335, 15 April 2017, pp. 718-735, DOI https://doi.org/10.1016/j.jcp.2017.01.051.

Contribution: My contribution to this work was the development of the method and the corresponding computer code for its implementation. I performed simulations and analyzed the results, and wrote the manuscript for the publication.

ELSEVIER LICENSE TERMS AND CONDITIONS

Jul 03, 2017

This Agreement between Institute of Aerodynamics and Fluid Mechanics, Technical University of Munich -- Lin Fu ("You") and Elsevier ("Elsevier") consists of your license details and the terms and conditions provided by Elsevier and Copyright Clearance Center.

License Number	4120700633284
License date	Jun 02, 2017
Licensed Content Publisher	Elsevier
Licensed Content Publication	Journal of Computational Physics
Licensed Content Title	A physics-motivated Centroidal Voronoi Particle domain decomposition method
Licensed Content Author	Lin Fu,Xiangyu Y. Hu,Nikolaus A. Adams
Licensed Content Date	Apr 15, 2017
Licensed Content Volume	335
Licensed Content Issue	n/a
Licensed Content Pages	18
Start Page	718
End Page	735
Type of Use	reuse in a thesis/dissertation
Portion	full article
Format	both print and electronic
Are you the author of this Elsevier article?	Yes
Will you be translating?	No
Order reference number	
Title of your thesis/dissertation	Numerical methods for computational fluid dynamics
Expected completion date	Aug 2017
Estimated size (number of pages)	126
Elsevier VAT number	GB 494 6272 12
Requestor Location	Institute of Aerodynamics and Fluid Mechanics, Technical University of Munich 85748 Garching Germany Munich, 85748 Germany Attn: Institute of Aerodynamics and Fluid Mechanics, Technical University of Munich
Publisher Tax ID	GB 494 6272 12
Total	**0.00 EUR**
Terms and Conditions	

INTRODUCTION

1. The publisher for this copyrighted material is Elsevier. By clicking "accept" in connection with completing this licensing transaction, you agree that the following terms and conditions apply to this transaction (along with the Billing and Payment terms and conditions established by Copyright Clearance Center, Inc. ("CCC"), at the time that you opened your Rightslink account and that are available at any time at http://myaccount.copyright.com).

GENERAL TERMS

2. Elsevier hereby grants you permission to reproduce the aforementioned material subject to the terms and conditions indicated.
3. Acknowledgement: If any part of the material to be used (for example, figures) has appeared in our publication with credit or acknowledgement to another source, permission must also be sought from that source. If such permission is not obtained then

that material may not be included in your publication/copies. Suitable acknowledgement to the source must be made, either as a footnote or in a reference list at the end of your publication, as follows:
"Reprinted from Publication title, Vol /edition number, Author(s), Title of article / title of chapter, Pages No., Copyright (Year), with permission from Elsevier [OR APPLICABLE SOCIETY COPYRIGHT OWNER]." Also Lancet special credit - "Reprinted from The Lancet, Vol. number, Author(s), Title of article, Pages No., Copyright (Year), with permission from Elsevier."
4. Reproduction of this material is confined to the purpose and/or media for which permission is hereby given.
5. Altering/Modifying Material: Not Permitted. However figures and illustrations may be altered/adapted minimally to serve your work. Any other abbreviations, additions, deletions and/or any other alterations shall be made only with prior written authorization of Elsevier Ltd. (Please contact Elsevier at permissions@elsevier.com). No modifications can be made to any Lancet figures/tables and they must be reproduced in full.
6. If the permission fee for the requested use of our material is waived in this instance, please be advised that your future requests for Elsevier materials may attract a fee.
7. Reservation of Rights: Publisher reserves all rights not specifically granted in the combination of (i) the license details provided by you and accepted in the course of this licensing transaction, (ii) these terms and conditions and (iii) CCC's Billing and Payment terms and conditions.
8. License Contingent Upon Payment: While you may exercise the rights licensed immediately upon issuance of the license at the end of the licensing process for the transaction, provided that you have disclosed complete and accurate details of your proposed use, no license is finally effective unless and until full payment is received from you (either by publisher or by CCC) as provided in CCC's Billing and Payment terms and conditions. If full payment is not received on a timely basis, then any license preliminarily granted shall be deemed automatically revoked and shall be void as if never granted. Further, in the event that you breach any of these terms and conditions or any of CCC's Billing and Payment terms and conditions, the license is automatically revoked and shall be void as if never granted. Use of materials as described in a revoked license, as well as any use of the materials beyond the scope of an unrevoked license, may constitute copyright infringement and publisher reserves the right to take any and all action to protect its copyright in the materials.
9. Warranties: Publisher makes no representations or warranties with respect to the licensed material.
10. Indemnity: You hereby indemnify and agree to hold harmless publisher and CCC, and their respective officers, directors, employees and agents, from and against any and all claims arising out of your use of the licensed material other than as specifically authorized pursuant to this license.
11. No Transfer of License: This license is personal to you and may not be sublicensed, assigned, or transferred by you to any other person without publisher's written permission.
12. No Amendment Except in Writing: This license may not be amended except in a writing signed by both parties (or, in the case of publisher, by CCC on publisher's behalf).
13. Objection to Contrary Terms: Publisher hereby objects to any terms contained in any purchase order, acknowledgment, check endorsement or other writing prepared by you, which terms are inconsistent with these terms and conditions or CCC's Billing and Payment terms and conditions. These terms and conditions, together with CCC's Billing and Payment terms and conditions (which are incorporated herein), comprise the entire agreement between you and publisher (and CCC) concerning this licensing transaction. In the event of any conflict between your obligations established by these terms and conditions and those established by CCC's Billing and Payment terms and conditions, these terms and conditions shall control.
14. Revocation: Elsevier or Copyright Clearance Center may deny the permissions described in this License at their sole discretion, for any reason or no reason, with a full refund payable to you. Notice of such denial will be made using the contact information provided by you. Failure to receive such notice will not alter or invalidate the denial. In no event will Elsevier or Copyright Clearance Center be responsible or liable for any costs, expenses or damage incurred by you as a result of a denial of your permission request, other than a refund of the amount(s) paid by you to Elsevier and/or Copyright Clearance Center for denied permissions.

LIMITED LICENSE

The following terms and conditions apply only to specific license types:
15. **Translation**: This permission is granted for non-exclusive world **English** rights only unless your license was granted for translation rights. If you licensed translation rights you may only translate this content into the languages you requested. A professional translator must perform all translations and reproduce the content word for word preserving the integrity of the article.
16. **Posting licensed content on any Website**: The following terms and conditions apply as follows: Licensing material from an Elsevier journal: All content posted to the web site must maintain the copyright information line on the bottom of each image; A hyper-text must be included to the Homepage of the journal from which you are licensing at http://www.sciencedirect.com/science/journal/xxxxx or the Elsevier homepage for books at http://www.elsevier.com; Central Storage: This license does not include permission for a scanned version of the material to be stored in a central repository such as that provided by Heron/XanEdu.
Licensing material from an Elsevier book: A hyper-text link must be included to the Elsevier homepage at http://www.elsevier.com . All content posted to the web site must maintain the copyright information line on the bottom of each image.

Posting licensed content on Electronic reserve: In addition to the above the following clauses are applicable: The web site must be password-protected and made available only to bona fide students registered on a relevant course. This permission is granted for 1 year only. You may obtain a new license for future website posting.
17. **For journal authors:** the following clauses are applicable in addition to the above:
Preprints:

A preprint is an author's own write-up of research results and analysis, it has not been peer-reviewed, nor has it had any other value added to it by a publisher (such as formatting, copyright, technical enhancement etc.).
Authors can share their preprints anywhere at any time. Preprints should not be added to or enhanced in any way in order to appear more like, or to substitute for, the final versions of articles however authors can update their preprints on arXiv or RePEc with their Accepted Author Manuscript (see below).
If accepted for publication, we encourage authors to link from the preprint to their formal publication via its DOI. Millions of researchers have access to the formal publications on ScienceDirect, and so links will help users to find, access, cite and use the best available version. Please note that Cell Press, The Lancet and some society-owned have different preprint policies. Information on these policies is available on the journal homepage.
Accepted Author Manuscripts: An accepted author manuscript is the manuscript of an article that has been accepted for publication and which typically includes author-incorporated changes suggested during submission, peer review and editor-author communications.
Authors can share their accepted author manuscript:

- immediately
  - via their non-commercial person homepage or blog
  - by updating a preprint in arXiv or RePEc with the accepted manuscript
  - via their research institute or institutional repository for internal institutional uses or as part of an invitation-only research collaboration work-group
  - directly by providing copies to their students or to research collaborators for their personal use
  - for private scholarly sharing as part of an invitation-only work group on commercial sites with which Elsevier has an agreement
- After the embargo period
  - via non-commercial hosting platforms such as their institutional repository
  - via commercial sites with which Elsevier has an agreement

In all cases accepted manuscripts should:

- link to the formal publication via its DOI
- bear a CC-BY-NC-ND license - this is easy to do
- if aggregated with other manuscripts, for example in a repository or other site, be shared in alignment with our hosting policy not be added to or enhanced in any way to appear more like, or to substitute for, the published journal article.

Published journal article (JPA): A published journal article (PJA) is the definitive final record of published research that appears or will appear in the journal and embodies all value-adding publishing activities including peer review co-ordination, copy-editing, formatting, (if relevant) pagination and online enrichment.
Policies for sharing publishing journal articles differ for subscription and gold open access articles:
Subscription Articles: If you are an author, please share a link to your article rather than the full-text. Millions of researchers have access to the formal publications on ScienceDirect, and so links will help your users to find, access, cite, and use the best available version.
Theses and dissertations which contain embedded PJAs as part of the formal submission can be posted publicly by the awarding institution with DOI links back to the formal publications on ScienceDirect.
If you are affiliated with a library that subscribes to ScienceDirect you have additional private sharing rights for others' research accessed under that agreement. This includes use for classroom teaching and internal training at the institution (including use in course packs and courseware programs), and inclusion of the article for grant funding purposes.
Gold Open Access Articles: May be shared according to the author-selected end-user license and should contain a CrossMark logo, the end user license, and a DOI link to the formal publication on ScienceDirect.
Please refer to Elsevier's posting policy for further information.
18. **For book authors** the following clauses are applicable in addition to the above: Authors are permitted to place a brief summary of their work online only. You are not allowed to download and post the published electronic version of your chapter, nor may you scan the printed edition to create an electronic version. **Posting to a repository:** Authors are permitted to post a summary of their chapter only in their institution's repository.
19. **Thesis/Dissertation**: If your license is for use in a thesis/dissertation your thesis may be submitted to your institution in either print or electronic form. Should your thesis be published commercially, please reapply for permission. These requirements include permission for the Library and Archives of Canada to supply single copies, on demand, of the complete thesis and include permission for Proquest/UMI to supply single copies, on demand, of the complete thesis. Should your thesis be published commercially, please reapply for permission. Theses and dissertations which contain embedded PJAs as part of the formal submission can be posted publicly by the awarding institution with DOI links back to the formal publications on ScienceDirect.

Elsevier Open Access Terms and Conditions
You can publish open access with Elsevier in hundreds of open access journals or in nearly 2000 established subscription journals that support open access publishing. Permitted third party re-use of these open access articles is defined by the author's choice of Creative Commons user license. See our open access license policy for more information.
Terms & Conditions applicable to all Open Access articles published with Elsevier:

Any reuse of the article must not represent the author as endorsing the adaptation of the article nor should the article be modified in such a way as to damage the author's honour or reputation. If any changes have been made, such changes must be clearly indicated.

The author(s) must be appropriately credited and we ask that you include the end user license and a DOI link to the formal publication on ScienceDirect.

If any part of the material to be used (for example, figures) has appeared in our publication with credit or acknowledgement to another source it is the responsibility of the user to ensure their reuse complies with the terms and conditions determined by the rights holder.

Additional Terms & Conditions applicable to each Creative Commons user license:

CC BY: The CC-BY license allows users to copy, to create extracts, abstracts and new works from the Article, to alter and revise the Article and to make commercial use of the Article (including reuse and/or resale of the Article by commercial entities), provided the user gives appropriate credit (with a link to the formal publication through the relevant DOI), provides a link to the license, indicates if changes were made and the licensor is not represented as endorsing the use made of the work. The full details of the license are available at http://creativecommons.org/licenses/by/4.0.

CC BY NC SA: The CC BY-NC-SA license allows users to copy, to create extracts, abstracts and new works from the Article, to alter and revise the Article, provided this is not done for commercial purposes, and that the user gives appropriate credit (with a link to the formal publication through the relevant DOI), provides a link to the license, indicates if changes were made and the licensor is not represented as endorsing the use made of the work. Further, any new works must be made available on the same conditions. The full details of the license are available at http://creativecommons.org/licenses/by-nc-sa/4.0.

CC BY NC ND: The CC BY-NC-ND license allows users to copy and distribute the Article, provided this is not done for commercial purposes and further does not permit distribution of the Article if it is changed or edited in any way, and provided the user gives appropriate credit (with a link to the formal publication through the relevant DOI), provides a link to the license, and that the licensor is not represented as endorsing the use made of the work. The full details of the license are available at http://creativecommons.org/licenses/by-nc-nd/4.0. Any commercial reuse of Open Access articles published with a CC BY NC SA or CC BY NC ND license requires permission from Elsevier and will be subject to a fee.

Commercial reuse includes:

- Associating advertising with the full text of the Article
- Charging fees for document delivery or access
- Article aggregation
- Systematic distribution via e-mail lists or share buttons

Posting or linking by commercial companies for use by customers of those companies.

20. **Other Conditions**:

v1.9

Questions? customercare@copyright.com or +1-855-239-3415 (toll free in the US) or +1-978-646-2777.

Journal of Computational Physics 335 (2017) 718–735

Contents lists available at ScienceDirect

Journal of Computational Physics

www.elsevier.com/locate/jcp

A physics-motivated Centroidal Voronoi Particle domain decomposition method

Lin Fu, Xiangyu Y. Hu *, Nikolaus A. Adams

Institute of Aerodynamics and Fluid Mechanics, Technische Universität München, 85748 Garching, Germany

ARTICLE INFO

Article history:
Received 27 April 2016
Received in revised form 22 December 2016
Accepted 24 January 2017
Available online 26 January 2017

Keywords:
Centroidal Voronoi Tessellation
Voronoi Particle
Centroidal Voronoi Particle
Partitioning
High-performance parallel computing

ABSTRACT

In this paper, we propose a novel domain decomposition method for large-scale simulations in continuum mechanics by merging the concepts of Centroidal Voronoi Tessellation (CVT) and Voronoi Particle dynamics (VP). The CVT is introduced to achieve a high-level compactness of the partitioning subdomains by the Lloyd algorithm which monotonically decreases the CVT energy. The number of computational elements between neighboring partitioning subdomains, which scales the communication effort for parallel simulations, is optimized implicitly as the generated partitioning subdomains are convex and simply connected with small aspect-ratios. Moreover, Voronoi Particle dynamics employing physical analogy with a tailored equation of state is developed, which relaxes the particle system towards the target partition with good load balance. Since the equilibrium is computed by an iterative approach, the partitioning subdomains exhibit locality and the incremental property. Numerical experiments reveal that the proposed Centroidal Voronoi Particle (CVP) based algorithm produces high-quality partitioning with high efficiency, independently of computational-element types. Thus it can be used for a wide range of applications in computational science and engineering.

1. Introduction

The need for domain decomposition is encountered in many scientific applications, such as numerical continuum mechanics, parallel computing, data processing, mesh generation, and shape optimization [1,2]. Domain decomposition methods follow the divide and conquer principle, i.e. to solve the global problem by a sequence of local problems. Classical domain decomposition methods can be classified roughly as geometry-based [3] and graph-based approaches [4]. Several open-source codes, such as Metis [5] and PT-Scotch [6], are available to the community. Centroidal Voronoi Tessellation [7] is a typical domain decomposition method and will be the main subject of this paper.

In the following, we denote by "tessellation" a domain decomposition without overlapping subdomains [8]. Given a set of sites $p = \{p_1, \cdots, p_n\}$ (Voronoi generators), a Voronoi Tessellation is a subdivision of a domain into n cells, with the property that a point q lies in the cell corresponding to a site p_i if $d(p_i, q) < d(p_j, q)$ for j distinct from i [9]. Centroidal Voronoi Tessellation (CVT) is a specific Voronoi tessellation of a domain characterized by a given density function, for which each Voronoi generator coincides with the mass centroid of the corresponding Voronoi cell. CVT is a partitioning with an optimized generator distribution, and thus is used in a wide range of applications, e.g. optimal mesh generation, data compression, signal processing and cellular biology [9,10]. For example, Du et al. [11] recently explored the CVT concept for

* Corresponding author.
E-mail addresses: lin.fu@tum.de (L. Fu), xiangyu.hu@tum.de (X.Y. Hu), nikolaus.adams@tum.de (N.A. Adams).

http://dx.doi.org/10.1016/j.jcp.2017.01.051
0021-9991/

unstructured isotropic mesh generation by utilizing the dual relation between Delaunay triangulation and Voronoi diagram. Moreover, it has been further extended to anisotropic meshing and geometric surface meshing [12,13].

A CVT can be computed by many methods, such as the deterministic Lloyd's iteration [14] and the probabilistic MacQueen's random algorithm [15]. Lloyd's method is popular for its numerical robustness and simplicity while decreasing the CVT energy function monotonically. A major drawback of Lloyd's method is that it is only linearly convergent, rendering it inefficient for large numbers of generators. Despite the fact that the MacQueen's random algorithm is intuitive to implement, it is not widely used owing to its weak convergence property. For improved efficiency, a parallel MacQueen random algorithm [16] and Lloyd's method in a multi-grid framework [17] have been developed. By recognizing that the CVT energy function has 2nd-order smoothness for convex domains with smooth density, Liu et al. [18] propose a quasi-Newton method to compute CVT and achieve a faster convergence. Nevertheless, to find the global minimum of the CVT energy function is numerically challenging due to its nonlinearity and non-convexity.

For CVT, Gersho's conjecture [19] states that "asymptotically speaking, all cells of the optimal CVT, while forming a tessellation, are congruent to a basic cell which depends on the dimension." Based on Gersho's conjecture, when the generator number tends to infinity and the density function is smooth enough, the following relation applies to any two Voronoi cells i and j,

$$\begin{aligned} &\rho_i h_i^{d+2} \approx \rho_j h_j^{d+2}, \\ &\rho_i |\Omega_i|^{2/d+1} \approx \rho_j |\Omega_j|^{2/d+1}, \end{aligned} \tag{1}$$

where h, d and $|\Omega|$ denote the local length-scale of a Voronoi cell, spatial dimension and Voronoi cell area ($2D$) or volume ($3D$). In the limit of large generator number, a uniform mass distribution is achieved for $\rho = \rho_t^2$ in two dimensions [20], i.e.

$$\rho_{t,i} |\Omega_i| \approx \rho_{t,j} \left|\Omega_j\right|, \; m_i \approx m_j, \tag{2}$$

where ρ_t denotes the target density function and $m_i = \rho_{t,i} |\Omega_i|$ denotes the mass. The error in satisfying the uniform mass distribution decays linearly with increasing generator number. Although CVT has been successfully used in many applications, it is unsuitable for domain decomposition problems with a strict mass-distribution constraint to be satisfied regardless of the smoothness of the density function and of generator number. In this paper, we first develop a Voronoi Particle method to achieve a target mass distribution, followed by a novel domain decomposition method based on Centroidal Voronoi Tessellation and Voronoi Particle concepts. Specifics of the numerical algorithms, such as boundary conditions, are addressed in detail. In the following, we mainly refer to domain decomposition for parallel computing in continuum mechanics although it should be emphasized that the proposed method has much wider applications. Numerical experiments demonstrate that the new Centroidal Voronoi Particle partitioning method achieves the optimization targets, and is highly robust, efficient and independent of specific mesh-element types, such as adaptive structured meshes, unstructured meshes and particles.

2. Domain decomposition method

2.1. Centroidal Voronoi Tessellation (CVT)

Given a set of points (generators) $\{\mathbf{x}_i\}_{i=0}^{k-1}$, in an open, simply-connected and convex domain $\Omega \subset \mathbb{R}^d$ without curved boundaries, the Voronoi region Ω_i corresponding to the generator x_i is defined as [10,9]

$$\Omega_i = \left\{\mathbf{x} \in \Omega | \, \|\mathbf{x} - \mathbf{x}_i\| \leqslant \left\|\mathbf{x} - \mathbf{x}_j\right\|, \forall j \neq i\right\}, \tag{3}$$

where $\|\cdot\|$ denotes the Euclidean distance in $\mathbb{R}^d$. For $i \neq j$, $\Omega_i \cap \Omega_j = \emptyset$ and $\cup_{i=0}^{k-1} \Omega_i = \Omega$. Such a set of polyhedra $\{\Omega_i\}_{i=0}^{k-1}$ is called the Voronoi tessellation (Voronoi diagram) of Ω.

Considering that we assign a density function $\rho(\mathbf{x}) > 0$ to Ω, the mass centroid of a Voronoi element Ω_i is defined by

$$\mathbf{z}_i = \frac{\int_{\Omega_i} \rho(\mathbf{x}) \mathbf{x} d\sigma}{\int_{\Omega_i} \rho(\mathbf{x}) d\sigma}, \tag{4}$$

where $d\sigma$ denotes the volume differential.

A Voronoi tessellation $\{\Omega_i\}_{i=0}^{k-1}$, for which the generators $\{\mathbf{x}_i\}_{i=0}^{k-1}$ coincide exactly with the mass centroids, i.e.

$$\mathbf{x}_i = \mathbf{z}_i, \tag{5}$$

is called Centroidal Voronoi Tessellation (CVT). With given density field and number of generators, a CVT always exists but may be not unique [21]. However, without the generator-position optimization, the Voronoi Tessellation of generally-placed generators does not happen to satisfy the requirement of CVT.

From the variational point of view [10], an energy functional can be defined as

$$F(\mathbf{x}) = \sum_{i=0}^{k-1} F_i(\mathbf{x}) = \sum_{i=0}^{k-1} \int_{\Omega_i} \rho(\mathbf{x}) \|\mathbf{x} - \mathbf{x}_i\|^2 d\sigma, \tag{6}$$

where $F_i(\mathbf{x})$ describes the compactness or inertia momentum [18] of Voronoi element Ω_i. The gradient of $F(\mathbf{x})$ is

$$\frac{\partial F}{\partial \mathbf{x}_i} = 2m_i(\mathbf{x}_i - \mathbf{z}_i), \tag{7}$$

with

$$m_i = \int_{\mathbf{x}\in\Omega_i} \rho(\mathbf{x}) d\sigma. \tag{8}$$

For continuous density functions, numerical integration over polyhedral domains is employed [22].

For CVT, we have, for all i,

$$\mathbf{x}_i = \mathbf{z}_i = \frac{\int_{\Omega_i} \rho(\mathbf{x})\mathbf{x} d\sigma}{\int_{\Omega_i} \rho(\mathbf{x}) d\sigma}, \tag{9}$$

thus $\frac{\partial F}{\partial \mathbf{x}_i}$ is zero, and the CVT configuration is a critical point of the energy functional. The energy functional Eq. (6) can be minimized by a CVT, but not every CVT configuration satisfying $\frac{\partial F}{\partial \mathbf{x}_i} = 0$ minimizes the energy functional due to the saddle point problem [10].

Since each Voronoi element depends on all generators $\{\mathbf{x}_i\}_{i=0}^{k-1}$, Eq. (9) constitutes a system of nonlinear equations. Through iteratively moving the generators to the mass centroid of Voronoi cells, the CVT can be computed by Lloyd's method, as shown in Algorithm. 1. Du and et al. [23] prove the convergence of the Lloyd's method and state that Lloyd's method decreases the energy function $F(\mathbf{x})$ without step-size constraint until a local minimum is reached. Due to its superior robustness and simplicity, Lloyd's method is widely used for the discrete K-Means clustering algorithm despite linear convergence [24].

Algorithm 1 Lloyd's method.

1: Given an initial set of points $\{\mathbf{x}_i\}_{i=0}^{k-1}$ in the computational domain Ω.
2: Construct Voronoi tessellation $\{\Omega_i\}_{i=0}^{k-1}$ corresponding to the generators $\{\mathbf{x}_i\}_{i=0}^{k-1}$.
3: Compute the mass centroids $\{\mathbf{z}_i\}_{i=0}^{k-1}$ of Voronoi elements; move each generator to the corresponding mass centroid, i.e. $\mathbf{x}_i = \mathbf{z}_i$.
4: Check whether the new generators satisfy a convergence criterion, e.g. the maximum generator displacement is less than a threshold value; if true, terminate; otherwise, return to step 2.

2.2. Voronoi Particle (VP) dynamics

Particle hydrodynamics with Voronoi techniques has been introduced before, see e.g. [25,26]. We adopt this concept for domain decomposition in the following. Hereafter, the generators in the Voronoi diagram are represented by partitioning particles.

We consider the differential form of the inviscid momentum equations for a fluid in Lagrangian form

$$\frac{d\mathbf{v}}{dt} = -\frac{\nabla p}{\rho}, \tag{10}$$

where $\mathbf{v}$ denotes the velocity vector, p denotes the pressure and ρ denotes the density.

Eq. (10) can be discretized based on the Voronoi mesh. For each partitioning particle i, the acceleration due to pressure gradient is computed as

$$\mathbf{a}_i = \frac{d\mathbf{v}_i}{dt} = -\frac{\int_{\Omega_i} \nabla p d\sigma}{\int_{\Omega_i} \rho d\sigma} = -\frac{\int_{\partial\Omega_i} p d\mathbf{S}}{m_i}, \tag{11}$$

where $\partial\Omega_i$ denotes the Voronoi-cell surface.

The partitioning particle pressure is defined as

$$p_i = f(\frac{m_i}{m_{tg,i}}), \tag{12}$$

where $f(x)$ is chosen as monotonically increasing, and $m_{tg,i}$ denotes a target mass of each Voronoi cell (the definition of $m_{tg,i}$ is application dependent). We set $f(x) = x$, i.e. $p_i = \frac{m_i}{m_{tg,i}}$ which is a suitable choice for our purpose. The target mass $m_{tg,i}$ should satisfy

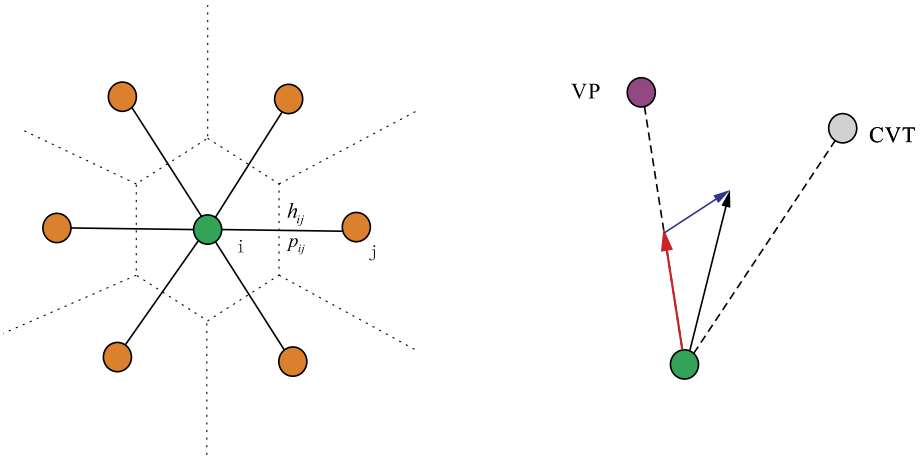

Fig. 1. Sketch of Voronoi cell and particle update. For the left panel, the dashed lines denote the Voronoi cell edges, h_{ij} denotes the distance between particle i and j, p_{ij} denotes the pressure on the Voronoi cell edge between particle i and j. The orange circles denote the nearest neighbors of particle i represented by the green circle. For the right panel, the purple circle represents the new particle position by the pure VP method while the gray circle denotes that by pure CVT requirement. The red line with arrow denotes the particle evolution path by the VP part of CVP method while the blue line denotes that by the CVT part. The gray line with arrow denotes the real evolution path. (For interpretation of the references to color in this figure legend, the reader is referred to the web version of this article.)

$$\sum_{i=0}^{k-1} m_{tg,i} = \int_{\Omega} \rho d\sigma, \tag{13}$$

e.g. for equal-sized partitioning, $m_{tg,i} = \frac{\int_{\Omega} \rho d\sigma}{k}$.

The pressure p_{ij} at the Voronoi interface between cell i and j is approximated as

$$p_{ij} = \frac{p_i + p_j}{2}. \tag{14}$$

With the computation of acceleration, the partitioning-particle coordinates $\mathbf{x}_i$ can be evolved as

$$\mathbf{x}_i^{n+1} = \mathbf{x}_i^n + \frac{1}{2}\mathbf{a}_i^n \Delta t^2, \tag{15}$$

where the timestep is constrained globally, i.e.

$$\Delta t = \min\left(0.25\sqrt{\frac{h_i^n}{|\mathbf{a}_i^n|}}\right), \tag{16}$$

for numerical stability. As shown on the left of Fig. 1, the length-scale h_i for partitioning particle i is calculated by averaging the distances between neighboring particles from

$$h_i = \frac{1}{2N}\sum_{j=0}^{N-1} h_{ij}, \tag{17}$$

where N denotes the number of neighboring Voronoi cells sharing an edge with cell i.

Provided that the target mass distribution has not been reached, p_i is not a constant, $\frac{\nabla p}{\rho} \neq 0$, and the particle will be accelerated by the pressure force. A stable relaxed configuration is achieved when $m_i = m_{tg,i}$ for all i.

2.3. Centroidal Voronoi Particle (CVP) based domain decomposition method

A typical partitioning problem for parallel large-scale continuum-mechanics simulations imposes several objectives [27]: (a) equal-sized partitioning or an unbalanced partitioning tailored to a specific computing system; (b) minimum communication; (c) connected partitioning and strong locality for data management and communication reduction; (d) incremental property to reduce data migration between processors after repartitioning; (e) efficiency.

In order to allow application of the proposed partitioning method for all computational-element types, the concept of an interaction particle, which is a basic representation of a computational element and is generated at the computational-element center or vertex $\mathbf{x}$, is introduced. The interaction particle possesses as physical property a mass, which is proportional to the computing cost assigned to the respective computational element. Assuming that all mesh elements require certain predefined amount of computational cost, the mass is set accordingly everywhere. With the mass distribution of

interaction particles, the density function $\rho(\mathbf{x})$ can be obtained immediately. In practice, a density function does not need to be explicitly defined, and the mass and mass centroid can be computed by

$$\begin{cases} m_i = \int_{\Omega_i} \rho(\mathbf{x}) d\sigma = \sum_{j=0}^{N_i-1} m_{j,i}, \\ \mathbf{z}_i = \frac{\int_{\Omega_i} \rho(\mathbf{x})\mathbf{x} d\sigma}{\int_{\Omega_i} \rho(\mathbf{x}) d\sigma} = \frac{\sum_{j=0}^{N_i-1} m_{j,i}\mathbf{x}_{j,i}}{m_i}, \end{cases} \tag{18}$$

where N_i represents the number of interaction particles in Voronoi cell i, $m_{j,i}$ and $\mathbf{x}_{j,i}$ denote mass and coordinates of interaction particle j in Voronoi cell i.

Based on the density function $\rho(\mathbf{x})$, we develop the Centroidal Voronoi Particle (CVP) partitioning method by merging the CVT and VP concepts. A set of partitioning particles are initialized in the computational domain and evolved according to Lloyd's method and particle dynamics. While Lloyd's method optimizes the energy function with respect to the global compactness (CVT), the particle dynamics relaxes the partitioning towards the target mass distribution.

With CVP based partitioning method, objectives (a) and (c) are achieved implicitly. Objective (d) is also satisfied as the solution of CVP is computed iteratively. As the number of partitioning particles corresponds to the number of partitioning subdomains and thus typically is very small, the proposed CVP method is highly efficient. Thus objective (e) is also achieved. Although the requirement of minimum communication cannot be proved strictly, previous research [28] implies a direct relation between communication minimization and compactness. The prominent feature of compactness from CVP method results in strictly convex partitioning subdomains with small aspect-ratio, which leads to well communication optimization. The advantage of partition-shape optimization over traditional edge-cut optimization method with respect to communication reduction is demonstrated in [28,29].

Considering that Lloyd's method is not subject to a step-size constraint, unlike the VP method, a straightforward combination leads to poor convergence.

Upon defining a global step-size condition for Lloyd's method as

$$\Delta\tau = \min(\min(\frac{h_i^n}{32}, \left|\mathbf{z}_i^n - \mathbf{x}_i^n\right|)/\left|\mathbf{z}_i^n - \mathbf{x}_i^n\right|), \tag{19}$$

to satisfy the requirement that one particle moves less than $\frac{1}{32}h$ in one explicit time integration step, the partitioning-particle location is updated by

$$\mathbf{x}_i^{n+1} = \mathbf{x}_i^n + \Delta\tau(\mathbf{z}_i^n - \mathbf{x}_i^n). \tag{20}$$

In order to improve convergence, an explicit two-step strategy for particle evolution is proposed. As shown on the right of Fig. 1, the partitioning particle first is updated by the VP method as

$$\mathbf{x}_i^* = \mathbf{x}_i^n + \alpha\frac{1}{2}\mathbf{a}_i^n\Delta t^2, \tag{21}$$

i.e. the red path. In a second step, the CVT shift is imposed as

$$\mathbf{x}_i^{n+1} = \mathbf{x}_i^* + (1-\alpha)\Delta\tau(\mathbf{z}_i^n - \mathbf{x}_i^*), \tag{22}$$

i.e. the blue path. α is a relaxation parameter, which affects convergence. We find that $\alpha > 0.5$ ensures that essentially VP dynamics dominates over CVT in relaxing the system. As VP dynamics is analogous to a physical pressure relaxation process, a stable equilibrium state of the system can be obtained. The relaxation process of VP dynamics ensures convergence and the CVT method optimizes compactness simultaneously. Extensive numerical experimentation shows that $\alpha = 0.8$ gives the best performance.

3. Numerical algorithms

3.1. Initial and boundary condition

The initial particle distribution should be chosen such that none of the particle has zero mass, i.e. $m_i > 0$ for all i, within the associated Voronoi tessellation. Concerning efficiency, sampling the initial partitioning particles by the Monte Carlo method according to the given density function, e.g. rejection sampling, can accelerate the convergence for large number of particles [16]. For demonstrating the robustness and convergence of CVP, we randomly sample particles in the computational domain.

The ghost particle method is employed to enforce the symmetry boundary condition, where the particle locations are pairwise symmetric about the domain boundary, scalar variables are the same and vector velocities are mirroring. The boundary condition is enforced in two steps. In the first step, the domain-interior particles for mirroring, i.e. boundary

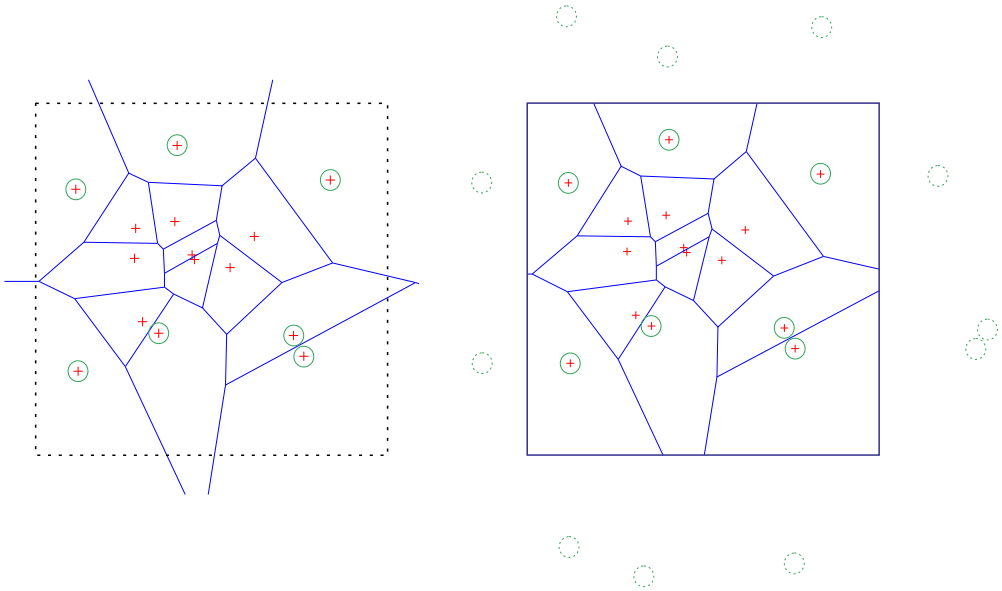

Fig. 2. Sketch of boundary condition. The general Voronoi diagram (left panel) and the Voronoi diagram with ghost particles (right panel). The blue lines represent the Voronoi cell edges while the dashed black lines represent the computational domain boundaries. The red crosses denote partitioning particles, the green circles denote boundary particles while the dashed circles denote the ghost particles. (For interpretation of the references to color in this figure legend, the reader is referred to the web version of this article.)

particles, are identified. As shown on the left of Fig. 2, particles in all Voronoi cells that contain Voronoi vertices outside the computational domain are marked as boundary particles. By mirroring these particles, a set of ghost particles is constructed, and all physical properties, such as mass and pressure, are copied from the corresponding particles. In the second step, a new Voronoi diagram is constructed including these ghost particles, as shown on the right of Fig. 2. The Voronoi cells cutting the boundary are now closed by the domain-boundary segments. The ghost particles are reconstructed for each iteration. Consequently, all numerical algorithms discussed in the last section now can be applied to all particles within the computational domain.

3.2. Convergence criteria

In order to check convergence, we define the maximum partitioning error as

$$E_{max} = \max(E_0, \cdots, E_{k-1}), \tag{23}$$

where $E_i = \frac{|m_i - m_{tg,i}|}{m_{tg,i}}$, $i = 0, \cdots, k-1$.

The convergence criterion is defined as follows: within a limited number of iterations, e.g. 100, both the averaged E_{max} and the E_{max} of the current iteration are smaller than a threshold, e.g. 5%.

The overall numerical algorithms for the CVP-based partitioning method are given as Algorithm. 2.

Algorithm 2 CVP-based domain decomposition method for general given density function $\rho(\mathbf{x})$.

1: Randomly initialize the partitioning particle distribution in the computational domain.
2: Initialize the density function $\rho(\mathbf{x})$ in the computational domain.
3: **while** convergence criteria are not satisfied **do**
4: Construct the Voronoi diagram, compute the partitioning particle mass (Eq. (8)) and mass centroid (Eq. (4)), define the partitioning particle pressure (Eq. (12)).
5: Construct the ghost particles enforcing the symmetric boundary condition (Section. 3.1).
6: Compute the partitioning particle scale (Eq. (17)), force and acceleration (Eq. (14), Eq. (11)).
7: Calculate the timestep (Eq. (16)) and update the partitioning particles according to VP method (Eq. (21)).
8: Calculate the step-size condition (Eq. (19)) and update the partitioning particles according to CVT method (Eq. (22)).
9: Check convergence (Section. 3.2); if true, terminate.
10: **end while**

4. Numerical validations

Since the application research of proposed CVP method concentrates on the parallel computing and considering the fact that modern parallel computing system utilizes the hybrid parallel framework (multi-thread parallelization inside one CPU node and MPI parallelization between CPU nodes), the number of the partitioning subdomains typically is moderately large.

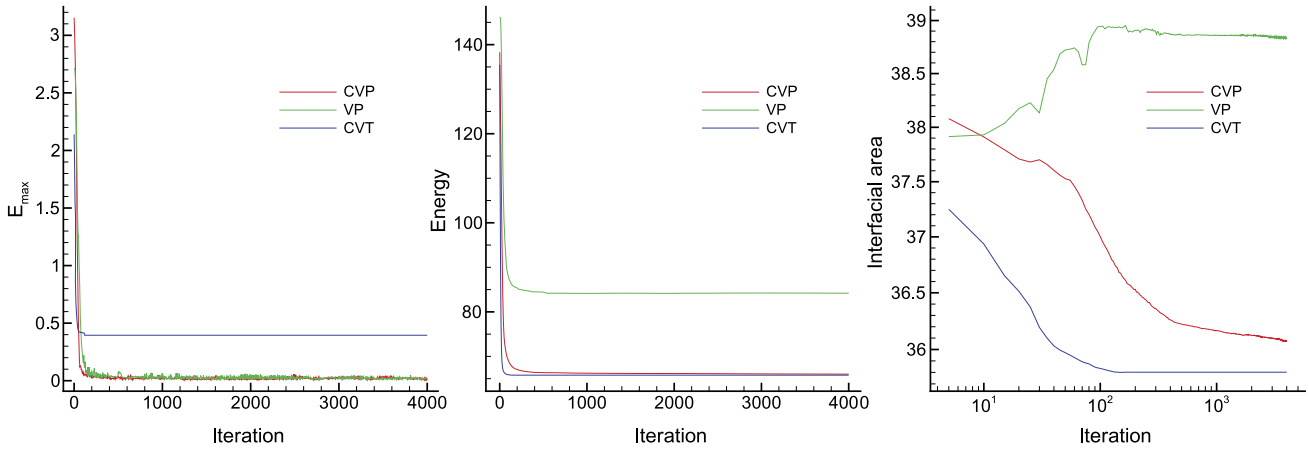

Fig. 3. The convergence histories of maximum load-imbalance error E_{max}, energy function and interfacial area for three different partitioning methods.

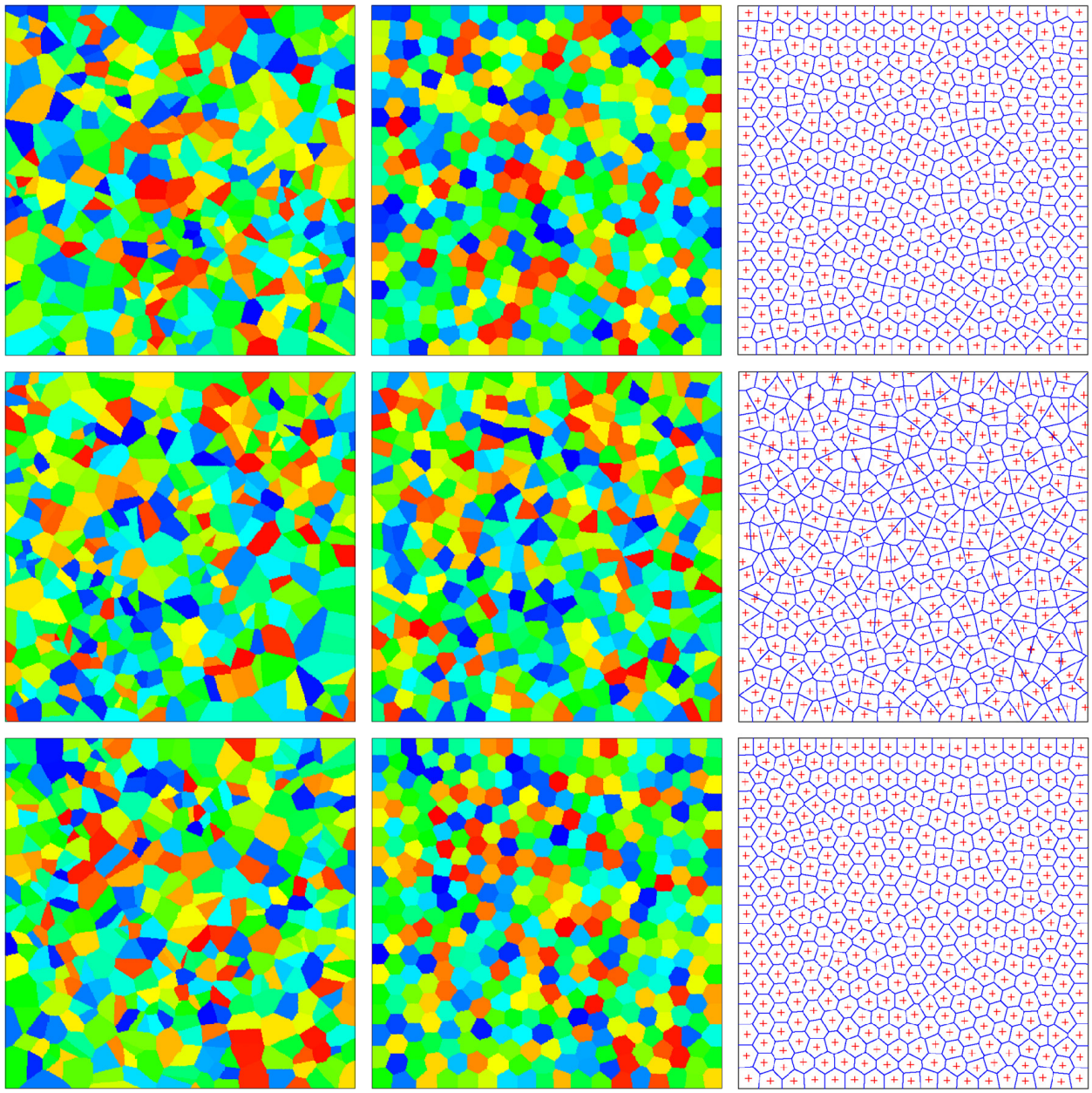

Fig. 4. Sketch of the partitionings and Voronoi diagrams. From left to right: initial partitioning, converged partitioning and Voronoi diagram. From top to bottom: results from CVP, VP and CVT methods. The cross symbols in the right panel represent the partitioning particles.

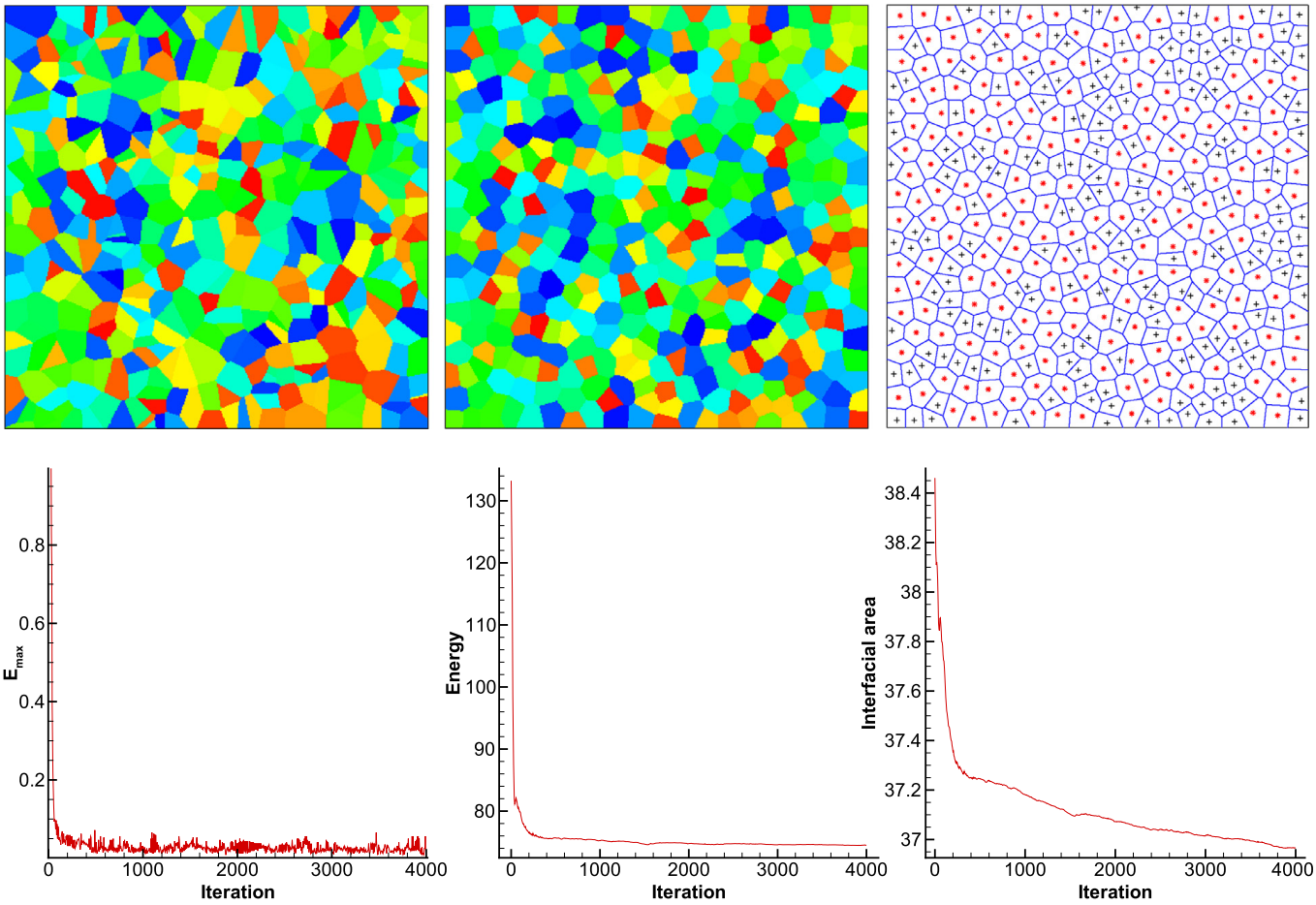

Fig. 5. Sketch of the partitioning results and convergence history. Top: initial partitioning, convergent partitioning and convergent Voronoi diagram. The black cross symbols denote partitioning particles of small target mass while the red star symbols denote those of large target mass. Bottom: convergence history of maximum load-imbalance error E_{max}, energy function and interfacial area. (For interpretation of the references to color in this figure legend, the reader is referred to the web version of this article.)

Fig. 6. Sketch of the partitioning results for uniform mesh with few generators. The partitioning number is 5, 7, and 14.

E.g. for the HPC system of Leibniz-Rechenzentrum, München (LRZ), 10000 CPU cores are available at 250 CPU nodes and 250 partitioning particles are needed correspondingly.

In order to measure and compare the computational efficiency, all simulations are carried out on the same desktop workstation equipped with 12 Intel(R) Xeon(R) CPU E5-2620 V2 cores (2.1 GHz and 32 G memory) and Scientific Linux 6.7 system.

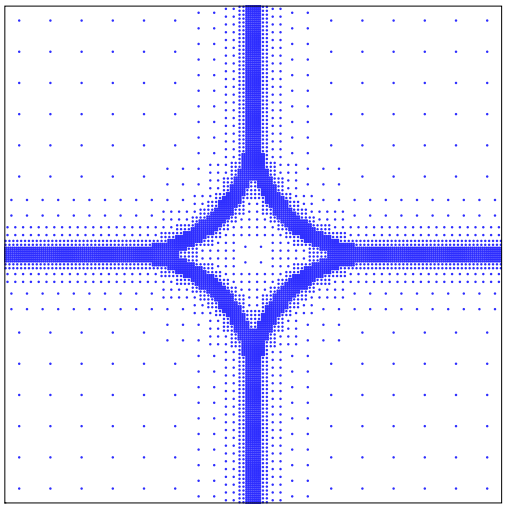

Fig. 7. Sketch of adaptive particle distribution.

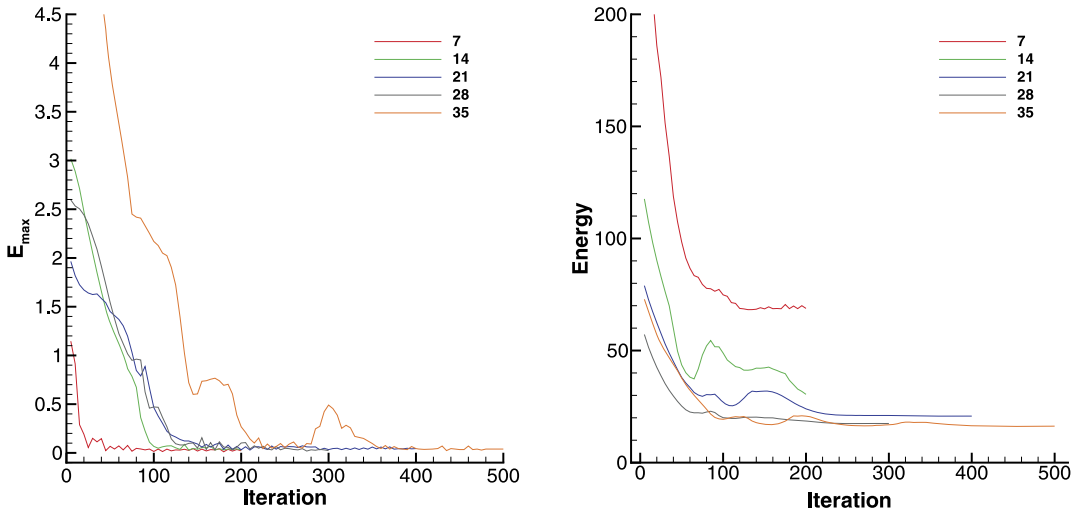

Fig. 8. Convergence histories of maximum load-imbalance error E_{max} and energy function for different partitioning number.

4.1. Uniform mesh partitioning

In this case, a uniform mesh of resolution 3200×3200 in a computational domain $[0, 1] \times [0, 1]$ is partitioned into 400 subdomains. Thus, 400 partitioning particles are involved. In order to demonstrate the convergence, the iteration number for each algorithm is fixed as 4000.

Fig. 3 gives the convergence histories of maximum load-imbalance error E_{max}, energy function and interfacial area. All three methods roughly converge within a few hundred iterations. For uniform meshes, the interfacial area represents the communication between distinct partitioning subdomains. It is observed that the CVT method produces large load-imbalance errors although the energy function and the interfacial area are minimized. While the load-imbalance error is minimized by the VP method, it fails to optimize the energy function and the interfacial area. Indeed, the total interfacial area increases slightly indicating larger communication overhead. The proposed CVP method optimizes all three objective functions simultaneously. Moreover, the total interfacial area asymptotically converges to the minimum value given by CVT.

From Fig. 4, we can see that most of partitioning subdomains from CVP and CVT methods converge to regular hexagons while that from the VP method are quite irregular. This can also be inferred from Gersho's conjecture, which states that "asymptotically speaking, all cells of the optimal CVT, while forming a tessellation, are congruent to a basic cell which depends on the dimension." For two dimensions, the basic cell for the optimal CVT is a regular hexagon while for three dimensions, although not theoretically verified, body-centered-cubic (BCC) lattice based CVT, i.e. the truncated octahedron, is numerically demonstrated to be the congruent cell [19]. H. Meyerhenke and et al. [30] point out that such convex subdomain shapes, e.g. hexagon, are the regular shapes which cover a two-dimensional domain with smallest interface areas and thus the total interfacial energy is minimum. This is also confirmed by the convergence history of interfacial area in Fig. 3. The current partitioning result is highly similar to that from representative diffusion BUBBLE-FOS/C graph (Re)partitioning heuristic (see Fig. 1 and Fig. 7 in [30]) and is better than the solutions delivered by well-established softwares, e.g. Metis [5].

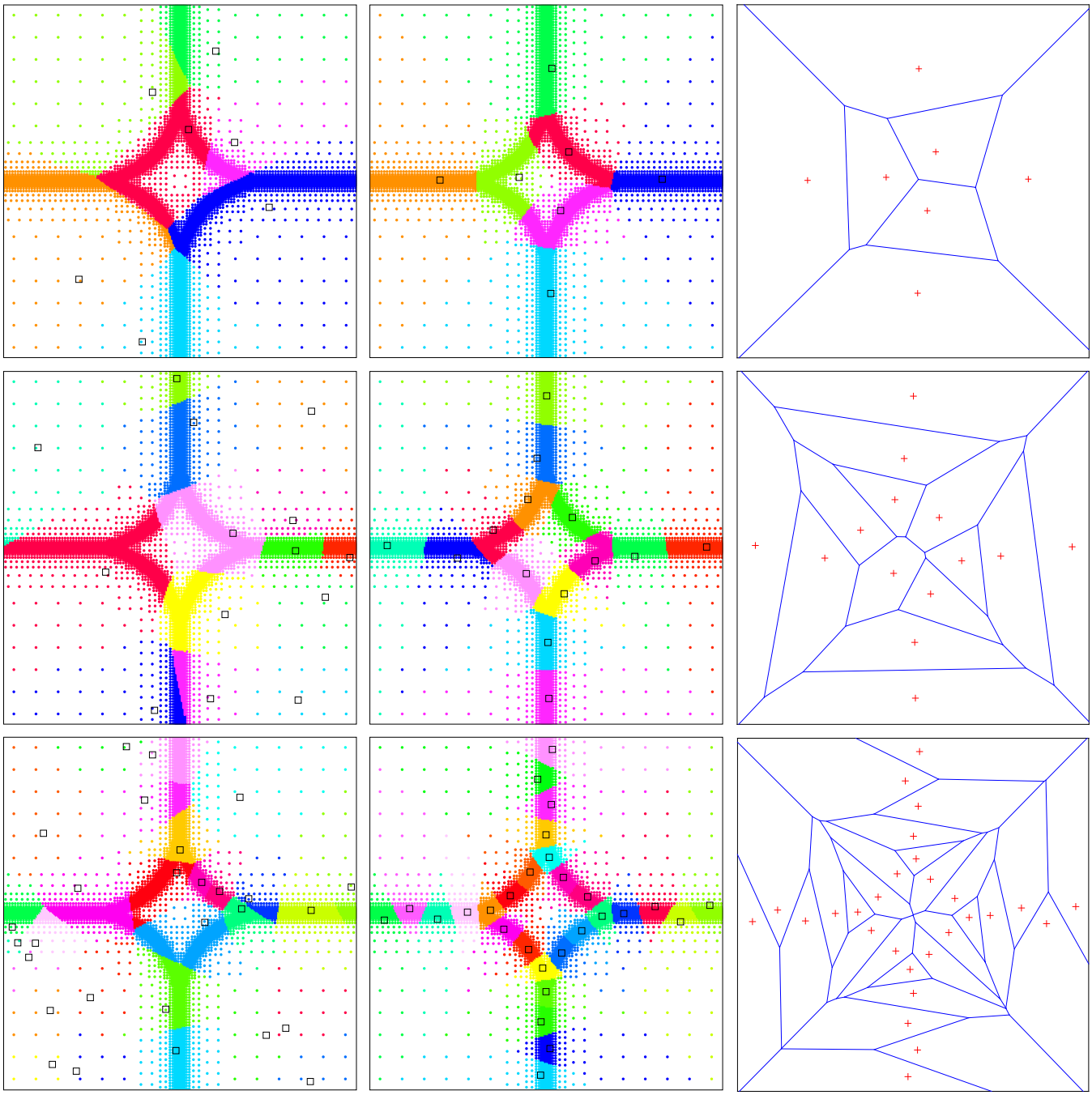

Fig. 9. Sketch of partitionings and Voronoi diagrams. From the left to right: initial partitioning, convergent partitioning and convergent Voronoi diagram. From the top to bottom: partitioning number 7, 14, 28. The square and cross symbols denote the partitioning particles.

Since in practice the computational capabilities of distinct processor cores may differ significantly, the target load-imbalance should be tailored to fit the computational capability of specific processor core. Assuming that 200 out of the 400 processor cores have a 50% higher computational capability than the others, an unbalanced partitioning simulation is performed. As shown in Fig. 5, three objective functions of E_{max}, energy function and interfacial area are well optimized.

Fig. 6 shows the partitioning topologies for uniform meshes with small partitioning numbers.

4.2. Partitioning of adaptive particle distribution

In this case, an adaptive particle distribution consisting of 6736 particles, as shown in Fig. 7, is employed as the target partitioning mesh. The partitioning number ranges from 7 to 35. Only one processor core is adopted.

Fig. 8 gives the convergence histories. It can be noticed that all five partitioning simulations converge rapidly in less than 500 iterations while load-imbalance error and energy function are well optimized. Furthermore, less than 2 seconds are consumed even for partitioning number 35, indicating high efficiency of the CVP method.

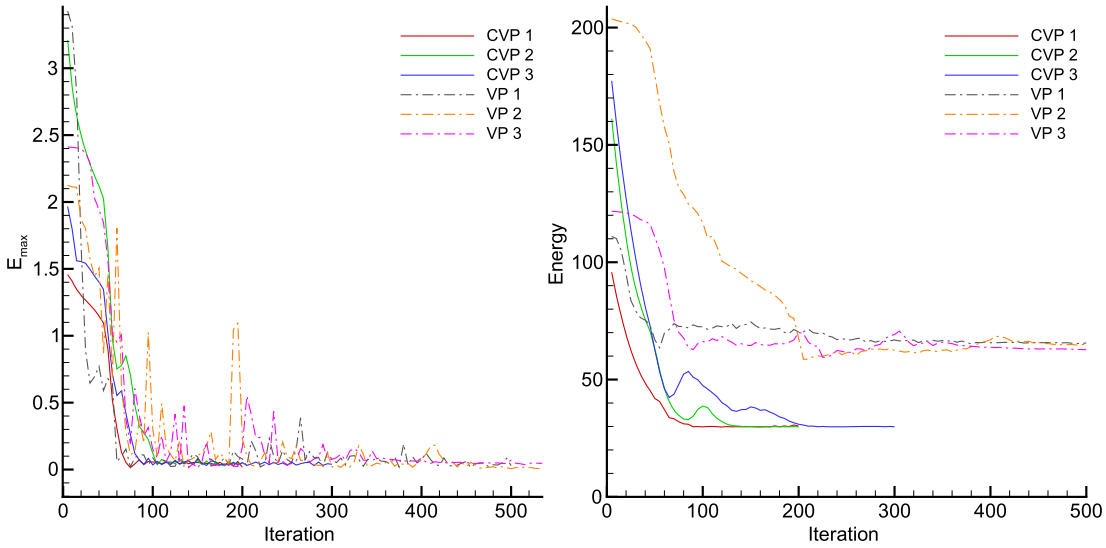

Fig. 10. Convergence history comparisons between CVP and VP method. Three sets of simulations are carried out with random initial conditions. The partitioning number is 14.

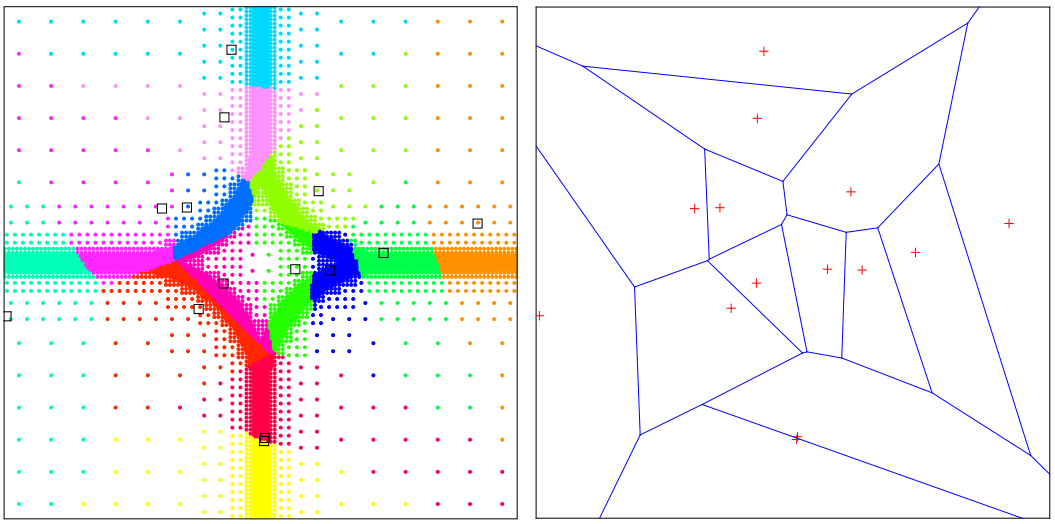

Fig. 11. Sketch of partitioning result from VP method. Left panel: partitioning subdomains; right panel: Voronoi diagram. The partitioning number is 14. The square and cross symbols denote the partitioning particles.

As shown in Fig. 9, all converged partitioning subdomains are compact with particles located around the Voronoi-cell mass-center. One interesting thing is that the convergent Voronoi diagram preserves a high-degree of symmetry as the background mesh is symmetric.

The performance comparisons between CVP and VP method are shown in Fig. 10. It can be concluded that the CVP method has significantly better convergence properties than the VP method for both load-imbalance error and energy functional. Furthermore, the converged level of the energy functional from the CVP method is much lower than that from the pure VP method. Another notable outcome is that the energy functions from the CVP method converge to the same value from different initial conditions. As indicated in Fig. 11, the resulting partitioning subdomains for the VP method are much less compact than that for the CVP method. This is also shown in Fig. 12, where compared with the pure VP method, the proposed CVP algorithm optimizes better the boundary element number, which is a proper measure of communication in parallel computing, during the entire iteration.

As shown in Fig. 13, it is observed that the relaxation parameter $\alpha = 0.8$ gives the best convergence in terms of both load-imbalance error and the energy function.

As shown in Fig. 14, the partitioning results from the CVT method are significantly different from those computed by the present CVP method. Since the load-imbalance error has magnitude $\mathcal{O}(1)$, the classical CVT domain decomposition method is unsuitable for parallel computing.

As shown in Fig. 15, by utilizing Gersho's conjecture to redefine the density function for CVT method [19], the load-imbalance error is improved compared with that without conjecture, but still has magnitude $\mathcal{O}(1)$. The reason is that the

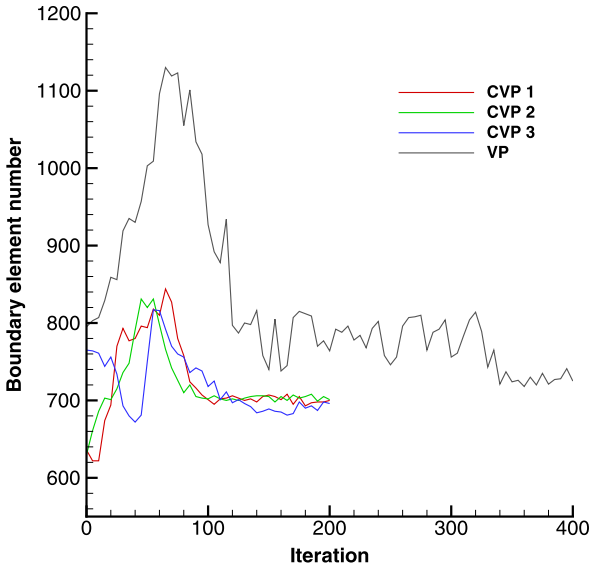

Fig. 12. Comparison of the boundary element number. The mesh element is defined as boundary element under the condition that among its nearest element neighbors there is at least one element located in different subdomains.

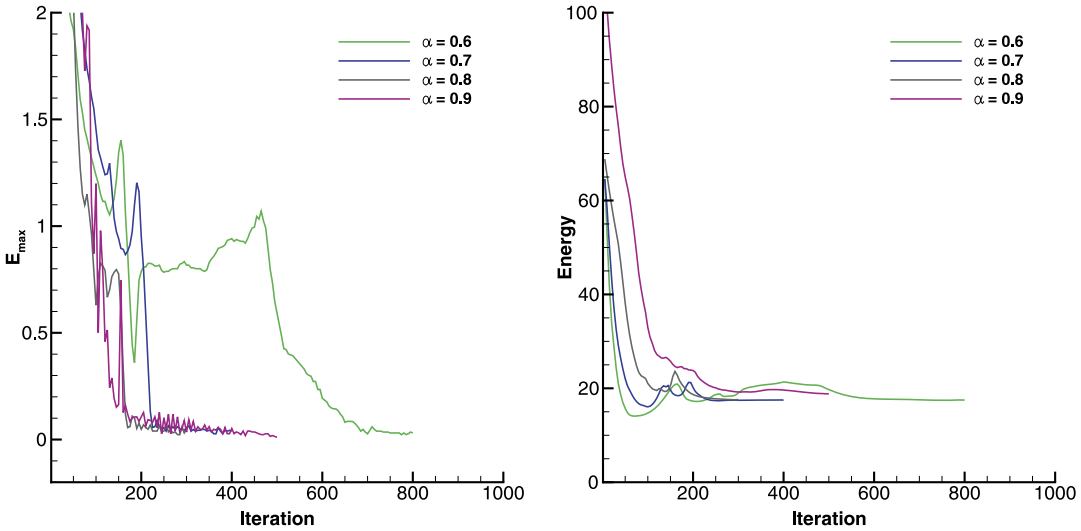

Fig. 13. Convergence history comparisons with different choice of α in CVP method. The partitioning number is 28.

two preconditions of the conjecture, i.e. smooth density function and infinite number of generators, are not satisfied in present applications.

As shown in Fig. 16, for non-convex domain with curved boundaries, the proposed CVP method performs well and the convergence is good. Here, the domain boundaries of CVP algorithm cover the real mesh domain. It is observed that the convergence property including the slight oscillation of error function can be improved by decreasing the timestep.

4.3. Partitioning of adaptive structured and unstructured meshes

In this case, the partitioning performance for adaptive structured and unstructured meshes is demonstrated. As shown in Fig. 17, the block-structured mesh consists of 6097 blocks while the anisotropic unstructured mesh contains 14197 elements with resolution adaptation of 200.

As shown in Fig. 18, the partitioning subdomains are fairly compact. As can be seen from Fig. 19, for all three partitioning numbers, the simulation converges rapidly in less than 500 iterations within 1.8 seconds. Both the load-imbalance error and the energy function are well optimized. For partitioning number 9, the partitioning simulation reaches the equilibrium in about 0.3 seconds indicating high efficiency.

In Fig. 20, we show the domain decomposition with partitioning number as large as 250, e.g. each subdomain only possesses 57 mesh elements. It can be noticed that the convergence is good even for this extreme case.

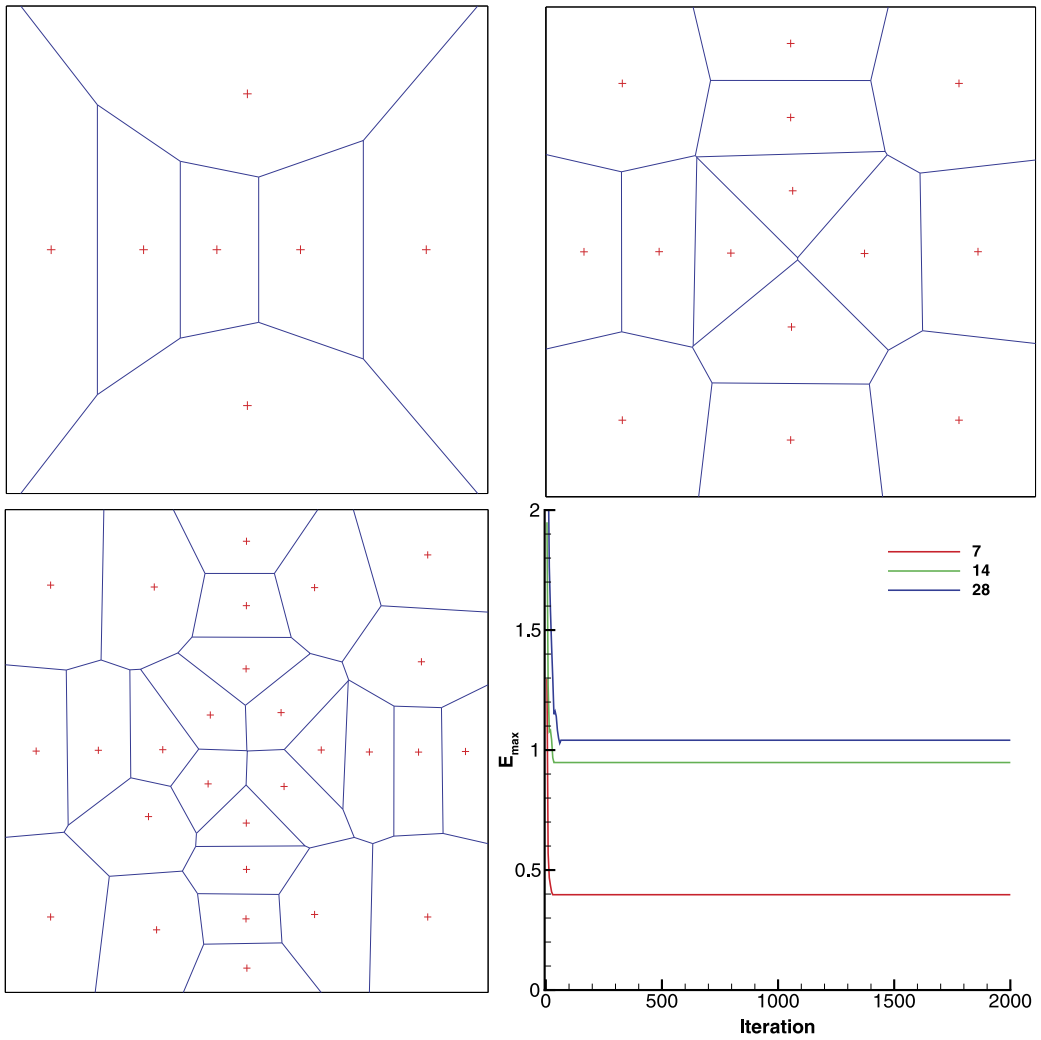

Fig. 14. Sketch of partitionings and convergence history from CVT method. The partitioning numbers are 7 (top left), 14 (top right) and 28 (bottom left). Bottom right: convergence history of maximum load-imbalance error. The crosses denote the partitioning particles.

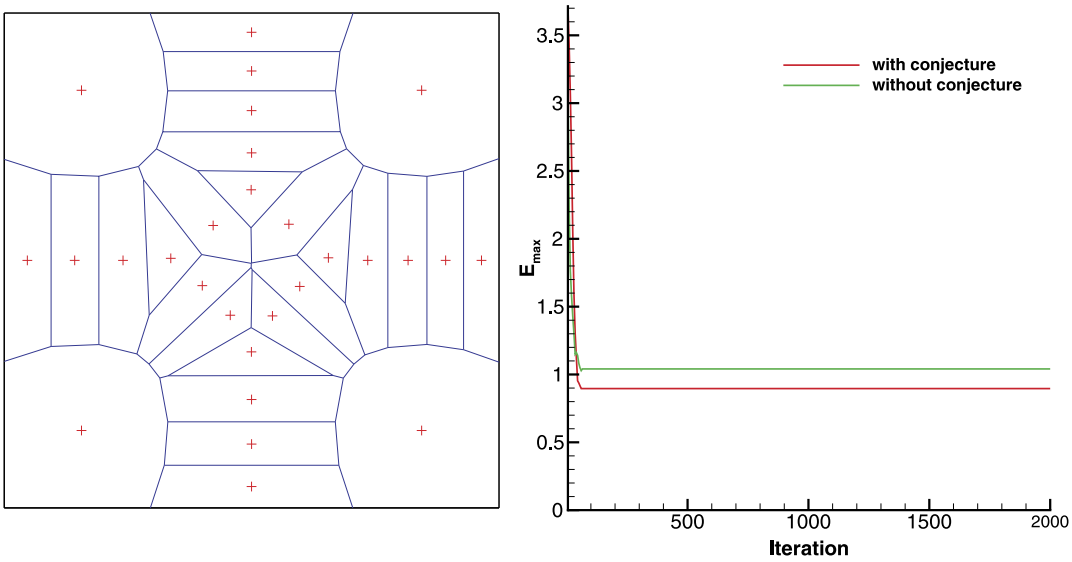

Fig. 15. Sketch of partitionings (left) and convergence history (right) from CVT method based on the asymptotic conjecture. The partitioning number 28.

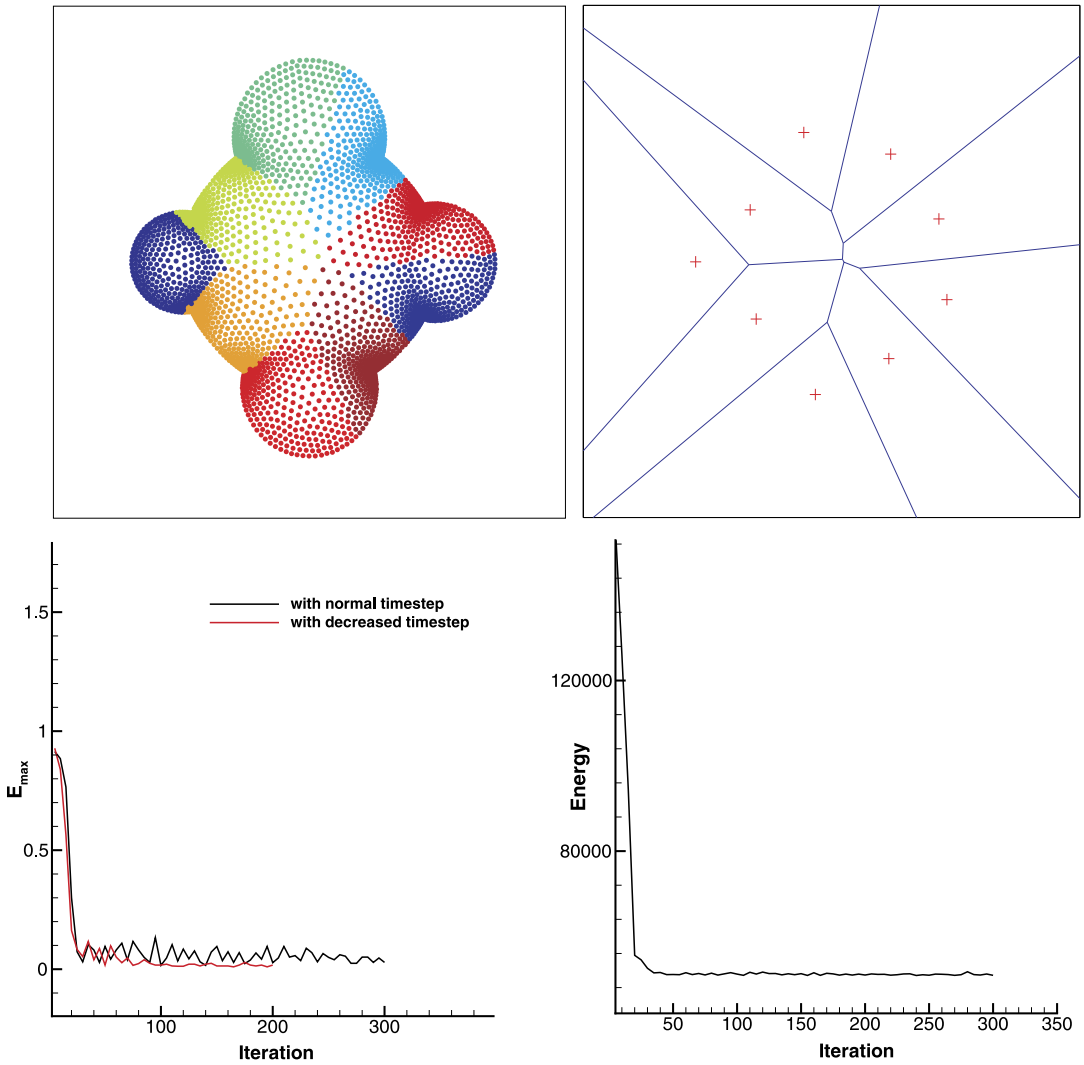

Fig. 16. Sketch of partitionings and convergence history from CVP method. The partitioning number is 9. Top: particle partitioning configuration (left) and the Voronoi diagram (right). Bottom: convergence history of maximum load-imbalance error (left) and energy function (right). The crosses denote the partitioning particles.

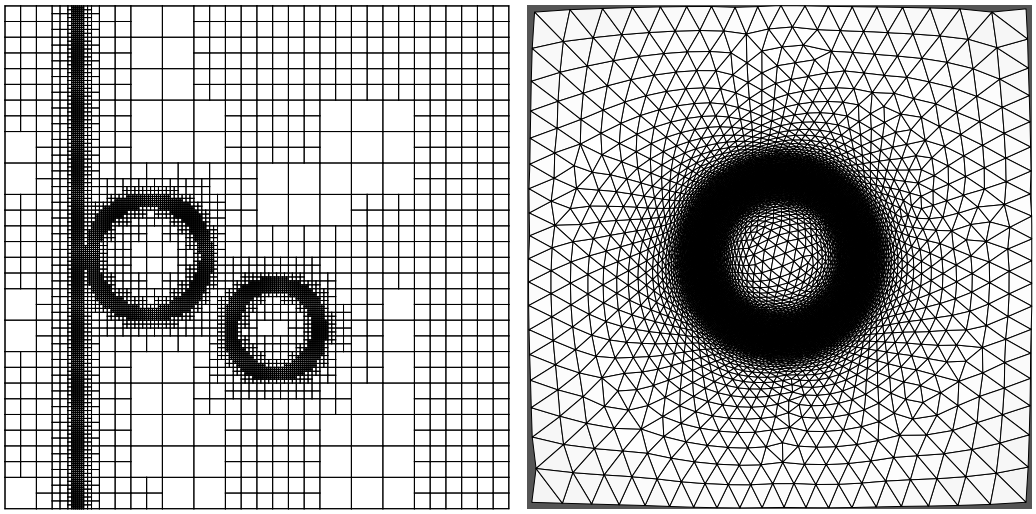

Fig. 17. Sketch of the block-structured mesh (left panel) and anisotropic unstructured mesh (right panel).

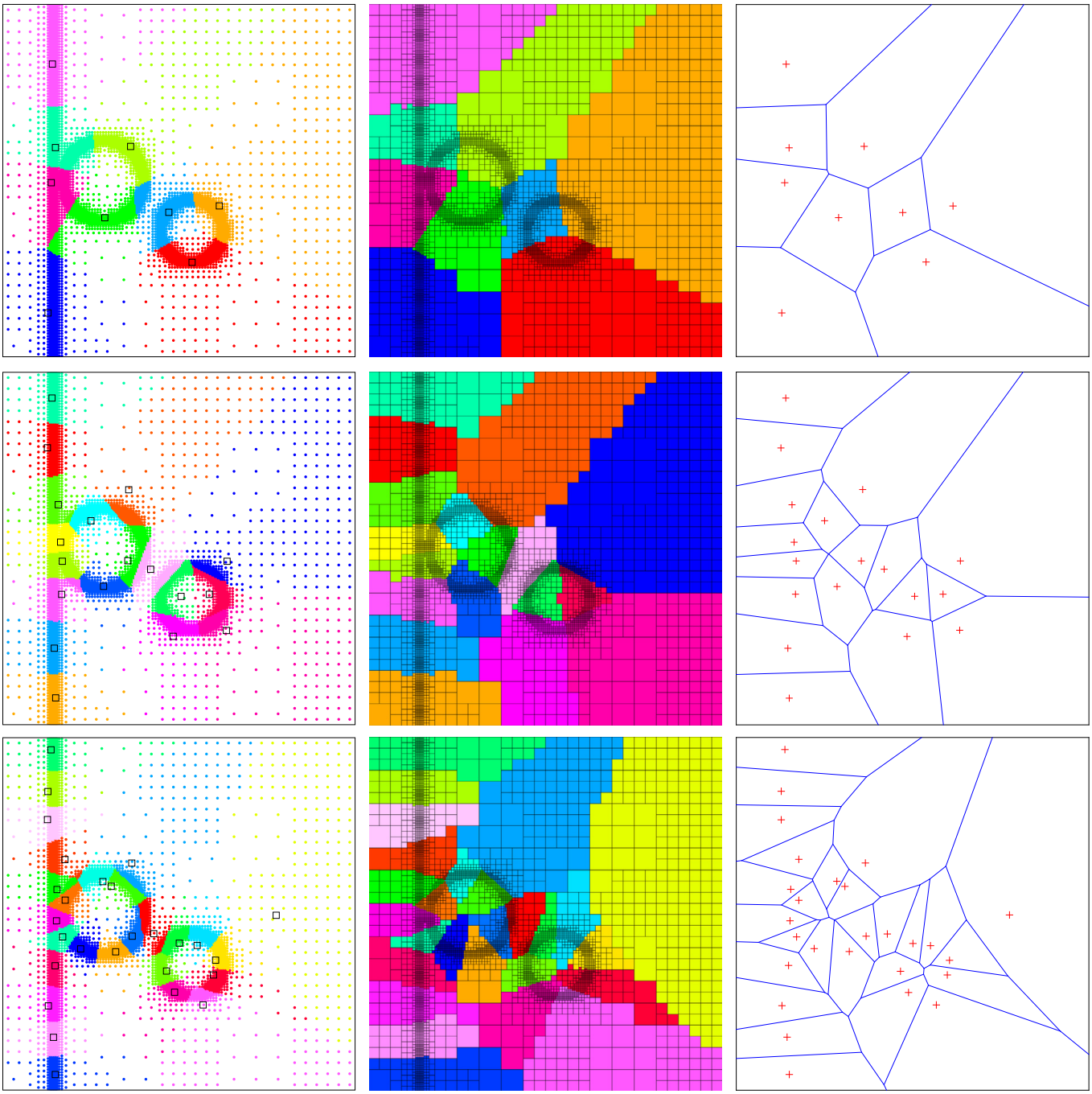

Fig. 18. Sketch of partitioning for block-structured mesh for partitioning number 9, 18, 27. From the top to bottom: the partitioning number is 9, 18 and 27. From the left to right: the converged interaction particle partitioning, block-structured mesh partitioning and Voronoi diagram. The square and cross symbols denote the partitioning particles.

4.4. 3D simulation

In this three-dimensional case, the total interaction particle number is 10000800 and the partitioning number is 64, 128 and 256 respectively. As shown in Fig. 21, the load-imbalance error and energy function converge very well.

5. Concluding remarks

In this paper, a novel domain decomposition method, the Centroidal Voronoi Particle method, for high-performance parallel computing is proposed by combining the Centroidal Voronoi Tessellation and Voronoi Particle method. The performances of proposed domain decomposition method are summarized as follows.

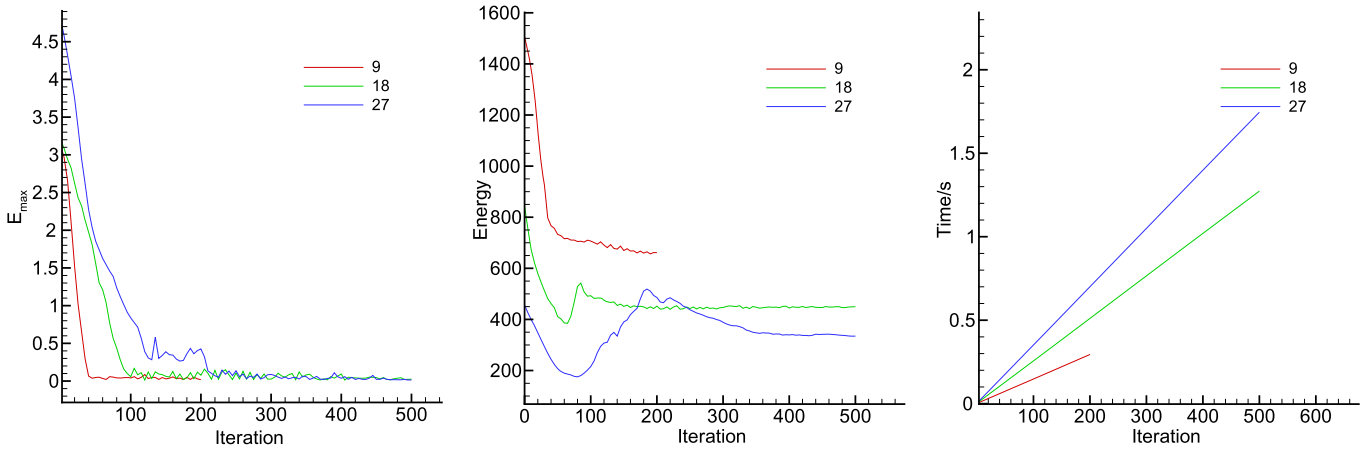

Fig. 19. Convergence history of the partitioning for block-structured mesh. Maximum load-imbalance error E_{max} (left), energy function (middle) and elapsed time (right).

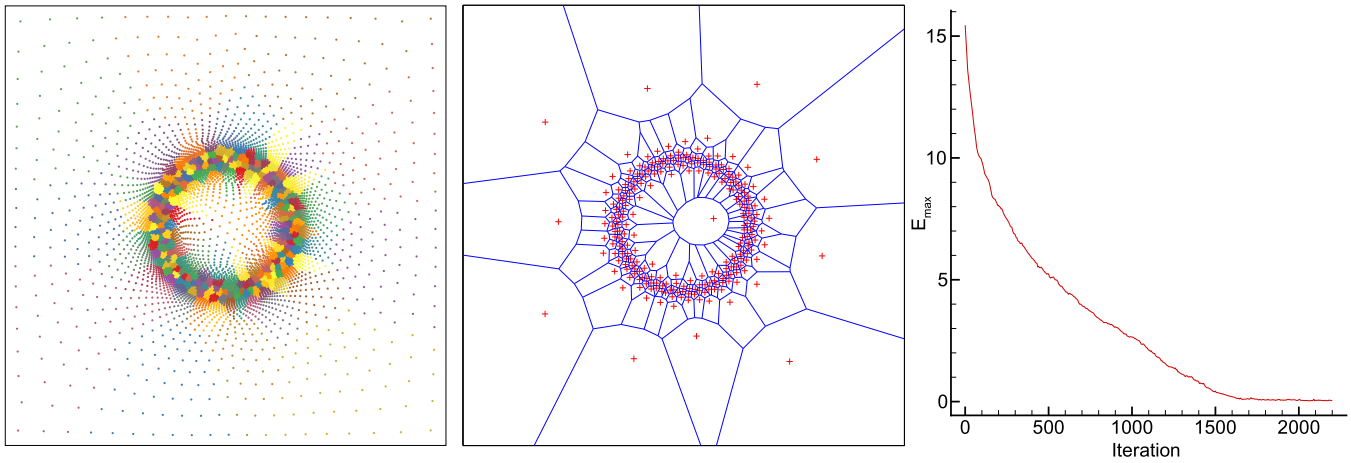

Fig. 20. Sketch of the partitioning for adaptive unstructured mesh with partitioning number 250. Left: interaction particle partitioning; middle: Voronoi diagram; right: convergence history of maximum load-imbalance error E_{max}.

- By generating the CVT diagram, Lloyd's method optimizes the energy function monotonically, which enhances the compactness of the partitioning subdomains. The resulting partitioning subdomains are convex, simply-connected and have small aspect-ratio. These properties are beneficial for interface-element number reduction, i.e. communication reduction. For uniform mesh partitioning, the analytical solution can be obtained asymptotically while most of popular partitioning methods fail [30].
- With the tailored equation of state incorporating the target mass, an equal-sized partitioning can be achieved through solving the particle evolution model equation by the Voronoi Particle method. In practice, with adequate error tolerance, the particle system can be relaxed to equilibrium quickly. Furthermore, by predefining target mass proportional to the computing capability of corresponding processor, nonequal-sized partitioning can be achieved straightforwardly.
- Since the partitioning is computed by solving a nonlinear PDE system, for which the solution continuously depends on the initial and boundary condition, the CVP partitioning method features good locality and the incremental property and thus is favorable with respect to data-migration reduction and data management.
- The proposed partitioning method is independent of mesh-element type and only mesh-element physical coordinates are necessary. The complex construction of mesh-element connectivity information is not necessary, making it generic for diverse applications. Generally speaking, the CVP method is highly efficient.
- Moreover, different from the CVT method, both the two concerned objectives, i.e. the arbitrary target mass distribution and compactness, can be optimized regardless of the smoothness of density function, the number of the generators and the boundary complexity.

Acknowledgements

The first author is partially supported by China Scholarship Council (No. 201206290022). The authors acknowledge our colleague Zhe Ji, who extends the code from 2D to 3D.

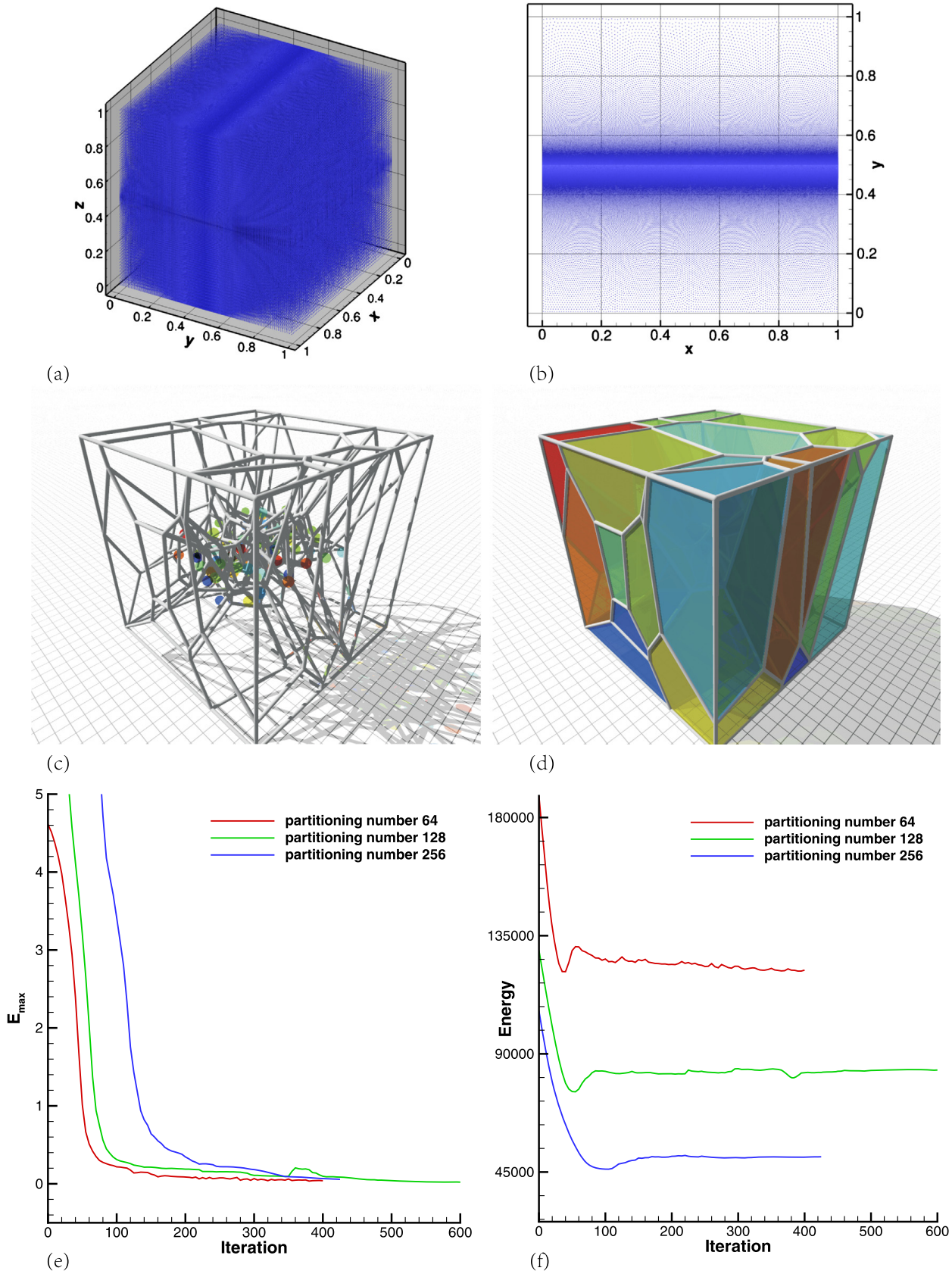

Fig. 21. 3D partitioning simulation. (a) The 3D interaction particle distribution; (b) a zoom view in the x–y plane; (c) the partitioning topology of partitioning number 64; (d) the partitioning Voronoi diagram of partitioning number 64; (e) the convergence history of the load-imbalance error; (f) the convergence history of energy function.

References

[1] D.E. Keyes, et al., in: Fifth International Symposium on Domain Decomposition Methods for Partial Differential Equations, vol. 55, SIAM, 1992.
[2] S. Nepomnyaschikh, Domain decomposition methods, Radon Series Comp. Appl. Math., vol. 1, 2007, pp. 89–160.
[3] M. Berger, S. Bokhari, A partitioning strategy for nonuniform problems on multiprocessors, IEEE Trans. Comput. 36 (1987) 570–580.
[4] G. Karypis, V. Kumar, A fast and high quality multilevel scheme for partitioning irregular graphs, SIAM J. Sci. Comput. 20 (1999) 359–392.
[5] G. Karypis, K. V, A software package for partitioning unstructured graph, partitioning meshes, and computing fill-reducing orderings of sparse matrices. User's guide version 4.0 and version 5.0 pre2, http://glaros.dtc.umn.edu/gkhome/metis/metis/overview, 1998, pp. 1–44.
[6] F. Pellegrini, Scotch and libScotch 5.1. user's guide, http://www.labri.fr/perso/pelegrin/scotch/, 2008, pp. 1–127.
[7] Q. Du, X. Wang, Centroidal Voronoi tessellation based algorithms for vector fields visualization and segmentation, in: Proceedings of the Conference on Visualization'04, IEEE Computer Society, 2004, pp. 43–50.
[8] A. Bowyer, Computing Dirichlet tessellations, Comput. J. 24 (2) (1981) 162–166.
[9] A. Okabe, B. Boots, K. Sugihara, S.N. Chiu, Spatial Tessellations: Concepts and Applications of Voronoi Diagrams, vol. 501, John Wiley & Sons, 2009.
[10] Q. Du, V. Faber, M. Gunzburger, Centroidal Voronoi tessellations: applications and algorithms, SIAM Rev. 41 (4) (1999) 637–676.
[11] Q. Du, M. Gunzburger, Grid generation and optimization based on centroidal Voronoi tessellations, Appl. Math. Comput. 133 (2) (2002) 591–607.
[12] S. Valette, J.-M. Chassery, R. Prost, Generic remeshing of 3d triangular meshes with metric-dependent discrete Voronoi diagrams, IEEE Trans. Vis. Comput. Graph. 14 (2) (2008) 369–381.
[13] Q. Du, D. Wang, Anisotropic centroidal Voronoi tessellations and their applications, SIAM J. Sci. Comput. 26 (3) (2005) 737–761.
[14] S.P. Lloyd, Least squares quantization in pcm, IEEE Trans. Inf. Theory 28 (2) (1982) 129–137.
[15] J. MacQueen, et al., Some methods for classification and analysis of multivariate observations, in: Proceedings of the Fifth Berkeley Symposium on Mathematical Statistics and Probability, vol. 1, Oakland, CA, USA, 1967, pp. 281–297.
[16] L. Ju, Q. Du, M. Gunzburger, Probabilistic methods for centroidal Voronoi tessellations and their parallel implementations, Parallel Comput. 28 (10) (2002) 1477–1500.
[17] Q. Du, M. Emelianenko, Acceleration schemes for computing centroidal Voronoi tessellations, Numer. Linear Algebra Appl. 13 (2–3) (2006) 173–192.
[18] Y. Liu, W. Wang, B. Lévy, F. Sun, D.-M. Yan, L. Lu, C. Yang, On centroidal Voronoi tessellation—energy smoothness and fast computation, ACM Trans. Graph. 28 (4) (2009) 101.
[19] Q. Du, D. Wang, The optimal centroidal Voronoi tessellations and the Gersho's conjecture in the three-dimensional space, Comput. Math. Appl. 49 (9) (2005) 1355–1373.
[20] W. Bo, M. Shashkov, Adaptive reconnection-based arbitrary Lagrangian Eulerian method, J. Comput. Phys. 299 (2015) 902–939.
[21] Q. Du, M. Gunzburger, L. Ju, Advances in studies and applications of centroidal Voronoi tessellations, Numer. Math. 3 (2) (2010) 119–142.
[22] A. Genz, R. Cools, An adaptive numerical cubature algorithm for simplices, ACM Trans. Math. Softw. 29 (3) (2003) 297–308.
[23] Q. Du, M. Emelianenko, L. Ju, Convergence of the Lloyd algorithm for computing centroidal Voronoi tessellations, SIAM J. Numer. Anal. 44 (1) (2006) 102–119.
[24] R. Ostrovsky, Y. Rabani, L.J. Schulman, C. Swamy, The effectiveness of Lloyd-type methods for the k-means problem, in: 47th Annual IEEE Symposium on Foundations of Computer Science, 2006. FOCS'06, IEEE, 2006, pp. 165–176.
[25] S. Heß, V. Springel, Particle hydrodynamics with tessellation techniques, Mon. Not. R. Astron. Soc. 406 (4) (2010) 2289–2311.
[26] P. Espanol, Fluid particle model, Phys. Rev. E 57 (3) (1998) 2930.
[27] B. Hendrickson, T.G. Kolda, Graph partitioning models for parallel computing, Parallel Comput. 26 (12) (2000) 1519–1534.
[28] H. Meyerhenke, B. Monien, S. Schamberger, Graph partitioning and disturbed diffusion, Parallel Comput. 35 (10) (2009) 544–569.
[29] W. Yu, X. Li, A geometry-aware data partitioning algorithm for parallel quad mesh generation on large-scale 2d regions, Proc. Eng. 124 (2015) 44–56.
[30] H. Meyerhenke, B. Monien, S. Schamberger, Graph partitioning and disturbed diffusion, Parallel Comput. 35 (10–11) (2009) 544–569.